INFORMATION TO USERS

This manuscript has been reproduced from the microfilm master. UMI films the text directly from the original or copy submitted. Thus, some thesis and dissertation copies are in typewriter face, while others may be from any type of computer printer.

The quality of this reproduction is dependent upon the quality of the copy submitted. Broken or indistinct print, colored or poor quality illustrations and photographs, print bleedthrough, substandard margins, and improper alignment can adversely affect reproduction.

In the unlikely event that the author did not send UMI a complete manuscript and there are missing pages, these will be noted. Also, if unauthorized copyright material had to be removed, a note will indicate the deletion.

Oversize materials (e.g., maps, drawings, charts) are reproduced by sectioning the original, beginning at the upper left-hand corner and continuing from left to right in equal sections with small overlaps.

Photographs included in the original manuscript have been reproduced xerographically in this copy. Higher quality 6" x 9" black and white photographic prints are available for any photographs or illustrations appearing in this copy for an additional charge. Contact UMI directly to order.

ProQuest Information and Learning
300 North Zeeb Road, Ann Arbor, MI 48106-1346 USA
800-521-0600



Downloaded from SHAREOK. Persistent Handle URL: https://hdl.handle.net/11244/465

UNIVERSITY OF OKLAHOMA

GRADUATE COLLEGE

DUAL-POROSITY APPROACH TO WELLBORE STABILITY IN NATURALLY FRACTURED RESERVOIRS

A Dissertation

SUBMITTED TO THE GRADUATE FACULTY

in partial fulfillment of the requirements for the

degree of

Doctor of Philosophy

By

JINCAI ZHANG
Norman, Oklahoma
2002

UMI Number: 3045843



UMI Microform 3045843

Copyright 2002 by ProQuest Information and Learning Company.
All rights reserved. This microform edition is protected against unauthorized copying under Title 17, United States Code.

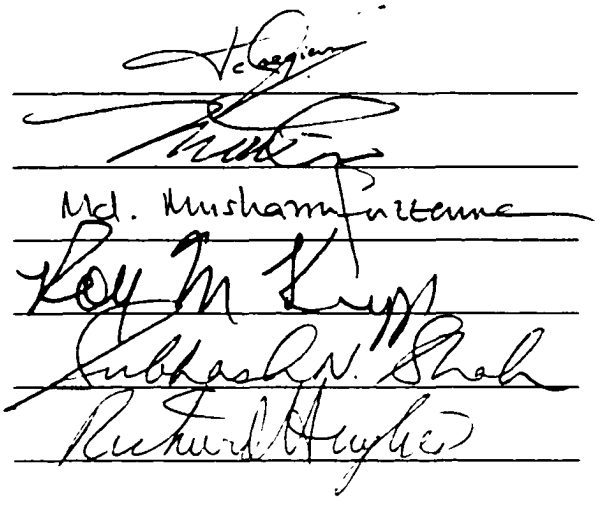
ProQuest Information and Learning Company
300 North Zeeb Road
P.O. Box 1346
Ann Arbor, MI 48106-1346

©Copyright by JINCAI ZHANG 2002
All Rights Reserved

DUAL-POROSITY APPROACH TO WELLBORE STABILITY IN NATURALLY FRACTURED RESERVOIRS

A Dissertation APPROVED FOR THE
MEWBOURNE SCHOOL OF PETROLEUM AND GEOLOGICAL ENGINEERING

BY



Dedicated to my wife,

Shuling Li

and our two sons,

Hal Haoshuang Zhang and *Owen Haoyu Zhang*

"A new commandment I give unto you, that ye love one another;

as I have loved you, that ye also love one another."

John 13:34

Acknowledgements

During my research and dissertation work, I have obtained so much support, collaboration and received encouragements from many special people, who make it possible for me to complete my degree.

My wholehearted thanks first go to my advisor, Dr. Jean-Claude Roegiers, who is the founding director of the Rock Mechanics Institute (RMI), for recruiting me in China and accepting me as a member of this Institute. His academic advice, guidance, encouragement, financial support, personal communication and kindness are greatly appreciated. It is his support that made it possible for me to present five papers and publish eight in five national/international rock mechanics/SPE conferences and journals in four years. His close reading, corrections and suggestions of innumerable drafts of this dissertation have been invaluable. Furthermore, his work enthusiasm and devotion to rock mechanics and petroleum engineering, his academic prestige, his scientific rigor, and his commitment to excellence have constantly encouraged me to strive for the best. He spent plenty of time and energy towards my studies, research and dissertation. Without his support, help, advice, encouragement and suggestion this dissertation would never have been completed. I deeply feel in debted to him.

My great thanks also go to Dr. Mao Bai, who was direct supervisor for my research work in RMI. His support, guidance, suggestions are highly appreciated. Innumerable technical discussions make this research and the IASRS software development possible. His overall friendship, personal help and encouragement enabled me to start this dissertation at an unfamiliar overseas environment.

My appreciation goes also to the help of other members of my advisory committee, Dr. Roy M. Knapp, Dr. Subhash Shah, Dr. Richard Hughes and Dr. Musharraf M. Zaman, who gave many constructive suggestions. From their courses I also learned some fundamentals in petroleum engineering and mechanics which are very essential for my dissertation and future career.

I also want to express my thanks to all the members of the Mewbourne School of Petroleum and Geological Engineering, especially Ms. Chyrl Yerdon.

I want to thank all my research group (IASRS) members, especially Mr. Don Cruickshank, Mr. Rajesh Nair and Mr. Weihong Zhang, for the many intellectual discussions and personal exchanges.

My appreciation goes to the support of all members of Rock Mechanics Institute at The University of Oklahoma, where I got partial financial support for my studies and research. Special thanks go to Dr. Younane Abousleiman for his administration, suggestion and academic exchange. Special thanks also to Ms. Carla Cates for making such a pleasant work environment in RMI.

Support and administration from The University of Oklahoma Graduate College are highly appreciated.

My profound gratitude goes to my family members. My parents (Mr. Chongji Zhang and Mrs. Guiqin Li) have given me so much love, support and inspiration from which I benefited so much. I would like to give my wholehearted thanks to them for their raising, loving, educating, encouraging and understanding. I also want to give thanks to my two brothers (Mr. Jinfu Zhang and Mr. Jinfa Zhang) and their families for taking care of our parents during my stay in the USA. I deeply appreciate my parents-in-law (Mr. Baozhen Li and Mrs. Xiuying Chen) for taking my responsibility of taking care of my little boy and my family. Also, help, support, inspiration from their whole family are greatly appreciated, so that I could concentrate my energy on my research and dissertation.

At last, but certainly not least, I give my earnest thanks to my wife and our two sons for their love, encouragement, patience and understanding. Without those this dissertation will never have been completed.

Contents

Acknowledgement v

List of Figures x

List of Tables xviii

Abstract xix

1 Introduction 1
1.1 Industry Concerns. . . . 1
1.2 Literature Review 5
1.2.1 Wellbore Stability. . . . 5
1.2.2 Naturally Fractured Reservoirs. . . . 10
1.2.3 Dual-porosity Approach. . . . 11
1.3 Objectives. . . . 15
1.4 Dissertation Description and Outline. . . . 15

2 Theoretical Background of Wellbore Problems 17
2.1 Elastic Solution. . . . 17
2.1.1 Vertical Borehole in An Isotropic Stress Field. . . . 17
2.1.2 Vertical Borehole in An Anisotropic Stress Field 18
2.1.3 Inclined Borehole in An Anisotropic Stress Field. . . . 20
2.2 Elastoplastic Solution. . . . 21

3 Dual-porosity Poromechanics 26
3.1 Dual-porosity Approaches. . . . 26
3.1.1 Dual-porosity Concept. . . . 26
3.1.2 Separate and Overlapping Model 30
3.2 Double Effective Law 31
3.3 Dual-porosity Formulations 34

4 Finite Element Implementation of Poro-mechanical Solutions 36
4.1 Introduction 36
4.2 Finite Element Method 37
4.3 Generalized Plane Strain Concept 38
4.4 Finite Element Discretization for Poroelastic Solution 42
4.4.1 Finite Element Mesh 42
4.4.2 Weighted Residuals Method 43
4.4.3 Shape Function 45
4.4.4 Conservation Equations 50
4.4.5 Finite Element Discretization in Time 53
4.4.6 Initial Condition and Ramp Loading 54

4.4.7 Computational Procedure and Computer Code 55
4.4.8 Elasticity and Steady-state Flow 57
4.4.9 Single-porosity Poroelasticity 58
4.5 Finite Element Method for Poroelastoplastic Solution 58
4.5.1 Initial Stress Method 60
4.5.2 Bi-linear Stress-strain Relationship 63
4.6 Wellbore Problem Solution 64
4.6.1 Stress Conversion for Inclined Borehole 64
4.6.2 Stress Transformation from Cartesian Coordinates into Polar Coordinates 69
4.6.3 Fluid Mudweight Considerations at the Borehole Wall 70

5 Finite Element Model Validation **73**
5.1 Introduction 73
5.2 One-dimensional Consolidation 73
5.3 Dual-porosity Elastoplastic One-dimensional Consolidation 79
5.3.1 Mathematical Formulation for One-dimensional Consolidation 79
5.3.2 Analyses for Dual-porosity Isothermal Consolidation 87
5.3.3 Analyses for Dual-porosity Non-isothermal Consolidation 94
5.4 Inclined Wellbore Problem 99
5.4.1 Inclined Borehole Without Mudweight 99
5.4.2 Inclined Borehole With Mudweight 106

6 Parametric Study **111**
6.1 Dual-porosity Effects 112
6.2 Time-dependent Effects 117
6.3 Fracture Spacing Effects 128
6.4 Fracture Stiffness Effects 135
6.5 Fracture and Matrix Permeability Effects 141
6.6 Borehole Inclination Effects 147
6.7 Mud Weight Effects 154
6.8 Mud Cake Effects 162

7 Wellbore Failure Analysis **166**
7.1 Compressive Failure 166
7.2 Tensile Failure 168
7.2.1 Spalling Failure 168
7.2.2 Fracturing Failure 171
7.3 Mohr-Coulomb Failure 173
7.4 Drucker-Prager Failure 176

8 Model Applications **181**
8.1 Inclined and Horizontal Wellbores 181
8.1.1 Wellbore in Normal Stress Regime 181
8.1.2 Wellbore in Tectonic Stress Regime 189
8.1.3 Drilling Directions for Horizontal Wellbores 193
8.1.4 Wellbore in Faulted Areas 203

8.2 Wellbore in Poorly-consolidated Formations. 207
8.3 Stress-dependent Permeability around A Wellbore. 212
8.4 Rock Comminution. 216

9 Conclusions and Recommendations **222**
9.1 Conclusions. 222
9.2 Recommendations for Future Research 224

References **226**

Appendix A Terms in Finite Element Matrices **238**

Appendix B Invariants of the Stress and Stress Deviator Tensors **239**

Appendix C Coefficients in Elastoplastic One-dimensional Consolidation **241**

Appendix D Stress-dependent Permeability in Fractured Media **244**

List of Figures

1.1.1 Example of borehole shearing observed when crossing a fault mapped using a BHTV (after Maury and Zurdo, 1996) 3
1.1.2 Schematic of stress-induced wellbore instability 4

2.1.1 A borehole in an isotropic stress field 17
2.1.2 A vertical borehole in an anisotropic stress field 19
2.2.1 A borehole in an ideal elastoplastic material 21
2.2.2 Stress states around a borehole in elastic and elastoplastic solutions 25

3.1.1 Dual-porosity models for the naturally fractured reservoir (from Kazemi et al., 1993) 27
3.1.2 Schematic dual-porosity medium 28
3.1.3 Naturally fractured and ideally dual-porosity reservoirs 29
3.1.5 Separate and overlapping model in dual-porosity media 30

4.4.1 Discretization of generalized plane strain problem domain 43
4.4.2 Ramp loading in approximation of initial condition 55
4.4.3 Finite element solution procedure 56
4.4.4 Structure of the finite element code 56
4.5.1 Bi-linear stress-strain relationship 63
4.5.2 Flowchart for the Bi-linear analysis 64
4.6.1 Schematic diagram for an inclined borehole 66
4.6.2 Local and global coordinate systems for an inclined borehole 66
4.6.3 Finite element mesh in local coordinate system 67
4.6.4 Boundary nodal forces at borehole wall 68
4.6.5 Superposition of mudweight pressure at the borehole wall for the permeable case in the FEM model 71
4.6.6 Superposition of mudweight pressure at the borehole wall for the impermeable case in the FEM model 72

5.2.1 Consolidation problem and boundary conditions 76
5.2.2 Comparison of temporal displacement at top column 78
5.2.3 Comparison of spatial pore pressure along the column 78
5.3.1 Schematic one-dimensional column 80
5.3.2 Temporal pressure comparison between single- and dual-porosity models 90
5.3.3 Temporal displacement comparison between single- and dual-porosity models 91
5.3.4 Temporal plastic zone comparison between single- and dual-porosity models . 91
5.3.5 Temporal fracture pressures for different fracture spacings 92
5.3.6 Temporal matrix pressures for different elastoplastic moduli 92
5.3.7 Temporal matrix pressures for different elastoplastic moduli 93
5.3.8 Temporal fracture pressures for different elastoplastic moduli 93
5.3.9 Matrix pressure comparison for single-, dual- and thermal dual-porosity Consolidations 95

5.3.10 Fracture pressure comparison for dual- and thermal dual-porosity Consolidations 95
5.3.11 Temperature comparison for dual- and thermal dual-porosity consolidations .. 96
5.3.12 Temporal matrix pressure for different fracture spacings 97
5.3.13 Temporal matrix temperature for different fracture spacings 97
5.3.14 Temporal fracture temperature for different fracture spacings 98
5.3.15 Temporal matrix temperature for different fluid thermal conductivities 98
5.3.16 Temporal fracture temperature for different fluid thermal conductivities 99
5.4.1 Comparison between the finite element and analytical solutions for pore pressure ($\theta = 84.4°$) 102
5.4.2 Comparison between the finite element and analytical solutions for pore pressure ($\theta = 5.7°$) 102
5.4.3 Comparison between the finite element and analytical solutions for Terzaghi's effective radial stress ($\theta = 84.4°$) 103
5.4.4 Comparison between the finite element and analytical solutions for Terzaghi's effective radial stress ($\theta = 5.7°$) 104
5.4.5 Comparison between the finite element and analytical solutions for Terzaghi's effective radial stress along different radial sections for t = 100 seconds 104
5.4.6 Comparison between the finite element and analytical solutions for tangential stress along different radial sections ($\theta = 5.7°$, $\theta = 84.4°$) and times (t = 1.3 min, t = 21.6 min) 105
5.4.7 Comparison between the finite element and analytical solutions for axial stress along different radial sections ($\theta = 0°$, $\theta = 90°$) and times (t = 1.3 min, t = 21.6 min) 106
5.4.8 Comparison between the finite element and analytical solutions for pore pressure ($\theta = 30°$) 107
5.4.9 Comparison between the finite element and analytical solutions for pore pressure ($\theta = 90°$) 107
5.4.10 Comparison between the finite element and analytical solutions for Terzaghi's effective radial stress ($\theta = 30°$) 108
5.4.11 Comparison between the finite element and analytical solutions for Terzaghi's effective radial stress ($\theta = 90°$) 108
5.4.12 Comparison between the finite element and analytical solutions for Terzaghi's effective tangential stress ($\theta = 30°$) 109
5.4.13 Comparison between the finite element and analytical solutions for Terzaghi's effective tangential stress ($\theta = 90°$) 109
5.4.14 Comparison between the finite element and analytical solutions for total radial and tangential stresses along the radial sections $\theta = 30°$ for impermeable model 110

6.1 State of stress in the borehole local coordinate after 70° inclination 111
6.1.1 Comparison of pore pressure for single- and dual-porosity models in the maximum stress direction at t = 100 s 113
6.1.2 Comparison of pore pressure for single- and dual-porosity models in the minimum stress direction at t = 100 s 113

6.1.3 Comparison of effective radial stress for single- and dual-porosity models in the maximum stress direction at t = 100 s 114
6.1.4 Comparison of total radial stress for single- and dual-porosity models in the maximum stress direction at t = 100 s 114
6.1.5 Comparison of effective radial stress for single- and dual-porosity models in the minimum stress direction at t = 100 s 115
6.1.6 Comparison of total radial stress for single- and dual-porosity models in the minimum stress direction at t = 100 s 115
6.1.7 Comparison of effective tangential stress for single- and dual-porosity models in the minimum stress direction at t = 100 s 116
6.1.8 Comparison of effective axial stress for single- and dual-porosity models in the maximum stress direction at t = 100 s 116
6.2.1 Pore pressure distribution around the wellbore at t = 10 s 117
6.2.2 Pore pressure distribution around the wellbore at t = 100 s 118
6.2.3 Pore pressure distribution around the wellbore at t = 1000 s 118
6.2.4 Pore pressure around the wellbore at θ = 0° for different times 119
6.2.5 Pore pressure around the wellbore at θ = 60° for different times 119
6.2.6 Pore pressure around the wellbore at θ = 90° for different times 120
6.2.7 Radial stress distribution around the wellbore at t = 10 s 121
6.2.8 Radial stress distribution around the wellbore at t = 100 s 121
6.2.9 Radial stress distribution around the wellbore at t = 1000 s 122
6.2.10 Effective radial stress in the maximum stress direction for different times ... 122
6.2.11 Effective radial stress in the minimum stress direction for different times 123
6.2.12 Tangential stress distribution around the wellbore at t = 10 s 124
6.2.13 Tangential stress distribution around the wellbore at t = 100 s 124
6.2.14 Tangential stress distribution around the wellbore at t = 1000 s 125
6.2.15 Effective tangential stress distribution, at θ = 0° and θ = 90°, for different times 125
6.2.16 Total tangential stress distribution, at θ = 0° and θ = 90°, for t = 100 s 126
6.2.17 Effective axial stress distribution in the maximum stress direction for different times 127
6.2.18 Effective axial stress distribution in the minimum stress direction for different times 127
6.3.1 Pore pressure distribution around the wellbore at t = 100 s, s = 0.1 m 128
6.3.2 Pore pressure distribution around the wellbore at t = 100 s, s = 10 m 129
6.3.3 Pore pressure around wellbore in maximum stress direction at t = 100 s for different fracture spacings 129
6.3.4 Pore pressure around wellbore in minimum stress direction at t = 100 s for different fracture spacings 130
6.3.5 Radial stress distribution around the wellbore at t = 100 s, s = 0.1 m 131
6.3.6 Radial stress distribution around the wellbore at t = 100 s, s = 10 m 131
6.3.7 Radial stress around wellbore in the minimum stress direction at t = 100 s for different fracture spacings 132
6.3.8 Radial stress around wellbore in the maximum stress direction at t = 100 s for different fracture spacings 132
6.3.9 Tangential stress distribution around the wellbore at t = 100 s, s = 0.1 m ... 133

6.3.10 Tangential stress distribution around the wellbore at t = 100 s, s = 10 m 134
6.3.11 Effective tangential around wellbore in the minimum stress direction at t = 100 s for different fracture spacings 134
6.3.12 Effective axial stress around wellbore in the maximum stress direction at t = 100 s for different fracture spacings 135
6.4.1 Radial stress distribution around the wellbore at t = 100 s and for K_n = 4.821GPa/m 136
6.4.2 Radial stress distribution around the wellbore at t = 100 s and for K_n = 48.21GPa/m 137
6.4.3 Pore pressure around wellbore in the maximum stress direction at t = 100 s for different fracture stiffnesses 137
6.4.4 Pore pressure around wellbore in the minimum stress direction at t = 100 s for different fracture stiffnesses 138
6.4.5 Radial stress distribution around the wellbore for K_n = 4.821GPa/m 138
6.4.6 Radial stress distribution around the wellbore for K_n = 48.21GPa/m 139
6.4.7 Radial stress around wellbore in the maximum stress direction at t = 100 s for different fracture stiffnesses 139
6.4.8 Radial stress around wellbore in the minimum stress direction at t = 100 s for different fracture stiffnesses 140
6.4.9 Tangential stress distribution around the wellbore for K_n = 4.821GPa/m 140
6.4.10 Tangential stress distribution around the wellbore for K_n = 4.821GPa/m 141
6.5.1 Pore pressure around wellbore in the maximum stress direction at t = 100 s for different permeability ratios 142
6.5.2 Pore pressure around wellbore in the minimum stress direction at t = 100 s for different permeability ratios 143
6.5.3 Pore pressure distribution at t = 100 s for a permeability ratio of k_{ma}/k_{fr} = 1 143
6.5.4 Pore pressure distribution at t = 100 s for a permeability ratio of k_{ma}/k_{fr} = 0.01 144
6.5.5 Radial stress distribution at t = 100 s for a permeability ratio of k_{ma}/k_{fr} = 1 144
6.5.6 Radial stress distribution at t = 100 s for a permeability ratio of k_{ma}/k_{fr} = 0.01 145
6.5.7 Radial stress around wellbore in the maximum stress direction at t = 100 s for different permeability ratios 145
6.5.8 Radial stress around wellbore in the maximum stress direction at t = 100 s for different permeability ratios 146
6.5.9 Effective tangential stress distribution, at t = 100 s, θ = 0° and θ = 90° for different permeability ratios 146
6.5.10 Effective axial stress distribution, at t = 100 s, θ = 0°, for different permeability ratios 147
6.6.1 Pore pressure distribution at t = 100 s, θ = 0° for different borehole plunges, φ_z 148
6.6.2 Pore pressure distribution at t = 100 s for a hole inclination of 0° 148
6.6.3 Pore pressure distribution at t = 100 s for a hole inclination of 90° 149
6.6.4 State of stress in the local coordinate systems after 0° and 90° inclinations ..149

6.6.5 Pore pressure distribution at t = 100 s, θ = 90° for different borehole plunges, φ_z 150
6.6.6 Effective radial stress distributions, at t = 100 s, θ = 0°, for different borehole plunges, φ_z 151
6.6.7 Effective radial stress distributions, at t = 100 s, θ = 90°, for different borehole plunges, φ_z 151
6.6.8 Radial stress distribution at t = 100 s for hole inclination of 0° 152
6.6.9 Radial stress distribution at t = 100 s for hole inclination of 90° 152
6.6.10 Effective tangential stress distributions, at t = 100 s, θ = 90°, for different plunges, φ_z 153
6.6.11 Effective axial stress distributions, at t = 100 s, θ = 90°, for different borehole plunges, φ_z 153
6.7.1 Pore pressure along the maximum stress direction at t = 100 s for different mud pressures 155
6.7.2 Pore pressure along the minimum stress direction at t = 100 s for different mud pressures 155
6.7.3 Pore pressure distribution at t = 100 s for a mud pressure of p_w = 6 MPa 156
6.7.4 Pore pressure distribution at t = 100 s for a mud pressure of p_w = 25 MPa 156
6.7.5 Radial stress distribution at t = 100 s for a mud pressure of p_w = 6 MPa 157
6.7.6 Radial stress distribution at t = 100 s for a mud pressure of p_w = 25 MPa 157
6.7.7 Effective radial stress along the maximum stress direction at t = 100 s for different mud pressures 158
6.7.8 Effective radial stress along the minimum stress direction at t = 100 s for different mud pressures 158
6.7.9 Effective tangential stress along the maximum stress direction at t = 100 s for different mud pressures 159
6.7.10 Effective tangential stress along the minimum stress direction at t = 100 s for different mud pressures 159
6.7.11 Tangential stress distribution at t = 100 s for a mud pressure of p_w = 6 MPa 160
6.7.12 Tangential stress distribution at t = 100 s for a mud pressure of p_w = 25 MPa 160
6.7.13 Effective axial stress along the maximum stress direction at t = 100 s for different mud pressures 161
6.7.14 Effective axial stress along the minimum stress direction at t = 100 s for different mud pressures 161
6.8.1 Pore pressure along the maximum stress direction at t = 100 s for wellbores with and without mud cake 163
6.8.2 Pore pressure along the minimum stress direction at t = 100 s for wellbores with and without mud cake 163
6.8.3 Radial stress along the maximum stress direction at t = 100 s for wellbores with and without mud cake 164
6.8.4 Radial stress along the minimum stress direction at t = 100 s for wellbores with and without mud cakes 164
6.8.5 Tangential stress along the maximum and minimum stress directions at t = 100 s for wellbore with and without mud cakes 165

7.1.1 Compressive failure area for a stress-free borehole wall 167

7.1.2 Effective compressive failure stresses for different hole inclinations along the minimum stress azimuth at t = 100 s 168
7.2.1 Spalling failure area for a stress-free borehole wall 170
7.2.2 Effective spalling stresses for different hole inclinations along the maximum stress direction at t = 100 s 170
7.2.3 Effective spalling stresses for different hole inclinations along the minimum stress direction at t = 100 s 171
7.2.4 Fracturing area for mud pressure p_w = 25 MPa 172
7.2.5 Effective fracturing stresses for different hole inclinations along the maximum stress direction at p_w = 25 MPa, t = 100 s 173
7.3.1 Mohr-Coulomb failure criterion 174
7.3.2 Mohr-Coulomb failure criterion in the principal stress space 174
7.3.3 Mohr-Coulomb failure area for a stress-free borehole wall 175
7.3.4 Effective Mohr-Coulomb failure stresses for different hole inclinations along the minimum stress direction at t = 100 s 176
7.4.1 Coulomb yield surface and different possibilities for corresponding Drücker-Prager yield conditions 178
7.4.2 Collapse failure area for a stress-free borehole wall 179
7.4.3 Effective collapse stresses for different hole inclinations along the minimum stress direction at t = 100 s 180

8.1.1 Mohr-Coulomb failure area in the normal stress region at t = 100 s for a borehole inclination of 50° 183
8.1.2 Mohr-Coulomb failure area in the normal stress region at t = 100 s for a borehole inclination of 90° 184
8.1.3 State of stress in local system for a borehole drilled in two different orientations (φ_z = 0 and 90°) 184
8.1.4 Collapse area in the normal stress region at t = 100 s for a hole inclination of 50° 185
8.1.5 Collapse area in the normal stress region at t = 100 s for a hole inclination of 90° 186
8.1.6 Spalling area in the normal stress region at t = 100 s for a hole inclination of 0° 186
8.1.7 Spalling area in the normal stress region at t = 100 s for a hole inclination of 90° 187
8.1.8 Effective radial stresses along borehole sidewall for a normal stress regime at t = 100 s for different hole inclinations 187
8.1.9 Mud weight range varying with the hole inclinations for collapse and fracturing at t = 100 s 188
8.1.10 Mud weight range varying with the hole inclinations for spalling and fracturing at t = 100 s 189
8.1.11 Mohr-Coulomb failure area in the tectonic stress region at t = 100 s for a borehole inclination of 0° 190
8.1.12 Mohr-Coulomb failure area in the tectonic stress region at t = 100 s for a borehole inclination of 90° 190
8.1.13 Collapse area in the tectonic stress region at t = 100 s for a borehole

inclination of 0° 191
8.1.14 Collapse area in the tectonic stress region at t = 100 s for a borehole inclination of 90° 191
8.1.15 Mud weight range varying with the hole inclinations for collapse and fracturing at t = 100 s in a tectonic stress regime 192
8.1.16 Mud weight range varying with the hole inclinations for spalling and fracturing at t = 100 s in a tectonic stress regime 193
8.1.17 Collapse area in the tectonic stress region at t = 100 s for a horizontal borehole drilled parallel to the minimum stress 195
8.1.18 Collapse area in the tectonic stress region for a horizontal borehole drilled parallel to the minimum stress during production (bottom pressure 10 MPa) . 195
8.1.19 Shear failure area in the tectonic stress region at t = 100 s for a horizontal borehole drilled parallel to the maximum stress 196
8.1.20 Shear failure area in the tectonic stress region at t = 100 s for a horizontal borehole drilled parallel to the minimum stress 196
8.1.21 Shear area in the tectonic stress region for a horizontal borehole drilled parallel to the minimum stress during production (bottom pressure 10 MPa) . 197
8.1.22 Shear failure area in normal stress region at t = 100 s for a horizontal borehole drilled parallel to the maximum stress 198
8.1.23 Shear failure area in normal stress region at t = 100 s for a horizontal borehole drilled parallel to the minimum stress 199
8.1.24 Mohr-Coulomb failure stresses in the hole crown at t = 100 s for a borehole without support and parallel to the minimum and maximum stress directions .199
8.1.25 Shear failure area in normal stress region at t = 100 s for a horizontal borehole drilled parallel to the maximum stress during production (bottom pressure 31.7 MPa) 200
8.1.26 Shear failure area in normal stress region at t = 100 s for a horizontal borehole drilled parallel to the minimum stress during production (bottom pressure 31.7 MPa) 200
8.1.27 Collapse area in normal stress region at t = 100 s for a horizontal borehole drilled parallel to the maximum stress 201
8.1.28 Collapse area in normal stress region at t = 100 s for a horizontal borehole drilled parallel to the minimum stress 201
8.1.29 Collapse area in normal stress region at t = 100 s for a horizontal borehole drilled parallel to the maximum stress during production (bottom pressure 31.7 MPa) 202
8.1.30 Collapse area in normal stress region at t = 100 s for a horizontal borehole drilled parallel to the minimum stress during production (bottom pressure 31.7 MPa) 202
8.1.31 Finite element mesh for a half of borehole with weak rock zone 203
8.1.32 Collapse area in tectonic stress regime for t = 100 s in case of an inclined borehole intersected with a weak rock zone without any internal support 205
8.1.33 Shear failure area in tectonic stress regime at t = 100 s for an inclined borehole intersected by a weak rock zone without any internal support 206
8.1.34 Fracturing area in tectonic stress regime at t = 100 s for an inclined borehole intersected by a weak rock zone with a mud pressure of 24 MPa 206

8.2.1 Pore pressure response for permeable and impermeable models in the minimum stress direction at t = 100 s 209
8.2.2 Radial stress response for permeable and impermeable models in the minimum stress direction at t = 100 s 209
8.2.3 Tangential stress response for permeable and impermeable models in the minimum stress direction at t = 100 s 210
8.2.4 Effective Mohr-Coulomb failure stresses for permeable and impermeable models in the minimum stress direction at t = 100 s. 211
8.2.5 Mud weight range varying with the hole inclinations for permeable model at t = 100 s 211
8.2.6 Mud weight range varying with the hole inclinations for impermeable model at t = 100 s 212

8.3.1 Contour of horizontal permeability ratio (k_x / k_0) in the fractured formation due to borehole excavation 214
8.3.2 Contour of vertical permeability (k_y / k_0) in the fractured formation due to borehole excavation 214
8.3.3 Permeability variations in the x-direction in the fractured formation due to borehole excavation 215
8.3.4 Permeability variations in the y-direction in the fractured formation due to borehole excavation 215

8.4.1 Finite element mesh for drilling bit cutting problem 216
8.4.2 Stress configration for the bit and rock interaction in normal stress regime . . . 217
8.4.3 Formation shear failure area around the cutter in normal stress regime for cutter loading 40 MPa at t = 100 s 217
8.4.4 Formation tensile failure area around the cutter in normal stress regime for cutter loading 50 MPa at t = 100 s 218
8.4.5 Stress configration for the bit and rock interaction in tectonic stress regime . . 219
8.4.6 Formation shear failure area around the cutter in normal stress regime for cutter loading 40 MPa at t = 100 s 219
8.4.7 Formation tensile failure area around the cutter in normal stress regime for cutter loading 40 MPa at t = 100 s 220
8.4.8 Schematic diagram of formation failure around the cutter in normal stress regime 220
8.4.9 Schematic diagram of formation failure around the cutter in tectonic stress regime 221

List of Tables

2.2.1 Parameters used for elastic and elastoplastic calculations. 24

4.5.1 Constants B_i defined by different yield surfaces (Chen and Han, 1995) 62

5.2.4 Parameters for comparative analysis in 1-D consolidation 77
5.3.1 Selected poroelastoplastic parametric ranges 88
5.3.2 Selected thermal parameters 94
5.4.1 Parameters for inclined borehole analysis 101

7.4.1 Material parameter conversion from the Coulomb criterion ($\varphi = 30°$ and $c = 11.5$ MPa) to the Drüker-Prager criterion 179

8.1.1 Parameters for analyses of the borehole in normal stress region 182
8.1.2 Material parameters in the weak and normal rock region 204

8.2.1 Parameters for inclined borehole analysis 208

Abstract

Borehole instabilities can be encountered at any stage in the life of a well, including drilling, completion and stimulation, flow tests, production, and depletion. Borehole instabilities are the main cause of drilling difficulties, resulting in substantial expenditures, expensive loss of time, sometimes even in the loss of part of or even whole boreholes.

One of the most prominent features of rock formations is the presence of joints and fractures at all scales. Many petroleum reservoirs are situated in fractured porous formations. When boreholes are drilled in such formations, wellbore stability has been a major concern. In order to accurately predict the wellbore behavior in fractured porous media, the matrix and fracture deformations as well as fluid flow in both pores and fractures need to be fully-coupled. This study was carried out to analyze the stability of boreholes in naturally fractured reservoirs.

The analytical method is applied to solve wellbore problems in elastic and plastic media, the closed-form solutions are given to validate the numerical solutions.

The naturally fractured reservoir was treated as a dual-porosity medium consisting of the primary rock matrix system and the fractured system. The fracture and matrix systems in the fractured reservoir are distinctly different in both porosity and permeability. The global flow occurs primarily through the high-permeability, low-porosity fracture system surrounding the matrix rock blocks. The matrix blocks contain the majority of the reservoir storage volume and act as local source to the fracture system. The fractures are interconnected and provide the main fluid flow path to the wells. Assuming the matrix and fractures in the fractured medium to be 'separate and overlapping', and applying the double effective law, the dual-porosity formulations that couple matrix and fracture deformations and fluid flow in the matrix and fracture systems for the fractured porous formations were presented.

To overcome the solution difficulties in the most general case, the numerical method was applied to solve the dual-porosity formulations. The finite element solution and a windows-based pseudo-three-dimensional finite element software for any directional

wellbore drilled in dual-porosity media were given, in which the mud weight considerations were presented for the permeable and impermeable boundary conditions. These allow to simulate borehole drilling with mud cake case as well as wellbores supported by a casing. Furthermore, the elastoplastic finite element method and computational procedure were presented in the dissertation.

The proposed theoretical formulation and the finite element model were validated with several cases where the analytical solutions are available. The one-dimensional single-porosity consolidation problem was used to verify the numerical algorithm for the coupled deformation and fluid flow systems. The finite element model was also validated against analytical solutions of elastic wellbore problems and single-porosity inclined wellbore problems with permeable and impermeable boundary conditions. In addition, an one-dimensional dual-porosity elastoplastic anisothermal consolidation solution was presented, which can be used for future validations.

The effects of single- and dual-porosity, time, hole inclination, fracture spacing and stiffness, permeabilities, and mud weight on the borehole solutions were parametrically studied. This allows a better understanding of the developed finite element model and the physical characteristics of the borehole problems. The failure criteria, including compressive failure, tensile failures (spalling and fracturing), shear failures (Mohr-Coulomb and Drücker-Prager/collapse) were introduced into the numerical model and failure stresses and failure areas around boreholes were examined.

Several application examples including inclined and horizontal wellbore in different in-situ stress regions, the best trajectory selections for horizontal borehole, rock cutting mechanism, and stress-dependent permeability around wellbores were investigated. The upper and lower bound critical mud weights were determined and the most stable orientations of the borehole were discussed.

Chapter 1

Introduction

1.1 Industry Concerns

The oil and gas industry is developing increasingly difficult reservoirs, challenging traditional approaches and proving the importance of rock mechanics. A large number of current oil and gas reservoirs in the world, including some major fields in the Gulf of Mexico, Campos basin, offshore Brazil, China Bohai Bay, are located in formations involving geologically young unconsolidated sands where grains are either lightly cemented or even unbonded (Monus et al., 1992). Main problems associated with these weak formations are wellbore stability and sand production. One area where operators experienced immense wellbore problems is the US Gulf Coast, where wellbore collapse and sanding are plaguing many completions because of the presence of unconsolidated sands and reactive shales (Li, 1998). In soft, weak rocks, the deformation, failure and flow processes are dominated by non-linear stress-deformation responses, high fluid flow rates, and shearing accompanied by dilantancy or compaction. Borehole stability issues in these formations have different characteristics; hence, new approaches and models are required.

Many innovative technologies have been applied in the oil and gas industry, such as underbalanced drilling, high pressure jet drilling, re-entry horizontal wells, and multilaterials from a single well which have definitely increased the demand for wellbore stability studies. Recently, technological advances have been pushing the reach of boreholes beyond 25,000 ft in length (Ramos et al., 1996). Highly inclined, extended-reach wellbores must remain open for prolonged time periods, not only during the drilling program but also over the life of a reservoir. New challenges also emerged since

the increasing use of horizontal wells, drilling in naturally fractured media, in very deep formations, and difficult geological conditions, where wellbore stability is of major concern (Willson and Willis, 1986). For example, a 8,715 m deep well was drilled in crystalline rock in Germany and some types of wellbore instabilities (breakouts, washout zones, undergauge sections) were observed (Hoffers et al., 1994). Some wellbore instabilities associated with complex geologic conditions, where the stress regime is controlled by active faulting wave, are reported in the Cusiana field (Colombia), the Pedernales field (Venezuela), the Alberta Basin (Canada), the Tarim Basin (China), certain areas of the Norwegian Sea, and offshore Indonesia (Willson et al., 1999; Plumb et al., 1998; Wiprut and Zoback, 1998; Ramos et al., 1998). When boreholes are drilled in a naturally fractured formation, excessively high mud density allows the drilling fluid to penetrate into fractures, mobilizing the rocky blocks and intensifing ovalisation (Charlez, 1999). When this occurs, the fractured blocks are no longer subject to the mud overbalance pressure, and the destabilized blocks can cave into the wellbore as a result of swabbing the formation when tripping (Willson et al., 1999). When boreholes cross a fault, mud may invade the discontinuity plane. Apart from mud losses, penetration of the fluid reduces the normal stress and induces a displacement along the crack planes which might shear the well, as shown in Figure 1.1.1 (Maury and Zurdo, 1996). The consequences can quickly become dramatic and could lead to partial or even total loss of a well. Two case histories in Aquitaine, France were described that resulted in the loss of the wells and the need for the drilling of two new wells, costing in the range of US$30 million (Maury and Zurdo, 1996).

Wellbore instability can result in lost circulation where tensile stresses have occurred (Figure 1.1.2a); breakouts and hole closure in case of compressive failure (Figure 1.1.2b). In severe cases the borehole instability can lead to stuck pipe and, eventually, loss of the open hole section (McLean and Addis, 1990). The borehole stability problem can be considered by separating the potential rock failure mechanisms into the following four categories (Roegiers, 1990):

1) failures related to pre-existing or drilling-induced formation damage;

2) failures caused by the induced stress concentrations;

3) failures attributed to deliberate or unintentional additional stresses; and,

4) failures related to shock-wave loading.

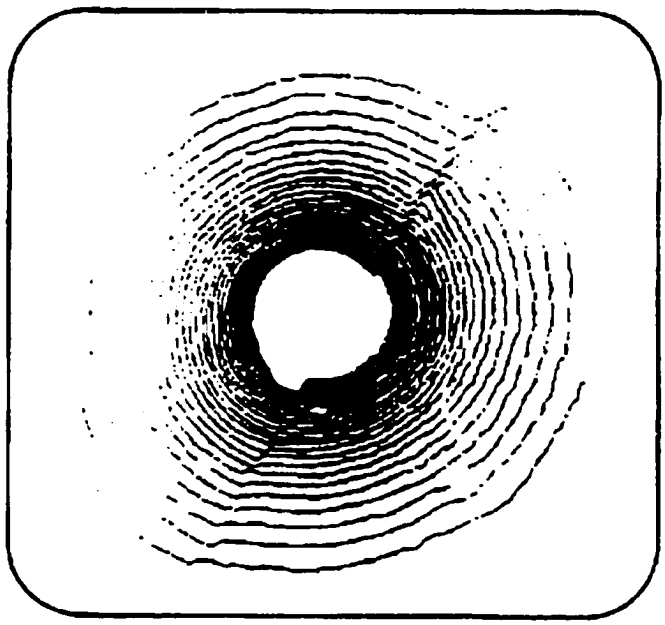


Figure 1.1.1 Example of borehole shearing observed when crossing a fault mapped using a BHTV (after Maury and Zurdo, 1996)

Borehole instabilities are the main cause of drilling difficulties, resulting in an expensive loss of time, sometimes in a loss of part of or even whole boreholes. Wellbore instabilities make logging very difficult to perform and also to interpret (Maury and Sauzay, 1987). A bad condition of the borehole wall alters artificially the annulus zone corresponding to the depth of investigation of most of the logging tools. The shape of the borehole can be strongly modified giving an elongated hole in one direction, diameter reduction in the other direction and also almost circular cavings in places. Cuttings removal can be affected, plugging the annulus and making trips difficult; moreover it can induce casing collapse. Wellbore instabilities result in substantial expenditure, loss of time and sometimes equipment with estimates running into a conservative US$ 500 million per year worldwide (Bol et al, 1992; Mody and Hale, 1993; Dusseault, 1994). In the Cusiana field in Colombia, even though some measures to prevent borehole

instability were taken, extensive breakouts in fissile and naturally fractured shales – of up to 44" in $12^{1}/_{4}$" hole – occurred (Willson et al., 1999). Approximately 10% of the well costs in the Cusiana field are spent coping with bad holes, mainly because of abnormally high tectonic stresses induced by an active thrust-faulting environment (Addis et al., 1993; Last and McLean, 1995). Borehole instabilities in naturally fractured reservoirs are reported in Venezuela (Roegiers, 2001). In addition to the cost associated with borehole instability while drilling, borehole stability also has a substantial impact on reservoir productions (Bradley, 1979).

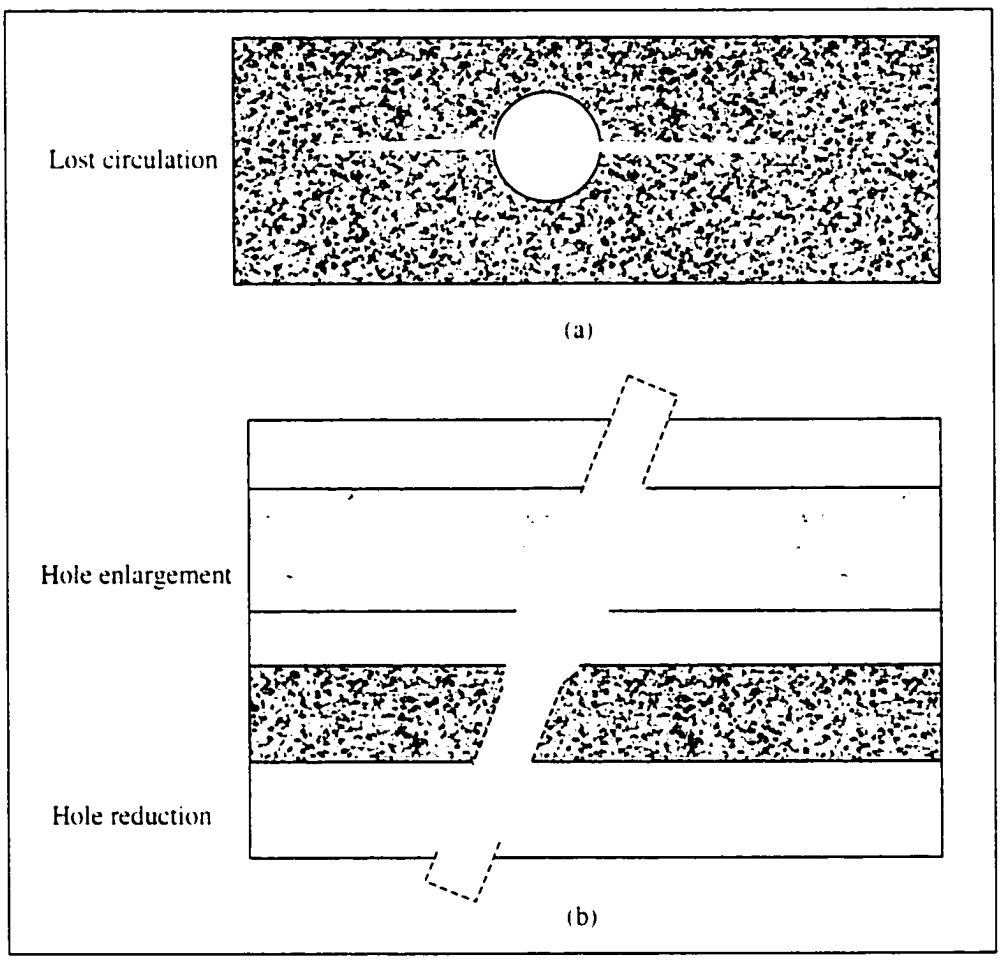


Figure 1.1.2 Schematic of stress-induced wellbore instability

There are several stages in the life of a well, i.e., drilling, completion and stimulation, and flow tests, production, and depletion. Borehole instabilities can be encountered in all

these stages (Ramos et al., 1996). In the drilling stage, the main concerns are to determine the mud composition and density which will maintain the integrity of the well, without the loss of drilling fluids. During the completion and stimulation stage, the reservoir must be connected to the well via perforations. This operation could fail if the rock adjacent to the cemented casing is non-brittle. Prior to full production, downhole tests include open-hole logging, fluid sampling, build-up, drawdown, injection, and deliverability tests. It is possible to induce wellbore failure and collapse during these processes. As hydrocarbons are depleted, the drained region compacts which could induce solids production, casing damage, surface subsidence and wellbore failure. All three stages in the life of a well, borehole integrated stability analyses are important to ensure the reservoir economical production and minimize the costly problems induced by the wellbore instabilities.

1.2 Literature Review

Study of borehole (circular opening) stability in naturally fractured reservoir is of critical importance in a number of disciplines including petroleum, civil, mining, and geothermal engineering. Study of borehole stability in naturally fractured porous media deals with several different disciplines and research areas, including solid mechanics, poromechanics, fluid mechanics, fractured porous media, coupling fluid flow and rock deformation etc. This review includes mainly three aspects, namely, wellbore stability, naturally fractured reservoir, and dual-porosity poromechanics.

1.2.1 Wellbore Stability

1.2.1.1 Elastic model

Hubbert and Willis (1957) first applied Kirsch's elastic solution (refer to Boresi and Chong, 1974) to predict the stability of a vertical borehole subjected to a non-hydrostatic

far field stress and constant borehole fluid pressure. For a borehole of arbitrary trajectory, Fairhurst (1968) derived a solution for the stress distribution around an inclined borehole by including the stresses induced by anti-plane shear. The stability of unsupported or pressurized inclined boreholes has been the subject of many investigations since the late 1970's. Early analyses addressing stress-induced lost circulation and borehole collapse were presented by Bradley (1979), in which the rock was assumed to be a linear elastic material, and fluid flow into or out of the formation was not considered.

The inclusion of stress-dependent elastic moduli into wellbore stability analyses was investigated by Santarelli (1987) and Santarelli and Brown (1987). Using a power law variation for Young's modulus as a function of the confining stress for a vertical borehole in an elastic medium with isotropic horizontal stresses, a generalized representation of Hooke's law was presented. The conclusions drawn from these studies were that the maximum tangential stress computed at the borehole was found to be lower than those predicted by linear elastic theory and that the maximum tangential stress concentration occurred within the rock, and not at the borehole wall for specific loading conditions.

Aadnøy (1987) and Aadnøy and Chenevert (1987) developed a semi-analytical model which took into account the influence of rock anisotropy on inclined borehole stability; but, this model can only solve for the stresses along the borehole wall, and it was limited to an isotropic shear failure criterion. Roegiers and Detournay (1988) gave an expression for the stresses and displacements and fracture initiation at inclined borehole walls. Ong and Roegiers (1993a, 1993b) modified Aadnøy's model by presenting the stress as a function of borehole radii and adopting an anisotropic shear failure criterion. Ong (1994) further improved and developed this anisotropic borehole model. Based on Ong and Roegiers' model, a wellbore stability analysis software (Bore-3D) was developed which is extensively used in oil and gas industry (Li et al., 1997). Gupta and Zaman (1994) presented borehole stability analyses for transversely isotropic media. Since only 10% of the rock formations exhibit isotropic material properties, and 30% of the rocks have an anisotropy ratio of more than 1.5 for Young's modulus (Ong, 1994), the anisotropic model is more realistic.

The chemical effect of drilling fluid on shales is an important factor affecting wellbore stability. Mody and Hale (1993) presented a model that couples the mechanics and chemistry of drilling fluid with shale interactions. Sherwood and Bailey (1994) gave a modified form of Biot's linear theory of poroelasticity for shale swelling around a cylindrical wellbore in the case of an axisymmetric, plane strain situation.

The borehole solution using linear elasticity is still widely used in the industry for mud weight design and borehole stability analyses because of its ease of use and because it needs only a few parameters.

1.2.1.2 Poroelastic model

For rocks that are permeated with fluids, the diffusion of pore pressure strongly modifies the effective stress field around a borehole. The analysis of borehole problems is based on the linear poroelasticity theory (Biot, 1941, 1955; Detournay and Cheng, 1993). Bratli et al. (1983) gave the solution for a borehole in a hydrostatic stress field. Detournay and Cheng (1988) presented the poroelastic solution for a borehole in a non-hydrostatic stress field by assuming a vertical borehole and a plane strain deformation geometry. For inclined boreholes drilled in isotropic media, Cui et al. (1997a) derived an analytical solution by applying the generalized plane strain concept. Abousleiman et al. (1995, 1996) gave a poroelastic solution for a special case of transversely isotropic materials and a poroviscoelastic solution for borehole and cylinder problems. When drilling very deep formations, the thermal effect has a potential impact on the stress and pore pressure distributions and wellbore stability. Li et al. (1998) presented a fully coupled thermoporomechanical model and concluded that thermal effect induces high pore pressure which could be crucial to wellbore stability. Ekbote et al. (2000, 2001) gave the analytical solution coupling thermal, chemical poroelastic solution and a wellbore analysis software (Pbore-3D) was developed (Cui et al., 1999b).

1.2.1.3 Elastoplastic and nonlinear model

The linearly elastic model is the base case because it assumes that failure is equal to the elastic limit, thus acquiring the label as 'conservative' or pessimistic (Charlez, 1994). An elasto-plastic method implies that even after portion of the borehole might be stressed beyond their elastic limit, the non-elastc region remains intact and load-bearing, i.e. not in a collapsed state. Elasto-plastic models extend the stress-strain analysis beyond the elastic limit. A mathematically convenient formulation is to assume that no stresses exceed the elastic limit, i.e., perfect plasticity, the most common feature among elasto-plastic models.

A number of elastoplastic and nonlinear analytical and semi-analytical models for analyzing wellbore stability have been developed. Gnirk (1972) recognized the existence of a plastic zone around an uncased hole, and calculated wellbore pressures to prevent yielding, assuming no fluid flow occurred. Risnes et al. (1982) presented an analytical solution describing the extent of the plastic zone about an uncased well during drawdown. In nonlinear elastic models (Santarelli 1987) the stress rate is a homogenous linear function of the deformation rate, with Young's modulus dependent on hydrostatic pressure. The nonlinear and elastoplastic models include damage mechanics models (e.g. Cheng and Dusseault, 1993; Shao and Khazrai, 1994), bifurcation models (e.g. Papamichos et al., 1994), elastic-perfectly plastic models (e.g. Detournay, 1986; Detournay and Fairhurst, 1987), strain hardening elastoplastic models (e.g. Bradford and Cook, 1994) and strain weakening, elastic-brittle-plastic models (e.g. Ladanyi, 1974; Kennedy and Lindberg, 1978; Wang and Dusseault, 1991; Hawkes and McLellan, 1996). Most models are only applicable to the hydrostatic stress state and do not consider fluid effects.

1.2.1.4 Numerical methods

Numerical methods include mainly the finite element method, the finite difference method, the boundary element, and the discrete element method. Goodman (1966) analyzed the distribution of stresses around circular openings and described the effect of weakness planes on them. The boundary element method was used to study borehole breakouts (Zheng et al (1989)). Kwong and Kaiser (1991) studied borehole breakouts in

rock with anisotropic strength and local weaknesses by using a 2D finite element model in which the weakness planes are represented by elements with lower strength. They noted that if the in-situ stress ratio is close to unity, the presence of weakness planes does not greatly affect the development of a continuous, uniform yield zone, as predicted by analytical or numerical solutions for a homogeneous continuum. Shen and Barton (1997) used the distinct element method to investigate the effect of joint spacing on the size and shape of the distributed zone around circular openings. Hoek et al. (1995) noted that further experience is required in the application of the distinct element method to explore its potential and limitations. This is because rock joint configuration and spacing cannot be faithfully reproduced in a model, and rock joint properties cannot be tested except for a few joints with limited sample size (Bashin and Hoeg, 1998).

Recently, reviews of modeling technology, wellbore stability, and drilling advances were given by McLean and Addis (1990), Charlez (1994), Payne et al. (1995), and Ramos et al. (1996). The significant advances belong to rock mass characterization, computation, modeling, monitoring, and logging tool developments. The availability of PC computers with numerical codes such as finite elements, finite differences, displacement discontinuity elements or boundary elements for wellbore stress-strain analyses have contributed to wider field applications and acceptance of rock mechanics models.

Application of the finite element to poroelasticity began in 1969 by Sandhu and Wilson for a special case of incompressible fluid and solid constituents for soil mechanics applications. Several other papers also appeared within the next few years (Christian and Boehmer, 1970; Ghaboussi and Wilson, 1973). All these papers were limited to a special version of linear poroelasticity. Since then, this work has been extended to the cases of compressible constituents (Ghaboussi and Wilson, 1973), dynamic problems (Zienkiewicz and Shiomi, 1984), nonlinear and thermally coupled problems (Lewis and Schrefler, 1987). Some efforts were made using the finite element method to model wellbore stability problems in porous medium. Aoki et al. (1993, 1994) studied the stability of the inclined boreholes in saturated shales using the finite element method. The induced pore pressure is included in the anisotropic constitutive model. Cui et al. (1997b) formulated a pseudo three-dimensional finite element program for coupled

anisotropic, nonlinear poroelasticity to simulate inclined wellbore problem in porous media. Li (1998) presented a fully coupled thermal-mechanical-hydraulic finite element model to analyze wellbore stability in porous media. Some commercial codes such as ABAQUS® can also treat poroelasticity problems. The finite element method that couples fluid flow and rock deformation in dual-porosity media has been reported by authors such as Khaled et al., 1984; Meng, 1998; but, those studies focused either on consolidation problem or on fluid flow problems. More recently, the finite element method, using the dual-porosity theory, was applied to borehole problems and some preliminary results were obtained (Bai et al., 1999; Zhang et al., 2000; Nair et al., 2000).

1.2.2 Naturally Fractured Reservoirs

One of the most prominent features of the earth's upper crust is the presence of joints and fractures at all scales (Brown and Scholz, 1986). Nearly every physical property of crustal rock such as mechanical properties; hydraulic, thermal, and electrical conductivities; and acoustic properties is determined to some extent on the these fractures and the fluids they contain. The success of many applications such as efficient recovery from fractured reservoirs, hazardous waste disposal, and geothermal energy extraction depends on a thorough understanding of fracture behavior. Many petroleum reservoirs are situated in fractured porous formations (Pruess and Tsang, 1990). Roegiers (2001) even maintains that all reservoirs are naturally fractured reservoirs, but that some of them may not behave as fractured reservoirs. Natural fractures affect all phases of the petroleum reservoir life from the accumulation of oil to the techniques used to manage oil production. The existence of fractures in oil reservoirs was known as early as the 1860's. However, in the last thirty or forty years, a significant interest in the effect of fractures on oil production has been developed. This interest was sparked by the discovery of the giant fields in the Middle East and the Spraberry Trend of West Texas. The interest aroused by these discoveries made the industry more aware of the presence and effects of fractures in other reservoirs (Kazemi and Gilman, 1993).

Naturally fractured reservoirs compose a wide variety of rock mineralogy (carbonate,

diatomite, granite, schist, sandstone, shale and coal), porosity and permeability. Carbonates include limestone, dolomite and chalk. Fractured limestones are prevalent in the giant and prolific fields of the Middle East. Fractured dolomites are exemplified by the San Andreas formation in many West Texas fields, and fractured chalks are found in Texas (Austin Chalk), the North Sea (Ekofisk) and other parts of the world (Kazemi and Gilman, 1993).

For solving fractured reservoir problems, there are two distinctly different approaches. The multi-porosity model approach characterizes a fractured rock mass as a statistically homogeneous medium consisting of a combination of fractures and porous rock matrix (Evans, 1981): the probability of finding a fracture at any point in the system is the same as finding one at any other point. The discrete model approach, on the other hand, attempts to model the actual geometry of both the fractures and the porous rock matrix (Evans, 1981). Thus, it is necessary to determine from the field, the geometry, locations, orientation, aperture variations and fluid-mechanical properties of each fracture, and to incorporate this information into the mathematical model. This could need a huge amount of computational time. This dissertation limits itself to the use of the dual-porosity model to simulate naturally fractured porous media.

1.2.3 Dual-porosity Approach

In the dual-porosity approach, the naturally fractured reservoirs are often classified as a system containing two different physical domains. The primary rock matrix contains large amount of fluids but has a rather low permeability; and the fractures constitute a small volume but have the ability to transmit a large portion of flow through the reservoir. The naturally fractured reservoir is usually conceptualized as a double-porosity medium: one porosity represents the matrix blocks and the other represents the fractures and vugs.

Naturally fractured reservoirs are often modeled by the dual-porosity model proposed first by Barenblatt et al. (1960). They considered the reservoir as two overlapping continua: matrix and fractures. Flow between the matrix and the fractures was accounted

for by the introduction of source functions. However, they did not consider the effects of stresses on both the matrix and fractures.

Warren and Root (1963) utilized a three-dimensional, interconnected network of fractures and developed an analytical solution to describe the flow through dual-porosity media. They assumed that the fractures are all interconnected, and that they were equally developed in three principal directions; thus, the fractured reservoir is isotropic in a macroscopic sense. They gave a radial model for well transient testing purposes. In their model, the double-porosity medium had two classes of porosity. The primary porosity was controlled by deposition and lithification. The void systems of sands, sandstones and limestones were typical of this class. The secondary porosity, on the other hand, was controlled by fracturing and jointing. Vugs, joints and fissures which occur in formations such as shale, siltstone, schist, limestone or dolomite were typical of this class of porosity. In Warren and Root's model, the matrix rock containing the primary porosity was homogeneous and isotropic and was contained within a systematic array of identical, rectangular blocks. These blocks provided flow to the fractures which, in turn, transported the fluid to the well. Superimposed on this system was an orthogonal system of continuous, uniform fractures which were oriented such that each fracture was parallel to one of the principal axes of permeability. Fluid flow in the reservoir occurred through the fractures, which were anisotropic, with local exchange of fluids between the fracture system and matrix blocks, but, flow communication between matrix blocks did not occur.

Odeh (1965) attempted to generalize the concept of Warren and Root to accommodate a fractured reservoir in which the pattern of fractures was not known. In his model, the matrix blocks acted like sources which continuously feed the fractures. The net fluid movement toward the wellbore occurred only in the fractures and the fractures' flow capacity as well as the degree of fracturing of the reservoir were uniform.

The solutions presented by Warren and Root, and Odeh were subsequently extended by Kazemi et al. (1969). Kazemi's model differed from Warren and Root's model in that the reservoir consisted of a set of uniformly spaced horizontal matrix layers with a set of horizontal fractures as spacers. The fractures were arranged horizontally, whereby the fracture flow converged radially towards the wellbore. According to this assumption, a

"layer cake" model wherein the porous blocks and fractured matrix each occupied a different layer was presented. Of significance in this model was the recognition that porous medium flow was not only orthogonal to the fractures, but also responded as a continuum over the entire model. As a result of this conceptualization, two mass balance equations appeared: one for the fractures and the other for the porous blocks. The equations describing the layer cake model were solved numerically.

Aifantis (1977) introduced the concept of multi-porosity to consider diffusion processes in multi-porous media. Wilson and Aifantis (1982) extended the dual-porosity concept to examine coupled flow-deformation scenarios in fractured poroelastic media using analytical means. Similar numerical approaches were made by Khaled et al. (1984). Their model provided a suitable framework in which the flow-deformation behavior of dual-porosity media was fully coupled. Barenblatt's equations can be recovered from Aifantis' equations as a special case when the rock is assumed to be rigid. Aifantis' theory first provided an alternative derivation of his fissured rock equations through a proper extension of Biot's classical model of flow in single porosity media; and, secondly, developed a finite element methodology for the numerical solution of the relevant equations. The derivation of the governing equations is done by viewing the system as an elastic skeleton infiltrated by a two-state fluid, one flowing through the fractures and the other flowing through the pores. Constitutive assumptions were made for both the fluid strains and total stress. In conformity with the classical theory of Biot, the basic postulates are the equilibrium equation for the total stress and a two-state Darcy's law specifying the flow process in the two types of pores. Under assumptions of solid isotropy, small strains, slight fluid compressibility, absence of macroscopic viscosity and complete saturation, five second-order linear partial differential equations for five unknowns (three solid displacements and two fluid pressures) are derived.

Elsworth and Bai (1992) presented a constitutive model to define the linear poroelastic response of fissured media and determine the influence of dual-porosity effects. In their model, a stress-strain relationship and two equations representing conservation of mass in the porous and fractured material are required. Bai et al. (1993) presented a generalized formulation for the multi-porosity/multi-permeability poroelastic media. Later, a series of papers were published to study the fluid flow and solute transport in

dual-porosity media (Bai et al., 1994; Bai and Meng, 1994; Bai and Roegiers, 1994; Bai et al., 1995; Bai and Roegiers, 1995; Bai et al., 1995). Bai and Roegiers (1997) extended the dual-porosity theory and proposed a triple-porosity analysis of solute transport. Zaman et al. (1998) presented a fluid flow model in heterogeneous dual-porosity media.

Lewis and Sukirman (1993a, 1993b), and Ghafouri and Lewis (1996) developed a model to study the fractured porous media via the dual-porosity concept. They considered that the imposed external loads and /or well production both create a pressure gradient between the fluid within the matrix pores and the fluid in the adjacent fractures. The fluid within the matrix is squeezed out into the fissured continuum due to the produced gradient. Hence, flow towards the producing well takes place through the fissured network. In their model, the fractured porous media are divided into two overlapping but distinct continua, the first represents flow and deformations in the porous matrix while the second represents flow in the fissures. They assumed that only pressure in the matrix affects the equilibrium equation and the pressure in the fissures has no influence; in addition, the compressibility of the fissures is ignored.

Lewis and Ghafouri (1997) considered multiphase flow through deformable fractured porous media. Their model was based on the theory of double-porosity and accounts for the significant influence of coupling between fluid flow and solid deformations. A Galerkin-based finite element method was applied to discretize the governing equations both in space and time domains. Their formulations are not derived from theory.

Meng (1998) presented oil and water flow through deformable fractured porous media using the dual-porosity theory. In his model, the porous matrix blocks and fractures were considered as overlapping systems. Nair (2001) presented oil and gas flow through deformable dual-porosity media.

When using the dual-porosity method, it should be noted that this approach is limited and only meaningful if the size of elements (in the finite element method) or gridblocks (in the finite difference method) are less than that of the matrix block (Mattax and Dalton, 1990).

Based on this literature review, it is found that to date, few of the existing models have been utilized to specifically study the combined effect of fluid flow and elastoplastic

behavior in naturally fractured reservoirs. Some published papers take into account the coupling effect between fluid flow and solid deformations of the reservoir, but the reservoir is considered as a homogeneous porous medium. Although many models are used to simulate wellbore stability in deformable fractured porous reservoirs, the solid phase is only considered as an elastic medium. Some models consider the solid phase as an elastoplastic medium, however, fluid flow effects in naturally fractured reservoirs are ignored. This dissertation presents the detailed fundamental theory and the numerical solutions for the coupled effect of fluid flow and solid elastoplastic behavior in deformable fractured reservoirs and provides wellbore problem solutions.

1.3 Objectives

The objective in this dissertation is to present an elastoplastic wellbore stability model that couples solid mechanics and fluid flow using the double porosity theory to simulate naturally fractured reservoirs. Specifically, there are four main objectives:

- Present the analytical solution for wellbore problems for simple cases, which can be used to verify the numerical solution. For the complicated cases, the finite element analysis will be applied.
- Present a finite element formulation coupling solid deformations and fluid flow in naturally fractured elastoplastic media employing the dual-porosity poromechanical theory.
- Develop wellbore stability analysis codes that incorporate the elastic, single-porosity, dual-porosity poroelastic and elastoplastic effects.
- Investigate different failure criteria and wellbore failure mechanisms.

1.4 Dissertation Description and Outline

Chapter 1 includes the general introduction laying out the objectives for this dissertation.

A critical literature review of wellbore stability modeling and fully coupled rock deformation and fluid flow system in naturally fractured media is given.

Chapter 2 gives the theoretical background of the wellbore problems. Different analytical solutions, such as, elastic and elastoplastic solutions are given. These can be used to validate the numerical model.

Chapter 3 presents the dual-porosity concept and double effective law. According to these, the formulations for separate and overlapping dual-porosity media are developed.

Chapter 4 contains the details of the numerical implementation and finite element formulations. The generalized plane strain theory is applied, which is able to solve three-dimensional problems by using two-dimensional geometry settings. The wellbore finite element solutions in elastoplastic dual-porosity medium are accomplished. Different wellbore boundary conditions are investigated for simulating practical cases.

Chapter 5 focuses on the validation of the numerical algorithm. The theoretical formulations and numerical solutions are validated against pure elasticity, consolidation cases and wellbore problems where the analytical solutions are readily available. Also, by using the finite difference method dual-porosity thermal elastoplastic consolidations are given, which can be used for new model validation in the future.

Chapter 6 examines the parametric influence. Through the parametric changes, the model allows the study of behaviors for pure elasticity, single-porosity, and dual-porosity problems. In addition, time-dependent, and fracture and matrix parametric effects are investigated.

Chapter 7 presents the wellbore failure analyses. Various wellbore failure criteria are examined and applied to analyze the wellbore instabilities, such as collapse, spalling, and fracturing.

Chapter 8 includes the application of the numerical model. Stress-dependent permeability around a wellbore, drilling mud selection, wellbore stability and rock cutting problems are numerically simulated.

Finally in Chapter 9, summary, conclusions and recommendations for future studies are given.

Chapter 2

Theoretical Background of Wellbore Problems

2.1 Elastic Solution

2.1.1 Vertical Borehole in An Isotropic Stress Field

Consider the plane strain solution (i.e. strain in z-direction, $\varepsilon_z = 0$) of a wellbore loaded on its external boundary by an isotropic stress, σ, and on its internal boundary by a fluid pressure, p_w (Figure 2.1.1); this is known as Lamé's problem (Charlez, 1997).

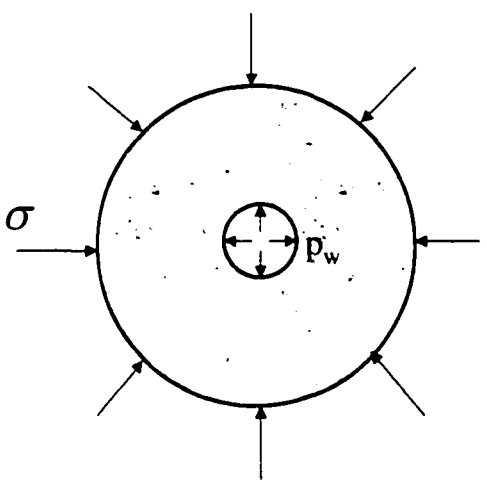


Figure 2.1.1 A borehole in an isotropic stress field.

In cylindrical coordinates, the stress components at a distance r from the wellbore are

given by:

$$\begin{cases} \sigma_r = \sigma\left(1-\dfrac{R^2}{r^2}\right)+\dfrac{p_w R^2}{r^2} \\ \sigma_\theta = \sigma\left(1+\dfrac{R^2}{r^2}\right)-\dfrac{p_w R^2}{r^2} \\ \sigma_z = \sigma_v \\ \tau_{r\theta} = \tau_{rz} = \tau_{\theta z} = 0 \end{cases} \tag{2.1.1}$$

where R is the wellbore radius; r is the distance from the wellbore; σ_r, σ_θ and σ_z are the radial, tangential and vertical stress components, respectively; $\tau_{r\theta}$, τ_{rz} and $\tau_{\theta z}$ are the shear stress components; σ and σ_v are the horizontal and vertical stresses in the far-field stress field, respectively.

At the wellbore, $r = R$, one obtains:

$$\begin{cases} \sigma_r = p_w \\ \sigma_\theta = 2\sigma - p_w \\ \sigma_z = \sigma_v \end{cases} \tag{2.1.2}$$

It can be seen that stress concentrations occur due to well drilling.

The radial displacement or well convergence, can be computed using the following expression:

$$u_r = \frac{\sigma - p_w}{2G}\frac{R^2}{r} \tag{2.1.3}$$

where G is Lamé's constant.

2.1.2 Vertical Borehole in An Anisotropic Stress Field

Kirsh's problem refers to a borehole subjected to a bi-axial stress state σ_H, σ_h ($\sigma_H > \sigma_h$)(Figure 2.1.2). The solution for the various stress components is now as follows:

$$\begin{cases} \sigma_r = \dfrac{(\sigma_H + \sigma_h)}{2}\left(1 + \dfrac{R^2}{r^2}\right) + \dfrac{(\sigma_H - \sigma_h)}{2}\left(1 - \dfrac{4R^2}{r^2} + \dfrac{3R^4}{r^4}\right)\cos 2\theta + p_w \dfrac{R^2}{r^2} \\ \sigma_\theta = \dfrac{(\sigma_H + \sigma_h)}{2}\left(1 + \dfrac{R^2}{r^2}\right) - \dfrac{(\sigma_H - \sigma_h)}{2}\left(1 + \dfrac{3R^4}{r^4}\right)\cos 2\theta - p_w \dfrac{R^2}{r^2} \\ \sigma_z = \sigma_v - \nu \dfrac{4R^2}{r^2}\dfrac{(\sigma_H - \sigma_h)}{2}\cos 2\theta \\ \tau_{r\theta} = -\dfrac{(\sigma_H - \sigma_h)}{2}\left(1 + \dfrac{2R^2}{r^2} - \dfrac{3R^4}{r^4}\right)\sin 2\theta \\ \tau_{z\theta} = \tau_{rz} = 0 \end{cases} \tag{2.1.4}$$

In particular, at the borehole wall, one can obtain the tangential stress component:

$$\sigma_\theta = (\sigma_H + \sigma_h) - 2(\sigma_H - \sigma_h)\cos 2\theta - p_w \tag{2.1.5}$$

or,

$$\begin{cases} \sigma_\theta = 3\sigma_h - \sigma_H - p_w & \text{at} \quad \theta = 0^\circ \\ \sigma_\theta = 3\sigma_H - \sigma_h - p_w & \text{at} \quad \theta = 90^\circ \end{cases} \tag{2.1.6}$$

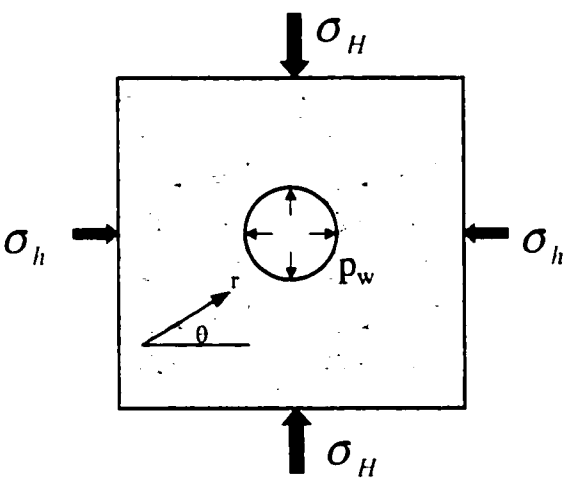


Figure 2.1.2 A vertical borehole in an anisotropic stress field.

2.1.3 Inclined Borehole in An Anisotropic Stress Field

For an inclined borehole, Bradley (1979) gave the stress distribution around a borehole located in an arbitrary stress field:

$$\begin{cases} \sigma_r = \dfrac{(\sigma_x+\sigma_y)}{2}\left(1-\dfrac{R^2}{r^2}\right)+\dfrac{(\sigma_x-\sigma_y)}{2}\left(1-\dfrac{4R^2}{r^2}+\dfrac{3R^4}{r^4}\right)\cos 2\theta+\tau_{xy}\left(1-\dfrac{4R^2}{r^2}+\dfrac{3R^4}{r^4}\right)\sin 2\theta+p_w\dfrac{R^2}{r^2} \\ \sigma_\theta = \dfrac{(\sigma_x+\sigma_y)}{2}\left(1+\dfrac{R^2}{r^2}\right)-\dfrac{(\sigma_x-\sigma_y)}{2}\left(1+\dfrac{3R^4}{r^4}\right)\cos 2\theta-\tau_{xy}\left(1+\dfrac{3R^2}{r^4}\right)\sin 2\theta-p_w\dfrac{R^2}{r^2} \\ \sigma_z = \sigma_{zz}-2\nu(\sigma_x-\sigma_y)\dfrac{R^2}{r^2}\cos 2\theta-4\nu\tau_{xy}\dfrac{R^2}{r^2}\sin 2\theta \\ \tau_{r\theta} = \left(\dfrac{\sigma_x-\sigma_y}{2}\sin 2\theta+\tau_{xy}\cos 2\theta\right)\left(1+\dfrac{2R^2}{r^2}-\dfrac{3R^4}{r^4}\right) \\ \tau_{rz} = (\tau_{yz}\sin\theta+\tau_{xz}\cos\theta)\left(1-\dfrac{R^2}{r^2}\right) \\ \tau_{\theta z} = (-\tau_{xz}\sin\theta+\tau_{yz}\cos\theta)\left(1+\dfrac{R^2}{r^2}\right) \end{cases} \tag{2.1.7}$$

where σ and τ with subscript of r and θ are the normal and shear stresses in a cylindrical coordinate system with the z-direction parallel to the drilling direction, σ and τ with subscript of x, y and z are the normal and shear stresses in a Cartesian coordinate system which has the same z-axis as the cylindrical system, with the z-direction parallel to the drilling direction, θ is the azimuthal angle measured from the x-axis. The conversion of this Cartesian coordinate system's stresses from in-situ principal stresses can be done through coordinate transformation (Jaeger and Cook, 1979), which is given in Chapter 4.

The stress at the wellbore wall can be written as:

$$\begin{cases} \sigma_r = p_w \\ \sigma_\theta = \sigma_x + \sigma_y + p_w - 2(\sigma_x - \sigma_y)\cos 2\theta - 4\tau_{xy}\sin 2\theta \\ \sigma_z = \sigma_{zz} - \nu[2(\sigma_x - \sigma_y)\cos 2\theta + 4\tau_{xy}\sin 2\theta] \\ \tau_{\theta z} = 2(-\tau_{xz}\sin\theta + \tau_{yz}\cos\theta) \\ \tau_{r\theta} = 0 \\ \tau_{rz} = 0 \end{cases} \tag{2.1.8}$$

2.2 Elastoplastic Solution

Considering a plane strain circular infinite domain loaded on its internal boundary by a pressure p_w and at infinity by an isotropic far-field stress σ (Figure 2.2.1) in an ideal elastoplastic material,

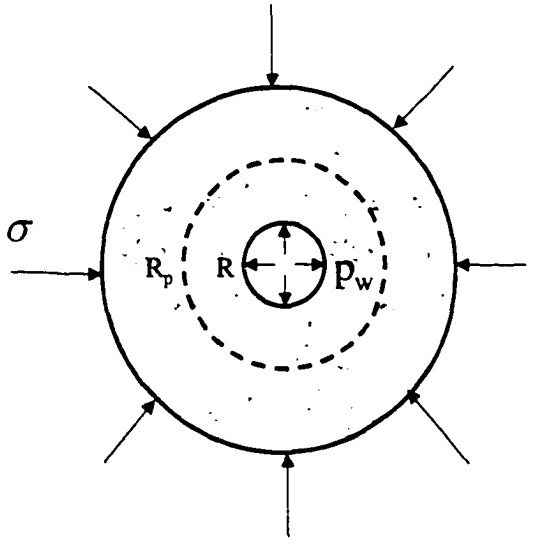


Figure 2.2.1 A borehole in an ideal elastoplastic material.

Assuming $\sigma_\theta > \sigma_r$ and an ideal plastic rock formation with a Mohr-Coulomb type yield locus, i.e.,

$$\sigma_\theta = \sigma_c + q\sigma_r \tag{2.2.1}$$

where σ_c is the uniaxial compressive strength of the rock, $q = (1+\sin\phi)/(1-\sin\phi)$ and ϕ is the angle of internal friction.

The equation of equilibrium is given by:

$$\frac{d\sigma_r}{dr} + \frac{\sigma_r - \sigma_\theta}{r} = 0 \tag{2.2.2}$$

Substituting Equation (2.2.1) into Equation (2.2.2) and solving it, one obtains:

$$\sigma_r = \frac{\sigma_c}{1-q} + C_1 r^{q-1} \tag{2.2.3}$$

$$\sigma_\theta = \frac{\sigma_c}{1-q} + C_1 q r^{q-1} \tag{2.2.4}$$

Using the boundary condition (for $r = R$, $\sigma_r = p_w$), a value for C_1 can be obtained:

$$C_1 = p_w - \frac{\sigma_c}{1-q} R^{1-q} \tag{2.2.5}$$

Therefore, in the failed zone the stresses are given by (Roegiers, 1999):

$$\begin{cases} \sigma_r = \dfrac{\sigma_c}{1-q} + \left(p_w - \dfrac{\sigma_c}{1-q} \right) \left(\dfrac{r}{R} \right)^{q-1} \\ \sigma_\theta = \dfrac{\sigma_c}{1-q} + q\left(p_w - \dfrac{\sigma_c}{1-q} \right) \left(\dfrac{r}{R} \right)^{q-1} \end{cases} \tag{2.2.6}$$

In the elastic zone, the stress can be obtained from elasticity theory, i.e.:

$$\begin{cases} \sigma_{re} = \sigma + \dfrac{C_2}{r^2} \\ \sigma_{\theta e} = \sigma - \dfrac{C_2}{r^2} \end{cases} \tag{2.2.7}$$

When $r = R_p$ (R_p is the radius of the failed zone), the radial stress can be obtained both from Equations (2.2.6) and (2.2.7). Using the continuity of the radial stress for $r = R_p$, the value C_2 can be obtained.

$$\sigma_r\Big|_{r=R_p} = \frac{\sigma_c}{1-q} + \left(p_w - \frac{\sigma_c}{1-q} \right) \left(\frac{r}{R} \right)^{q-1} = \sigma + \frac{C_2}{r^2} \tag{2.2.8}$$

and,

$$C_2 = R_p^2 \left[\frac{\sigma_c}{1-q} - \sigma + \left(p_w - \frac{\sigma_c}{1-q} \right) \left(\frac{R_p}{R} \right)^{q-1} \right] \tag{2.2.9}$$

Therefore, the stresses in the elastic zone are as follows:

$$\begin{cases} \sigma_{re} = \sigma + \left[\dfrac{\sigma_c}{1-q} - \sigma + \left(p_w - \dfrac{\sigma_c}{1-q} \right) \left(\dfrac{R_p}{R} \right)^{q-1} \right] \left(\dfrac{R_p}{r} \right)^2 \\ \sigma_{\theta e} = \sigma - \left[\dfrac{\sigma_c}{1-q} - \sigma + \left(p_w - \dfrac{\sigma_c}{1-q} \right) \left(\dfrac{R_p}{R} \right)^{q-1} \right] \left(\dfrac{R_p}{r} \right)^2 \end{cases} \tag{2.2.10}$$

In the elastic region, when $r = R_p$, the stresses also satisfy Mohr-Coulomb's failure criterion; i.e.

$$\sigma_\theta = \sigma_c' + q' \sigma_r \tag{2.2.11}$$

where σ_c' is the uniaxial compressive strength for the failed rock, $q' = (1+\sin\phi')/(1-\sin\phi')$ and ϕ' is the angle of internal friction for the failed rock.

Substituting Equations (2.2.10) into Equation (2.2.11), one gets the failure radius:

$$R_p = R\left\{\frac{(2\sigma - \sigma_c')(1-q) - \sigma_c(q'+1)}{[p_w(1-q) - \sigma_c](q'+1)}\right\}^{\frac{1}{q-1}} \tag{2.2.12}$$

Equation (2.2.12) shows that the entire rock block will remain purely elastic if the well pressure is such that:

$$p_w > \frac{(2\sigma - \sigma_c')}{(q'+1)} \tag{2.2.13}$$

The elastoplastic solution and the purely elastic solution are compared in Figure 2.2.2, in which the parameters used are listed in Table 2.2.1. The calculated plastic radius is $R_p = 1.3R$. In the plastic zone, the tangential stress strongly reduces compared to the elastic solution. However, the radial stress only reduces slightly. Tangential stress reduction in the well vicinity means that the difference of the radial and tangential stresses will be considerably reduced. This is why an elastoplastic model is much less pessimistic regarding borehole instability than a purely elastic model.

Table 2.2.1 Parameters used for elastic and elastoplastic calculations

Parameters	Magnitude
Far-field stress σ (MPa)	50
Fluid pressure p_w (MPa)	10
Uniaxial compressive strength σ_c (MPa)	20
Compressive strength for failed rock σ_c' (MPa)	10
Angle of internal friction ϕ, ϕ' (°)	30

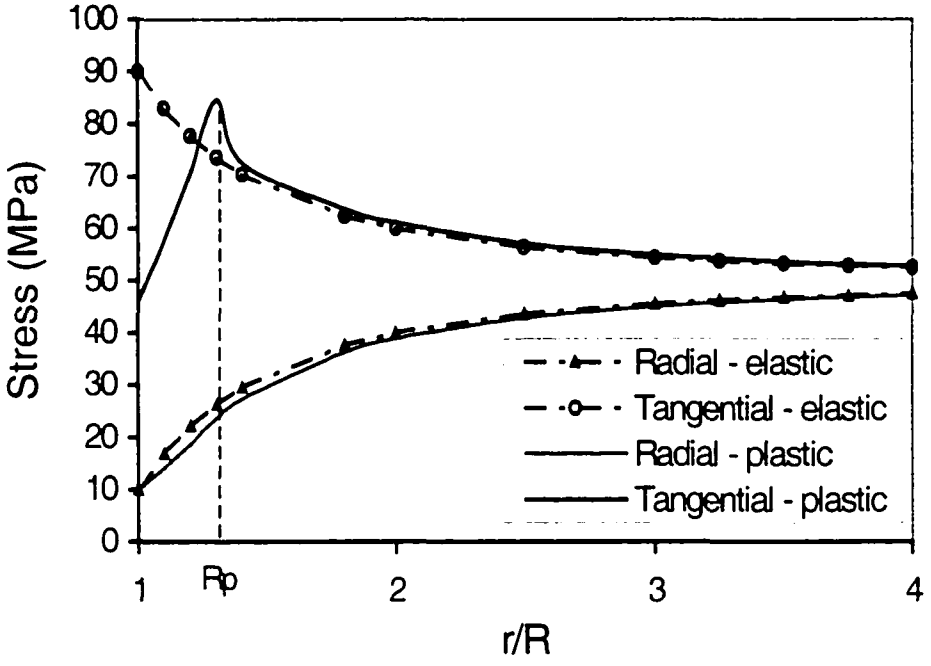


Figure 2.2.2 Stress states around a borehole in elastic and elastoplastic solutions.

Chapter 3

Dual-porosity Poromechanics

3.1 Dual-porosity approaches

3.1.1 Dual-porosity Concept

Many rock formations are heterogeneous due to the existence of discontinuities and natural fractures. Thus, the porous rock as a homogeneous continuum with an associated single porosity may not simulate properly the rockmass behavior. However, the chaotic distributions of the natural fractures and discontinuities within the rock mass make it almost impossible to model each fracture independently. If these fractures and rock matrix can be considered using a multi-porosity continuum concept, the task of modeling such rock masses becomes reasonable. Naturally fractured reservoirs are often treated ideally as different dual-porosity media (Barenblatt et al., 1960; Warren and Root, 1963; Kazemi et al., 1969; Aifantis, 1977; Kazemi et al., 1993; Bai et al., 1993; Bai and Roegiers, 1994; Lewis and Ghafouri, 1997; Zaman et al., 1998; etc.), which has two classes of porosity (Figure 3.1.1). The void systems of sands, sandstones and limestones are typical of dual-porosity media; the primary porosity being controlled by deposition. The secondary porosity, on the other hand, is controlled by fracturing and jointing. Vugs, joints and fissures which occur in formations such as shale, siltstone, schist, limestone or dolomite are typical of this class of porosity.

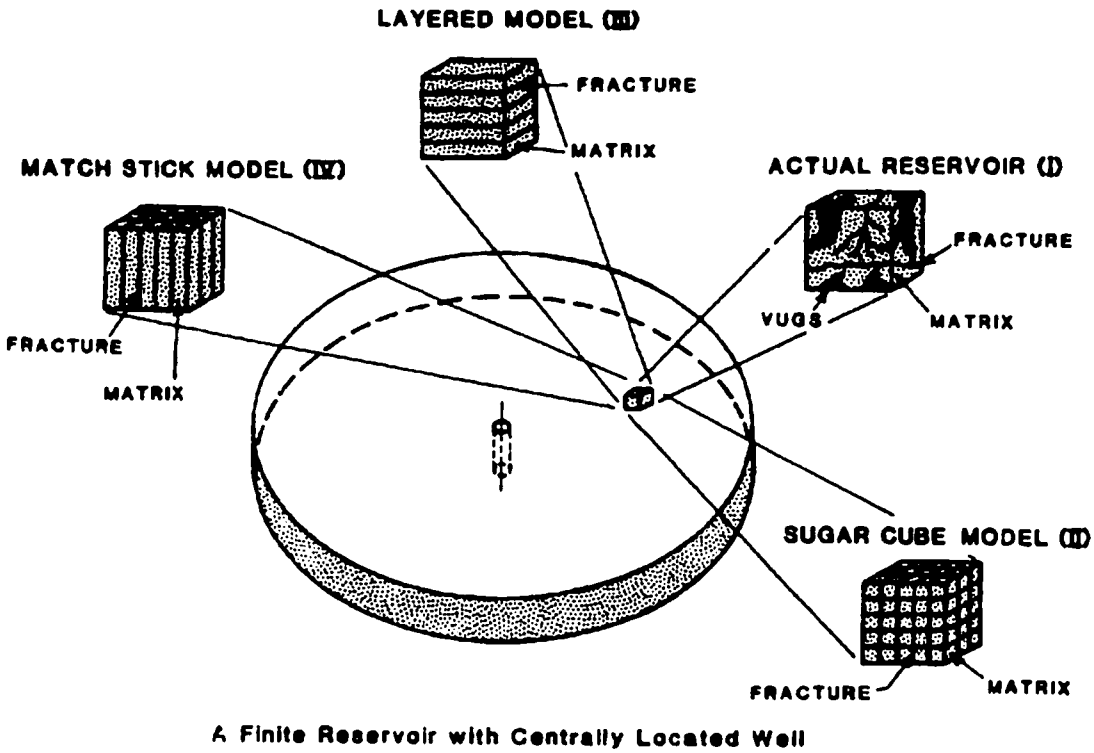


Figure 3.1.1 Dual-porosity models for the naturally fractured reservoir (from Kazemi et al., 1993).

In the dual-porosity model, a fractured rockmass is thought of as a number of porous blocks separated from each other by a system of randomly distributed fractures (as shown in Figure 3.1.2). Thus, the fracture and matrix systems in the fractured rock are distinctly different in both porosity and permeability. The global flow occurs primarily through the high-permeability, low-porosity fracture system surrounding the matrix rock blocks. The matrix blocks contain the majority of the reservoir storage volume and act as local source or sink terms to the fracture system. The fractures are interconnected and provide the main fluid flow path to the wells.

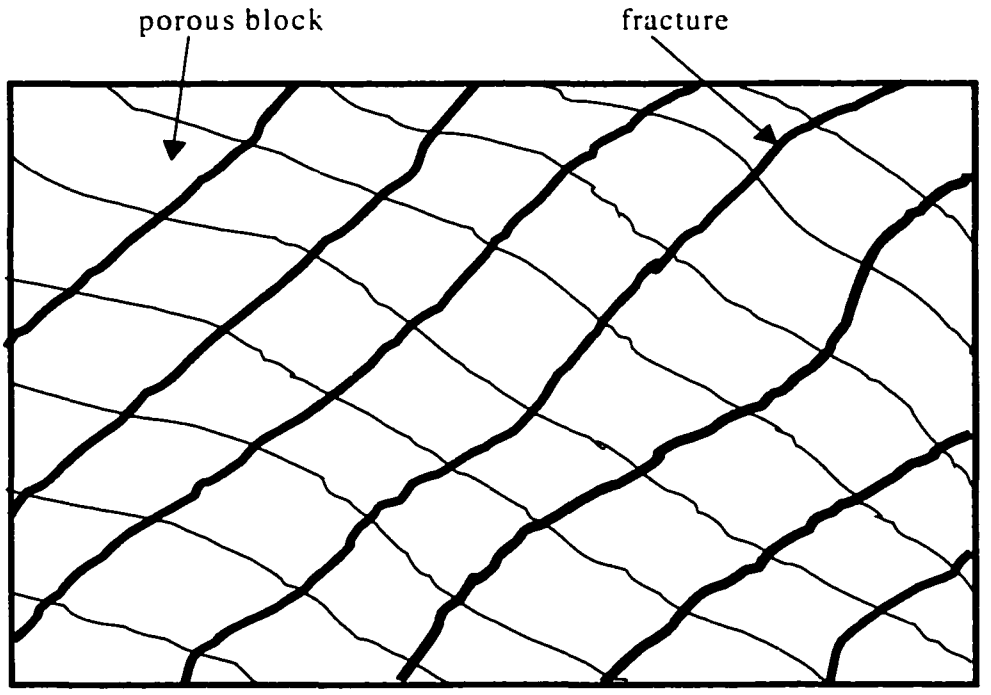
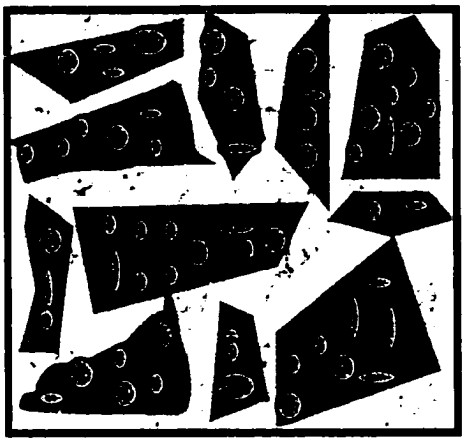


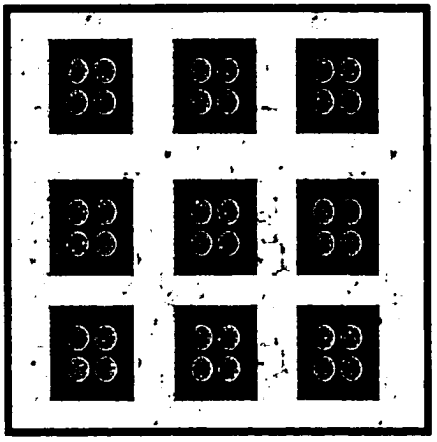
Figure 3.1.2 Schematic dual-porosity medium

In this dissertation, the naturally fractured reservoir is assumed as an ideal dual-porosity, dual-permeability model[1] (such as 'sugar cubic model' in Figure 3.1.1) as shown in Figure 3.1.3. In this model, the system including matrix and fractures is considered as a continuous medium; therefore, continuum mechanics can be applied to deal with this problem.

[1] In this dissertation, dual-porosity refers to dual-porosity and dual-permeability.



a). Naturally fractured reservoir



b). Ideally fractured reservoir

Figure 3.1.3 Naturally fractured and ideally dual-porosity reservoirs.

3.1.2 Separate and Overlapping Models

There are two different kinds of approaches to model dual-porosity media. One assumes that the medium is 'overlapping' between the matrix and fractures; the other assumes that the matrix and fractures in the medium are 'separate and overlapping'. The total volume in the overlapping model is the sum of the volumes of pores, fractures and solids (Aifantis, 1977, 1980; Meng, 1998). However, in the separate and overlapping model, the total volume is the sum of the volumes of pores and solids or of the volumes of fractures and solids, i.e.,

$$V = V_{ma} + V_{s1} = V_{fr} + V_{s2} \tag{3.1.1}$$

where V is the total volume, V_{ma} is the void space occupied by fluid in the matrix, V_{s1} is the solid volume in the porous medium (Figure 3.1.4), V_{fr} is the void space occupied by fluid in the fractures, V_{s2} is the solid volume in the fractured medium (Figure 3.1.4).

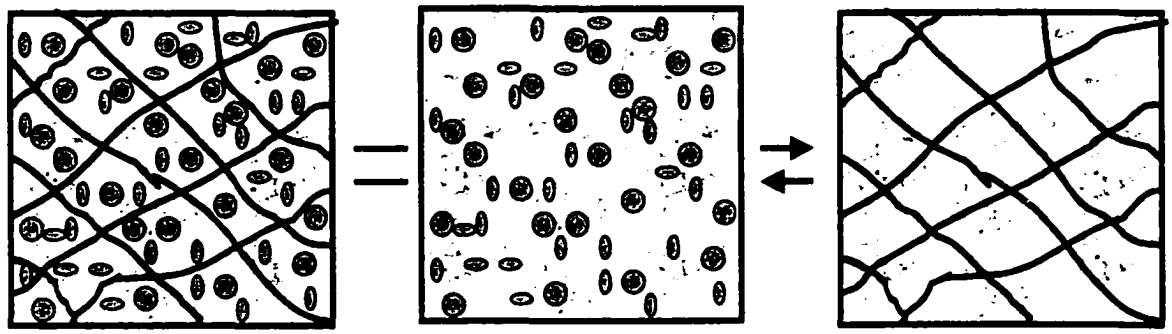


Figure 3.1.4 Separate and overlapping model in dual-porosity media.

3.2 Double Effective Stress Law

The relationship between changes in total stress (σ_{ij}) and effective stress (σ_{ij}') is given by Terzaghi (1943) and Biot (1941, 1955). For dual-porosity media, the effective stress can be expressed as:

$$\begin{cases} \sigma_{maij} = \sigma'_{maij} + \alpha_{ma} p_{ma} \delta_{ij} \\ \sigma_{frij} = \sigma'_{frij} + \alpha_{fr} p_{fr} \delta_{ij} \end{cases} \tag{3.2.1}$$

where subscript '*ma*' and '*fr*' represent matrix and fracture, respectively.

For separate overlapping porous medium and fractured medium, the local stress equilibrium requires that changes in total stress within adjacent phases must remain in equilibrium, such that (Elsworth and Bai, 1992):

$$\sigma_{maij} = \sigma_{frij} = \sigma_{ij} \tag{3.2.2}$$

The linear elastic constitutive relationships among the effective stresses and strains for the separate matrix and fracture systems are defined as:

$$\begin{cases} \sigma'_{maij} = D_{maijkl}\varepsilon_{makl} \\ \sigma'_{frij} = D_{frijkl}\varepsilon_{frkl} \end{cases} \tag{3.3.3}$$

The inverse relations from above two equations can be expressed as:

$$\begin{cases} \varepsilon_{makl} = C_{maijkl}\sigma'_{maij} \\ \varepsilon_{frkl} = C_{fraijkl}\sigma'_{frij} \end{cases} \tag{3.2.4}$$

where D_{maijkl} and D_{frijkl} are the elasticity tensors for the rock matrix and for the fractures, C_{maijkl} and C_{frijkl} are the compliance tensors for the rock matrix and the fracture systems, respectively.

The total strain due to the elastic deformation in each of the systems is given by:

$$\varepsilon_{ij} = \varepsilon_{makl} + \varepsilon_{frkl} \tag{3.2.5}$$

Substituting double effective law, i.e., Equations (3.3.1) into Equations (3.2.4) while combining with Equation (3.2.5) one obtains:

$$\varepsilon_{ij} = (C_{maijkl} + C_{frijkl})\sigma_{kl} - C_{maijkl}\alpha_{ma}p_{ma}\delta_{kl} - C_{frijkl}\alpha_{fr}p_{fr}\delta_{kl} \tag{3.2.6}$$

or,

$$\sigma_{ij} = D_{mf}(\varepsilon_{kl} + C_{maklmn}\alpha_{ma}p_{ma}\delta_{mn} + C_{frklmn}\alpha_{fr}p_{fr}\delta_{mn}) \tag{3.2.7}$$

The combined elasticity matrix D_{mf} can be defined explicitly in the three-dimensional geometry for an isotropic medium as (Bai et al., 1995):

$$D_{mf} = (C_{maijkl} + C_{frijkl})^{-1} \tag{3.2.8}$$

therefore,

$$D_{mf} = \frac{1}{|D_{mfijkl}|}\begin{bmatrix} d_{1111} & d_{1122} & d_{1133} & 0 & 0 & 0 \\ d_{2211} & d_{2222} & d_{2233} & 0 & 0 & 0 \\ d_{3311} & d_{3322} & d_{3333} & 0 & 0 & 0 \\ 0 & 0 & 0 & d_{4444} & 0 & 0 \\ 0 & 0 & 0 & 0 & d_{55555} & 0 \\ 0 & 0 & 0 & 0 & 0 & d_{6666} \end{bmatrix} \tag{3.2.9}$$

The compliance matrices are given as follows:

$$C_{matijkl} = \frac{1}{E}\begin{bmatrix} 1 & -\nu & -\nu & 0 & 0 & 0 \\ -\nu & 1 & -\nu & 0 & 0 & 0 \\ -\nu & -\nu & -\nu & 0 & 0 & 0 \\ 0 & 0 & 0 & 2(1+\nu) & 0 & 0 \\ 0 & 0 & 0 & 0 & 2(1+\nu) & 0 \\ 0 & 0 & 0 & 0 & 0 & 2(1+\nu) \end{bmatrix} \tag{3.2.10}$$

$$C_{trijkl} = \frac{1}{E}\begin{bmatrix} \frac{1}{K_n s} & 0 & 0 & 0 & 0 & 0 \\ 0 & \frac{1}{K_n s} & 0 & 0 & 0 & 0 \\ 0 & 0 & \frac{1}{K_n s} & 0 & 0 & 0 \\ 0 & 0 & 0 & \frac{1}{K_{sh} s} & 0 & 0 \\ 0 & 0 & 0 & 0 & \frac{1}{K_{sh} s} & 0 \\ 0 & 0 & 0 & 0 & 0 & \frac{1}{K_{sh} s} \end{bmatrix} \tag{3.2.11}$$

and,

$$|D_{mfijkl}| = \left[\frac{1}{K_{sh}s} + \frac{2(1+\nu)}{E}\right]^3 \left[\left(\frac{1}{E} + \frac{1}{K_n s}\right)^3 - \frac{3\nu^2}{E^2}\left(\frac{1}{E} + \frac{1}{K_n s}\right) - \frac{2\nu^2}{E^2}\right] \tag{3.2.12}$$

$$d_{1111} = d_{2222} = d_{3333} = \left[\frac{1}{K_{sh}s} + \frac{2(1+\nu)}{E}\right]^3 \left[\left(\frac{1}{E} + \frac{1}{K_n s}\right)^2 - \frac{\nu^2}{E^2}\right] \tag{3.2.13}$$

$$d_{1122} = d_{2211} = d_{1133} = d_{3311} = d_{2233} = d_{3322} = \left[\frac{1}{K_{sh}s} + \frac{2(1+\nu)}{E}\right]^3 \left[\frac{\nu}{E}\left(\frac{1}{E} + \frac{1}{K_n s}\right)^2 - \frac{\nu^2}{E^2}\right] \tag{3.2.14}$$

$$d_{4444} = d_{55555} = d_{6666} = \left[\frac{1}{K_{sh}s} + \frac{2(1+\nu)}{E}\right]^2 \left[\left(\frac{1}{E} + \frac{1}{K_n s}\right)^2 - \frac{3\nu^2}{E^2}\left(\frac{1}{E} + \frac{1}{K_n s}\right) - \frac{2\nu^3}{E^3}\right] \tag{3.2.15}$$

where K_n and K_{sh} are the fracture normal and shear stiffness, respectively.

3.3 Dual-porosity Formulations

A typical dual-porosity formulation is usually written as (Barenblatt et al., 1960):

$$\begin{cases} \dfrac{k_{ma}}{\mu}\nabla^2 p_{ma} = c_{ma} n_{ma} \dfrac{\partial p_{ma}}{\partial t} + \Gamma(p_{fr} - p_{ma}) \\ \dfrac{k_{fr}}{\mu}\nabla^2 p_{fr} = c_{fr} n_{fr} \dfrac{\partial p_{fr}}{\partial t} - \Gamma(p_{fr} - p_{ma}) \end{cases} \tag{3.3.1}$$

where p_{ma} and p_{fr} are the fluid pressures for the matrix and fractures, respectively; k_{ma} and p_{fr} are the permeabilities for the matrix and fractures, respectively; μ is the fluid dynamic viscosity, n_{ma} and n_{fr} are the porosities for the matrix and fracture, respectively; c_{ma} and c_{fr} are the compressibilities for the matrix and fractures, respectively; t is the time, Γ is the geometric leakage factor. It can be seen that no solid deformation is be considered in this formulation.

Alternatively, Barenblatt et al. (1990) proposed a more complete dual-porosity formulation than that expressed by Equations (3.3.1) by considering the cross-phase storativity interaction:

$$\begin{cases} \dfrac{k_{ma}}{\mu}\nabla^2 p_{ma} = c_{ma} n_{ma} \dfrac{\partial p_{ma}}{\partial t} - c_{mf} n_{ma} \dfrac{\partial p_{fr}}{\partial t} + \Gamma(p_{fr} - p_{ma}) \\ \dfrac{k_{fr}}{\mu}\nabla^2 p_{fr} = c_{fr} n_{fr} \dfrac{\partial p_{fr}}{\partial t} - c_{fm} n_{fr} \dfrac{\partial p_{ma}}{\partial t} - \Gamma(p_{fr} - p_{ma}) \end{cases} \tag{3.3.2}$$

where c_{mf} and c_{fm} are the cross-coefficients.

The governing equations for solid deformations and fluid phase in the dual-porosity poromechanical formation may be expressed as follows (Wilson and Aifantis, 1982; Bai et al., 1993):

$$\begin{cases} G u_{i,jj} + (\lambda + G) u_{k,ki} + \alpha_{ma} p_{ma,i} + \alpha_{fr} p_{fr,i} = 0 \\ -\dfrac{k_{ma}}{\mu} p_{ma,kk} = \alpha_{ma} \dfrac{\partial \varepsilon_{kk}}{\partial t} - \beta_{ma} \dfrac{\partial p_{ma}}{\partial t} + \omega(p_{fr} - p_{ma}) + q_{ma} \\ -\dfrac{k_{fr}}{\mu} p_{fr,kk} = \alpha_{fr} \dfrac{\partial \varepsilon_{kk}}{\partial t} - \beta_{fr} \dfrac{\partial p_{fr}}{\partial t} - \omega(p_{fr} - p_{ma}) + q_{fr} \end{cases} \tag{3.3.3}$$

where, λ and G are Lamé's constants, α_{ma} and α_{fr} are the effective stress coefficients for the matrix and fractures, respectively; β is the relative compressibility representing the lumped deformability of the fluid and the solid, u is the solid displacement, ε_{kk} is the total body strain, ω is the transfer coefficient and $\omega = 60k_{ma}/(\mu s^2)$ for three mutually orthogonal fracture sets (Warren and Root, 1963), s is the fracture spacing.

For the separate and overlapping model, the double effective stress law needs to be considered, and combined elasticity matrix D_{mf} defined in Equation (3.2.9) and other related elastic constants need to be introduced to Equations (3.3.3). Then, the governing equations for solid deformation and fluid phase in the dual-porosity poromechanical formation are slightly different and may be written as:

$$\begin{cases} G_{mf} u_{i,jj} + (\lambda_{mf} + G_{mf}) u_{k,ki} + \alpha_{ma} D_{mf} C_{maijkl} p_{ma,l} + \alpha_{fr} D_{mf} C_{frijkl} p_{fr,l} = 0 \\ -\dfrac{k_{ma}}{\mu} p_{ma,kk} = \alpha_{ma} D_{mf} C_{maijkl} \dfrac{\partial \varepsilon_{kk}}{\partial t} - \beta_{ma} \dfrac{\partial p_{ma}}{\partial t} + \omega(p_{fr} - p_{ma}) + q_{ma} \\ -\dfrac{k_{fr}}{\mu} p_{fr,kk} = \alpha_{fr} D_{mf} C_{frijkl} \dfrac{\partial \varepsilon_{kk}}{\partial t} - \beta_{fr} \dfrac{\partial p_{fr}}{\partial t} - \omega(p_{fr} - p_{ma}) + q_{fr} \end{cases} \tag{3.3.4}$$

where, λ_{mf} and G_{mf} are Lamé's constants for the combined dual porosity media, which can be obtained by the following relationships:

$$G_{mf} = \frac{D_{mf}}{2(1+\nu)} \tag{3.3.5}$$

$$\lambda_{mf} = \frac{\nu D_{mf}}{(1+\nu)(1-2\nu)} \tag{3.3.6}$$

Chapter 4

Finite Element Implementation of Poro-mechanical Solutions

4.1 Introduction

In solving practical problems, numerical approaches are often superior to analytical methods due to their versatility in replicating the complex geologic and hydrological conditions that exist in nature. Nearly all the numerical procedures involve replacing the continuous form of the governing differential equation by a finite number of algebraic equations. To develop these equations, it is necessary to subdivide the problem region. Three of the most widely used numerical methods are the finite difference, the finite element and the boundary methods. Among these three, the finite element method is perhaps the most versatile technique since it can handle irregular meshes and boundary conditions and is able to represent heterogeneities in a medium.

The basic mechanism of fluid flow in fractured porous media may be explained as follows: applied external loads and/or well production both create a pressure gradient between the fluid within the matrix pores and the fluid in the fractures. The fluid within the matrix is squeezed out into the fractured medium due to this gradient (Meng, 1998) (When the fluid is injected, the opposite result will take place.). Subsequently, flow towards the producing well takes place through the fissured network. In this dissertation, the naturally fractured reservoir is considered as two separate and overlapping continua, one representing the porous matrix while the other represents the deformable fractures. Based on the dual-porosity poromechanics and generalized plane strain concepts, the

derivations of the governing equations for fluid flow in a deformable naturally fractured reservoir include the equilibrium and the continuity equations and the finite element formulations will be given in the ongoing sections.

The following assumptions were made:

- The reservoir is treated as a dual-porosity medium. One porosity is associated with the primary rock matrix and the other is associated with the fractures;
- The fracture network is idealized as an equivalent porous continuum; this piecewise continuum is represented by an equivalent anisotropic permeability, controlled by fracture spacing and mean aperture.
- The rock is a compressible solid subject to small deformations;
- Fluid velocities in both the rock matrix and the fractures are assumed to be small. In such case, Darcy's law is valid;
- The analysis is related to a macroscopic level that contains a representative sample of rock matrix and fracture geometry;
- The fluid pressures, porosities, permeabilities and other properties of both the matrix and fractures are considered separately;
- The fluid flow in the porous matrix and the fracture is controlled only through a interchange term which is assumed to be in quasi-steady state; and,
- The rock matrix and fracture systems are assumed to be fully saturated.

4.2 Finite element method

Javandel and Witherspoon (1968) introduced the finite element method into the fluid flow through porous media problems. Pinder and Frind (1972) were among the first to utilize the finite element method for prediction of regional aquifer performance. Gupta and Tanki (1976) reported an application of a three-dimensional finite model for the simulation of flow in California. For heterogeneous systems with complex geometries and arbitrary boundary conditions, the finite element method is effective (Desai and

Johnson, 1972; Ghaboussi and Wilson, 1973). The single porosity poroelasticity, originated by Biot (1941, 1955) has been implemented with numerical tools (Verruijt, 1969; Zienkiewicz et al., 1977; Huyakorn and Pinder, 1983; Simon et al., 1984; Lewis and Schrefler, 1987; Cul et al., 1997b).

The dual-porosity conceptualization of a fractured medium considers fractures and porous blocks to behave as separate but interacting continua. Both the fluid flows and solid deformations in the rock matrix and fractures are affected by the interaction between the two systems. The numerical method of dual-porosity poroelasticity has been presented (Huyakorn and Pinder, 1983; Khaled et al, 1984; Elsworth and Bai, 1992; Meng, 1998.).

This dissertation develops a three-dimensional finite element model based on the dual-porosity poroelastic and poroelastoplastic conceptualizations and generalized plane strain theory. The finite element implementation and computer code for directional wellbore problems is also presented.

4.3 Generalized Plane Strain Concept

Most problems in engineering applications are three-dimensional in nature. A class of problems, such as, tunnels, wellbores and dikes are characterized by a cross-sectional geometry that is usually invariant along the longitudinal direction. These problems are defined as pseudo-two-dimensional geometry. However, anisotropic material properties and nonhomogeneous in-situ stress conditions generally render these problems three-dimensional. If a three-dimensional solution technique is applied, the computational efforts become intensive when time is a dependent variable. Under certain conditions; e.g., the boundary conditions along the generator are invariant, then, it is possible to develop a two-dimensional solution algorithm. One such condition is defined by the generalized plane strain problem. In these situations, material anisotropy and a three-dimensional stress and strain state are considered, but they have a functional dependence

of only two spatial variables (Cheng, 1998). Therefore, only a two-dimensional domain discretization is needed for numerical solutions.

The generalized plane strain analytical solutions for elastic continua have been presented by Saada (1974) for the case of a rotating cylinder free to deform in the longitudinal direction. In the case of wellbore and tunnel solutions in anisotropic media, the analytical development has been presented by Lekhnitskii (1981) and Amadei (1983). Numerical solutions in the generalized plane strain conditions, using the boundary element method, were developed by Brady and Bray (1978). Also, finite element solutions for these conditions were developed by Pande et al. (1990).

However, the above developments and applications were all designed for elastic continua and time was never a factor. In engineering applications, where saturated porous media are the common encounter, pore fluid pressure perturbations need to be taken into account. In general, when fluid saturated homogeneous porous rocks are subjected to an external load, a coupled hydro-mechanical response will take place. This phenomenon and its corresponding physical behavior are well prescribed and modeled using Biot's theory of poroelasticity (Biot, 1941). It has been demonstrated that poroelastic solutions present quantitative and qualitative results that are very different from their elastic counterparts.

Analytical solutions for several poroelastic generalized plane strain problems have been developed (Abousleiman et al., 1996; Cui et al., 1997a; Abousleiman and Cui, 1998; etc.). Also, the finite element formulation and solutions for single porosity porous media have been developed by Cui et al. (1997b). Recently, a dual-porosity poroelastic generalized plane strain finite element solution has been presented and the dual-porosity poroelastic behaviors of wellbores subjected to an inhomogeneous in-situ state of stress were studied (Bai et al., 1999; Zhang et al., 2000).

It is well-known in plane strain problems, i.e., in an x-y plane, that the displacement and the shear stresses are restricted along the z-direction. In the generalized plane strain scenarios, however, these restrictions are removed. As a result, the number of tensor components for stresses and strains are identical to that of a three-dimensional setting. In a general generalized plane strain formulation, it is assumed that boundary conditions in the form of surface tractions, pore pressure, displacements, and normal flux, do not

change along the z-direction. As a result, and taking into account the dual-porosity continuum concept where fluid pressure exists in the porous matrix, as well as in the natural fracture system, the displacements, stresses, strains and pore pressure are only functions of x, y and time t, i.e.,

$$\mathbf{u}^T(x, y, t) = \{u_1, u_2, u_3\} \tag{4.3.1}$$

$$\boldsymbol{\varepsilon}^T(x, y, t) = \{\varepsilon_{xx}, \varepsilon_{yy}, \varepsilon_{zz}, \gamma_{xy}, \gamma_{yz}, \gamma_{zx}\} \tag{4.3.2}$$

$$\boldsymbol{\sigma}^T(x, y, t) = \{\sigma_{xx}, \sigma_{yy}, \sigma_{zz}, \tau_{xy}, \tau_{yz}, \tau_{zx}\} \tag{4.3.3}$$

$$\mathbf{p}^T(x, y, t) = \{p_{ma}, p_{fr}\} \tag{4.3.4}$$

where the superscript 'T' represents the vectorial transposition, ε and γ are the components of strain.

It is obvious that the z-component stresses and strains do not vanish and the above quantities are independent of z. Taking into consideration the z-independence, the St. Venant compatibility equations are reduced to the following forms:

$$\frac{\partial^2 \varepsilon_{xx}}{\partial y^2} + \frac{\partial^2 \varepsilon_{yy}}{\partial x^2} = \frac{\partial^2 \gamma_{xy}}{\partial x \partial y} \tag{4.3.5}$$

$$\frac{\partial^2 \gamma_{zx}}{\partial x \partial y} - \frac{\partial^2 \gamma_{yz}}{\partial x^2} = 0 \tag{4.3.6}$$

$$\frac{\partial^2 \gamma_{yz}}{\partial x \partial y} - \frac{\partial^2 \gamma_{zz}}{\partial x^2} = 0 \tag{4.3.7}$$

$$\frac{\partial^2 \varepsilon_{zz}}{\partial x^2} = 0 \tag{4.3.8}$$

$$\frac{\partial^2 \varepsilon_{zz}}{\partial y^2} = 0 \tag{4.3.9}$$

$$\frac{\partial^2 \varepsilon_{zz}}{\partial x \partial y} = 0 \tag{4.3.10}$$

From the above three equations, one knows that ε_z must be a linear function of x and y, i.e.,

$$\varepsilon_z = A(t)x + B(t)y + C(t) \tag{4.3.11}$$

where, A, B and C are arbitrary functions of time.

By using the kinematic equation,

$$\varepsilon_z = \frac{\partial u_z}{\partial z} \tag{4.3.12}$$

it is easy to obtain the displacement components (Cheng, 1998)

$$u_z = [A(t)x + B(t)y + C(t)]z + h(x, y, t) \tag{4.3.13}$$

$$u_x = -\frac{A(t)}{2}z^2 - D(t)yz + F(t)z + f(x, y, t) \tag{4.3.14}$$

$$u_y = -\frac{B(t)}{2}z^2 - D(t)xz + H(t)z + g(x, y, t) \tag{4.3.15}$$

Without considering the torsion and pure bending solutions, which do not generate pore pressure due to the lack of volumetric deformation, one shows $A = B = D = F = H = 0$ (Cheng, 1998). Thus, the displacements are simplified and become:

$$\begin{aligned} u_z &= C(t)z + h(x, y, t) \\ u_x &= f(x, y, t) \\ u_y &= g(x, y, t) \end{aligned} \tag{4.3.16}$$

It should be noted that the elastic counterparts of the above three equations are the "complete plane strain" case studied by Brady and Bray (1978). Lekhnitskii (1981) referred to the case of $A = B = D = F = H = 0$ as "generalized plane strain". In the

present study the Equations (4.3.16) are adopted, in which the plane strain, a warping and uni-axial strain components are included.

4.4 FInite Element Discretization for Poroelastic Solution

4.4.1 FInite Element Mesh

The first step in the solution of the coupled fluid flow and solid deformations problem by the finite element method is to discretize the problem domain. This is done by replacing the problem domain with a collection of nodes and elements referred to as the finite element mesh (Figure 4.4.1). Elements may be of any size and the size and shape of each element in the mesh can be different. In this dissertation, elements with four-nodes are chosen for the generalized plane strain problem. The values of the material properties are usually assumed to be constant within each element but are allowed to vary from one element to the next. This property of the finite element method makes it possible to simulate nonhomogeneous problems.

The level of computational effort required to obtain a solution will be determined to a great extent by the number of nodes. A coarse mesh has a smaller number of nodes and meshes and will give a lower precision than a fine mesh. However, the larger the number of nodes and meshes, the greater will be the required computational effort and cost. Therefore, when preparing the finite element mesh it is important to know the precision of the solution obtained. In this dissertation, the comparison between the analytical and finite element solutions is made to determine the rational numbers of elements.

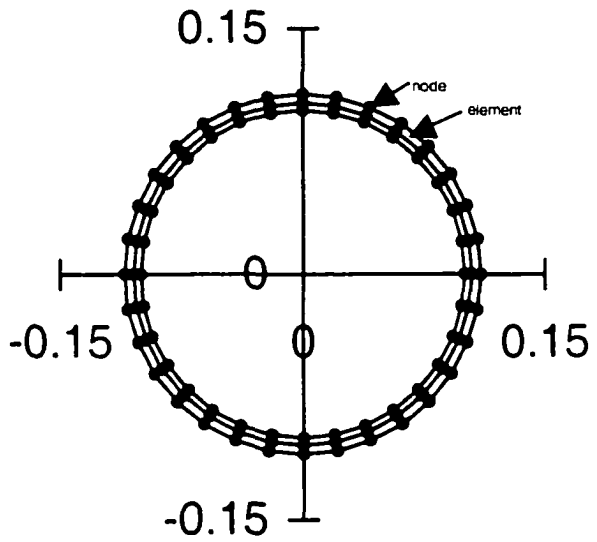


Figure 4.4.1 Discretization of generalized plane strain problem domain.

4.4.2 Weighted Residuals Method

The second step in the finite element method is to derive an integral formulation for the governing equations. This integral formulation leads to a system of algebraic equations that can be solved for values of the field variable at each node in the mesh. Several methods can be used to derive the integral formulation for a particular differential equation. The method of weighted residuals is a more general approach that is widely used in fluid flow and solid deformation modeling (Istok, 1989).

In the method of weighted residuals, an approximate solution to the boundary or initial value problem is defined. When this approximate solution is substituted into the governing differential equations, an error or residual occurs at each point in the problem domain. Then the weighted average of the residuals for each node in the finite element mesh is forced to equal zero.

Consider a differential equation of the form:

$$L[\Phi(x, y, z)] - F(x, y, z) = 0 \tag{4.4.1}$$

where L is the differential operator, Φ is the field variable, and F is a known function. An approximate solution, $\hat{\Phi}$, is defined as:

$$\hat{\Phi}(x, y, z) = \sum_{i=1}^{m} N_i(x, y, z)\Phi_i \tag{4.4.2}$$

where N_i are shape functions; Φ_i are the unknown values at the nodes; and m is the number of nodes in the mesh. When the approximate solution is substituted into Equation (4.4.1), the differential equation is no longer satisfied exactly and has the following residual term:

$$L\left[\hat{\Phi}(x, y, z)\right] - F(x, y, z) = R(x, y, z) \tag{4.4.3}$$

where R is the residual or error due to the approximate solution. The residual varies from point to point within the problem domain. At some point it may be large and at other points it may be small.

In the method of weighted residuals, the weighted residuals at the nodes are forced to be equal to zero, i.e.,

$$\iiint_{\Omega} W(x, y, z)R(x, y, z)d\Omega = 0 \tag{4.4.4}$$

where $W(x,y,z)$ is a weighting function and Ω represents the problem domain. Substituting Equation (4.4.3) into Equation (4.4.4) gives:

$$\iiint_{\Omega} W(x, y, z)\{L[\hat{\Phi}(x, y, z)] - F(x, y, z)\}d\Omega = 0 \tag{4.4.5}$$

so that the partial differencial equation has been replaced by an equation in the discretised space variables. The problem now reduces to one of finding the values Φ_i at the nodes. Galerkin's method is the most widely used in the finite element method to achieve this.

The Galerkin's method is then used whereby the weighting function for a node is identical to the interpolation function (shape function) used to define the approximate solution $\hat{\Phi}$.

4.4.3 Shape function

In the finite element method, the interpolation or shape functions are used to map the element displacements and fluid pressures at the nodal points, in other word, the shape function, N_i, is used to obtain the expressions for the variation of the unknown variables within an element in terms of the nodal values. Let $\Phi(x,y,z)$ = unknown functions, then one can write:

$$\{\Phi(x,y,z)\} = [\mathbf{N}]\{\Phi(x,y,z)_i\} = [N_1 \quad N_2 \quad \cdots \quad N_n]\begin{Bmatrix}\Phi_1\\ \Phi_2\\ \vdots\\ \Phi_n\end{Bmatrix} \tag{4.4.6}$$

The element, N_i, of this matrix must be such that it takes on a value of unity when evaluated at the geometric coordinates of the i^{th} selected node and has zero value at all the other remaining selected nodes. It should be noted that the shape function, N_i, must satisfy the following conditions (Zienkiewicz, 1977):

- The number of shape functions, N_i, must be equal to the number of nodal values of the element at the selected nodes;
- Continuity must be provided at nodes and also at element interfaces;

- The shape function must provide completeness for rigid body displacements and satisfy the constant strain criterion; and,
- The shape function must possess derivatives to the highest order appearing in the variational functional or the differential equation for the problem.

For the fluid pressure approximation at phase *i*, one has:

$$p_i^* = \mathbf{M}\mathbf{p}_i \tag{4.4.7}$$

where **M** is the shape function for the fluid pressure $\mathbf{p}_i$.

At nodal level, for four-point two-dimensional element:

$$p_i^* = \sum_{j=1}^{4} M_j p_{ij} \tag{4.4.8}$$

For the eight-point three-dimensional elements:

$$p_i^* = \sum_{j=1}^{8} M_j p_{ij} \tag{4.4.9}$$

The vector of shape function for pressure, **M**, can be given in following forms:

While for eight-point three-dimensional elements:

$$M_1 = \frac{1}{8}(1-\xi)(1-\eta)(1-\zeta) \tag{4.4.10}$$

$$M_2 = \frac{1}{8}(1+\xi)(1-\eta)(1-\zeta) \tag{4.4.11}$$

$$M_3 = \frac{1}{8}(1+\xi)(1-\eta)(1+\zeta) \tag{4.4.12}$$

$$M_4 = \frac{1}{8}(1-\xi)(1-\eta)(1+\zeta) \tag{4.4.13}$$

$$M_5 = \frac{1}{8}(1-\xi)(1+\eta)(1-\zeta) \tag{4.4.14}$$

$$M_6 = \frac{1}{8}(1+\xi)(1+\eta)(1-\zeta) \tag{4.4.15}$$

$$M_7 = \frac{1}{8}(1+\xi)(1+\eta)(1+\zeta) \tag{4.4.16}$$

$$M_8 = \frac{1}{8}(1-\xi)(1+\eta)(1+\zeta) \tag{4.4.17}$$

and for four-point two-dimensional elements:

$$M_1 = \frac{1}{4}(1-\xi)(1-\eta) \tag{4.4.18}$$

$$M_2 = \frac{1}{4}(1+\xi)(1-\eta) \tag{4.4.19}$$

$$M_3 = \frac{1}{4}(1+\xi)(1+\eta) \tag{4.4.20}$$

$$M_4 = \frac{1}{4}(1-\xi)(1+\eta) \tag{4.4.21}$$

where ξ, η and ζ represent local coordinates, and $-1 \le \xi \le 1$, $-1 \le \eta \le 1$ and $-1 \le \zeta \le 1$.

A similar expression for the approximation in mapping nodal displacements can be described as:

$$\mathbf{u}^* = \mathbf{N}\mathbf{u} \tag{4.4.22}$$

at nodal level, for four-point two-dimensional elements:

$$u_i^* = \sum_{j=1}^{4} N_j u_{ij}, \qquad u_i^* = \sum_{j=1}^{4} N_j u_{ij} \tag{4.4.23}$$

for eight-point three-dimensional elements:

$$u_x^* = \sum_{j=1}^{8} N_j u_{xj}, \qquad u_y^* = \sum_{j=1}^{8} N_j u_{yj}, \qquad u_z^* = \sum_{j=1}^{8} N_j u_{zj} \tag{4.4.24}$$

where **u** is a vector of nodal displacements, **N** is a vector of shape function for displacement. In this approach, **N** is identical to **M**. For simplicity, the superscript '*' for variables in the above equations indicate that the finite element approximations are omitted in the subsequent description.

Strains within a single element are related to nodal displacements through the derivatives of the shape functions **B** as:

$$\boldsymbol{\varepsilon} = \mathbf{B}\mathbf{u} \tag{4.4.25}$$

where **B** is the strain-displacement matrix.

The generalized plane strain solutions maintain compatibility with the primary unknown terms equivalent to the three-dimensional formulation, but geometrically they are not related to the z-coordinate, similar to the two-dimensional cases. With reference to the finite element formulation, the major differences among the generalized plane strain, the plane strain and the three-dimensional situation are exhibited in the strain-displacement matrix **B**. In a two-dimensional geometry the matrix **B** can be expressed as:

$$\mathbf{B} = \begin{bmatrix} \dfrac{\partial}{\partial x} & 0 \\ 0 & \dfrac{\partial}{\partial y} \\ \dfrac{\partial}{\partial y} & \dfrac{\partial}{\partial x} \end{bmatrix} \mathbf{N} \tag{4.4.26}$$

For a three-dimensional geometry, **B** is slightly more complicated:

$$\mathbf{B} = \begin{bmatrix} \frac{\partial}{\partial x} & 0 & 0 \\ 0 & \frac{\partial}{\partial y} & 0 \\ 0 & 0 & \frac{\partial}{\partial z} \\ \frac{\partial}{\partial y} & \frac{\partial}{\partial x} & 0 \\ 0 & \frac{\partial}{\partial z} & \frac{\partial}{\partial y} \\ \frac{\partial}{\partial z} & 0 & \frac{\partial}{\partial x} \end{bmatrix} \mathbf{N} \tag{4.4.27}$$

For the generalized plane strain formulation, **B** can be written as:

$$\mathbf{B} = \begin{bmatrix} \frac{\partial}{\partial x} & 0 & 0 \\ 0 & \frac{\partial}{\partial y} & 0 \\ 0 & 0 & 0 \\ \frac{\partial}{\partial y} & \frac{\partial}{\partial x} & 0 \\ 0 & 0 & \frac{\partial}{\partial y} \\ 0 & 0 & \frac{\partial}{\partial x} \end{bmatrix} \mathbf{N} \tag{4.4.28}$$

The partial derivatives of the shape functions are given by:

$$\begin{Bmatrix} \frac{\partial N_i}{\partial \xi} \\ \frac{\partial N_i}{\partial \eta} \\ \frac{\partial N_i}{\partial \zeta} \end{Bmatrix} = J \begin{Bmatrix} \frac{\partial N_i}{\partial x} \\ \frac{\partial N_i}{\partial y} \\ \frac{\partial N_i}{\partial z} \end{Bmatrix} \tag{4.4.29}$$

where, J is called the Jacobian determinant (Zienkiewicz, 1977) and can be found explicitly in terms of the element local coordinates, (ξ, η, ζ), and the element nodal coordinates, (x, y, z), i.e.,

$$J = \begin{bmatrix} \frac{\partial x}{\partial \xi} & \frac{\partial y}{\partial \xi} & \frac{\partial z}{\partial \xi} \\ \frac{\partial x}{\partial \eta} & \frac{\partial y}{\partial \eta} & \frac{\partial z}{\partial \eta} \\ \frac{\partial x}{\partial \zeta} & \frac{\partial y}{\partial \zeta} & \frac{\partial z}{\partial \zeta} \end{bmatrix} = \begin{bmatrix} \sum \frac{\partial N_i}{\partial \xi} x_i & \sum \frac{\partial N_i}{\partial \xi} y_i & \sum \frac{\partial N_i}{\partial \xi} z_i \\ \sum \frac{\partial N_i}{\partial \eta} x_i & \sum \frac{\partial N_i}{\partial \eta} y_i & \sum \frac{\partial N_i}{\partial \eta} y_i \\ \sum \frac{\partial N_i}{\partial \zeta} x_i & \sum \frac{\partial N_i}{\partial \zeta} y_i & \sum \frac{\partial N_i}{\partial \zeta} z_i \end{bmatrix} = \begin{bmatrix} \frac{\partial N_1}{\partial \xi} & \frac{\partial N_2}{\partial \xi} & \cdots \\ \frac{\partial N_1}{\partial \eta} & \frac{\partial N_2}{\partial \eta} & \cdots \\ \frac{\partial N_1}{\partial \zeta} & \frac{\partial N_2}{\partial \zeta} & \cdots \end{bmatrix} \begin{bmatrix} x_1 & y_1 & z_1 \\ x_2 & y_2 & z_2 \\ \vdots & \vdots & \vdots \end{bmatrix} \tag{4.4.30}$$

Equation (4.4.29) can, therefore, be rewritten as follows:

$$\begin{Bmatrix} \frac{\partial N_i}{\partial x} \\ \frac{\partial N_i}{\partial y} \\ \frac{\partial N_i}{\partial z} \end{Bmatrix} = J^{-1} \begin{Bmatrix} \frac{\partial N_i}{\partial \xi} \\ \frac{\partial N_i}{\partial \eta} \\ \frac{\partial N_i}{\partial \zeta} \end{Bmatrix} \tag{4.4.31}$$

4.4.4 Conservation equations

The general force equilibrium equation in generalized plane strain domain is given by:

$$\int_{\Omega} \mathbf{B}^{\mathrm{T}} \mathbf{D}_{\mathrm{mf}} \partial \boldsymbol{\sigma} d\Omega - \partial \mathbf{f} = 0 \tag{4.4.32}$$

where, Ω is the area of integral domain for generalized plane strain problem and the volume of integral domain for three-dimensional problem, and $\mathbf{f}$ is a vector of applied boundary tractions.

Substituting the dual-porosity stress-strain relationships (Equation 3.2.10) and $\partial p_i = \mathbf{M}\partial \mathbf{p}_i$ (differential of Equation 4.4.7) into Equation (4.4.32) in terms of nodal variables, one obtains:

$$\int_{\Omega} \mathbf{B}^{\mathrm{T}}\mathbf{D}_{\mathrm{mf}}\varepsilon d\Omega + \sum_{i=1}^{2}\left(\alpha_i \int_{\Omega} \mathbf{B}^{\mathrm{T}}\mathbf{D}_{\mathrm{mf}}\mathbf{C}_i\mathbf{m}\mathbf{M}\mathbf{p}_i d\Omega\right) = \mathbf{f} \tag{4.4.33}$$

where, C_1 is the matrix compliance matrix defined in Equation (3.2.13) and $C_1 = C_{maijkl}$. C_2 is the fracture compliance matrix defined in Equation (3.2.14) and $C_2 = C_{frijkl}$.

Substituting Equation (4.4.25) and dividing through by Δt, the momentum balance in finite element form can be expressed as:

$$\int_{\Omega} \mathbf{B}^{\mathrm{T}}\mathbf{D}_{\mathrm{mf}}\mathbf{B}\frac{\partial \mathbf{u}}{\partial t} d\Omega + \sum_{i=1}^{2}\left(\alpha_i \int_{\Omega} \mathbf{B}^{\mathrm{T}}\mathbf{D}_{\mathrm{mf}}\mathbf{C}_i\mathbf{m}\mathbf{M}\frac{\partial \mathbf{p}_i}{\partial t} d\Omega\right) = \frac{\partial \mathbf{f}}{\partial t} \tag{4.4.34}$$

or,

$$\mathbf{K}\frac{\partial \mathbf{u}}{\partial t} + \mathbf{R}_1\frac{\partial \mathbf{p}_{\mathrm{ma}}}{\partial t} + \mathbf{R}_2\frac{\partial \mathbf{p}_{\mathrm{fr}}}{\partial t} = \frac{\partial \mathbf{f}}{\partial t} \tag{4.4.35}$$

where detailed expressions of the coefficients are given in Appendix A.

The integration of the equation usually requires the use of numerical techniques, and a standard method is that of *Gaussian quadrature*, where the integrands are evaluated at specific points of the element and boundary surfaces and then weighted and summed (Zienkiewicz, 1977). The dual-porosity mass balance equations (Equations 3.3.9 and 3.3.10) in finite element form may be given for each system as following:

For the rock matrix system:

$$\frac{1}{\mu}\int_{\Omega}\mathbf{M}^{\mathrm{T}}\mathbf{k}_{ma}\nabla\mathbf{M}d\Omega\mathbf{p}_{ma}=\alpha_{ma}\int_{\Omega}\mathbf{N}^{\mathrm{T}}\mathbf{m}\mathbf{D}_{mf}\mathbf{C}_{ma}\mathbf{B}d\Omega\frac{\partial\mathbf{u}}{\partial\mathbf{t}}$$
$$-\beta_{ma}\int_{\Omega}\mathbf{M}^{\mathrm{T}}\mathbf{M}d\Omega\frac{\partial\mathbf{p}_{ma}}{\partial\mathbf{t}}+\omega\int_{\Omega}\mathbf{M}^{\mathrm{T}}\mathbf{M}d\Omega\Delta\mathbf{p}+\int_{\Omega}\mathbf{M}^{\mathrm{T}}\mathbf{M}d\Omega\mathbf{q}_{ma} \tag{4.4.36}$$

or,

$$\mathbf{M}_1\frac{\partial\mathbf{u}}{\partial\mathbf{t}}+(\mathbf{Q}-\mathbf{L}_1)\mathbf{p}_{ma}-\mathbf{Q}\mathbf{p}_{fr}-\mathbf{N}_1\frac{\partial\mathbf{p}_{ma}}{\partial\mathbf{t}}=-\mathbf{q}_{ma} \tag{4.4.37}$$

For the fracture system:

$$\frac{1}{\mu}\int_{\Omega}\mathbf{M}^{\mathrm{T}}\mathbf{k}_{fr}\nabla\mathbf{M}d\Omega\mathbf{p}_{fr}=\alpha_{fr}\int_{\Omega}\mathbf{N}^{\mathrm{T}}\mathbf{m}\mathbf{D}_{mf}\mathbf{C}_{ma}\mathbf{B}d\Omega\frac{\partial\mathbf{u}}{\partial\mathbf{t}}-\beta_{fr}\int_{\Omega}\mathbf{M}^{\mathrm{T}}\mathbf{M}d\Omega\frac{\partial\mathbf{p}_{fr}}{\partial\mathbf{t}}-\omega\int_{\Omega}\mathbf{M}^{\mathrm{T}}\mathbf{M}d\Omega\Delta\mathbf{p}+\int_{\Omega}\mathbf{M}^{\mathrm{T}}\mathbf{M}d\Omega\mathbf{q}_{fr} \tag{4.4.38}$$

where, $\Delta\mathbf{p}=\mathbf{p}_{fr}-\mathbf{p}_{ma}$, $\mathbf{m}^{\mathrm{T}}=(1\ 1\ 1\ 0\ 0\ 0)$, ω is the interporosity flow coefficient and, α is Biot effective stress coefficient (Biot, 1941), which can be evaluated as:

$$\alpha_{ma}=1-\frac{K_{sk}}{K_s} \tag{4.4.39}$$

$$\alpha_{fr}=1-\frac{K^{*}_{sk}}{K_{fr}} \tag{4.4.40}$$

where K_{sk} and K^{*}_{sk} are the bulk moduli of the skeleton for the matrix blocks and the fractures, respectively, and K_s and K_{fr} are the bulk moduli of the solid grains and fractures, respectively. Since $K^{*}_{sk}<<K_{fr}$, $\alpha_{fr}=1$, and β is the relative compressibility, which can be written as:

$$\beta_{ma}=\frac{n_{ma}}{K_f}+\frac{\alpha_{ma}-n_{ma}}{K_s} \tag{4.4.41}$$

$$\beta_{fr}=\frac{n_{fr}}{sK_n}+\frac{\alpha_{fr}-n_{fr}}{sK_n} \tag{4.4.42}$$

in which K_f and K_n are the bulk moduli of the fluid and the normal stiffness of the fractures, respectively, n_{ma} and n_{fr} are the matrix and fracture porosities, respectively, and s is the fracture spacing.

or,

$$\mathbf{M}_2 \frac{\partial \mathbf{u}}{\partial \mathbf{t}} - \mathbf{Q}\mathbf{p}_{ma} + (\mathbf{Q} - \mathbf{L}_2)\mathbf{p}_{fr} - \mathbf{N}_2 \frac{\partial \mathbf{p}_{fr}}{\partial \mathbf{t}} = -\mathbf{q}_{fr} \tag{4.4.43}$$

Detailed expressions of the above coefficients are listed in Appendix A. Equations (4.4.35), (4.4.37) and (4.4.43) represent a set of differential equations in time and can be expressed in matrix form as follows:

$$\begin{bmatrix} \mathbf{0} & \mathbf{0} & \mathbf{0} \\ \mathbf{0} & \mathbf{Q}-\mathbf{L}_1 & -\mathbf{Q} \\ \mathbf{0} & -\mathbf{Q} & \mathbf{Q}-\mathbf{L}_2 \end{bmatrix} \begin{bmatrix} \mathbf{u} \\ \mathbf{p}_{ma} \\ \mathbf{p}_{fr} \end{bmatrix} + \begin{bmatrix} \mathbf{K} & \mathbf{R}_1 & \mathbf{R}_2 \\ \mathbf{M}_1 & -\mathbf{N}_1 & \mathbf{0} \\ \mathbf{M}_2 & \mathbf{0} & -\mathbf{N}_2 \end{bmatrix} \frac{d}{dt} \begin{bmatrix} \mathbf{u} \\ \mathbf{p}_{ma} \\ \mathbf{p}_{fr} \end{bmatrix} = \begin{bmatrix} \mathbf{df} \\ \mathbf{dt} \\ -\mathbf{q}_{ma} \\ -\mathbf{q}_{fr} \end{bmatrix} \tag{4.4.44}$$

The discretization in space has been completed; Equation (4.4.44) now represents a set of differential equations in time. The values of $\mathbf{u}$, $\mathbf{p}_{ma}$ and $\mathbf{p}_{fr}$ at different values in time may be obtained by means of appropriate time-stepping algorithms.

4.4.5 Finite Element Discretization in Time

The finite element formulation can be obtained by integrating in time. Using a fully implicit finite difference scheme in the time discretization domain, such that:

$$\begin{cases} \dfrac{d\mathbf{u}^{t+\Delta t}}{dt} = \dfrac{1}{\Delta t}(\mathbf{u}^{t+\Delta t} - \mathbf{u}^{t}) \\ \dfrac{d\mathbf{p}_{ma}^{t+\Delta t}}{dt} = \dfrac{1}{\Delta t}(\mathbf{p}_{ma}^{t+\Delta t} - \mathbf{p}_{ma}^{t}) \\ \dfrac{d\mathbf{p}_{fr}^{t+\Delta t}}{dt} = \dfrac{1}{\Delta t}(\mathbf{p}_{fr}^{t+\Delta t} - \mathbf{p}_{fr}^{t}) \end{cases} \tag{4.4.45}$$

Substituting Equation (4.4.45) into Equations (4.4.44), the finite element equations in matrix form for the dual-porosity poroelastic medium can be expressed as follows:

$$\frac{1}{\Delta t}\begin{bmatrix} \mathbf{K} & \mathbf{R}_1 & \mathbf{R}_2 \\ \mathbf{M}_1 & (\mathbf{Q}-\mathbf{L}_1)\Delta t-\mathbf{N}_1 & -\mathbf{Q}\Delta t \\ \mathbf{M}_2 & -\mathbf{Q}\Delta t & (\mathbf{Q}-\mathbf{L}_2)\Delta t-\mathbf{N}_2 \end{bmatrix}\begin{bmatrix} \mathbf{u} \\ \mathbf{p}_{ma} \\ \mathbf{p}_{fr} \end{bmatrix}^{t+\Delta t}$$
$$=\frac{1}{\Delta t}\begin{bmatrix} \mathbf{K} & \mathbf{R}_1 & \mathbf{R}_2 \\ \mathbf{M}_1 & -\mathbf{N}_1 & 0 \\ \mathbf{M}_2 & 0 & -\mathbf{N}_2 \end{bmatrix}\begin{bmatrix} \mathbf{u} \\ \mathbf{p}_{ma} \\ \mathbf{p}_{fr} \end{bmatrix}^{t}+\begin{bmatrix} \frac{\mathbf{f}}{\Delta t} \\ \mathbf{q}_{ma} \\ \mathbf{q}_{fr} \end{bmatrix}^{t+\Delta t}-\begin{bmatrix} \frac{\mathbf{f}}{\Delta t} \\ 0 \\ 0 \end{bmatrix}^{t} \tag{4.4.46}$$

4.4.6 Initial condition and ramp loading

It is generally assumed that the rock displacement **u** and pore pressure **p** are continuous functions in time. However, this assumption cannot be made at the time that the loading is instantaneously applied (Bai and Meng, 1994). As a result, special treatment of the initial condition is required. Normally, the initial displacement field and fluid pressure distribution can be evaluated through solving the static undrained governing equation:

$$\begin{bmatrix} \mathbf{K} & \mathbf{R}_1 & \mathbf{R}_2 \\ \mathbf{M}_1 & (\mathbf{Q}-\mathbf{L}_1)-\mathbf{N}_1 & -\mathbf{Q} \\ \mathbf{M}_2 & -\mathbf{Q} & (\mathbf{Q}-\mathbf{L}_2)-\mathbf{N}_2 \end{bmatrix}\begin{bmatrix} \mathbf{u} \\ \mathbf{p}_{ma} \\ \mathbf{p}_{fr} \end{bmatrix}=\begin{bmatrix} 0 \\ 0 \\ 0 \end{bmatrix} \tag{4.4.47}$$

However, for slightly compressible fluids, the static governing equation may be ill-conditioned and an alternative method is to use a ramp loading to approximate the initial conditions. As shown in Figure 4.4.2, a linear function in the first time step is used to avoid violent oscillations that may result from the step loading.

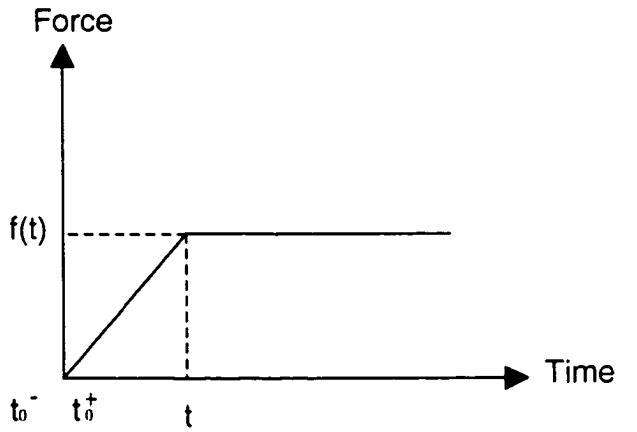


Figure 4.4.2 Ramp loading in approximation of initial condition

4.4.7 Computational Procedure and Computer Code

There are 5 unknowns (u_x , u_y , u_z , p_{ma} , p_{fr}) and 5 equations per node, therefore, displacements and pressures can be solved from Equation (4.4.46). Stress and strain, then, can be obtained through the following relations:

$$\varepsilon_{ij} = \frac{1}{2}(u_{i,j} + u_{j,i}) \tag{4.4.48}$$

$$\sigma_{ij} = D_{mj}(\varepsilon_{kl} + C_{maklmn}\alpha_{ma}p_{ma}\delta_{mn} + C_{frklmn}\alpha_{fr}p_{fr}\delta_{mn}) \tag{3.2.10}$$

The finite element equations (Equation 4.4.46) are solved by using a Fortran program according to the flowchart shown in Figure 4.4.3. The iterative steps to solve this problem are as follows:

(1) Start from $t = t_0$, input data for given initial values of boundary forces, pressures, displacements and solid, matrix and fracture properties;

(2) Solve unknowns, **u**, p_{ma}, p_{fr}, at each Gaussian points;

(3) Calculate strains and stresses from **u**, p_{ma}, p_{fr}, at each Gaussian points;

(4) Go to next time step and repeat steps (2) and (3).

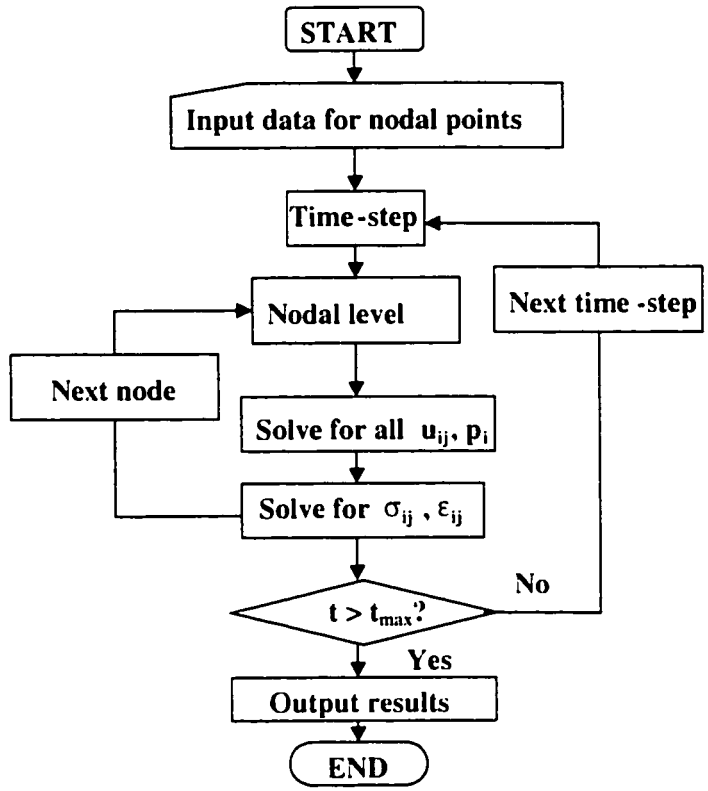


Figure 4.4.3 Finite element solution procedure.

The preprocessor and postprocessor are written in Microsoft Visual Basic language®. Figure 4.4.4 illustrates the structure and functions of this finite element code (IASRS).

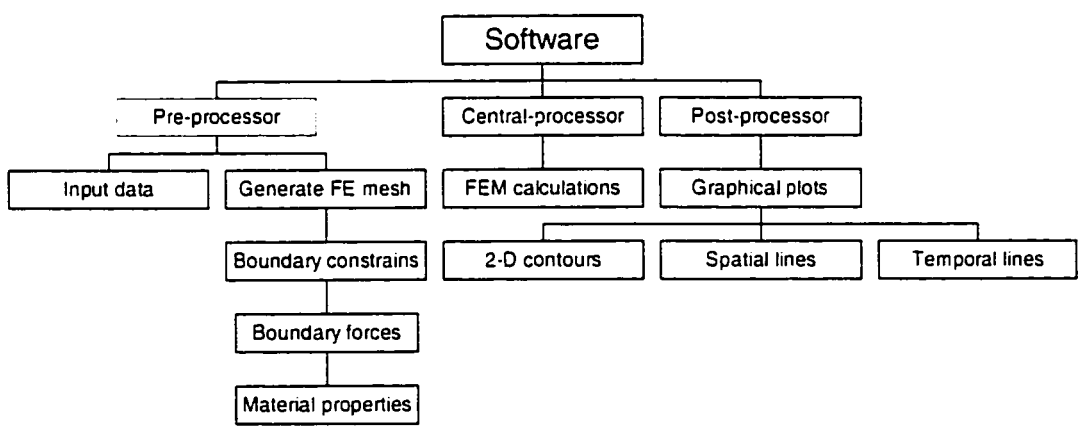


Figure 4.4.4 Structure of the finite element code.

4.4.8 Elasticity and Steady-state Flow

The proposed finite element model and the computer code can easily be used for other problems that include elasticity, steady-state flow, single-porosity, and dual-porosity problems. The formulations are derived directly from Equations (4.4.35), (4.4.37) and (4.4.43), which are the basic equations for the coupling problems of solid deformations and fluid flow in dual-porosity media.

For pure elastic problems, Equation (4.4.46) could be simplified according to the following conditions:

- Fluid pressures have no influence on the solid media;
- No time effect; and,
- No fracture effect, which means that the solid material is similar to a single-porosity homogeneous medium.

For steady-state flow conditions, the following items need to be considered in Equation (4.4.46):

- No time effect;
- No fracture influence;
- Solid material is an homogeneous medium;
- No fluid exchange between rock matrix and fracture;
- Single-phase fluid flow; and,
- No volumetric strain effect on the fluid flow.

Under all the above assumptions, Equation (4.4.46) can be simplified as:

$$\begin{bmatrix} \mathbf{K} & 0 & 0 \\ 0 & -\mathbf{L}_1 & 0 \\ 0 & 0 & 0 \end{bmatrix} \begin{bmatrix} \mathbf{u} \\ \mathbf{p}_{ma} \\ \mathbf{p}_{fr} \end{bmatrix} = \begin{bmatrix} \mathbf{f} \\ \mathbf{q}_{ma} \\ 0 \end{bmatrix} \tag{4.4.49}$$

Equation (4.4.49) can be used to solve pure elastic and steady-state flow problems.

4.4.9 Single-porosity Poroelasticity

The proposed model can also be used to simulate the coupled processes between the solid rock deformations and fluid flow for single-porosity porous media. Neglecting the contribution from the fracture fluid pressure; hence, for single-porosity media, the following changes need to be considered in Equation (4.4.46):

- No fracture influence on the porous media; and,
- No fluid interchange between the rock matrix and the fractures.

Therefore, Equation (4.4.46) can be simplified as:

$$\frac{1}{\Delta t}\begin{bmatrix} \mathbf{K} & \mathbf{R}_1 & 0 \\ \mathbf{M}_1 & -\mathbf{L}_1\Delta t - \mathbf{N}_1 & 0 \\ 0 & 0 & 0 \end{bmatrix}\begin{bmatrix} \mathbf{u} \\ \mathbf{p}_{ma} \\ \mathbf{p}_{fr} \end{bmatrix}^{t-\Delta t} = \frac{1}{\Delta t}\begin{bmatrix} \mathbf{K} & \mathbf{R}_1 & 0 \\ \mathbf{M}_1 & -\mathbf{N}_1 & 0 \\ 0 & 0 & 0 \end{bmatrix}\begin{bmatrix} \mathbf{u} \\ \mathbf{p}_{ma} \\ \mathbf{p}_{fr} \end{bmatrix}^{t} + \begin{bmatrix} \frac{\mathbf{f}}{\Delta t} \\ \mathbf{q}_{ma} \\ 0 \end{bmatrix}^{t-\Delta t} + \begin{bmatrix} \frac{\mathbf{f}}{\Delta t} \\ 0 \\ 0 \end{bmatrix}^{t} \tag{4.4.50}$$

Equation (4.4.50) can be used to solve the coupled solid deformation and fluid flow problems for single porosity medium.

4.5 Finlte Element Method for Poroelastoplastic Solution

In practical finite element analyses two main types of solution procedures can be adopted to model material non-linearity. The first approach involves 'constant stiffness' iterations in which non-linearity is introduced by iteratively modifying the 'load vector'. The global stiffness matrix in such an analysis is formed. Each iteration thus represents an elastic analysis (Smith and Griffiths, 1988). The second approach is referred to as the

variable or tangent stiffness method. The method takes into account the reduction in stiffness of the material as failure is approached.

The constant stiffness methods use repeated elastic solutions to achieve convergence by iteratively varying the loads on the system. Within each load increment, the system of equations:

$$\mathbf{K}\Delta\mathbf{u}^{i} = \Delta\mathbf{p}^{i} \tag{4.5.1}$$

must be solved for displacement increment $\Delta\mathbf{u}^{i}$, where i represents the iteration number. The total strain increments can be obtained by:

$$\Delta\varepsilon^{i} = \mathbf{B}\Delta\mathbf{u}^{i} \tag{4.5.2}$$

When the material is yielding, the strain will contain both elastic and plastic components; thus,

$$\Delta\varepsilon^{i} = (\Delta\varepsilon^{e} + \Delta\varepsilon^{p})^{i} \tag{4.5.3}$$

Only the elastic strain increments $\Delta\varepsilon^{e}$ generate stresses through the elastic stress-strain matrix; hence,

$$\Delta\sigma^{i} = \mathbf{D}_{mf}(\Delta\varepsilon^{e})^{i} \tag{4.5.4}$$

These stress increments are added to stresses already existing from the previous load step and updated stresses are then substituted into the failure criterion.

In general, the load increment vector $\Delta\mathbf{p}^{i}$ holds two types of load:

$$\Delta\mathbf{p}^{i} = \Delta\mathbf{p}_{a} + \Delta\mathbf{p}_{b}^{i} \tag{4.5.5}$$

where $\Delta \mathbf{p}_a$ is the actual applied load increment and $\Delta \mathbf{p}_b'$ is the body-loads vector that varies from one iteration to the next. The body-loads can be obtained from the 'initial stress' method.

4.5.1 Initial Stress Method

The initial stress method involves an explicit relationship between increments of stress and increments of strain (Smith and Griffiths, 1988). The elastoplastic stress-strain can be described by:

$$\Delta \boldsymbol{\sigma} = \mathbf{D}_{mf}^{ep} \Delta \boldsymbol{\varepsilon} \tag{4.5.6}$$

where $\mathbf{D}_{mf}^{ep} = \mathbf{D}_{mf} - \mathbf{D}_{mf}^{p}$, $\mathbf{D}^{p}{}_{mf}$ is the plastic modulus.

The total strain increment is assumed to be the sum of the elastic and plastic strain increments:

$$\Delta \boldsymbol{\varepsilon} = \Delta \boldsymbol{\varepsilon}^{e} + \Delta \boldsymbol{\varepsilon}^{p} \tag{4.5.7}$$

The body-loads $\Delta \mathbf{p}_b'$ in the stress redistribution process are changed at each iteration by summing the following integral for all elements that possess yield Gauss points, namely:

$$\Delta \mathbf{p}_b' = \sum_{elements}^{all} \iiint \mathbf{B}^{T} (\mathbf{D}_{mf}^{p} \Delta \boldsymbol{\varepsilon})' dx dy dz \tag{4.5.8}$$

For perfect plasticity it is assumed that once a stress state reaches a failure surface, subsequence changes in stress may shift the stress to a different position on the failure surface, but not outside it (Smith and Graffiths, 1988); thus,

$$\frac{\partial f}{\partial \boldsymbol{\sigma}} \Delta \boldsymbol{\sigma} = 0 \tag{4.5.9}$$

where f is the yield function.

Allowing for the possibility of non-associated flow, plastic strain increments occur normal to a plastic potential surface. The plastic strain increment can be obtained from the flow rule; i.e.

$$\Delta \boldsymbol{\varepsilon}^{\mathrm{p}} = d\lambda \frac{\partial f}{\partial \boldsymbol{\sigma}} \tag{4.5.10}$$

where $d\lambda$ is a positive scalar factor of proportionality, and $d\lambda = \dfrac{\dfrac{\partial f}{\partial \sigma_{ij}} D_{mfijkl} d\varepsilon_{kl}}{\dfrac{\partial f}{\partial \sigma_{rs}} D_{mfrstu} \dfrac{\partial f}{\partial \sigma_{tu}}}$.

The plastic modulus can be expressed explicitly in the following form:

$$D^{p}_{mfijkl} = -\frac{H_{ij} H_{kl}}{h} \tag{4.5.11}$$

where $\begin{cases} h = \dfrac{\partial f}{\partial \sigma_{rs}} D_{mfrstu} \dfrac{\partial f}{\partial \sigma_{tu}} \\ H_{ij} = D_{mfijmn} \dfrac{\partial f}{\partial \sigma_{mn}} \end{cases}$

In terms of the elastic constants G_{mf} and ν, and the coefficients B_0, B_1, and B_2 (refer to Table 4.5.1) for different yield surfaces, h and H_{ij} can be expressed as follows:

$$\begin{cases} h = 2G_{mf}\left(3B_0^2 \dfrac{1+\nu}{1-2\nu} + 2B_1^2 J_2 + \dfrac{2}{3} B_2^2 J_2^2 + 6B_1 B_2 J_3 \right) \\ H_{ij} = 2G_{mf}\left(B_0 \dfrac{1+\nu}{1-2\nu} \delta_{ij} + 2B_1 s_{ij} + B_2 t_{ij} \right) \end{cases} \tag{4.5.12}$$

where J_2 and J_3 are the invariants of the stress and stress deviator tensor (refer to Appendix B), s_{ij} is the deviatoric stress, $s_{ij} = \sigma_{ij} - I_1/3$, I_1 is the stress invariant (refer to Appendix B) and $t_{ij} = s_{ik}s_{kj} - 2J_2\delta_{ij}/3$.

Table 4.5.1 Constants B_i defined by different yield surfaces (Chen and Han, 1995)

Yield surface	B_0	B_1	B_2
von Mises	0	1	0
Tresca	0	$[\sin(\theta + \frac{\pi}{3})/\sqrt{J_2}][1 + \cot(\theta + \frac{\pi}{3})\cot 3\theta]$	$[-\sqrt{3}\sin(\theta + \frac{\pi}{3})/J_2 \sin 3\theta]$
Mohr-Coulomb	$\frac{\sin\phi}{3}$	$[\sin(\theta + \frac{\pi}{3})/2\sqrt{J_2}][\{1 + \cot(\theta + \frac{\pi}{3})\cot 3\theta] + \sin\phi[\cot(\theta + \frac{\pi}{3}) - \cot 3\theta]/\sqrt{3}\}$	$\frac{1}{2J_2 \sin 3\theta}[\sin(\theta + \frac{\pi}{3})\sin\phi - \sqrt{3}\cos(\theta + \frac{\pi}{3})]$
Drücker-Prager	α	$1/2\sqrt{J_2}$	0

Where $\theta = \arccos\left(\frac{3\sqrt{3}}{2}\frac{J_3}{J_2^{\frac{3}{2}}}\right)$.

4.5.2 Bi-linear Stress-strain Relationship

In general, the stress-strain behavior of rock is non-linear, especially in the case where external loads exceed the elastic strength of material and the material becomes plastic. In this study, a strain-hardening and bi-linear stress-strain relationship is assumed, as shown in Figure 4.5.1. Several yield criteria are used to determine the elastic and plastic transition of the rocks (refer to Chapter 7).

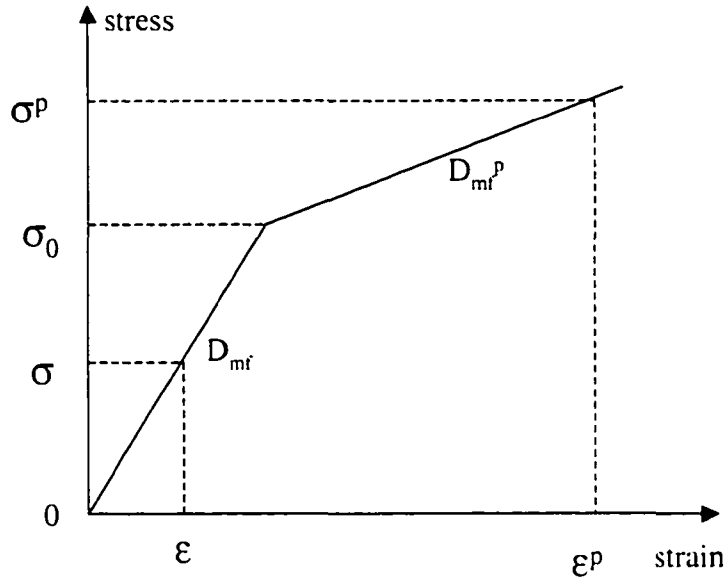


Figure 4.5.1 Bi-linear stress-strain relationship.

The computed steps to solve this problem using the finite element method are as follows (Figure 4.5.2):

(1) Start from $t = t_0$, input data for given initial values of boundary forces, pressures, displacements and solid, matrix and fracture properties;

(2) Solve unknowns, **u**, p_{ma}, p_{fr}, at each nodal point;

(3) Calculate strains and stresses from **u**, p_{ma}, p_{fr}, at each Gaussian point;

(4) Check whether or not failure occurs using a particular failure criterion.

(5) If materials have failed, calculate plastic modulus (D_{mf}^{p}) and repeat steps (2) and (3) and go to step (6). Otherwise, go directly to step (6).

(6) Go to next time step and repeat steps (2), (3), (4) and (5).

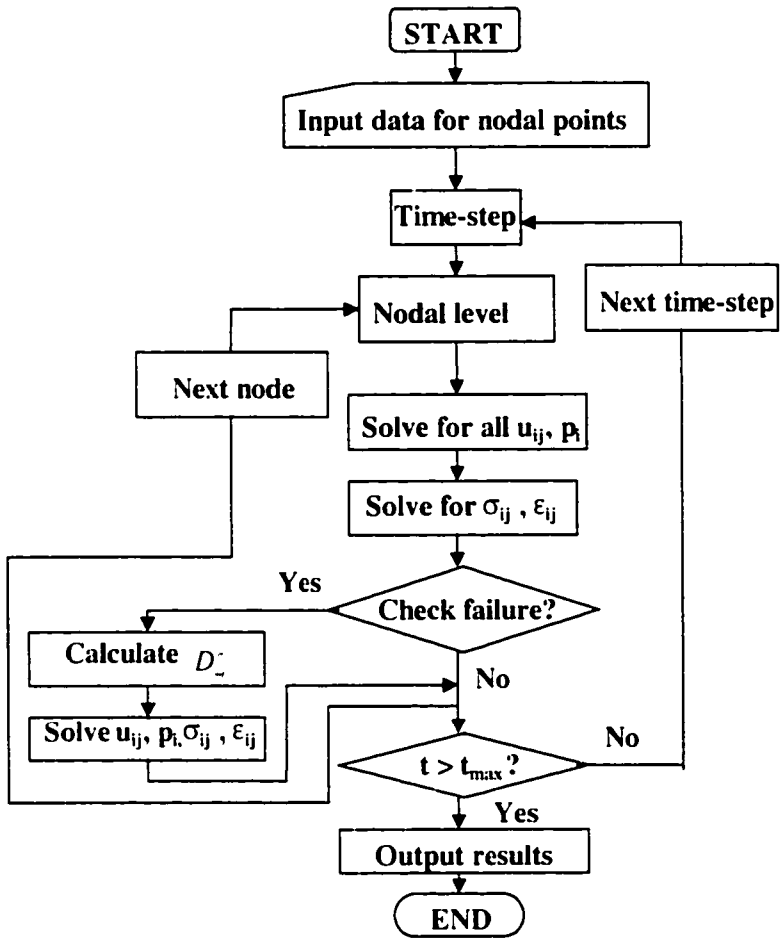


Figure 4.5.2 Flowchart for the Bi-linear analysis.

4.6 Wellbore Problem Solution

4.6.1 Stress Conversion for Inclined Borehole

In recent years, in order to improve oil recovery efficiency, horizontal and inclined boreholes have been implemented with some success. Directional borehole instability

then becomes a major concern. In order to model such situations, some stress transformations and conversions are required.

4.6.1.1 Stress conversion formulation

For an inclined borehole with its axis inclined with respect to the principal axes of the far-field uniform stresses, as shown in Figure 4.6.1, the following equations can be used to convert the global coordinates (far-field stress coordinate, x', y', z') into the local coordinates (borehole coordinate, x, y, z, see Figure 4.6.2) system.

$$\begin{Bmatrix} S_x \\ S_y \\ S_z \\ S_{xy} \\ S_{yz} \\ S_{zx} \end{Bmatrix} = \begin{bmatrix} l_{xx'}^2 & l_{xy'}^2 & l_{xz'}^2 \\ l_{yx'}^2 & l_{yy'}^2 & l_{yz'}^2 \\ l_{zx'}^2 & l_{zy'}^2 & l_{zz'}^2 \\ l_{xx'}l_{yx'} & l_{xy'}l_{yy'} & l_{xz'}l_{yz'} \\ l_{yx'}l_{zx'} & l_{zy'}l_{yy'} & l_{zz'}l_{yz'} \\ l_{zx'}l_{xx'} & l_{zy'}l_{xy'} & l_{zz'}l_{xz'} \end{bmatrix} \begin{Bmatrix} S_{x'} \\ S_{y'} \\ S_{z'} \end{Bmatrix} \tag{4.6.1}$$

where,

$$\begin{Bmatrix} l_{xx'} & l_{xy'} & l_{xz'} \\ l_{yx'} & l_{yy'} & l_{yz'} \\ l_{zx'} & l_{zy'} & l_{zz'} \end{Bmatrix} = \begin{bmatrix} \cos\varphi_x \cos\varphi_z & \sin\varphi_x \cos\varphi_x & -\sin\varphi_z \\ -\sin\varphi_x & \cos\varphi_x & 0 \\ \cos\varphi_x \sin\varphi_z & \sin\varphi_x \sin\varphi_z & \cos\varphi_z \end{bmatrix} \tag{4.6.2}$$

$S_{x'}$, $S_{y'}$, and $S_{z'}$ are the far-field stresses, S_x, S_y, S_z, S_{xy}, S_{yz} and S_{zx} are the local borehole coordinate stresses, φ_x is the angle between the global and local coordinates (Figure 4.6.2), φ_z is the borehole deviation. After the conversion, the finite element analysis can be worked out in the local coordinates, i.e., the section perpendicular to the borehole axial direction (Figure 4.6.3).

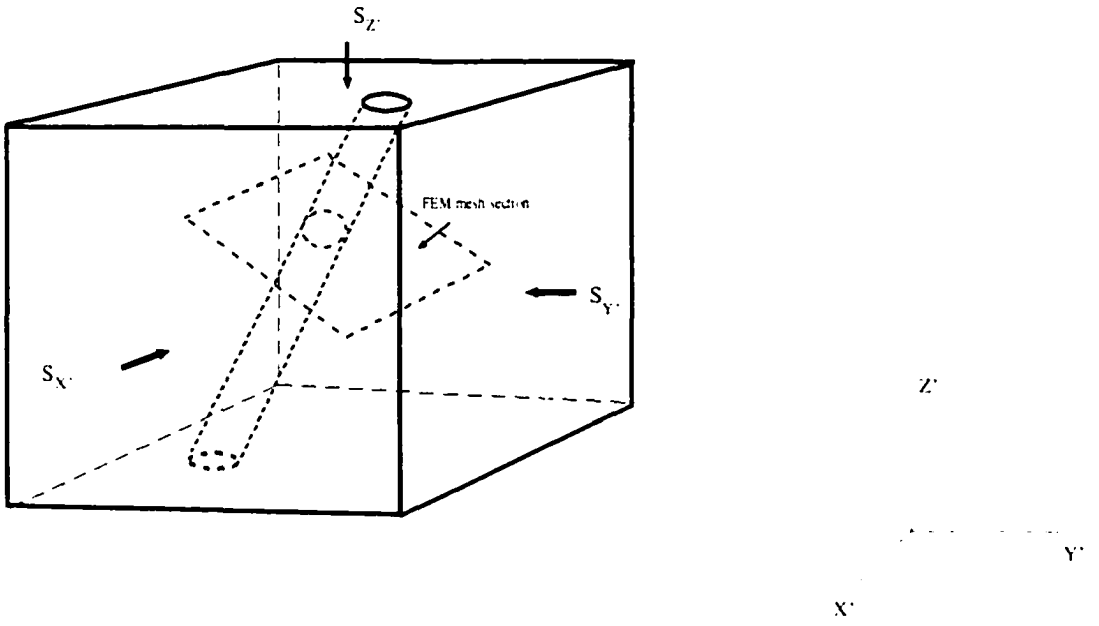


Figure 4.6.1 Schematic diagram for an inclined borehole

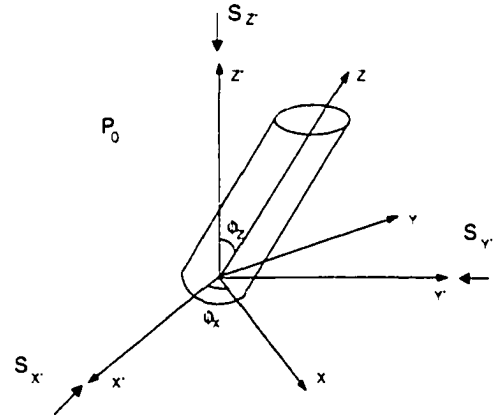


Figure 4.6.2 Local and global coordinate systems for an inclined borehole.

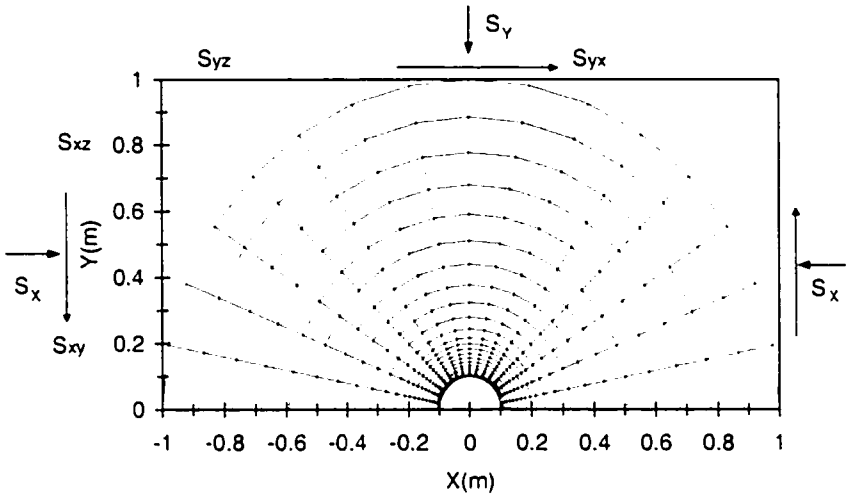


Figure 4.6.3 Finite element mesh in local coordinate system.

4.6.1.2 Boundary stress and forces determination

In the finite element analysis, the common approach is to subtract the constant far-field stresses and pore pressures from the field quantities. The boundary conditions are thus modified, i.e., on the outer boundary surfaces of the finite domain, all the tractions and pore pressure vanish, and at the borehole wall the equivalent stresses and pressures are given. After solving this problem, the final solution can be obtained by adding back the constant background stresses and pressures.

The equivalent stresses and pressures at any node at the borehole wall can be calculated by using the following equations:

$$
\begin{aligned}
\sigma_{t} &= lS_{x} + mS_{yx} + nS_{zx} \\
\sigma_{n} &= mS_{y} + nS_{zy} + lS_{xy} \\
\tau_{tn} &= nS_{z} + lS_{xz} + mS_{yz} \\
p_{ma} &= -p_{ma}^{0} \\
p_{fr} &= -p_{fr}^{0}
\end{aligned}
\tag{4.6.3}
$$

where, l, m, and n are the direction cosines between the normal to the inclined plane and the x, y, and z axes, respectively.

The boundary nodal forces along the wellbore can be determined by using the following equations:

$$
\begin{aligned}
F_{t} &= \sigma_{t} A \\
F_{n} &= \sigma_{n} A \\
F_{z} &= \tau_{tn} A
\end{aligned}
\tag{4.6.4}
$$

where A is the elemental area shown in Figure 4.6.4.

A Fortran code was written according to Equations (4.6.1) to (4.6.4) to transform the in-situ stress (far-field stress) to borehole local stresses and calculate the boundary nodal forces for different finite element domains. This code can be used for the data preparation in the finite element calculation. For any given in-situ stress and borehole deviation, this code can automatically calculate the boundary nodal forces and generate a data file that applied for the finite element calculation.

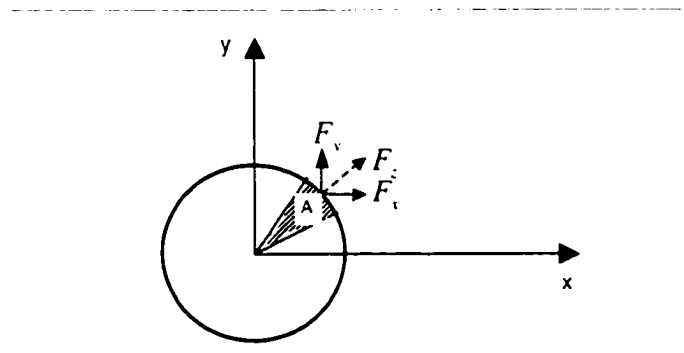


Figure 4.6.4 Boundary nodal forces at borehole wall.

4.6.2 Stress Transformation from Cartesian Coordinates into Polar Coordinates

In the analysis of stress and pore pressure distributions in and around the wellbore, the polar coordinate system is generally adopted. For the generalized plane strain formulation, the stresses in polar coordinates are related to the Cartesian coordinate stresses according to the following rules:

$$\begin{aligned}
\sigma_r &= \sigma_x \cos^2\theta + \sigma_y \sin^2\theta + 2\tau_{xy} \sin\theta\cos\theta \\
\sigma_\theta &= \sigma_x \sin^2\theta + \sigma_y \cos^2\theta - 2\tau_{xy} \sin\theta\cos\theta \\
\sigma_z &= \sigma_z \\
\tau_{r\theta} &= (\sigma_y - \sigma_x)\sin\theta\cos\theta + \tau_{xy}(\cos^2\theta - \sin^2\theta) \\
\tau_{rz} &= \tau_{xz}\cos\theta + \tau_{yz}\sin\theta \\
\tau_{\theta z} &= \tau_{yz}\cos\theta - \tau_{xz}\sin\theta
\end{aligned} \tag{4.6.5}$$

where r and θ are the radius and the angle with reference to the center of the wellbore in the polar coordinate system.

The strains relate to the Cartesian coordinate strains as:

$$\begin{aligned}
\varepsilon_r &= \varepsilon_x \cos^2\theta + \varepsilon_y \sin^2\theta + 2\gamma_{xy} \sin\theta\cos\theta \\
\varepsilon_\theta &= \varepsilon_x \sin^2\theta + \varepsilon_y \cos^2\theta - 2\gamma_{xy} \sin\theta\cos\theta \\
\varepsilon_z &= \varepsilon_z \\
\gamma_{r\theta} &= (\varepsilon_y - \varepsilon_x)\sin\theta\cos\theta + \gamma_{xy}(\cos^2\theta - \sin^2\theta) \\
\gamma_{rz} &= \gamma_{xz}\cos\theta + \gamma_{yz}\sin\theta \\
\gamma_{\theta z} &= \gamma_{yz}\cos\theta - \gamma_{xz}\sin\theta
\end{aligned} \tag{4.6.6}$$

4.6.3 Fluid Mudweight Considerations at the Borehole Wall

4.6.3.1 Permeable boundary

During the hole drilling, the suitable mudweight of the drilling fluid plays a very important role in protecting the borehole wall from breakouts and failures. The mudweight pressure, p_w, acts both as a radial stress and a fluid pressure at the borehole wall when the wellbore formation is permeable. Figure 4.6.5 illustrates the superposition principle allowing to consider the mudweight pressure at the borehole wall for the dual-porosity finite element modeling. In this figure p^0 represents both the initial pore and fracture pressures. Considering mud pressure effects, the stresses at the borehole wall can be expressed as:

$$\begin{aligned}
\sigma_x &= l(S_x - S_{mx}) + m(S_{xy} - S_{mxy}) + nS_{zx} \\
\sigma_y &= m(S_y - S_{my}) + nS_{zy} + l(S_{xy} - S_{mxy}) \\
\tau_{xy} &= nS_z + lS_{xz} + mS_{yz} \\
p_{ma} &= -p_{ma}^0 + p_w \\
p_{fr} &= -p_{fr}^0 + p_w
\end{aligned} \tag{4.6.7}$$

where S_{mx}, S_{my}, and S_{mxy} are stresses induced by the mud pressure (p_w) as the radial stress, which can be obtained by:

$$\begin{aligned}
S_{mx} &= l^2 p_w \\
S_{my} &= m^2 p_w \\
S_{mxy} &= lmp_w
\end{aligned} \tag{4.6.8}$$

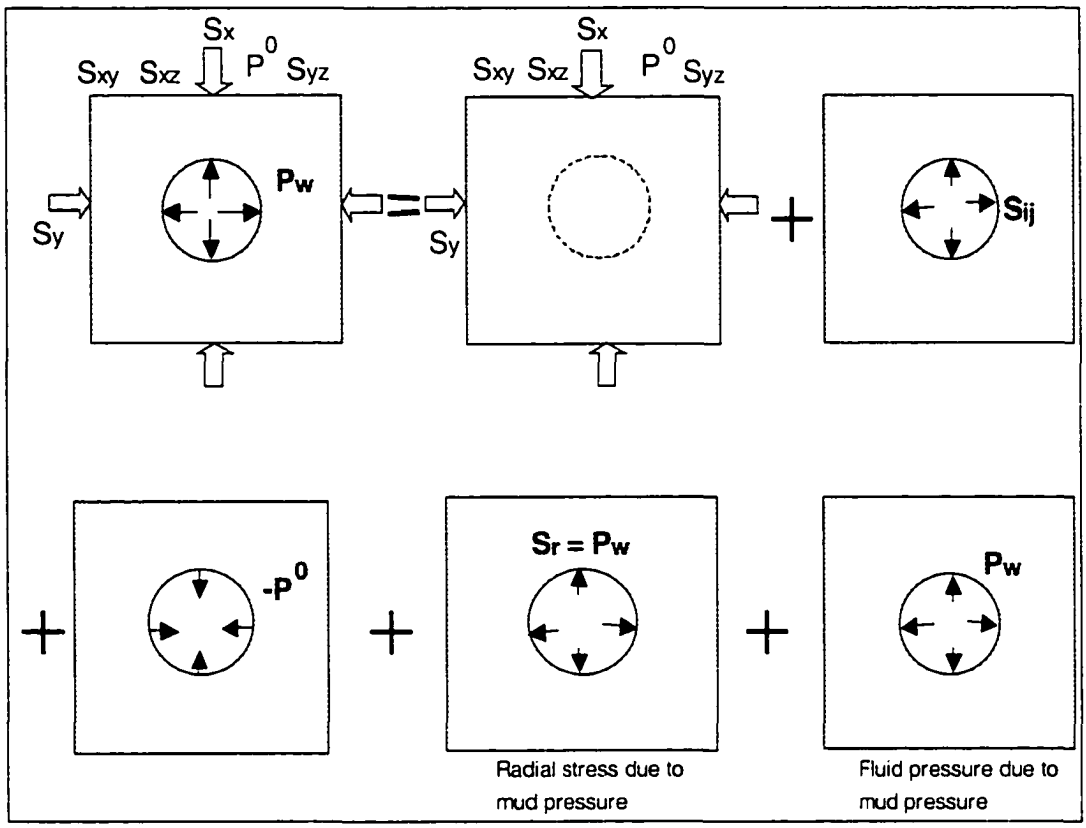


Figure 4.6.5 Superposition of mudweight pressure at the borehole wall for the permeable case in the FEM model

4.6.3.2 Impermeable boundary

Mud cake can be formed during drilling which may make the borehole wall impermeable. In this case, the flow rate at the borehole wall is zero and the mudweight pressure, p_w, acts only as a radial stress at the borehole wall under such conditions. Figure 4.6.6 illustrates the superposition principle for considering the mudweight pressure at the borehole wall for the dual-porosity finite element modeling. Therefore, the stresses at the borehole wall can be written as:

$$
\begin{aligned}
\sigma_{x} &= l(S_{x} - S_{mx}) + m(S_{xy} - S_{myx}) + nS_{zx} \\
\sigma_{y} &= m(S_{y} - S_{my}) + nS_{zy} + l(S_{xy} - S_{mxy}) \\
\tau_{xy} &= nS_{z} + lS_{xz} + mS_{yz} \\
p_{ma} &= -p_{ma}^{0} \\
p_{fr} &= -p_{fr}^{0}
\end{aligned}
\tag{4.6.9}
$$

where S_{mx}, S_{my}, and S_{myx} can be obtained by Equation (4.6.8).

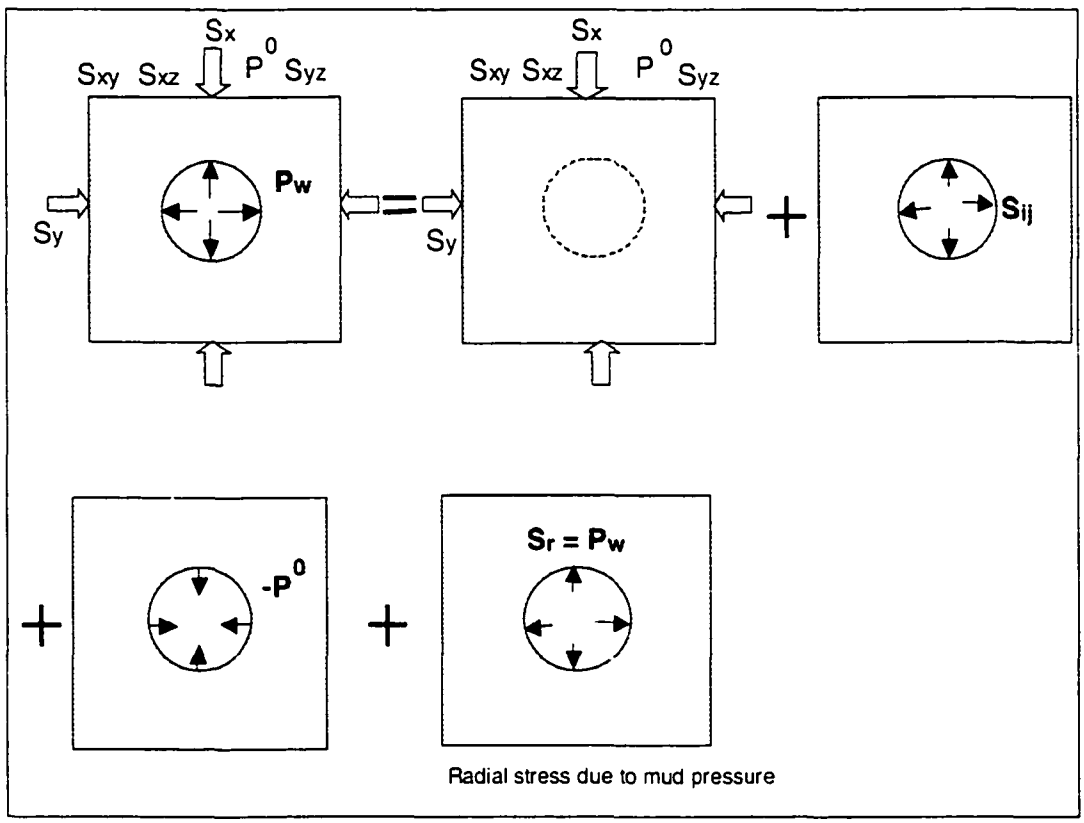


Figure 4.6.6 Superposition of mudweight pressure at the borehole wall for the impermeable case in the FEM model.

Chapter 5

FInIte Element Model Validation

5.1 Introduction

The formulations presented in the foregoing chapters were coded using the Fortran language in pseudo-three-dimensional and time domain, using four-node rectangular elements. Some analytical problems should be examined to validate the computer program. However, there are no suitable dual-porosity analytical problems available in the current literature; only a few simple elastic and poroelastic analytical solutions exist.

Among those validation problems, the poroelastic one-dimensional consolidation problem is a classic example for the coupled fluid-rock system. Elastic and poroelastic analytical solutions for inclined wellbore problems were also validated. In addition, the dual-porosity elastoplastic non-isothermal one-dimensional consolidation solution is given in this section. It can be used for validating the finite element solution.

5.2 One-dimensional Consolidation

One-dimensional consolidation is one of the most well-known examples of poroelasticity, and its analytical solution for single porosity homogeneous medium is available. The solid column displacements and the single-phase fluid flow are fully coupled in this problem.

A porous media column is subjected to a constant load F and confined on the sides and bottom by rigid, frictionless, impermeable walls. The boundary and loading conditions of

the column are depicted in Figure 5.2.1. The analytical solution for the pore pressure in this one-dimensional consolidation problem using Biot's poroelasticity theory (Biot, 1941) is given by Detournay and Cheng (1993) as:

$$p(x,t) = p_u[1 - F(X,T)] \tag{5.2.1}$$

where,

$$F(X,T) = 1 - \sum_{m=1,3,\ldots}^{\infty} \frac{4}{m\pi}\left(\frac{m\pi X}{2}\right)\exp\left(-m^2\pi^2 T\right) \tag{5.2.2}$$

and,

$$p_u = -\frac{B(1+\nu_u)}{3(1-\nu_u)}\sigma_z \tag{5.2.3}$$

$$X = \frac{x}{L}, \quad T = \frac{ct}{4L^2} \tag{5.2.4}$$

in which c is the material compressibility, m is a coefficient and m = 1,3,5 ..., B is Skempton's coefficient (Skempton, 1954), L is the column length, x and t are the coordinate and time, respectively; σ_z is the instantaneously applied stress, and ν_u is the undrained Poisson's ratio.

The related equations for the relationships among poroelastic parameters are listed below:

$$
\begin{cases}
E = 2G(1+\nu) \rightarrow \text{Young's modulus} \\
\alpha = \dfrac{3(\nu_u - \nu)}{B(1-2\nu)(1+\nu_u)} \rightarrow \text{Boit's coefficient} \\
M = \dfrac{2G(\nu_u - \nu)}{\alpha^2(1-2\nu_u)(1-2\nu)} \rightarrow \text{Biot modulus} \\
K = \dfrac{E}{3(1-2\nu)} \rightarrow \text{Bulk modulus of skeleton} \\
K_s = \dfrac{K}{(1-\alpha)} \rightarrow \text{Bulk modulus of solid grain} \\
\dfrac{1}{M} = \dfrac{\alpha-\phi}{K_s} + \dfrac{\phi}{K_f} \rightarrow \text{Storage coefficient} \\
\dfrac{k}{\mu} = c\dfrac{\alpha^2(1-\nu_u)(1-2\nu)^2}{2G(1-\nu)(\nu_u-\nu)} \rightarrow \text{Fluid mobility}
\end{cases}
\tag{5.2.5}
$$

At the top of the layer, the analytically derived settlement is given by:

$$
u = \frac{\sigma_s L(1-2\nu_u)}{2G(1-\nu_u)}\left[1 + \frac{\nu_u - \nu}{(1-\nu_u)(1-2\nu_u)} f(T)\right] \tag{5.2.6}
$$

where,

$$
f(T) = \sum_{m=1,3,\ldots}^{\infty} \frac{8}{m^2\pi^2}\left[1 - \exp\left(-m^2\pi^2 T\right)\right] \tag{5.2.7}
$$

and G is the shear modulus.

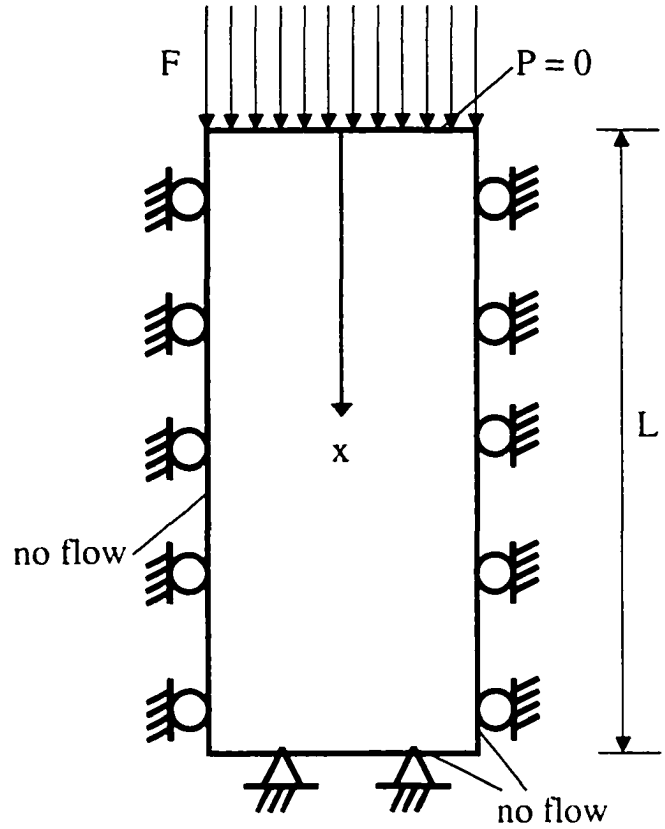


Figure 5.2.1 Consolidation problem and boundary conditions (p is the pressure).

The column, with L = 1 m, is subjected, at $t = 0^+$ sec, to a vertical uniform compressive distribution of σ_v = 1 MPa on the top surface; the surface is otherwise free from stress and exposed to the atmosphere. Twenty elements and forty nodes are used in the finite element calculations. With the input material parameters given in Table 5.2.1, the finite element solution using the developed dual-porosity model are compared with the results from the analytical solution. Applying an exceptionally large fracture stiffness and fracture spacing which approximate an equivalent homogeneous single-porosity medium, the maximum temporal displacements and spatial pore pressure at different times calculated by the analytical and numerical methods are compared in Figures 5.2.2 and 5.2.3. Excellent agreement is achieved for the displacements. As far as the pore pressures are concerned, only small discrepancies can be observed for the early-time (t = 0.005) scenario, this is caused by the effect of initial conditions in the finite element method.

Table 5.2.1 Parameters for comparative analysis in 1-D consolidation

Parameter	Definition	Magnitude	Unit
E	Modulus of elasticity	2.4	MN/m^2
G	Shear modulus	1.0	MN/m^2
α	Biot coefficient	1.0	-
ν	Poisson's ratio	0.2	-
K_f	Fluid bulk modulus	419.7	MN/m^2
n_{ma}	Matrix porosity	0.02	-
n_{fr}	Fracture porosity	0.002	-
K_s	Grain bulk modulus	10^{10}	MN/m^2
B	Skempton coefficient	1.0	-
ν_u	Undrained Poisson's ratio	0.5	-
K_{ma}/μ	Matrix mobility	0.375	$M^4/(MN\ s)$
K_{fr}/μ	Fracture mobility	3.75	$M^4/(MN\ s)$
K_n	Fracture normal stiffness	10^7	MN/m^2
K_{sh}	Fracture shear stiffness	10^7	MN/m^2
s	Fracture spacing	10^7	M

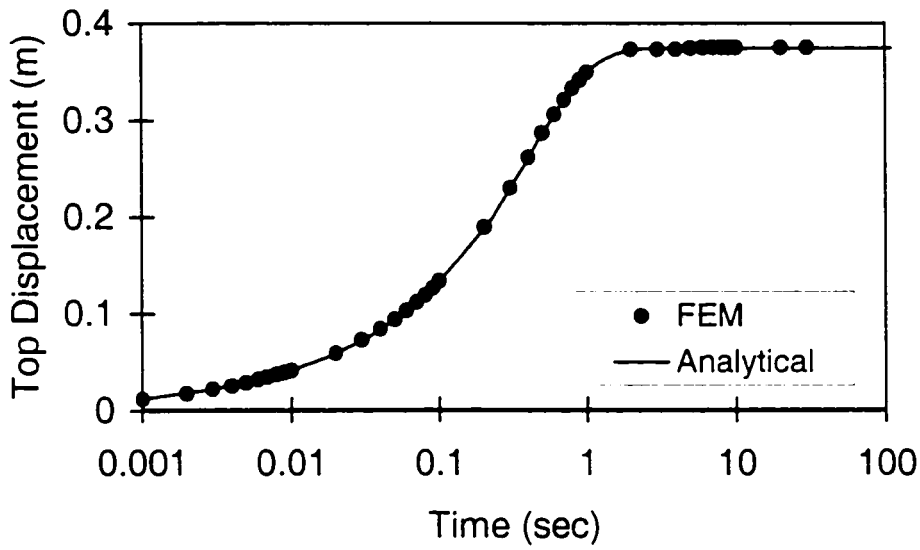


Figure 5.2.2 Comparison of temporal displacement at top column.

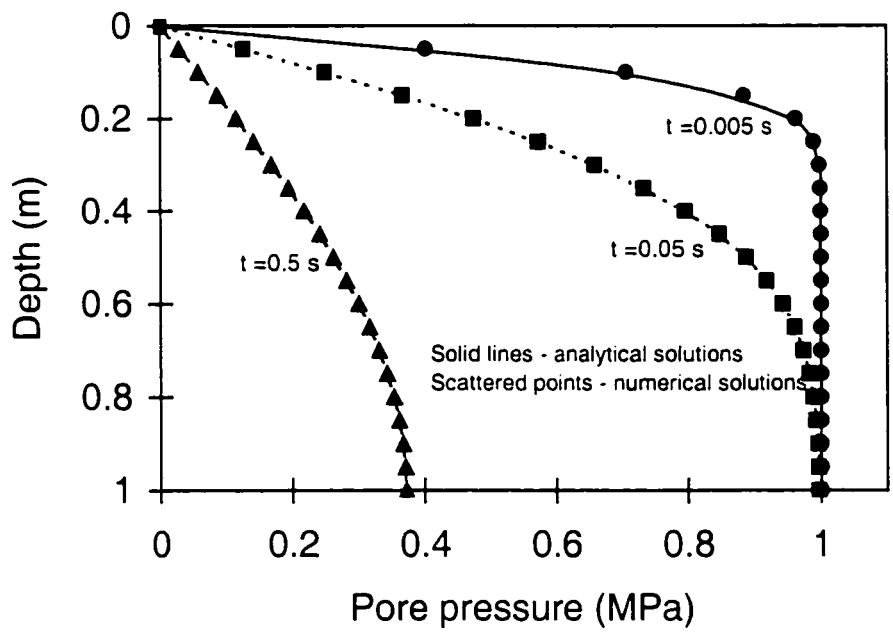


Figure 5.2.3 Comparison of spatial pore pressure along the column.

5.3 Dual-porosity Elastoplastic One-dimensional Consolidation

In this section, one-dimensional dual-porosity elastoplastic anisothermal consolidation is presented which can be used for future validations of the elastoplastic non-isothermal finite element solution.

5.3.1 Mathematical Formulation for One-dimensional Consolidation

5.3.1.1 Elastoplastic stress-strain relationships for dual-porosity media

Consider a fractured porous rock column of height h (Figure 5.3.1), which is laterally confined and positioned over a rigid, impermeable, and adiabatic base. The x-axis pointing downwards is the axis of symmetry of the column, the top surface ($x = 0$) is assumed to be a free drainage surface. A uniformly distributed load of intensity F_0 per unit cross-sectional area is applied instantaneously at the top of the column, and results in the consolidation of the column, along with the dissipation of pore and fracture pressures and temperatures from the top as shown in Figure 5.3.1. As time elapses, the induced stress becomes progressively larger until it exceeds the material yield strength and part of the column, x_p, develops plastic deformations.

For such a problem, the compressive column is in a three-dimensional state of stress, but can be simplified geometrically as a one-dimensional case. For the dual-porosity porous media, the effective stress in the column, considering the stress coupling due to the compression of solid grains and fractures, interstitial pore and fracture pressures, and the variations of fluid as well as solid temperatures, may be written as:

$$\sigma' = \sigma_t + D_{12}(C_1\alpha_1 p_1 + C_2\alpha_2 p_2 + C_1\beta_1 T_1 + C_2\beta_2 T_2) \tag{5.3.1}$$

where σ' is the effective stress in the material; σ_t is the total stress (the tensile stress is positive); p_1, p_2 are the matrix and fracture pressures; T_1, T_2 are the matrix and fracture temperatures; C_1, C_2 are the matrix and fracture compliance matrices defined in this one-dimensional case as:

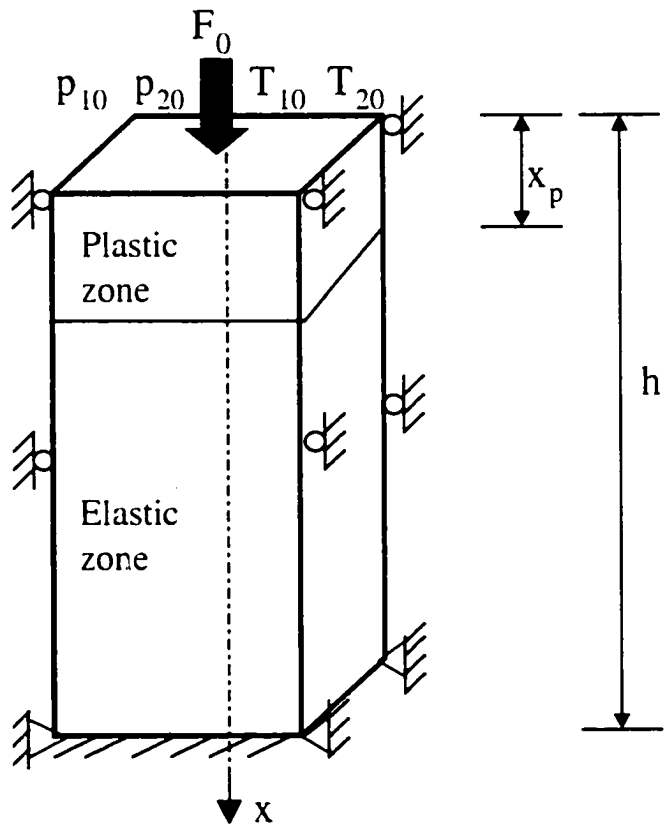


Figure 5.3.1 Schematic one-dimensional column.

$$C_1 = \frac{1}{E} \tag{5.3.2}$$

$$C_2 = \frac{1}{K_n s} \tag{5.3.3}$$

where E, ν are Young's modulus and Poisson ratio, respectively; K_n is the fracture normal stiffness; s is the fracture spacing,

$$D_{12} = \frac{1}{C_1 + C_2} \; ; \tag{5.3.4}$$

α_1, α_2 are Biot's coefficient for matrix and fractures, respectively, $\alpha_1 = 1 - K/K_s$ and $\alpha_2 = 1 - K/(K_n s)$; K is the bulk modulus of the skeleton for the matrix blocks; K_s is the bulk modulus of the solid grains; β_1, β_2 are the thermal expansion factors for the matrix and fracture, respectively defined as:

$$\begin{cases} \beta_1 = \alpha_{h1}(3\lambda_{12} + 2G_{12}) \\ \beta_2 = \alpha_{h2}(3\lambda_{12} + 2G_{12}) \end{cases} \tag{5.3.5}$$

where, α_{h1}, α_{h2} are the expansion coefficients for the matrix and fracture, respectively; and,

$$G_{12} = \frac{D_{12}}{2(1+\nu)} \tag{5.3.6}$$

$$\lambda_{12} = \frac{D_{12}\nu}{(1+\nu)(1-2\nu)} \tag{5.3.7}$$

In general, the stress-strain behavior of rock is non-linear, especially in the case where external loads exceed the elastic strength of material and the material becomes plastic. In this study, a strain-hardening bi-linear stress-strain relationship is assumed. The Tresca yield criterion is used to determine the elastic/plastic transition of the column. Thus, the plastic yield condition can be expressed as:

$$\sigma' + \sigma_0 = 0 \tag{5.3.8}$$

where, σ_0 is the yield stress of the material.

Since the maximum load is imposed at the top of the column, accompanied by fluid drainage, yielding will be initiated at that location. As time elapses, the induced plastic zone propagates downward. The strains in the elastic and plastic zones (with superscript p) for the dual-porosity medium can be defined as:

$$\varepsilon = \frac{\sigma'}{D_{12}} \tag{5.3.9}$$

$$\varepsilon^p = \frac{\sigma' + \sigma_0}{D_{12}^p} - \frac{\sigma_0}{D_{12}} \tag{5.3.10}$$

where, ε and ε^p are the elastic and plastic strains, respectively.

5.3.1.2 *Fully coupled thermal elastoplastic formulation for a dual-porosity medium*

In the solid phase, temporal and spatial changes are averaged over the matrix and the fractures. In the fluid and temperature phases, temporal and spatial changes in fractures and matrix blocks are incorporated individually. For the dual-porosity media, the fully coupled governing equations of a porous thermal and mechanical model for solid, fluid, and temperature fields may be modified according to Bai and Roegiers (1994); i.e.,

$$G_{12}u_{i,jj} + (\lambda_{12} + G_{12})u_{k,ki} + \sum_{m=1}^{2} D_{12}C_m(\alpha_m p_{m,i} + \beta_m T_{m,i}) = 0 \tag{5.3.11}$$

$$\frac{k_m}{\mu} p_{m,kk} - \alpha_m D_m C_m \frac{\partial \varepsilon_{kk}}{\partial t} - \phi_m^{\bullet} \frac{\partial p_m}{\partial t} + \alpha_{hm}^{\bullet} \frac{\partial T_m}{\partial t} \pm \omega(\Delta p) = 0 \tag{5.3.12}$$

$$k_m^{\bullet} T_{m,kk} - T_m^0 \beta_m \frac{\partial \varepsilon_{kk}}{\partial t} - S_m^{\bullet} \frac{\partial T_m}{\partial t} \pm \Gamma^{\bullet}(\Delta T) = 0 \tag{5.3.13}$$

where, m = 1, and 2 represent the matrix and fractures, respectively; α and β are the fluid pressure and thermal ratio factors; k is the permeability; $\phi^{\bullet}$ is the lumped compressibility;

k^* is the thermal conductivity; μ is the fluid dynamic viscosity; ω and Γ^* are the fluid and thermal transfer coefficients, respectively; $\omega = 60k_f/(\mu s^2)$; $\Gamma^* = 60k_1^*/s^2$; u is the solid displacement; p is the fluid pressure; T is the temperature; ε_{kk} is the total body strain; Δp and ΔT are the pressure and temperature differences between the matrix blocks and fractures, respectively; S^* is the lumped intrinsic heat capacity; and, T^0 is the reference temperature.

With reference to the governing equations, a fully coupled one-dimensional dual-porosity thermoporoelastic formulation may be described as:

$$\eta_{12}\frac{\partial^2 u}{\partial x^2} = D_{12}\left(C_1\alpha_1\frac{\partial p_1}{\partial x} + C_2\alpha_2\frac{\partial p_2}{\partial x} + C_1\beta_1\frac{\partial T_1}{\partial x} + C_2\beta_2\frac{\partial T_2}{\partial x}\right) \tag{5.3.14}$$

$$\frac{k_1}{\mu}\frac{\partial^2 p_1}{\partial x^2} = D_{12}C_1\alpha_1\frac{\partial^2 u}{\partial x\partial t} + \phi_1^*\frac{\partial p_1}{\partial t} + \alpha_{h1}\frac{\partial T_1}{\partial t} + \Gamma(p_1 - p_2) \tag{5.3.15}$$

$$\frac{k_2}{\mu}\frac{\partial^2 p_2}{\partial x^2} = D_{12}C_2\alpha_2\frac{\partial^2 u}{\partial x\partial t} + \phi_2^*\frac{\partial p_2}{\partial t} + \alpha_{h2}\frac{\partial T_2}{\partial t} + \Gamma(p_2 - p_1) \tag{5.3.16}$$

$$k_1^*\frac{\partial^2 T_1}{\partial x^2} = \beta_1 T_{10}\frac{\partial^2 u}{\partial x\partial t} + S_1^*\frac{\partial T_1}{\partial t} + \Gamma^*(T_1 - T_2) \tag{5.3.17}$$

$$k_2^*\frac{\partial^2 T_2}{\partial x^2} = \beta_2 T_{20}\frac{\partial^2 u}{\partial x\partial t} + S_2^*\frac{\partial T_1}{\partial t} + \Gamma^*(T_2 - T_1) \tag{5.3.18}$$

where,

$$\phi_1^* = \frac{n_1}{K_f} + \frac{1-n_1}{K_s} \tag{5.3.19}$$

$$\phi_2^* = \frac{n_2}{K_f} + \frac{1-n_2}{K_n s} \tag{5.3.20}$$

$$\alpha_m = n_m\alpha_f + (1-n_m)\alpha_s \tag{5.3.21}$$

$$k_m^* = n_m k_{sf} + (1-n_m)k_{ss} \tag{5.3.22}$$

$$S_m^* = \rho_f c_f n_m + (1-n_m)\rho_s c_s \tag{5.3.23}$$

m = 1,2, represent the matrix and fractures; α_f, α_s are the coefficients of thermal expansion for the fluid and solid, respectively; k_{sf}, k_{ss} are the thermal conductivities for

the fluid and solid, respectively; ρ_f , ρ_s are the densities for the fluid and solid, respectively; c_f , c_s are the heat capacities for the fluid and solid, respectively; $\eta_{12} = \lambda_{12} + 2G_{12}$.

The boundary and initial conditions are:

$$\frac{\partial u(0,t)}{\partial x} = \frac{-F_0}{\eta_{12}} \text{ (constant strain at the top)}$$

$$p_1(0,t) = p_2(0,t) = 0$$

$$T_1(0,t) = T_2(0,t) = 0$$

$$\frac{\partial p_1(h,t)}{\partial x} = \frac{\partial p_2(h,t)}{\partial x} = 0 \text{ (no hydraulic gradient at the bottom)}$$

$$u(h,t) = 0$$

$$p_1(x,0) = p_{10}$$

$$p_2(x,0) = p_{20}$$

$$T_1(x,0) = T_{10}$$

$$T_2(x,0) = T_{20}$$

Integrating Equation (5.3.15) with respect to x, and then substituting the result into Equations (5.3.16), (5.3.17), (5.3.18) and (5.3.19), the following equations can be obtained for the elastic zone:

$$\frac{\partial u}{\partial x} = \frac{-F_0 + D_{12}(C_1\alpha_1 p_1 + C_2\alpha_2 p_2 + C_1\beta_1 T_1 + C_2\beta_2 T_2)}{\eta_{12}} \tag{5.3.24}$$

$$\frac{\partial^2 p_1}{\partial x^2} = g_{11}\frac{\partial p_1}{\partial t} + g_{12}\frac{\partial p_2}{\partial t} + g_{13}(p_1 - p_2) + g_{14}\frac{\partial T_1}{\partial t} + g_{15}\frac{\partial T_2}{\partial t} \tag{5.3.25}$$

$$\frac{\partial^2 p_2}{\partial x^2} = g_{21}\frac{\partial p_1}{\partial t} + g_{22}\frac{\partial p_2}{\partial t} + g_{23}(p_2 - p_1) + g_{24}\frac{\partial T_1}{\partial t} + g_{25}\frac{\partial T_2}{\partial t} \tag{5.3.26}$$

$$\frac{\partial^2 T_1}{\partial x^2} = g_{31}\frac{\partial p_1}{\partial t} + g_{32}\frac{\partial p_2}{\partial t} + g_{34}\frac{\partial T_1}{\partial t} + g_{35}\frac{\partial T_2}{\partial t} + g_{36}(T_1 - T_2) \tag{5.3.27}$$

$$\frac{\partial^2 T_2}{\partial x^2} = g_{41}\frac{\partial p_1}{\partial t} + g_{42}\frac{\partial p_2}{\partial t} + g_{44}\frac{\partial T_1}{\partial t} + g_{45}\frac{\partial T_2}{\partial t} + g_{46}(T_2 - T_1) \tag{5.3.28}$$

where detailed explanations of the coefficients are given in Appendix C.

Similarly, the modified governing equation for the plastic zone can be expressed as:

$$\frac{\partial u^p}{\partial x} = \frac{-F_0 + D_{12}^p(C_1^p\alpha_1 p_1^p + C_2\alpha_2 p_2^p + C_1^p\beta_1^p T_1^p + C_2\beta_2^p T_2^p) + \sigma_0}{\eta_{12}^p} - \frac{\sigma_0}{\eta_{12}} \tag{5.3.29}$$

$$\frac{\partial^2 p_1^p}{\partial x^2} = g_{11}^p\frac{\partial p_1^p}{\partial t} + g_{12}^p\frac{\partial p_2^p}{\partial t} + g_{13}^p(p_1^p - p_2^p) + g_{14}^p\frac{\partial T_1^p}{\partial t} + g_{15}^p\frac{\partial T_2^p}{\partial t} \tag{5.3.30}$$

$$\frac{\partial^2 p_2^p}{\partial x^2} = g_{21}^p\frac{\partial p_1^p}{\partial t} + g_{22}^p\frac{\partial p_2^p}{\partial t} + g_{23}^p(p_2^p - p_1^p) + g_{24}^p\frac{\partial T_1^p}{\partial t} + g_{25}^p\frac{\partial T_2^p}{\partial t} \tag{5.3.31}$$

$$\frac{\partial^2 T_1^p}{\partial x^2} = g_{31}^p\frac{\partial p_1^p}{\partial t} + g_{32}^p\frac{\partial p_2^p}{\partial t} + g_{34}^p\frac{\partial T_1^p}{\partial t} + g_{35}^p\frac{\partial T_2^p}{\partial t} + g_{36}^p(T_1^p - T_2^p) \tag{5.3.32}$$

$$\frac{\partial^2 T_2^p}{\partial x^2} = g_{41}^p\frac{\partial p_1^p}{\partial t} + g_{42}^p\frac{\partial p_2^p}{\partial t} + g_{44}^p\frac{\partial T_1^p}{\partial t} + g_{45}^p\frac{\partial T_2^p}{\partial t} + g_{46}^p(T_2^p - T_1^p) \tag{5.3.33}$$

where the superscript 'p' represents the plastic zone, and detailed expressions of the coefficients are given in Appendix C.

The continuity conditions must be satisfied at the interface between the elastic and the plastic zones, i.e.

$$u\Big|_{x=x_p} = u^p\Big|_{x=x_p}$$

$$p_1\Big|_{x=x_p} = p_1^p\Big|_{x=x_p}$$

$$p_2\Big|_{x=x_p} = p_2^p\Big|_{x=x_p}$$

$$T_1\Big|_{x=x_p} = T_1^p\Big|_{x=x_p}$$

$$T_2\Big|_{x=x_p} = T_2^p\Big|_{x=x_p}$$

The explicit finite difference method is employed. The governing Equations (5.3.24) through (5.3.28) for the elastic zone can be discretized as:

$$\frac{u_{i,j+1}-u_{i,j}}{\Delta x}=\frac{-F_0+D_{12}(C_1\alpha_1 p_{1i,j}+C_2\alpha_2 p_{2i,j}+C_1\beta_1 T_{1i,j}+C_2\beta_2 T_{2i,j})}{\eta_{12}} \tag{5.3.34}$$

$$\begin{aligned}\frac{p_{1i,j+1}-2p_{1i,j}+p_{1i,j-1}}{\Delta x^2}&=g_{11}\frac{p_{1i+1,j}-p_{1i,j}}{\Delta t}+g_{12}\frac{p_{2i+1,j}-p_{2i,j}}{\Delta t}\\&+g_{13}(p_{1i,j}-p_{2i,j})+g_{14}\frac{T_{1i+1,j}-T_{1i,j}}{\Delta t}+g_{15}\frac{T_{2i+1,j}-T_{2i,j}}{\Delta t}\end{aligned} \tag{5.3.35}$$

$$\begin{aligned}\frac{p_{2i,j+1}-2p_{2i,j}+p_{2i,j-1}}{\Delta x^2}&=g_{21}\frac{p_{1i+1,j}-p_{1i,j}}{\Delta t}+g_{22}\frac{p_{2i+1,j}-p_{2i,j}}{\Delta t}\\&+g_{23}(p_{2i,j}-p_{1i,j})+g_{24}\frac{T_{1i+1,j}-T_{1i,j}}{\Delta t}+g_{25}\frac{T_{2i+1,j}-T_{2i,j}}{\Delta t}\end{aligned} \tag{5.3.36}$$

$$\begin{aligned}\frac{T_{1i,j+1}-2T_{1i,j}+T_{1i,j-1}}{\Delta x^2}&=g_{31}\frac{p_{1i+1,j}-p_{1i,j}}{\Delta t}+g_{32}\frac{p_{2i+1,j}-p_{2i,j}}{\Delta t}\\&+g_{34}\frac{T_{1i+1,j}-T_{1i,j}}{\Delta t}+g_{35}\frac{T_{2i+1,j}-T_{2i,j}}{\Delta t}+g_{36}(T_{1i,j}-T_{2i,j})\end{aligned} \tag{5.3.37}$$

$$\begin{aligned}\frac{T_{2i,j+1}-2T_{2i,j}+T_{2i,j-1}}{\Delta x^2}&=g_{41}\frac{p_{1i+1,j}-p_{1i,j}}{\Delta t}+g_{42}\frac{p_{2i+1,j}-p_{2i,j}}{\Delta t}\\&+g_{44}\frac{T_{1i+1,j}-T_{1i,j}}{\Delta t}+g_{45}\frac{T_{2i+1,j}-T_{2i,j}}{\Delta t}+g_{46}(T_{2i,j}-T_{1i,j})\end{aligned} \tag{5.3.38}$$

where subscripts 1 and 2 represent the matrix and fractures, respectively; i, j are increment numbers of differential mesh for time and depth, respectively.

The governing equations (5.3.29) through (5.3.33) for the plastic zone can be discretized as:

$$\frac{u^p_{i,j+1}-u^p_{i,j}}{\Delta x}=\frac{-F_0+D_{12}(C_1\alpha_1 p^p_{1i,j}+C_2\alpha_2 p^p_{2i,j}+C_1\beta_1 T^p_{1i,j}+C_2\beta_2 T^p_{2i,j})+\sigma_0}{\eta^p_{12}}-\frac{\sigma_0}{\eta_{12}} \tag{5.3.39}$$

$$\begin{aligned}\frac{p^p_{1i,j+1}-2p^p_{1i,j}+p^p_{1i,j-1}}{\Delta x^2}&=g^p_{11}\frac{p^p_{1i+1,j}-p^p_{1i,j}}{\Delta t}+g^p_{12}\frac{p^p_{2i+1,j}-p^p_{2i,j}}{\Delta t}\\&+g^p_{13}(p^p_{1i,j}-p^p_{2i,j})+g^p_{14}\frac{T^p_{1i+1,j}-T^p_{1i,j}}{\Delta t}+g^p_{15}\frac{T^p_{2i+1,j}-T^p_{2i,j}}{\Delta t}\end{aligned} \tag{5.3.40}$$

$$\frac{p^p_{2i,j+1} - 2p^p_{2i,j} + p^p_{2i,j-1}}{\Delta x^2} = g^p_{21}\frac{p^p_{1i+1,j} - p^p_{1i,j}}{\Delta t} + g^p_{22}\frac{p^p_{2i+1,j} - p^p_{2i,j}}{\Delta t}$$
$$+ g^p_{23}(p^p_{2i,j} - p^p_{1i,j}) + g^p_{24}\frac{T^p_{1i+1,j} - T^p_{1i,j}}{\Delta t} + g^p_{25}\frac{T^p_{2i+1,j} - T^p_{2i,j}}{\Delta t} \quad (5.3.41)$$

$$\frac{T^p_{1i,j+1} - 2T^p_{1i,j} + T^p_{1i,j-1}}{\Delta x^2} = g^p_{31}\frac{p^p_{1i+1,j} - p^p_{1i,j}}{\Delta t} + g^p_{32}\frac{p^p_{2i+1,j} - p^p_{2i,j}}{\Delta t}$$
$$+ g^p_{34}\frac{T^p_{1i+1,j} - T^p_{1i,j}}{\Delta t} + g^p_{35}\frac{T^p_{2i+1,j} - T^p_{2i,j}}{\Delta t} + g^p_{36}(T^p_{1i,j} - T^p_{2i,j}) \quad (5.3.42)$$

$$\frac{T^p_{2i,j+1} - 2T^p_{2i,j} + T^p_{2i,j-1}}{\Delta x^2} = g^p_{41}\frac{p^p_{1i+1,j} - p^p_{1i,j}}{\Delta t} + g^p_{42}\frac{p^p_{2i+1,j} - p^p_{2i,j}}{\Delta t}$$
$$+ g^p_{44}\frac{T^p_{1i+1,j} - T^p_{1i,j}}{\Delta t} + g^p_{45}\frac{T^p_{2i+1,j} - T^p_{2i,j}}{\Delta t} + g^p_{46}(T^p_{2i,j} - T^p_{1i,j}) \quad (5.3.43)$$

The boundary and initial conditions can be discretized as:

$$p_{1i,j} = p_{2i,j} = 0, \quad T_{1i,j} = T_{2i,j} = 0, \text{ at } x = 0$$
$$p_{1i,j+1} = p_{1i,j}, \quad p_{2i,j+1} = p_{2i,j}, \quad T_{1i,j+1} = T_{1i,j}, \quad T_{2i,j+1} = T_{2i,j}, \quad u_{i,j} = 0, \text{ at } x = h$$
$$p_{1i,j} = p_{10}, \quad p_{2i,j} = p_{20}, \quad T_{1i,j} = T_{10}, \quad T_{2i,j} = T_{20}, \text{ at } t = 0$$

5.3.2 Analyses of Dual-porosity Isothermal Consolidation

In order to examine the elastoplastic solution, a dual-porosity elastoplastic isothermal consolidation model is studied first. The calculated results are compared with the single porosity elastoplastic solution (Zhang et al., 1999). The particular objective is to identify the differences between double and single porosity elastoplastic consolidation. The selected parameter ranges, with respect to the hydraulic, mechanical and geometrical categories, are listed in Table 5.3.1. The pore and fracture pressures, p_1, p_2, displacement, u, and plastic zone depth, x_p, are normalized with respect to their initial values. The dimensionless time is defined in following form:

Table 5.3.1 Selected poroelastoplastic parametric ranges

Category	Symbol	Value or range	Unit
Hydraulic	k_1	1×10^{-13}	m^2
	b	1.062	mm
	k_2	1×10^{-9} - 1×10^{-12}	m^2
	μ	20	kg/(m,h)
	n_1	0.5	-
	n_2	0.05	-
	p_{10}	8×10^{6}	Pa
	p_{12}	8×10^{6}	Pa
Mechanical	ν^e	0.25	-
	ν^p	0.45	-
	E^e	5×10^{9}	Pa
	E^p	5×10^{8}	Pa
	K	7.5×10^{9}	Pa
	K_f	5×10^{9}	Pa
	K_s	2×10^{10}	Pa
	k_n	1.5×10^{9}	Pa
	F_0	3×10^{7}	Pa
	σ_0	2.5×10^{7}	Pa
	s	20	m
Geometric	h	100	m
	x	6	m

$$\tau = \frac{c_v t}{h^2} \tag{5.3.44}$$

where h is the height of the consolidating column; c_v is the coefficient of the consolidation; and,

$$c_v = \frac{k_1 \eta_{12}}{\mu} \tag{5.3.45}$$

The point of interest is selected at 6 m from the top of the column. The material at this location is expected to change from the initial elastic state to the plastic state as time increases. The following equation is used for evaluating the fracture permeability, k_2, (Bai et al., 1993):

$$k_2 = \frac{b^3}{12s} \tag{5.3.46}$$

where, b is the fracture aperture.

A comparison of temporal pressure dissipation between the single- and dual-porosity models with various fracture spacings is given in Figure 5.3.2. It is apparent that the pressure dissipates faster as the medium is more fractured. When the fracture spacing is large enough (such as s = 1000 m representing the intact porous rock), the pore pressure matches the single porosity solution (Zhang et al., 1999). The one-dimensional Mandel's effect (Mandel, 1953) is induced by the pressure transfer between the matrix and fractures in the dual-porosity medium. It is obvious that Mandel's effect is greater for more fractured medium (Figure 5.3.2), because this medium has a larger deformation. A corresponding behavior for the temporal solid normalized displacements is shown in Figure 5.3.3. More highly fractured media represent greater initial displacements and more gradual changes in displacements. In view of temporal evolution of the normalized depth of the plastic zone defined as the plastic depth over the column height, Figure 5.3.4 gives different normalized plastic zones (plastic zone length/column length) for single- and dual-porosity media. It indicates that media changes to plasticity faster for more intense fractured media. The temporal evolution of fracture pressure appears to be less uniform, especially at later stages of pressure dissipation, as shown in Figure 5.3.5. It can

be seen that as fracture spacing increases, fracture pressure dissipation reduces in an earlier time; however, the pressure dissipation increases at larger times. For dimensionless time $\tau = 10^{-4}$ to 10^{-3}, the pressure appears to be the non-monotonic, especially for small fracture spacing; this may be associated with the Mandel's effect in pore pressure shown in Figure 5.3.2. The variable fracture pressure changes can be attributed to the fluid exchanges between the fractures and the porous matrix.

For different elastic and elastoplastic moduli, the temporal matrix pressure is depicted in Figure 5.3.6. It is obvious that the pressure dissipates faster with stiffer material moduli. Slight pressure buildup at early stages of pressure evolution, known as Mandel's effect (Mandel, 1953) can be observed. The temporal displacements are shown in Figure 5.3.7, where less stiff material moduli lead to a more dramatic displacement magnification. The temporal fracture pressure for various elastic and elastoplastic moduli is shown in Figure 5.3.8. Between dimensionless time $\tau = 10^{-4}$ to 10^{-3}, the pressure appears the non-monotonic behavior, especially for small elastoplastic modulus; this may be associated with the Mandel's effect in pore pressure shown in Figure 5.3.6. Again, non-uniform pressure profiles (indicated as the dramatic pressure slope changes in Figure 5.3.8) are evidence of fluid exchange between the fractures and the matrix.

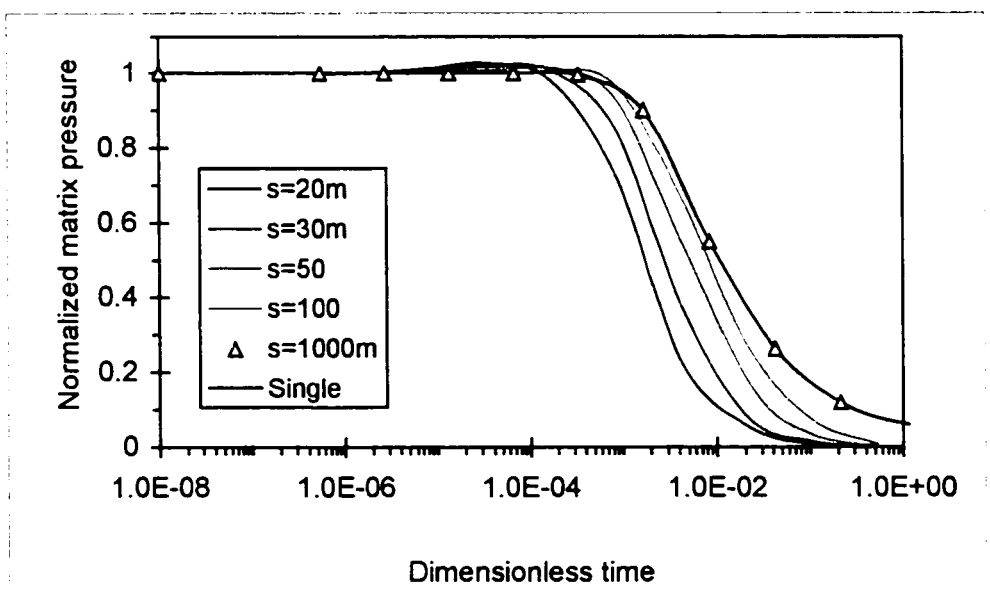


Figure 5.3.2 Temporal pressure comparison between single- and dual-porosity models.

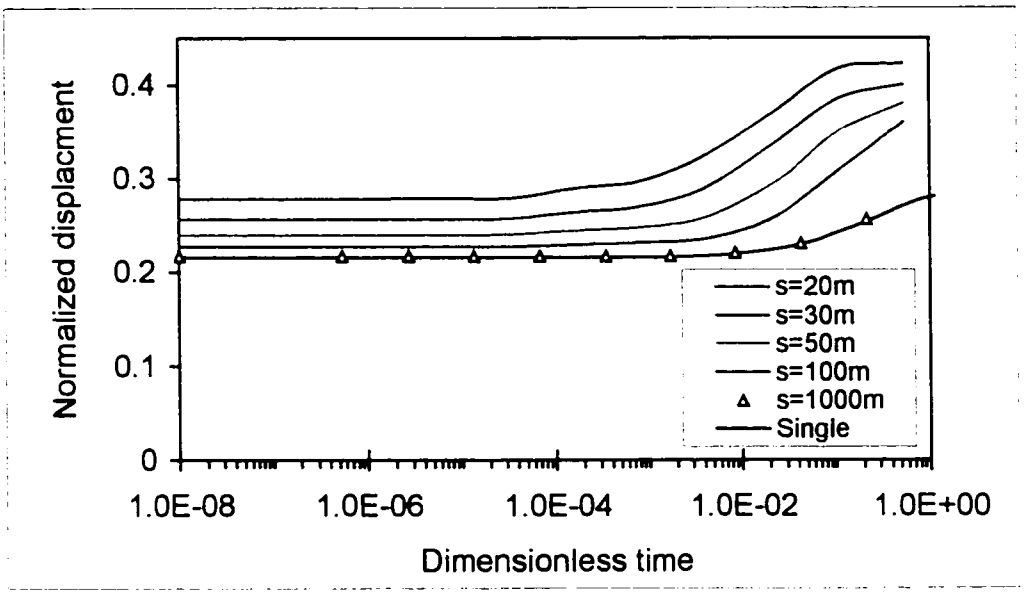


Figure 5.3.3 Temporal displacement comparison between single- and dual-porosity models.

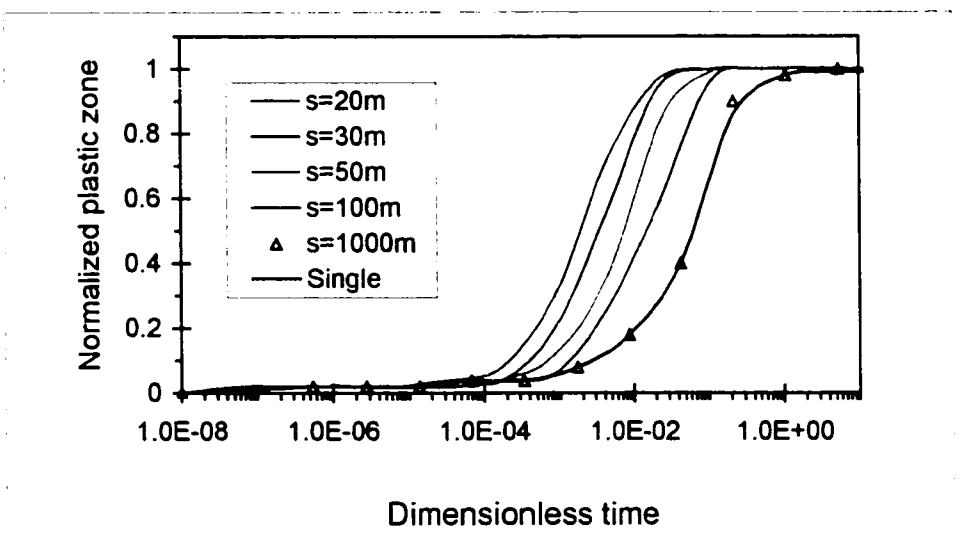


Figure 5.3.4 Temporal plastic zone comparison between single- and dual-porosity models.

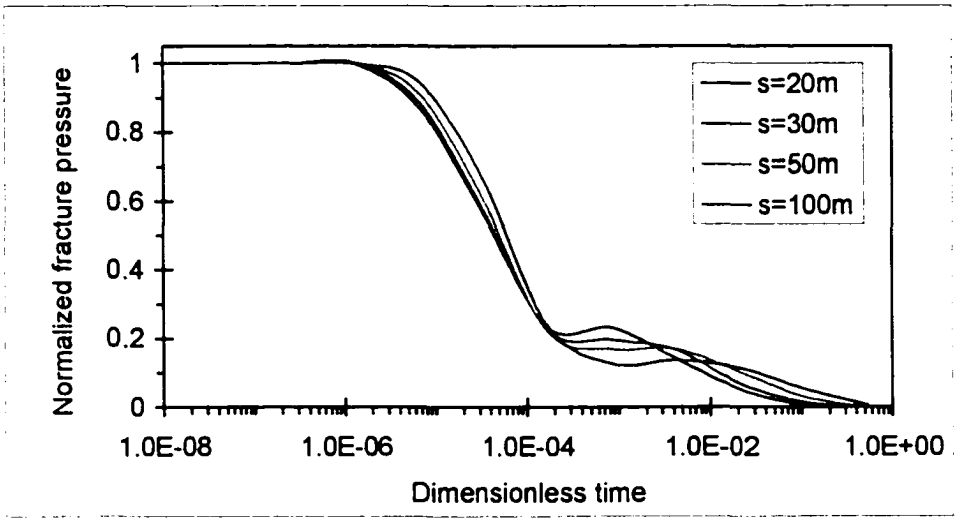


Figure 5.3.5 Temporal fracture pressures for different fracture spacings.

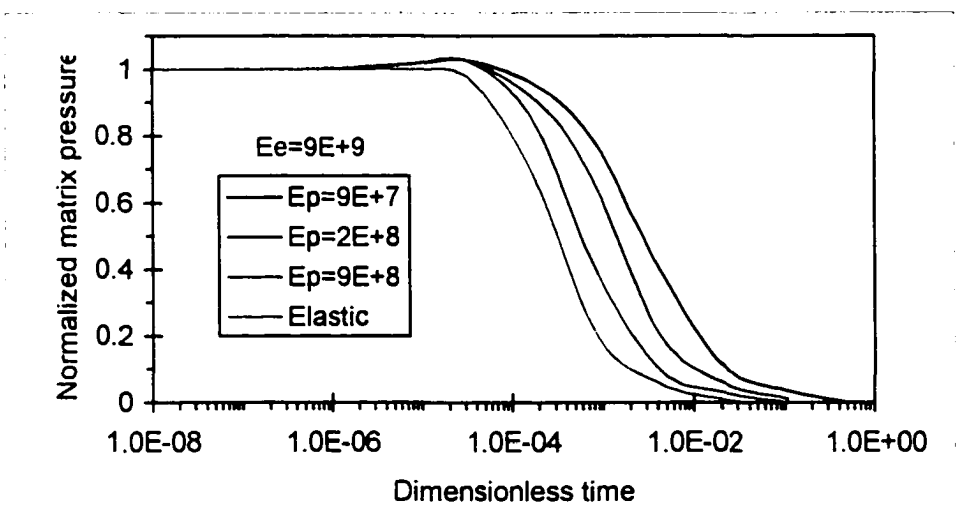


Figure 5.3.6 Temporal matrix pressures for different elastoplastic moduli.

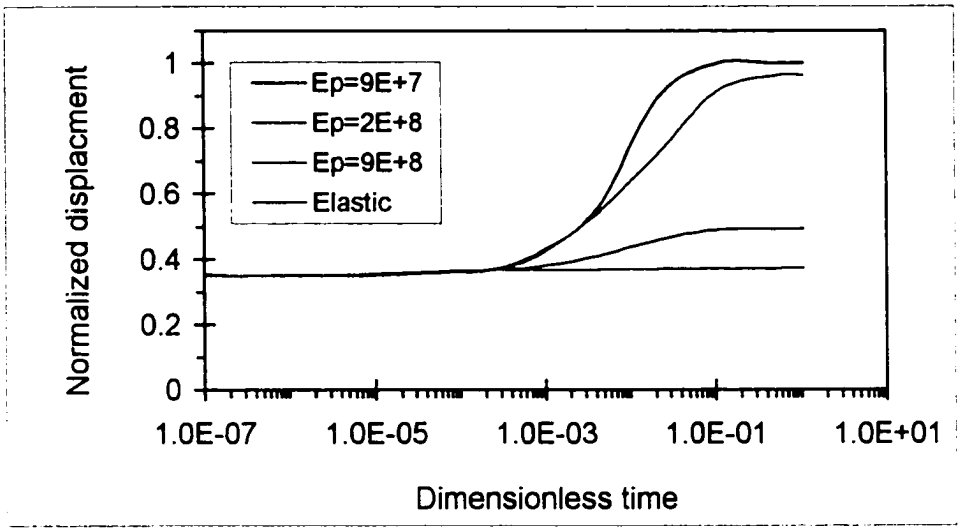


Figure 5.3.7 Temporal matrix pressures for different elastoplastic moduli.

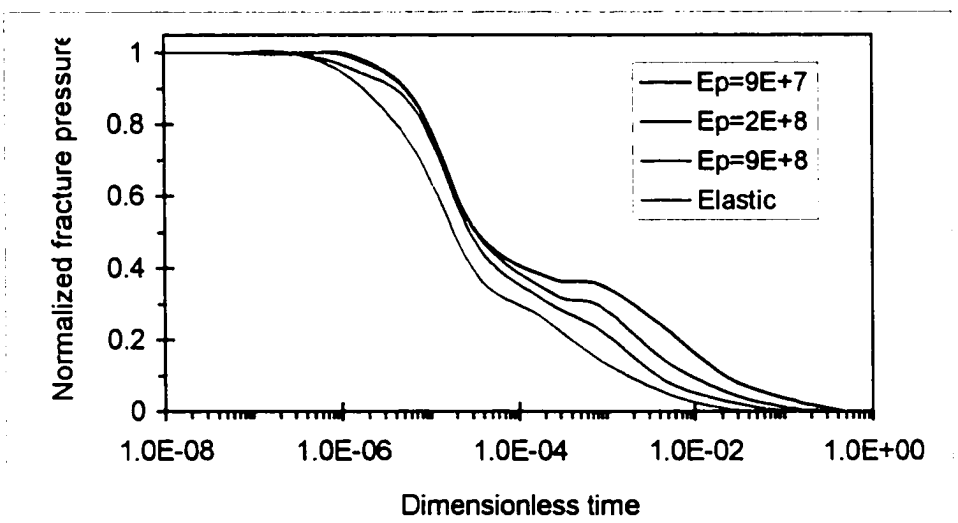


Figure 5.3.8 Temporal fracture pressures for different elastoplastic moduli.

5.3.3 Analyses of Dual-porosity Non-isothermal Consolidation

The input poromechanical parameters were listed previously in Table 5.3.1, while the thermal parameters are given in Table 5.3.2.

Table 5.3.2 Selected thermal parameters

Thermal	Symbol	Value	Unit
	α_f	1×10^{-5}	1/°C
	α_s	1×10^{-6}	1/°C
	k_{sf}	1000	J/(m.h.°C)
	k_{ss}	100	J/(m.h.°C)
	ρ_f	1000	kg/m^3
	ρ_s	500	kg/m^3
	c_f	200	J/(kg.°C)
	c_s	500	J/(kg.°C)
	T_{10}	100	°C
	T_{20}	100	°C

A comparison of matrix pressure for three different scenarios, i.e., single-porosity, isothermal dual-porosity, and non-isothermal dual-porosity, is shown in Figure 5.3.9. It is interesting to note that the Mandel's effect is most pronounced for the non-isothermal case, which also has the fastest pressure decline; this is due to the fact that the non-isothermal case has a larger total stress (refer to Equation 5.3.1), which induces a larger deformation. For the temporal fracture pressure, a comparison between isothermal and non-isothermal dual-porosity cases is given in Figure 5.3.10. It is seen that fluid exchange observed as the pressure slope change is apparent only for the isothermal case.

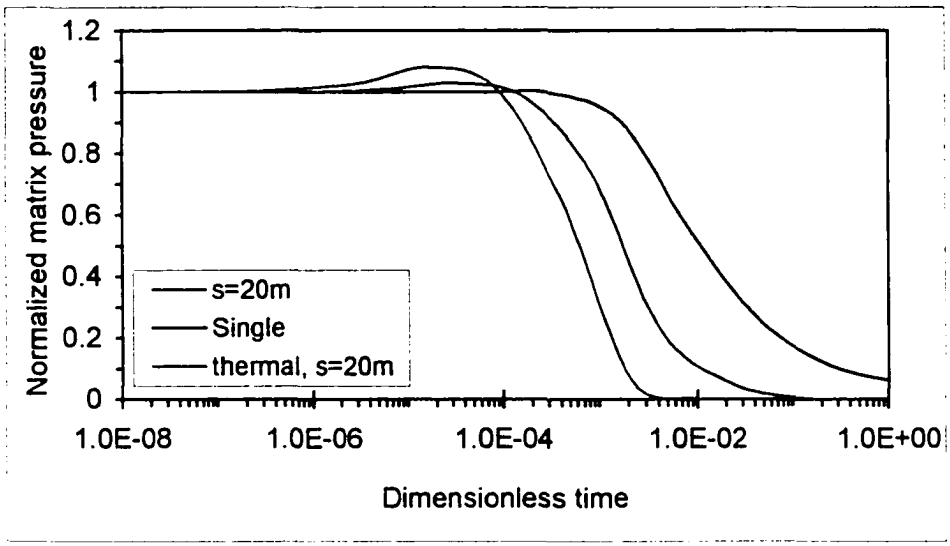


Figure 5.3.9 Matrix pressure comparison for single-, dual- and thermal dual-porosity consolidations.

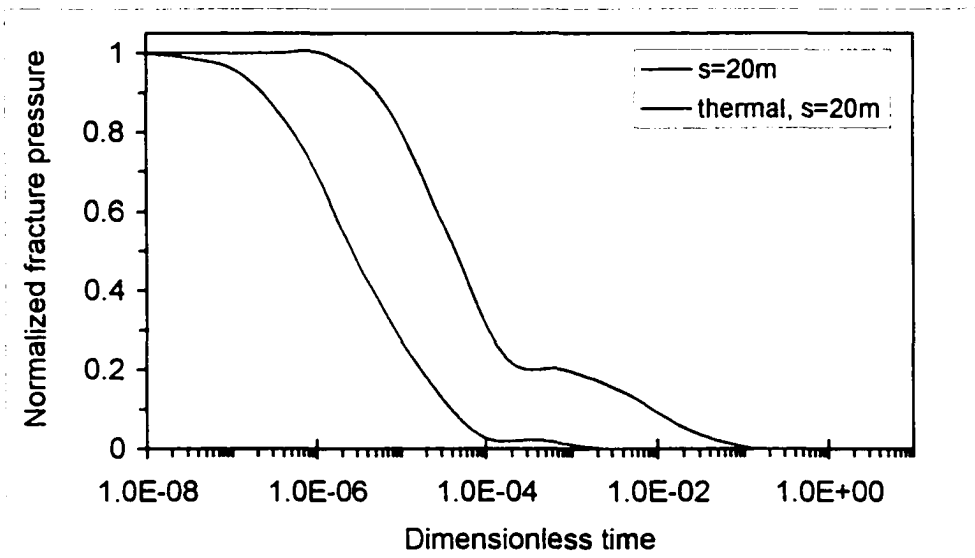


Figure 5.3.10 Fracture pressure comparison for dual- and thermal dual-porosity consolidations.

For temporal temperature variations, Figure 5.3.11 depicts significant differences between the matrix and the fracture temperatures, with the latter dissipating much faster.

This is physically understandable since the fluid acts as a heat carrier, which flows much faster in the fractures. The temporal matrix pressure is shown in Figure 5.3.12. Different from the isothermal case (refer to Figure 5.3.2), the initial pressure buildup (i.e., Mandel effect) seems to be more significant, implying noticeable impact of heat expansion.

The temporal temperature profiles in the matrix are illustrated in Figure 5.3.13 for the fractured porous media with various fracture spacings. Again, a more intense fractured media leads to a more rapid temperature dissipation. The slope changes in the temperature profiles, ranging from convex to concave, are the consequence of the exchange of thermal flux between the fractures and the porous matrix. In comparison, the changes of temperature in the fractures are much less dramatic, as shown in Figure 5.3.14. This is due to less variations of temperature within the fracture.

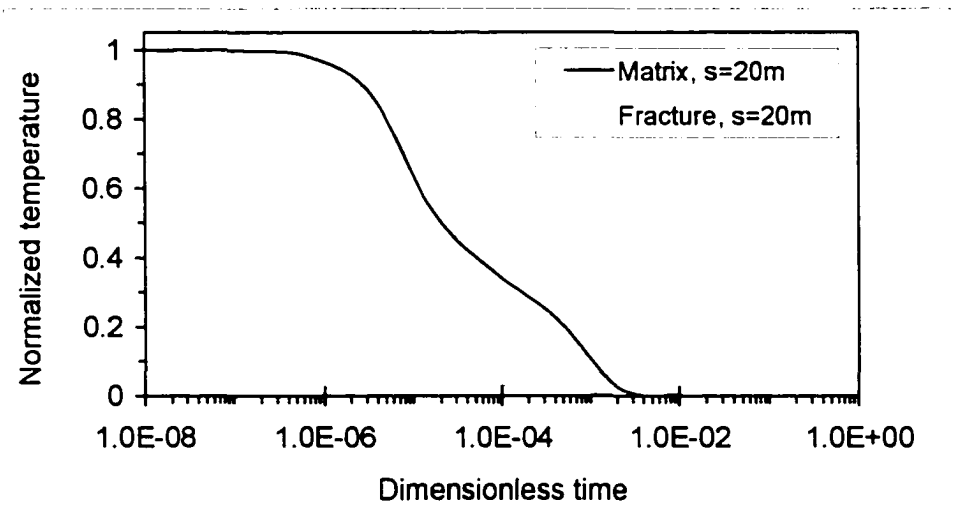


Figure 5.3.11 Temperature comparison for dual- and thermal dual-porosity consolidations.

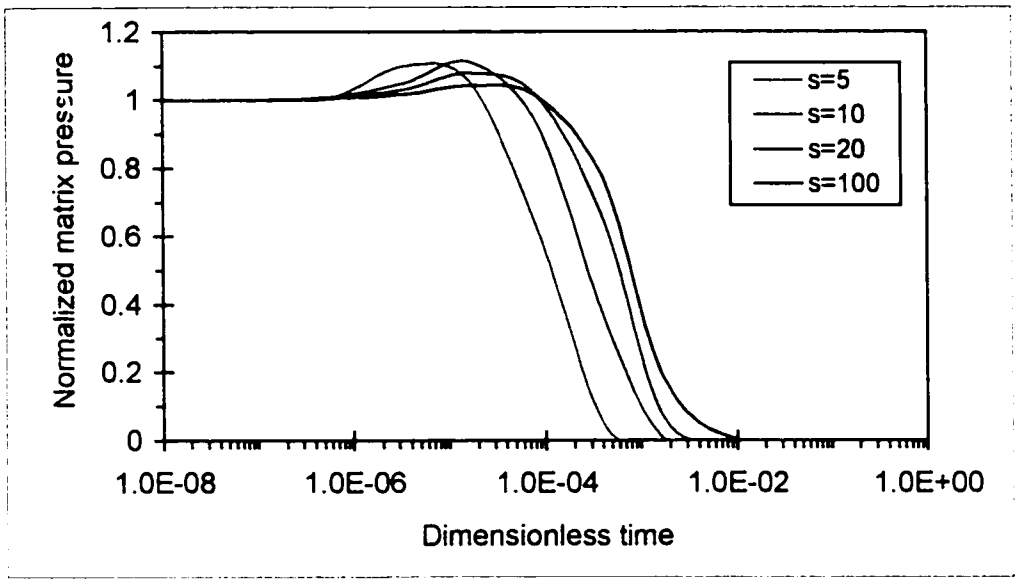


Figure 5.3.12 Temporal matrix pressure for different fracture spacings.

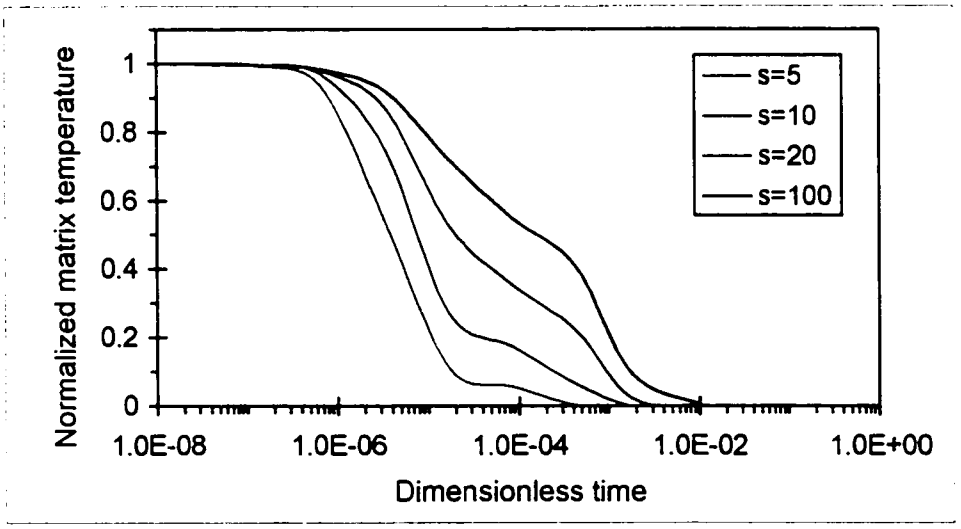


Figure 5.3.13 Temporal matrix temperature for different fracture spacings.

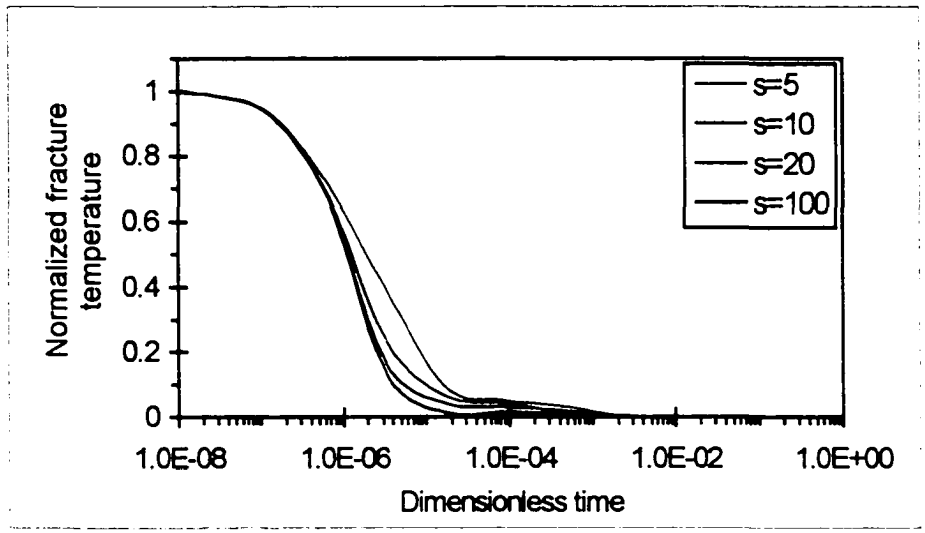


Figure 5.3.14 Temporal fracture temperature for different fracture spacings.

Using various thermal fluid conductivities, Figures 5.3.15 and 5.3.16 indicate the distributions of the matrix and fracture temperatures, respectively. In Figure 5.3.15, the larger fluid thermal conductivity leads to more significant temperature slope changes, along with a faster temperature dissipation in the matrix. In Figure 5.3.16, the larger fluid thermal conductivity results in an earlier temperature dissipation in fractures.

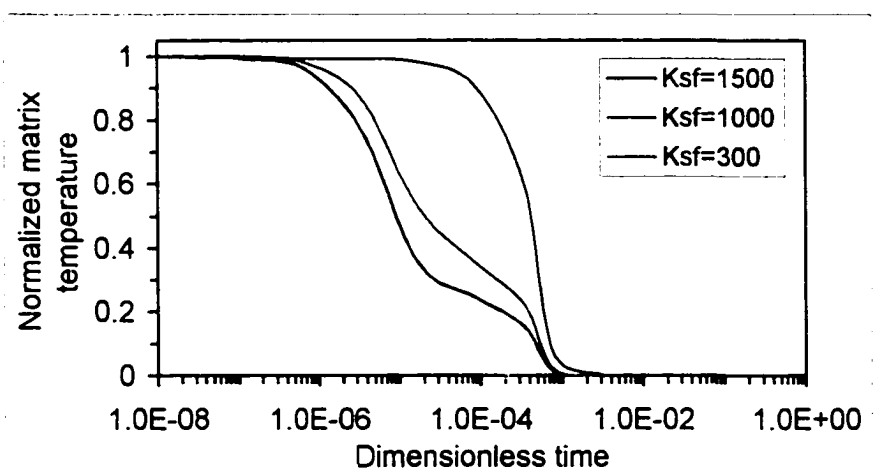


Figure 5.3.15 Temporal matrix temperature for different fluid thermal conductivities.

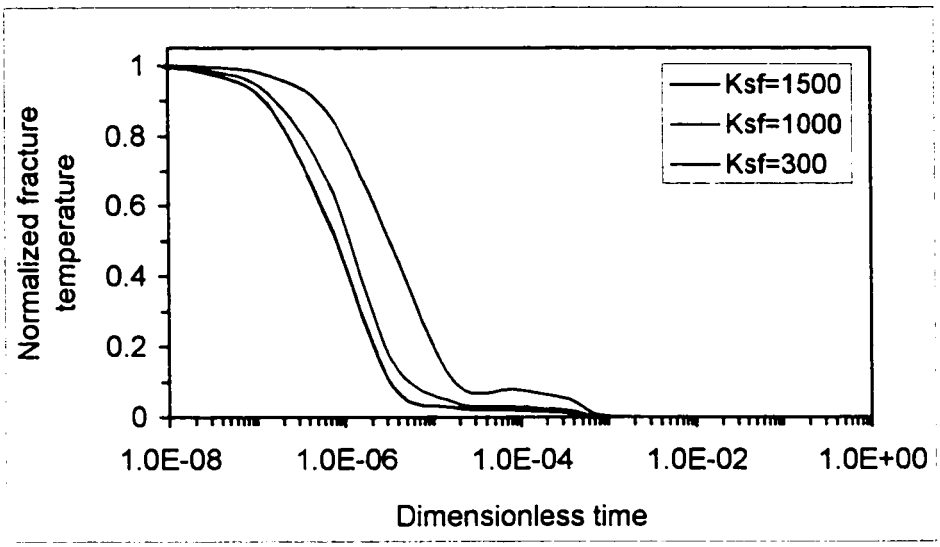


Figure 5.3.16 Temporal fracture temperature for different fluid thermal conductivities.

5.4 Inclined wellbore problems

5.4.1 Inclined Borehole Without Mudweight

The proposed finite element model was also validated by analyzing an inclined borehole problem. The geometric loading is depicted in Figures 4.6.1 and 4.6.2. The Cartesian coordinate system ($x'y'z'$) is chosen to coincide with the principal axes of the in-situ compressive stresses, respectively, designated as S_x, S_y and S_z. The initial formation pore pressure is denoted by p^0. It should be noted that the borehole axis is not coincident with the components of the in-situ stresses. In other words, 'inclined' is used to indicate that the borehole axis is inclined to the principal axes ($x'y'z'$) of the far field stresses. When the borehole coordinate system (xyz) is adopted, shear stresses are generated on the borehole wall. The local coordinate system (Figure 4.6.2) is formed by a rotation of the

azimuth angle, φ_x, about the x'-axis, and then by an inclination of the zenith angle, φ_z, from the z'-axis toward the z-axis.

Then, at the local coordinate system, the boundary conditions at the far field ($r \to \infty$) are characterized by the normal stresses:

$$\sigma_x^0 = S_x, \qquad \sigma_y^0 = S_y, \qquad \sigma_z^0 = S_z \tag{5.4.1}$$

and the shear stresses:

$$\tau_{xy}^0 = S_{xy}, \qquad \tau_{yz}^0 = S_{yz}, \qquad \tau_{xz}^0 = S_{xz} \tag{5.4.2}$$

as well as the matrix and fracture pore pressures:

$$p_{ma}^0 = p_{ma}^0, \qquad p_{fr}^0 = p_{fr}^0 \tag{5.4.3}$$

where the superscript '0' indicates the virgin (initial) state.

In the analysis, the in-situ stresses and initial pore pressures were: $S_{x'}$ = 29 MPa, $S_{y'}$ = 20 MPa, $S_{z'}$ = 25 MPa, and $p^0 = p_{ma}{}^0 = p_{fr}{}^0$ =10 MPa. The wellbore inclination is defined as $\varphi_x = 0°$ and $\varphi_z = 70°$. The wellbore radius is R = 0.1 m. The load at the wellbore is assumed as being applied instantaneously. In the local coordinate system (after 70° inclination), these values are determined by Equation (4.6.1) as: S_x = 25.5 MPa, S_y = 20 MPa, S_z = 28.5 MPa, S_{xz} = 1.3 MPa, $S_{xy} = S_{yz} = 0$ MPa and $p^0 = p_{ma}{}^0 = p_{fr}{}^0$ =10 MPa. The formation materials are assumed to be isotropic, characterized by the following properties: elastic modulus E = 20.6 GPa, Poisson ratio ν = 0.189, Biot modulus M =15.8 GPa, Biot's effective stress coefficient α_{ma} = 0.771, permeability $k_{ma} = 1\times10^{-7}$ darcy, and fluid dynamic viscosity μ = 0.001 Pa s. The analytical solution for this particular generalized plane strain poroelastic problem was provided by Cui et al. (1997). The corresponding equivalent parameters for the dual-porosity poroelastic model are listed in Table 5.4.1, in which the selection of an exceptionally large fracture spacing, s, denotes the approximation of a homogeneous single-porosity medium.

Table 5.4.1 Parameters for inclined borehole analysis

Parameter	Unit	Magnitude
Elastic modulus (E)	GN/m^2	20.6
Poisson's ratio (ν)	-	0.189
Fracture stiffness (K_n, K_{sh})	$MN/m^2/m$	4.821×10^5
Fluid bulk modulus (K_f)	MN/m^2	419.17
Grain bulk modulus (K_s)	GN/m^2	48.21
Matrix porosity (n_{ma})	-	0.02
Fracture porosity (n_{fr})	-	0.002
Matrix mobility (k_{ma}/μ)	$M^4/MN\ s$	10^{-10}
Fracture mobility (k_{fr}/μ)	$M^4/MN\ s$	10^{-9}
Fracture spacing (s)	m	10^7

Figures 5.4.1 and 5.4.2 represent the pore pressure variations into the rock formation. The comparative results between the analytical solution and the numerical dual-porosity solution, for large s, along the radial directions θ = 84.4° and θ = 5.7°, are shown at two different times. It is noted that the pore pressure distribution along the radial direction θ = 84.4° at the early time is non-monotonic, with a peak value appearing at a short distance from the wellbore wall, which is attributed to the poroelastic effect (Detournay and Cheng, 1993, Cheng et al., 1993). Except for a small discrepancy, the numerical results appear to agree well with the analytical solution.

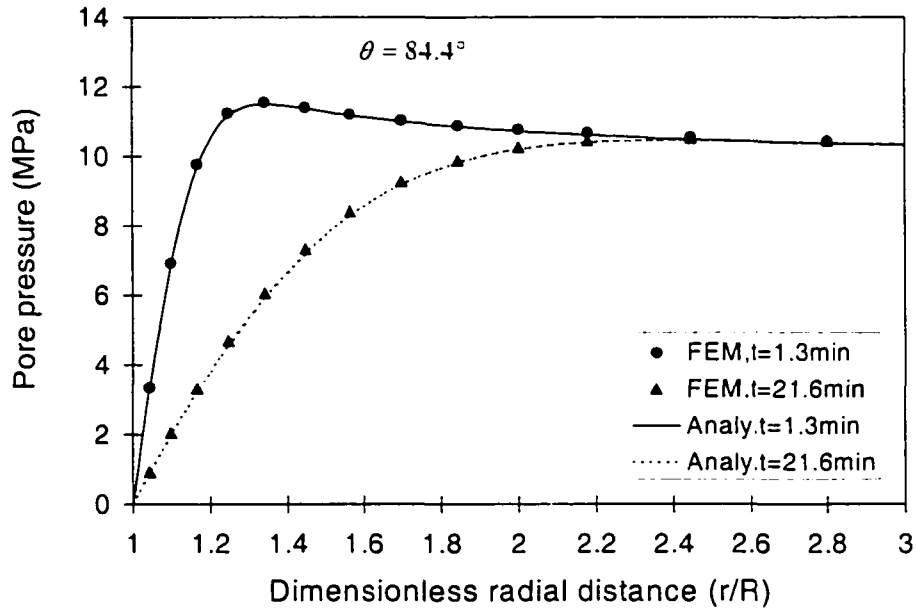


Figure 5.4.1 Comparison between the finite element and analytical solutions for pore pressure (θ = 84.4°)

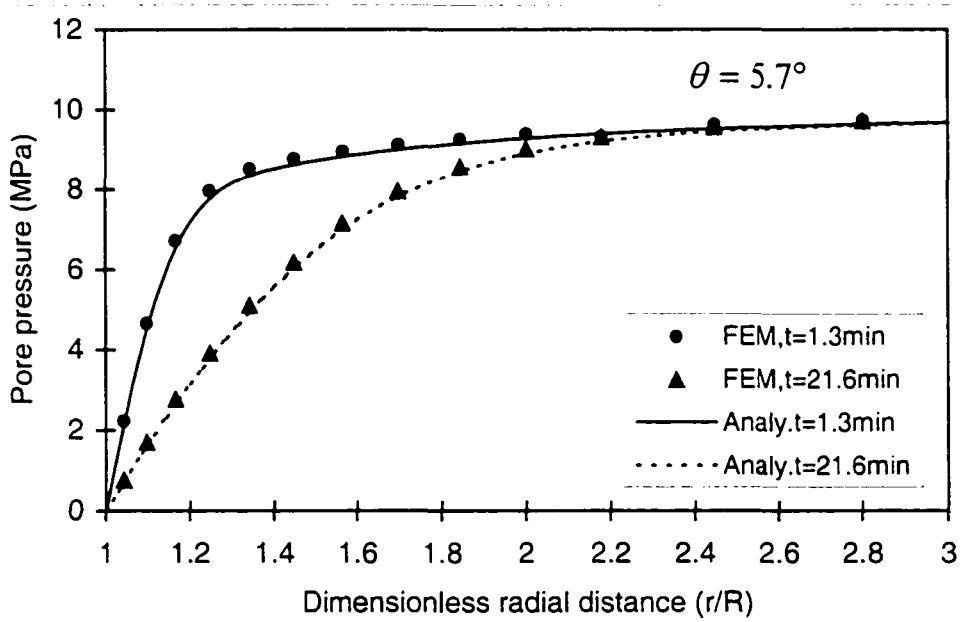


Figure 5.4.2 Comparison between the finite element and analytical solutions for pore pressure (θ = 5.7°)

For the same data set, the Terzaghi's effective radial stresses, defined as the difference between the total radial stress and the pore pressure, are plotted in Figure 5.4.3 and 5.4.4 for $\theta = 84.4°$ and $\theta = 5.7°$. Except for a slight difference in the near-wellbore region, the analytical and finite element solutions match well. The tensile region developed at early time is due to the non-monotonic pore pressure distribution, consistent with the case reported in Cheng et al. (1993). The contour of Terzaghi's effective radial stress calculated by the proposed model for t = 100 seconds is drawn in Figure 5.4.5 and the counterparts of analytical solutions along five radial sections are compared. The analytical and numerical solutions again agree well.

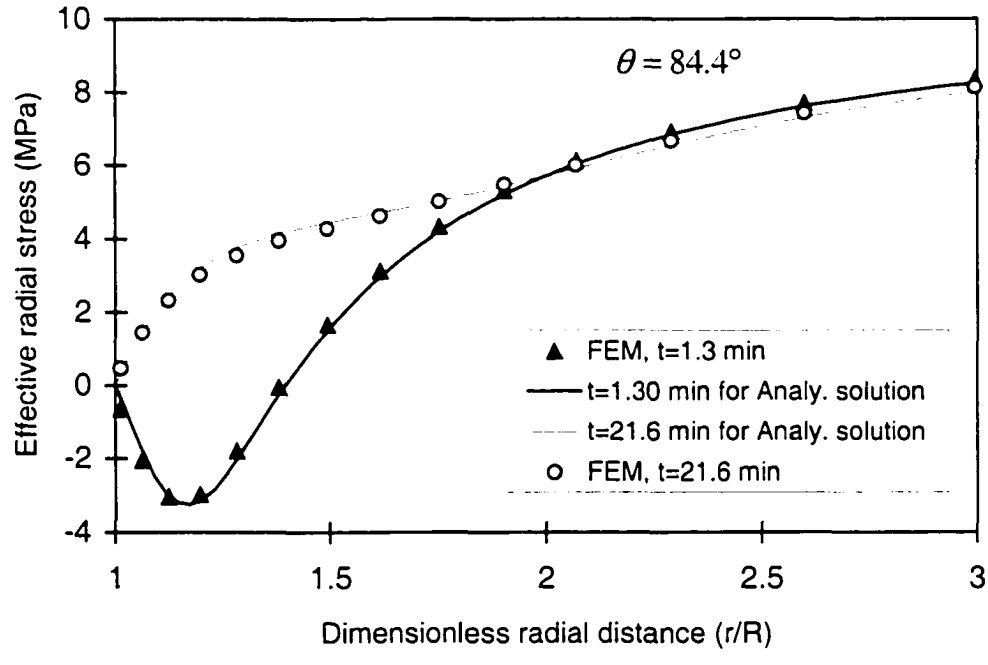


Figure 5.4.3 Comparison between the finite element and analytical solutions for Terzaghi's effective radial stress (θ = 84.4°)

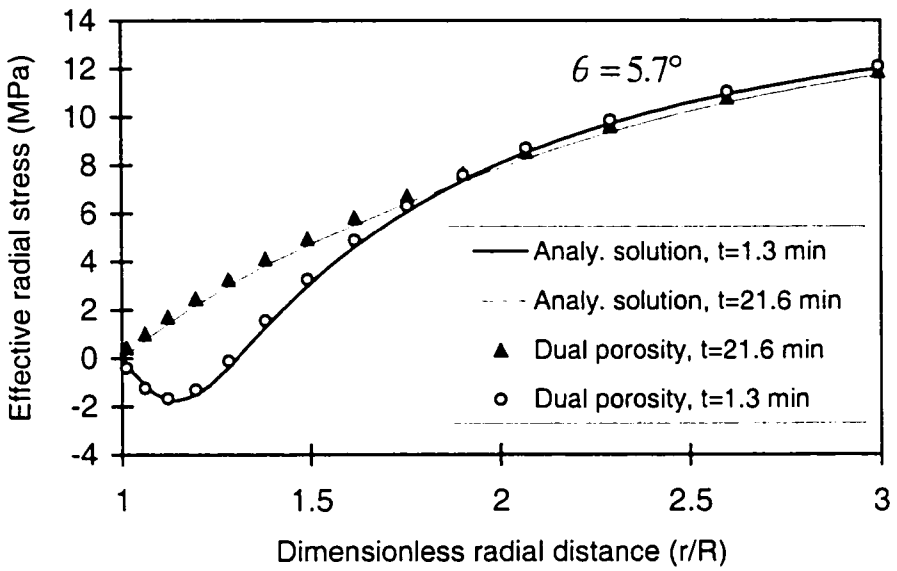


Figure 5.4.4 Comparison between the finite element and analytical solutions for Terzaghi's effective radial stress (θ = 5.7°).

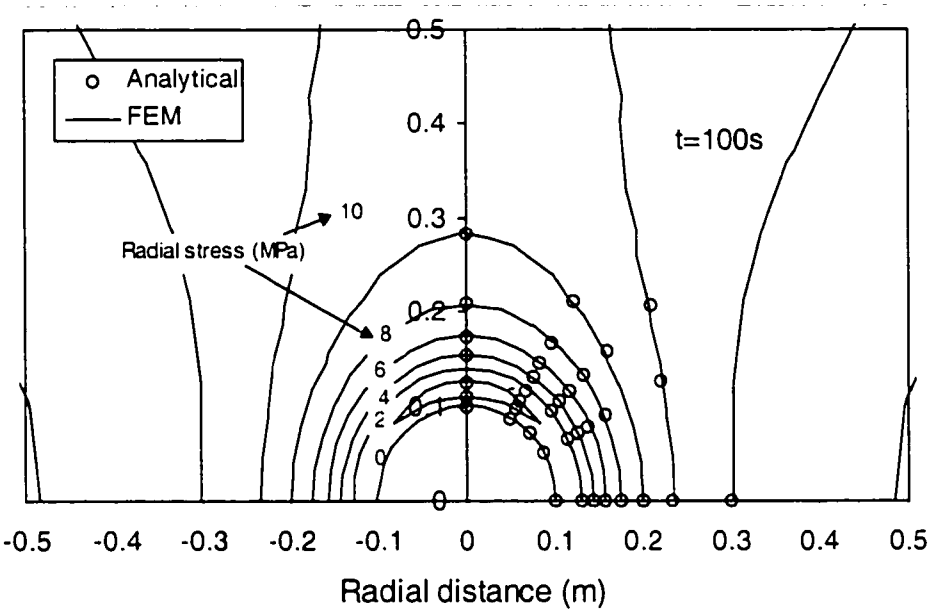


Figure 5.4.5 Comparison between the finite element and analytical solutions for Terzaghi's effective radial stress along different radial sections for t = 100 seconds.

Figure 5.4.6 is the total tangential stresses for two different radial directions (θ = 5.7 and 84.4°) and two different times (t = 1.3 and 21.6 min), it can be seen that very excellent agreements are obtained for the larger time (t = 21.6 min). For the smaller time (t = 1.3 min), there are slight differences in the near wellbore region, which are induced by initial conditions, time steps and boundary effects in the finite element method.

Also, good matches are obtained for the total axial stress stresses for two different radial directions (θ = 0 and 90°) and two different times (t = 1.3 and 21.6 min), (refer to Figure 5.4.7).

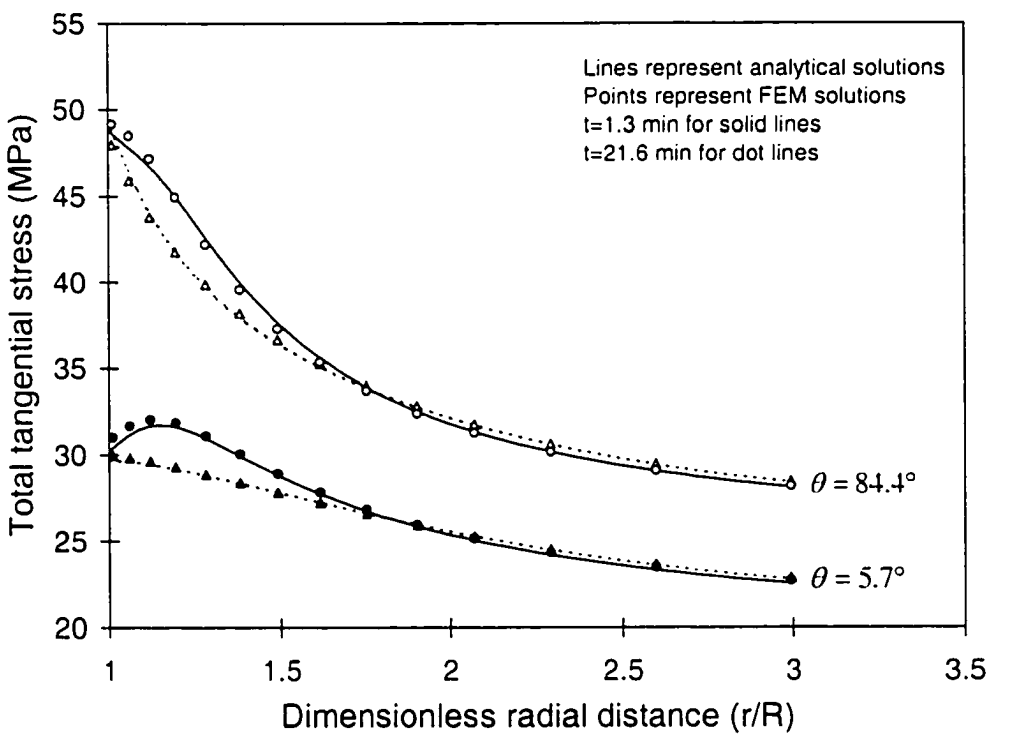


Figure 5.4.6 Comparison between the finite element and analytical solutions for tangential stress along different radial sections (θ = 5.7°, θ = 84.4°) and times (t = 1.3 min, t = 21.6 min).

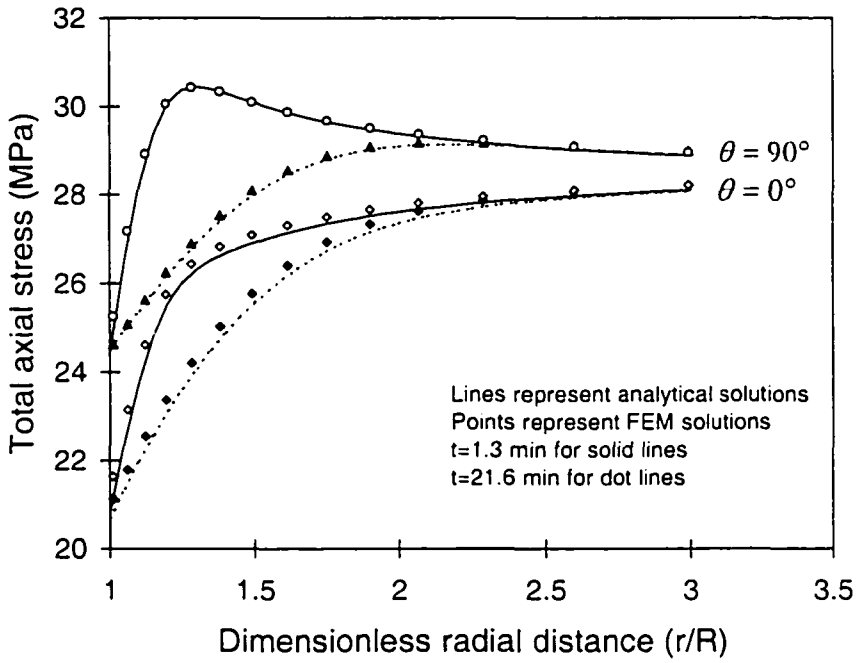


Figure 5.4.7 Comparison between the finite element and analytical solutions for axial stress along different radial sections (θ = 0°, θ = 90°) and times (t = 1.3 min, t = 21.6 min).

5.4.2 Inclined Borehole With Mudweight

For permeable models, the dual-porosity solution, assuming extreme large spacing ($s = 10^7$) can be used to present the approximation of the single porosity case. For this consideration, the dual-porosity model was compared with the solution of PBORE-3D – a software for single porosity poroelastic analytical solution (Cui et al., 1999; Ekbote, 2001). The parameters used are the same as in the previous section except that a mud pressure (p_w = 12 MPa) was applied along the wellbore. Along two different radial sections (θ = 30°, θ = 90°), the numerical solution and analytical solutions for pore pressures, radial and tangential stresses are compared in Figures 5.4.8 to 5.4.13. It can be

seen that the proposed finite element solutions have excellent matches with the analytical solutions, except for small discrepancies at the wellbore for radial and tangential stresses.

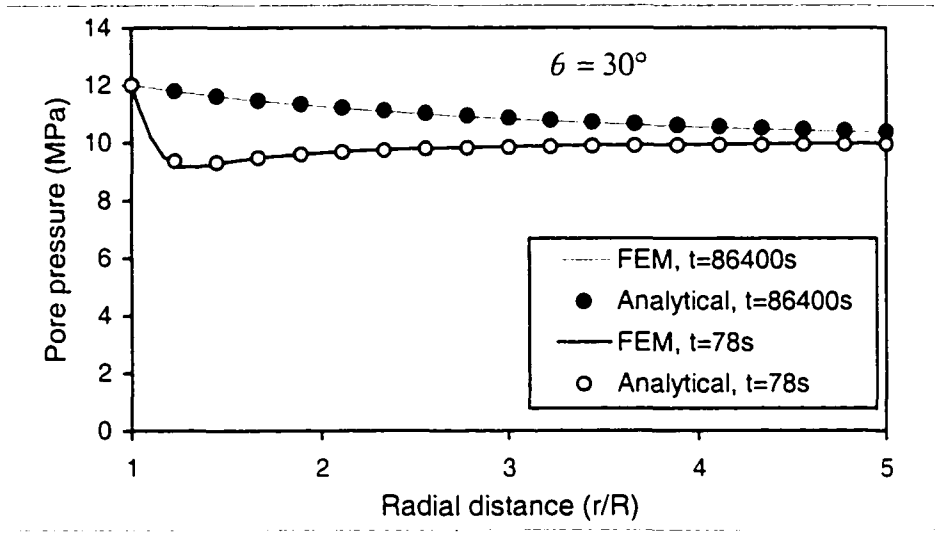


Figure 5.4.8 Comparison between the finite element and analytical solutions for pore pressure ($\theta = 30°$).

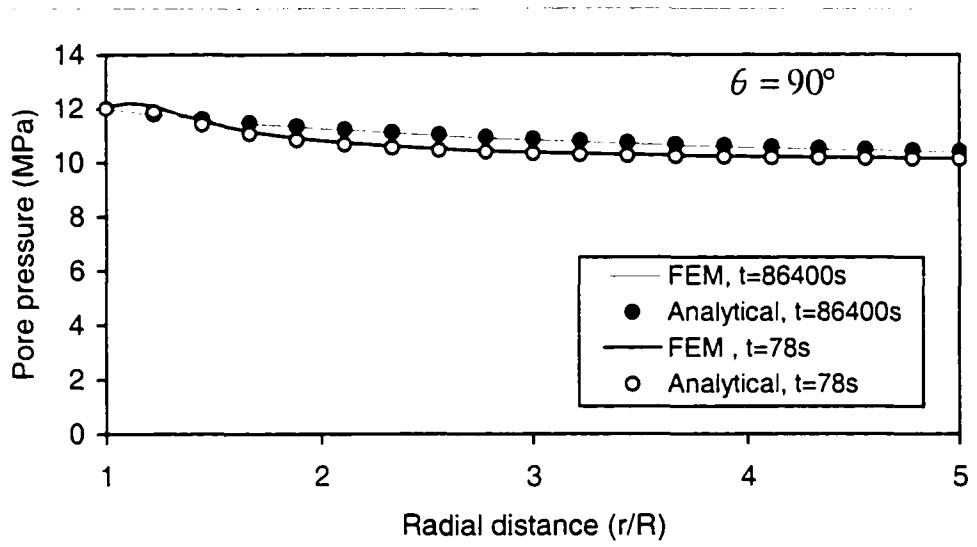


Figure 5.4.9 Comparison between the finite element and analytical solutions for pore pressure ($\theta = 90°$).

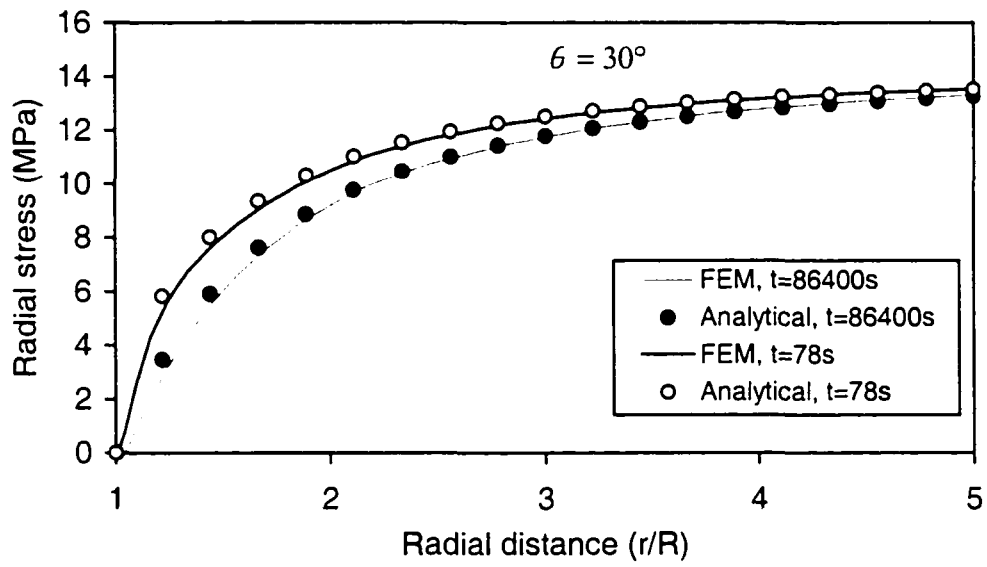


Figure 5.4.10 Comparison between the finite element and analytical solutions for Terzaghi's effective radial stress ($\theta = 30°$).

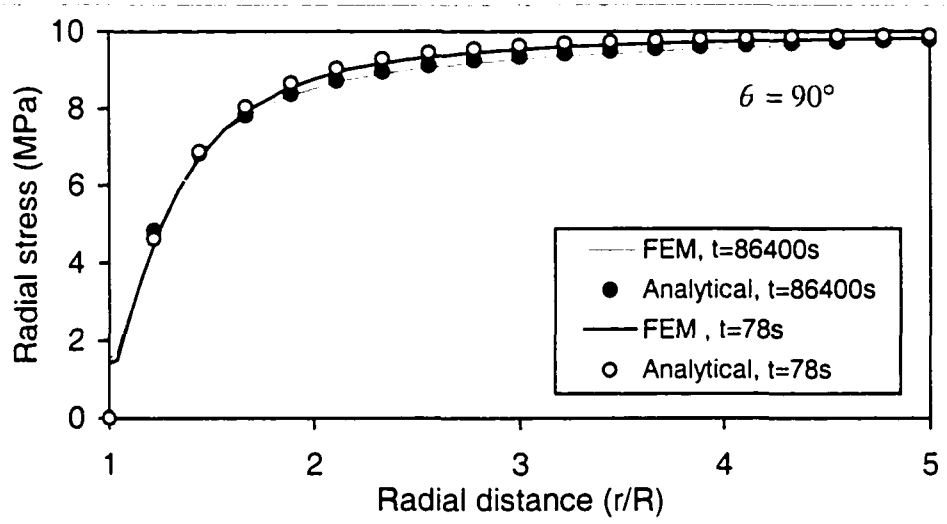


Figure 5.4.11 Comparison between the finite element and analytical solutions for Terzaghi's effective radial stress ($\theta = 90°$).

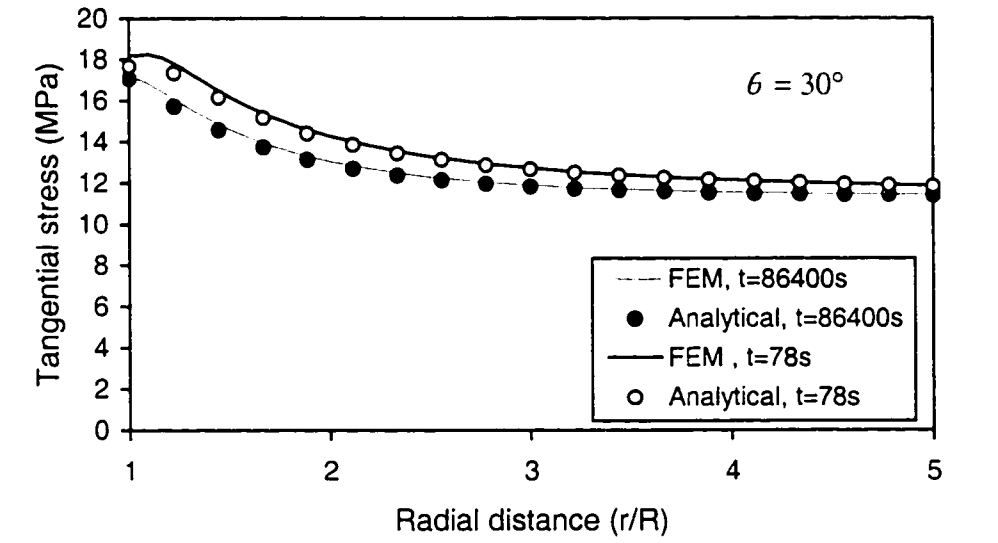


Figure 5.4.12 Comparison between the finite element and analytical solutions for Terzaghi's effective tangential stress ($\theta = 30°$).

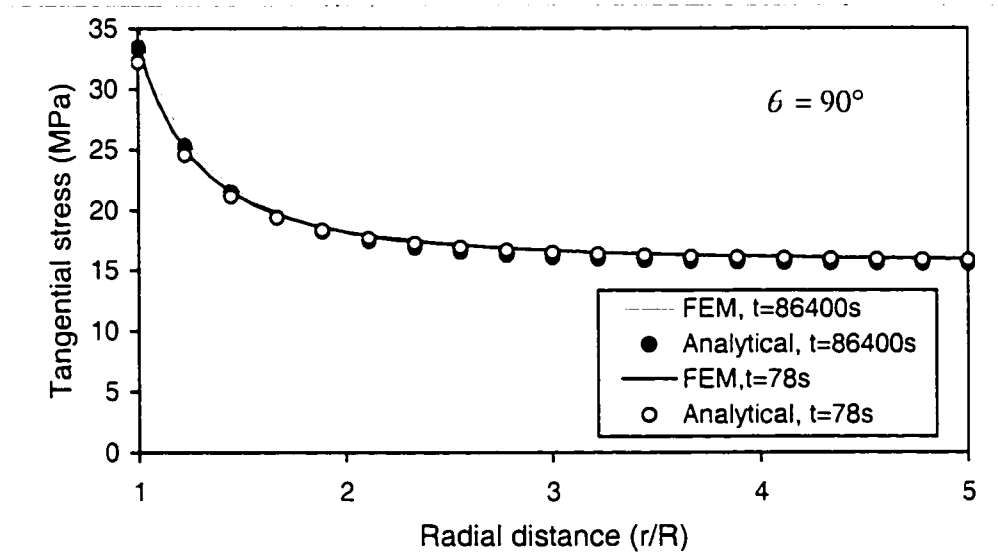


Figure 5.4.13 Comparison between the finite element and analytical solutions for Terzaghi's effective tangential stress ($\theta = 90°$).

For the impermeable case, the dual-porosity finite element model with extreme large spacing and zero pore and fracture pressures present the approximation of the elastic solution. The analytical solution for this inclined borehole problem is calculated using Equations (2.2.17) and (2.2.18). The parameters used for the finite element model were same as in the previous section except a mud pressure (p_w = 10 MPa) is applied along the borehole wall. Along the radial section (θ = 30°), the numerical solution and analytical solutions for radial and tangential stresses are compared in Figure 5.4.14. It can be seen that the proposed finite element solutions have good matches with the analytical solutions except small discrepancies near the borehole wall.

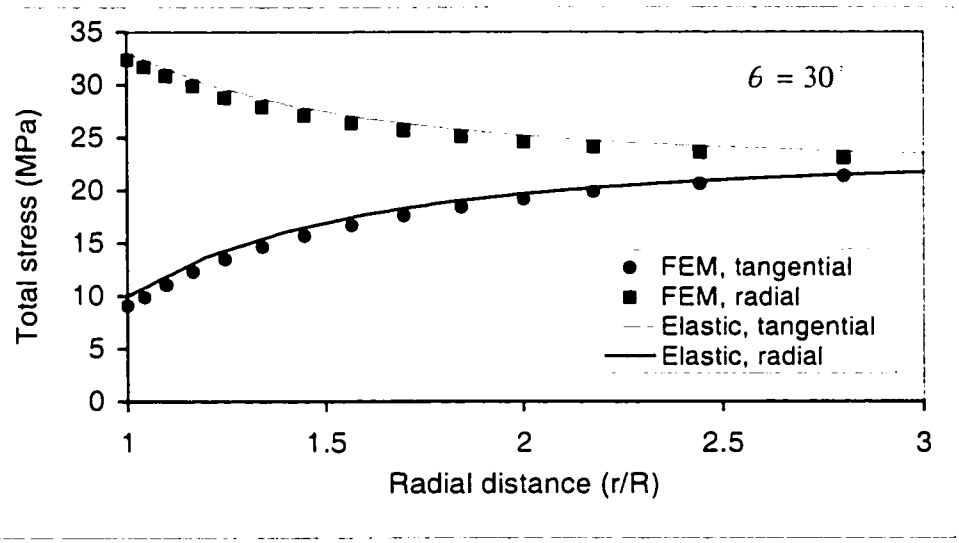


Figure 5.4.14 Comparison between the finite element and analytical solutions for total radial and tangential stresses along the radial sections θ = 30° for impermeable model.

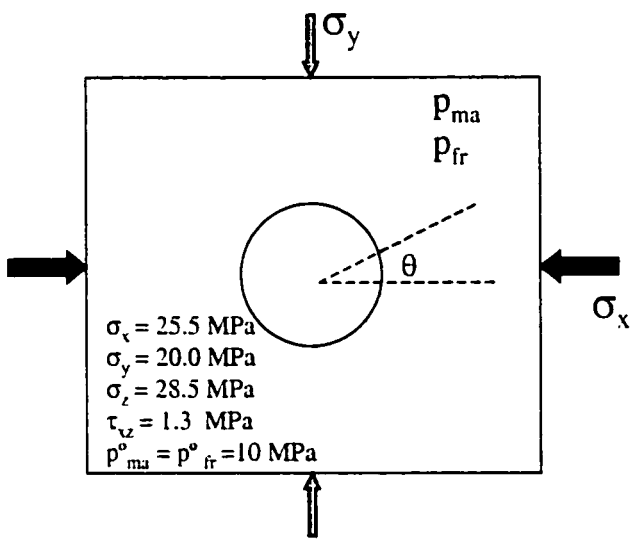
In this chapter, the presented numerical solution was validated by elastic, single-porosity analytical solutions for wellbore and consolidation problems, and excellent agreements were obtained. Furthermore, the one-dimensional dual-porosity elastoplastic non-isothermal consolidation was presented and can be used for future validations. The dual-porosity parametric analyses will be given to further examine the proposed finite element model in the following chapter.

Chapter 6

Parametric Study

In this chapter, examples are given to demonstrate how certain parameters in dual-porosity media affect the pore pressure and stress results. The in-situ stresses, initial pore pressures, geometry and material properties used in the ongoing analyses are identical to those listed in Section 5.4 and Table 5.4.1 except for the fracture spacing s = 1m. All the results are presented at a borehole inclination angle $\varphi_z = 70°$ except Section 6.6. Figure 6.1 shows the far field and local stress states; it can be seen that the x-direction ($\theta = 0°$) is the local maximum stress direction and the y-direction ($\theta = 90°$) is the local minimum one.

In the following parametric analyses, time, hole inclination, fracture parameters, matrix permeability, mud weight and mud cake effects are considered. For each analysis, only one specific parameter was allowed to be varied.



Original conditions
(far-field stress):

S'_x = 29 MPa
S'_y = 20 MPa
S'_z = 25 MPa
$p^{\circ}_{ma} = p^{\circ}_{fr}$ =10 MPa

Figure 6.1 State of stress in the borehole local coordinate after 70° inclination.

6.1 Dual-porosity Effect

The pore pressure distributions at t = 100 s and θ = 0° and 90° for the single-porosity model as well as the ones for the dual-porosity model are compared in Figures 6.1.1 and 6.1.2. The difference is evidenced by the increase in pore pressure in the matrix for the dual-porosity media due to the associated large fracture compliance which induces the non-monotonic pressure distribution (Figure 6.1.2). A similar comparison can be made for Terzaghi's effective radial stresses (Figures 6.1.3 and 6.1.5). Although the pore pressure induced by dual-porosity effect increases, the tensile stress does not increase, but decreases (Figures 6.1.3 and 6.1.5). This is due to the fact that the total radial stress has a larger increment than the pore pressure for the dual-porosity medium, as shown in Figures 6.1.4 and 6.1.6. Therefore, the effective compressive stress, which equals to the difference of the total stress and the pore pressure, increases and the effective tensile stress decreases, which reduces the potential for borehole spalling. The reason of this phenomenon in the dual-porosity medium is that the total deformation increases due to the introduction of a fracture elastic modulus $K_n s$ in the dual-porosity governing equations shown in Chapter 3, which leads to increase in the total radial stress.

The dual-porosity models lead to little changes in Terzaghi's effective tangential stresses (Figure 6.1.7) and to a small increase in the effective axial stress, as shown in Figure 6.1.8, which are also associated with the introduction of the fracture compliance. Comparing to the in-situ stress magnitudes, stress concentrations occur at the wellbore due to drilling.

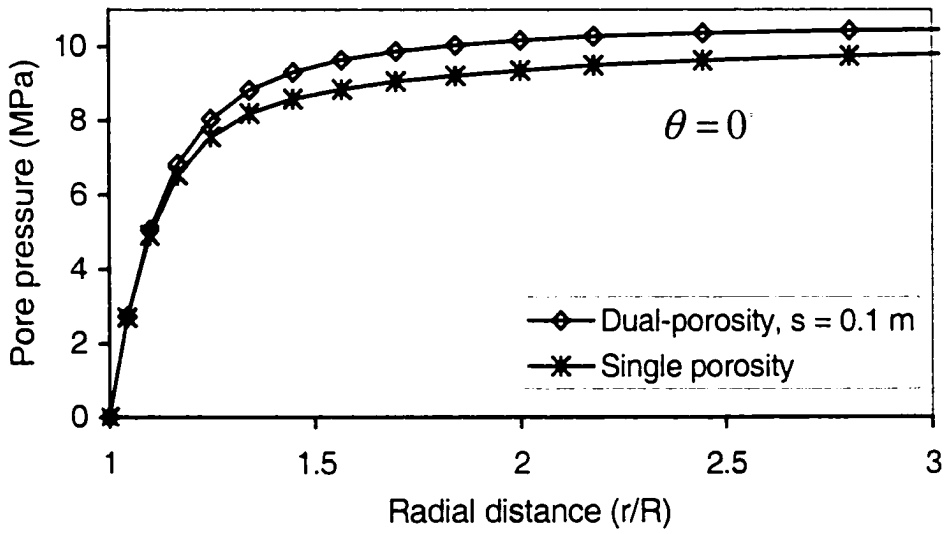


Figure 6.1.1 Comparison of pore pressure for single- and dual-porosity models in the maximum stress direction at t = 100 s.

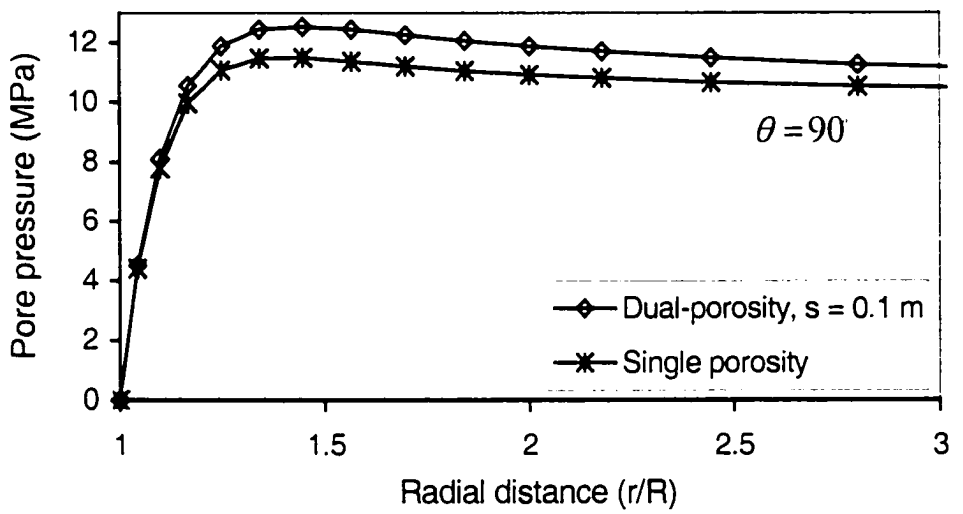


Figure 6.1.2 Comparison of pore pressure for single- and dual-porosity models in the minimum stress direction at t = 100 s.

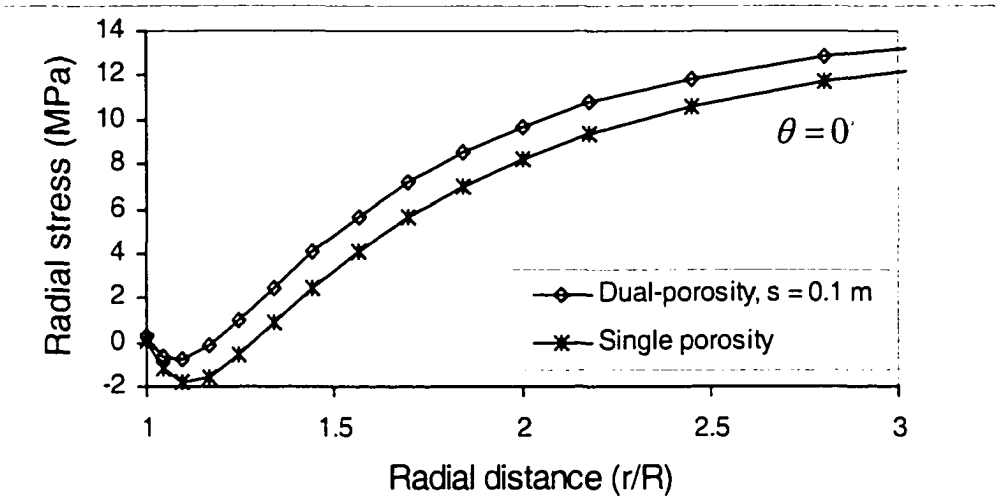


Figure 6.1.3 Comparison of effective radial stress for single- and dual-porosity models in the maximum stress direction at t = 100 s.

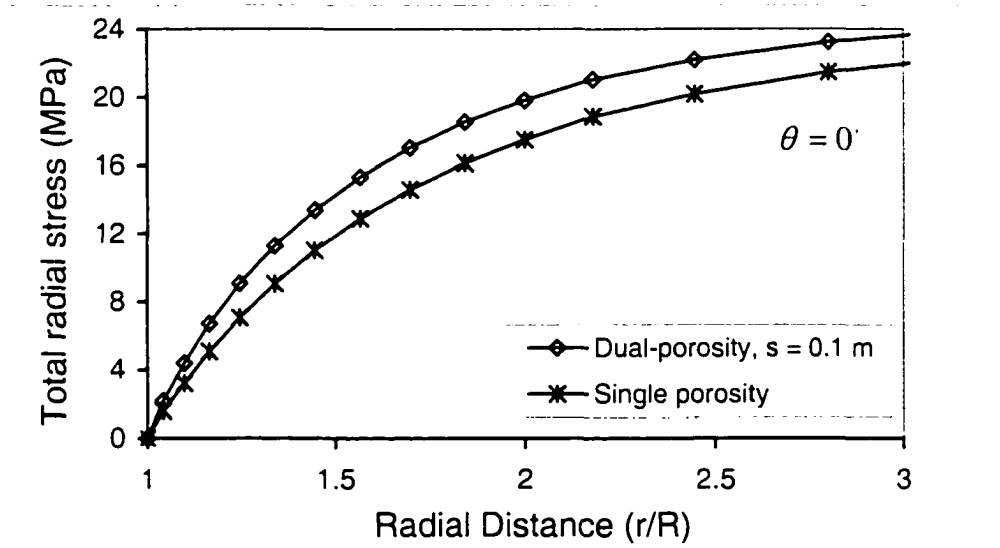


Figure 6.1.4 Comparison of total radial stress for single- and dual-porosity models in the maximum stress direction at t = 100 s.

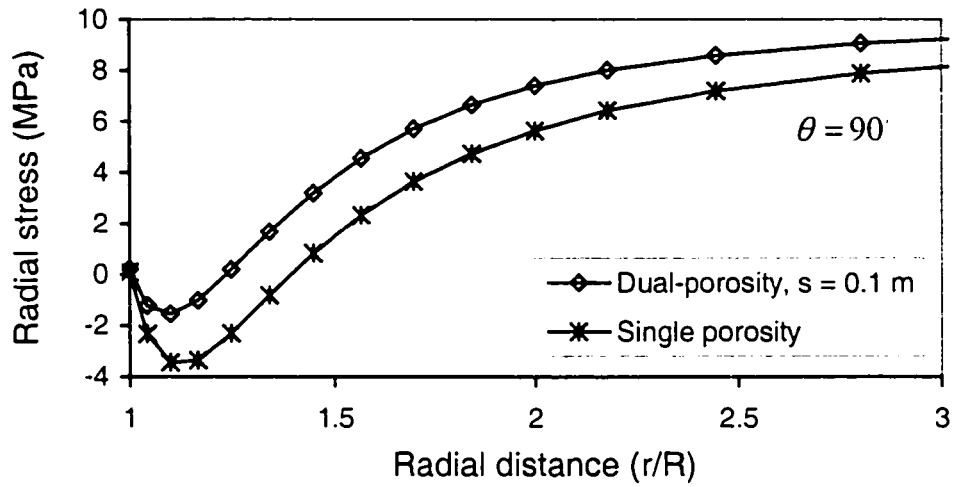


Figure 6.1.5 Comparison of effective radial stress for single- and dual-porosity models in the minimum stress direction at t = 100 s.

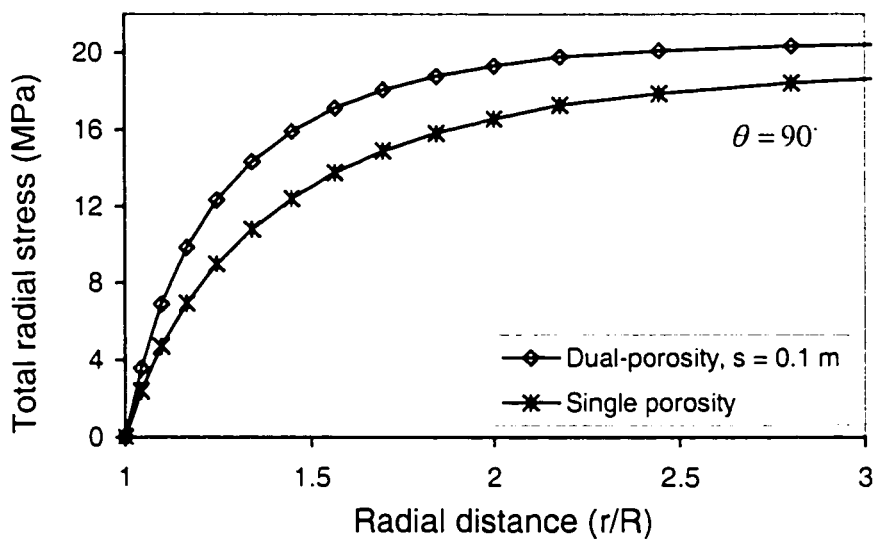


Figure 6.1.6 Comparison of total radial stress for single- and dual-porosity models in the minimum stress direction at t = 100 s.

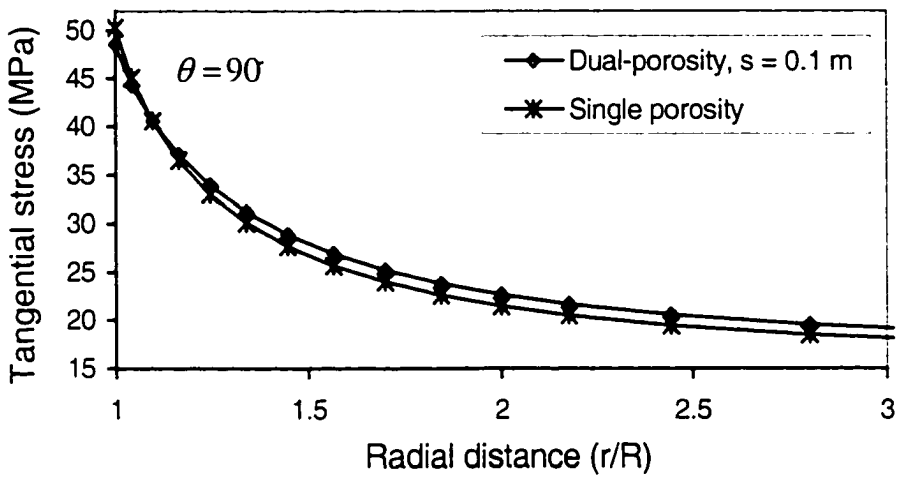


Figure 6.1.7 Comparison of effective tangential stress for single- and dual-porosity models in the minimum stress direction at t = 100 s.

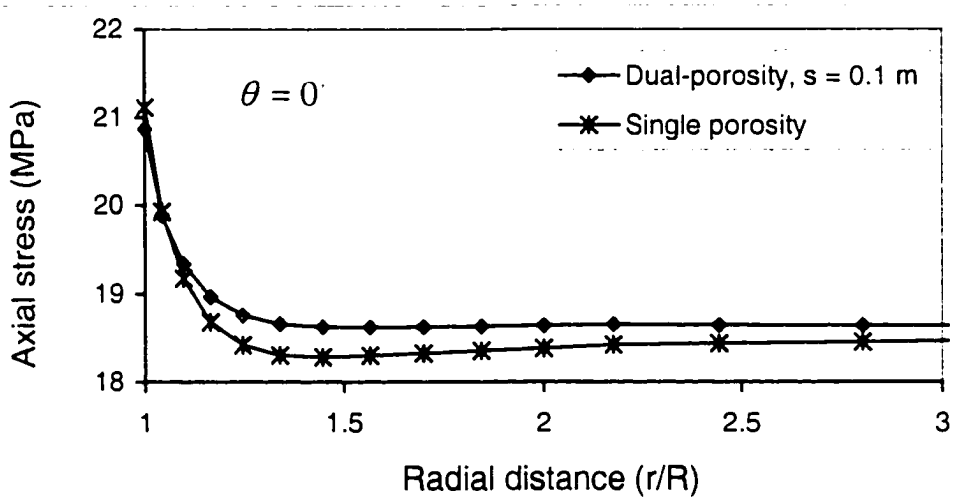


Figure 6.1.8 Comparison of effective axial stress for single- and dual-porosity models in the maximum stress direction at t = 100 s.

6.2 Time-dependent Effects

The following analyses are for the dual porosity media (s = 1m). In Figures 6.2.1 through 6.2.3 the pore pressure distributions around the wellbore is presented at three different times. Observe that the pore pressure concentrations in the near field occur at smaller times (for t = 10 s in Figure 6.2.1 and t = 100 s in Figure 6.2.2) around the minimum stress direction (θ = 90°). The pore pressure decreases as time increases, as shown in Figures 6.2.1 to 6.2.3. The pore pressure responses at different times can clearly be seen in different radial directions in Figures 6.2.4 through 6.2.6. The pore pressure in the near field is larger as θ increases, which is due to Skempton's effect, because at 90° a larger far-field compressive normal stress prevails (See Figure 6.1). Note also that at 60° (Figure 6.2.5) and 90° (Figure 6.2.6) non-monotonic pressure distributions and pressure peaks are found at a small distance inside the wall at small times, which is attributed to the poroelastic effect. At larger time, this effect disappears. At large distances, the pore pressure approaches asymptotically the far-field value of 10 MPa; and, as time increases, this poroelastic effect become negligible.

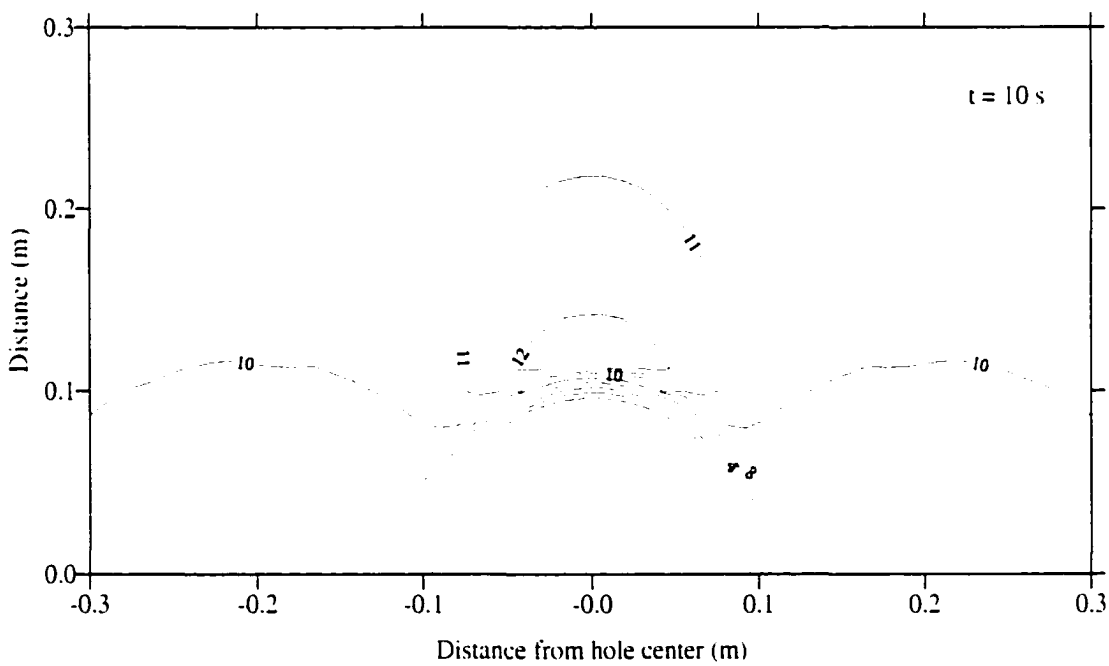


Figure 6.2.1 Pore pressure distribution around the wellbore at t = 10 s.

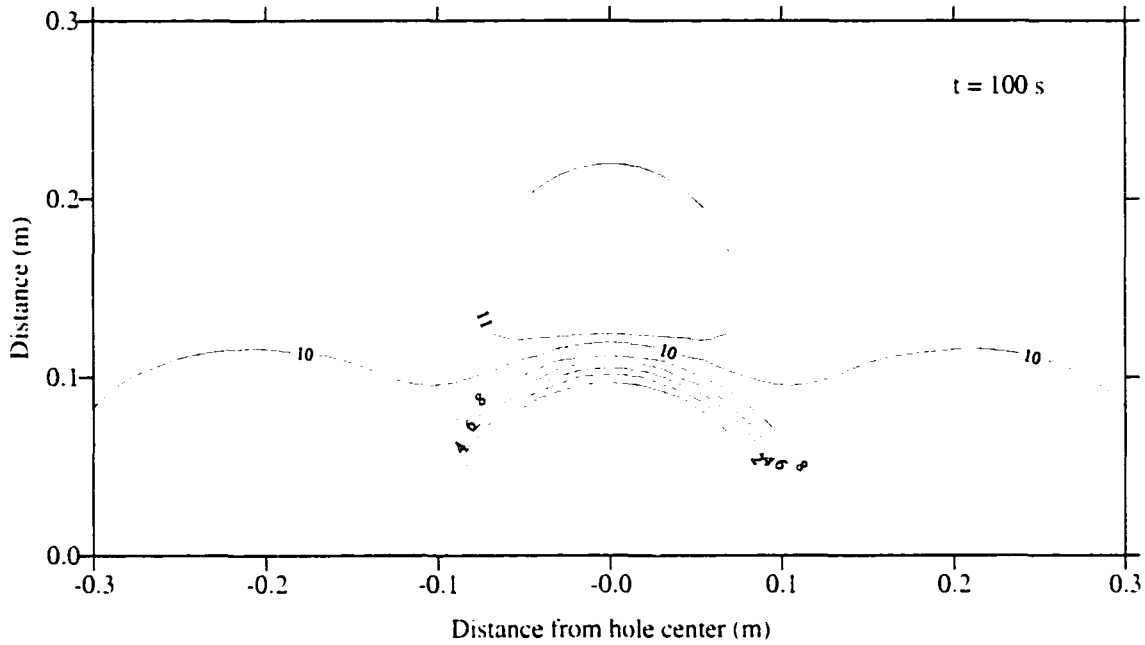


Figure 6.2.2 Pore pressure distribution around the wellbore at t = 100 s.

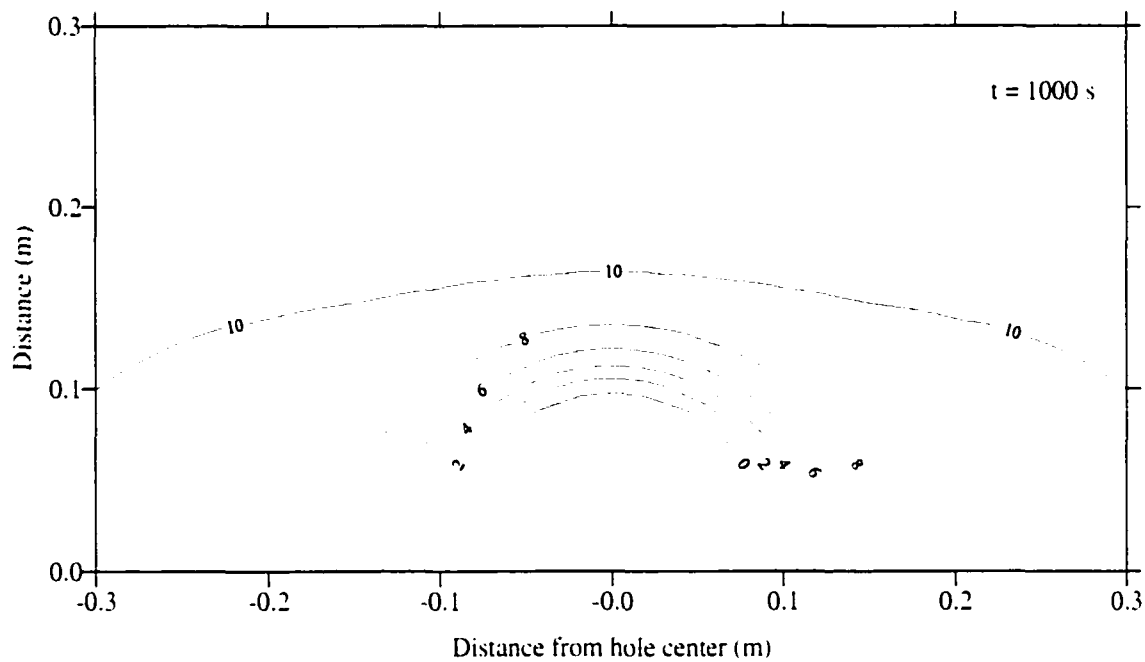


Figure 6.2.3 Pore pressure distribution around the wellbore at t = 1000 s.

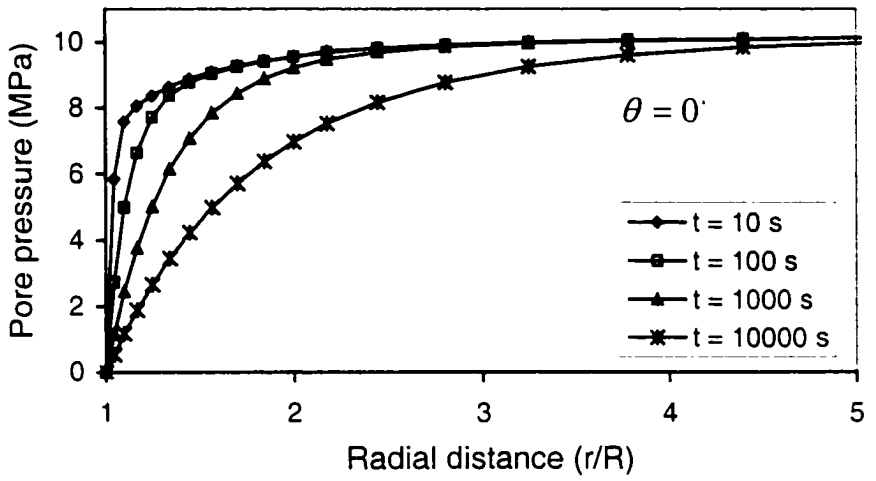


Figure 6.2.4 Pore pressure around the wellbore at $\theta = 0°$ for different times.

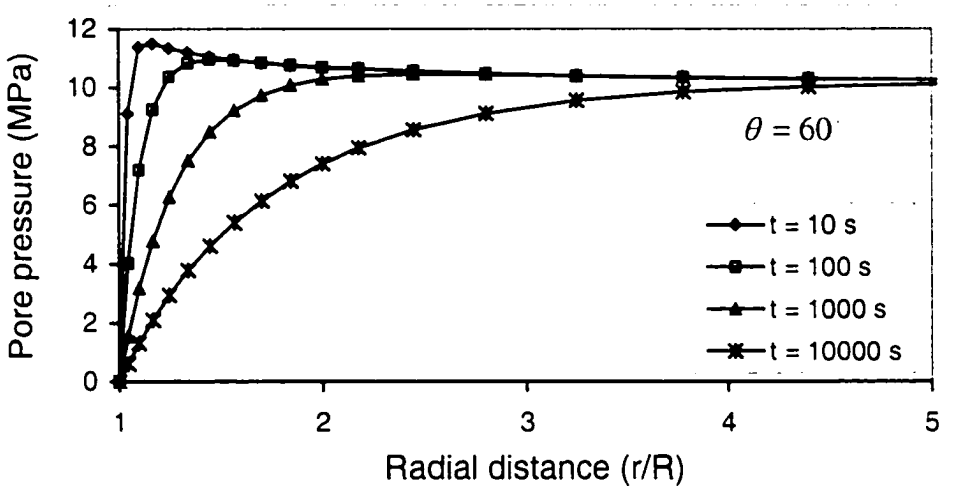


Figure 6.2.5 Pore pressure around the wellbore at $\theta = 60°$ for different times.

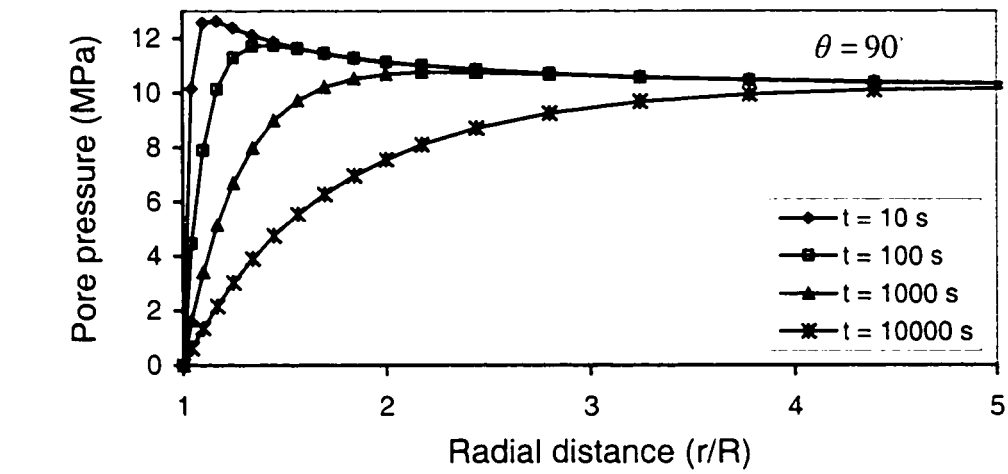


Figure 6.2.6 Pore pressure around the wellbore at $\theta = 90°$ for different times.

The Terzaghi's effective radial stress distribution contours for three different times, t = 10 s, t = 100 s and t = 1000 s, are ploted in Figures 6.2.7 to 6.2.9. The results clearly show a tensile region near the wellbore at small times in Figures 6.2.7 and 6.2.8. The elliptical tensile stress area around the wellbore is larger in the minimum stress direction than that in the maximum stress direction. Away from the tensile stress area, the stress gradually approaches to the local far-field stress. Futhermore, the tensile radial stress magnitude in the near field is much larger in the minimum stress direction ($\theta = 90°$) than that in maximum stress direction ($\theta = 0°$), as shown in Figures 6.2.10 and 6.2.11. This is due to higher pore pressure values (refer to Figures 6.2.4 and 6.2.6). It can also be seen that radial stress has very strong time effects; i.e., the tensile stress reduces significantly as time elapses. There is no tensile stress as time becomes large enough as illustrated in Figure 6.2.9.

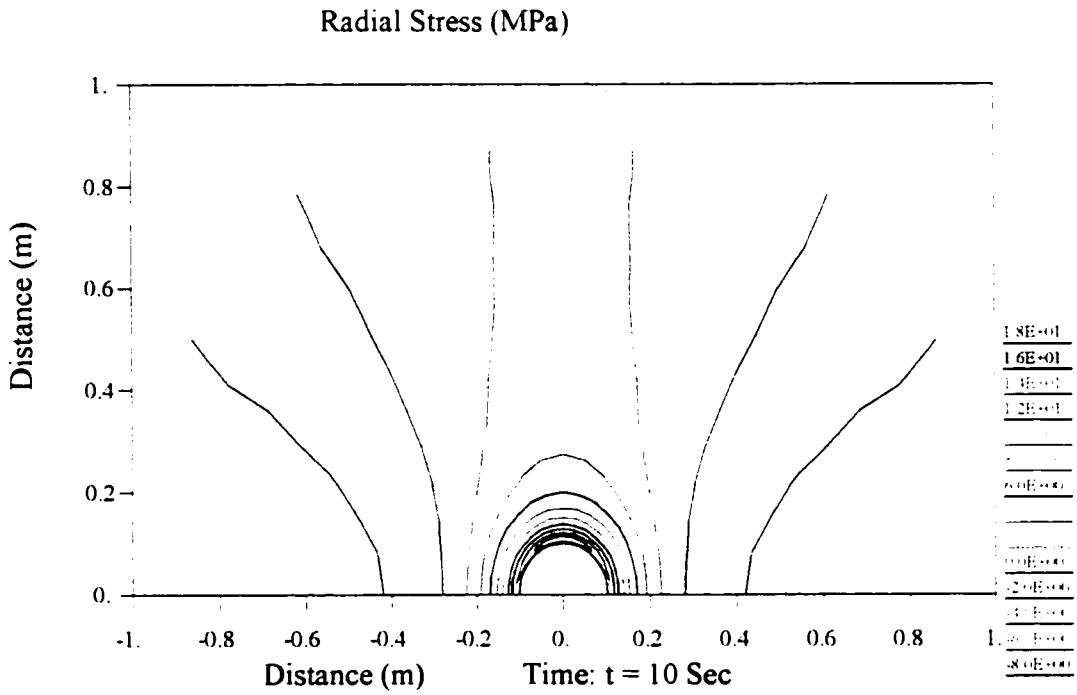


Figure 6.2.7 Radial stress distribution around the wellbore at t = 10 s.

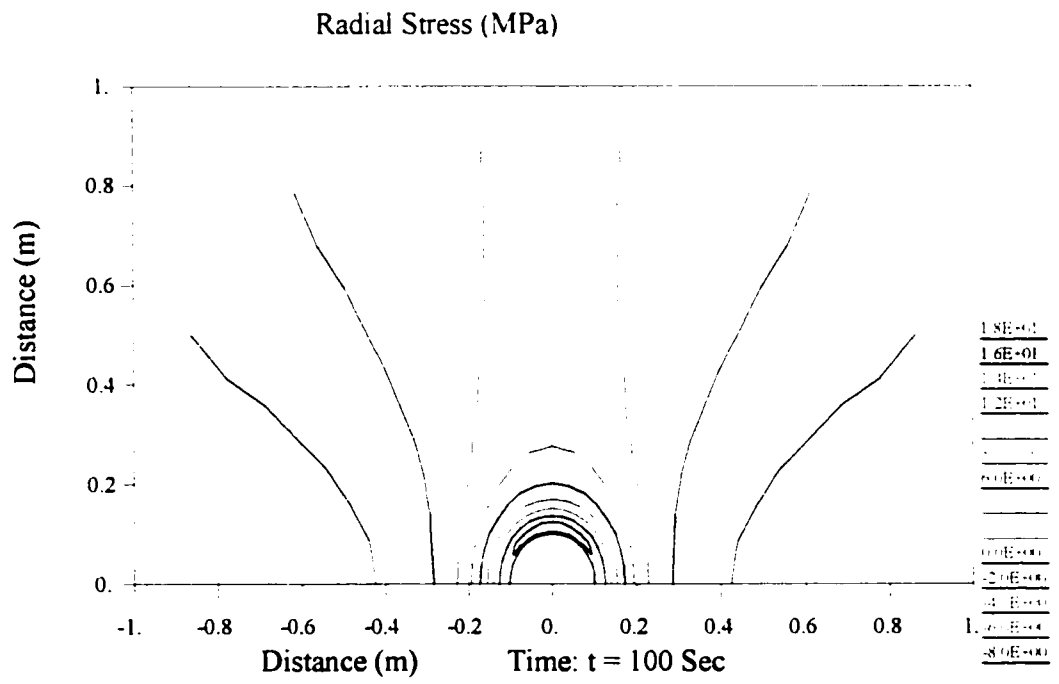


Figure 6.2.8 Radial stress distribution around the wellbore at t = 100 s.

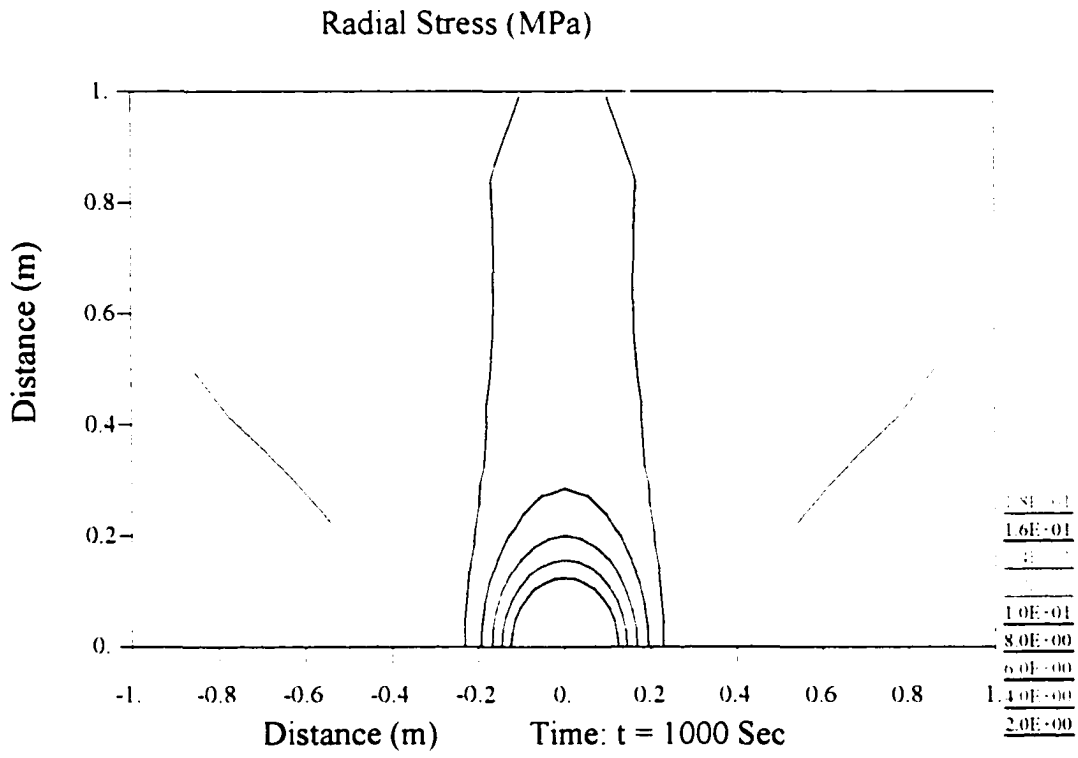


Figure 6.2.9 Radial stress distribution around the wellbore at t = 1000 s.

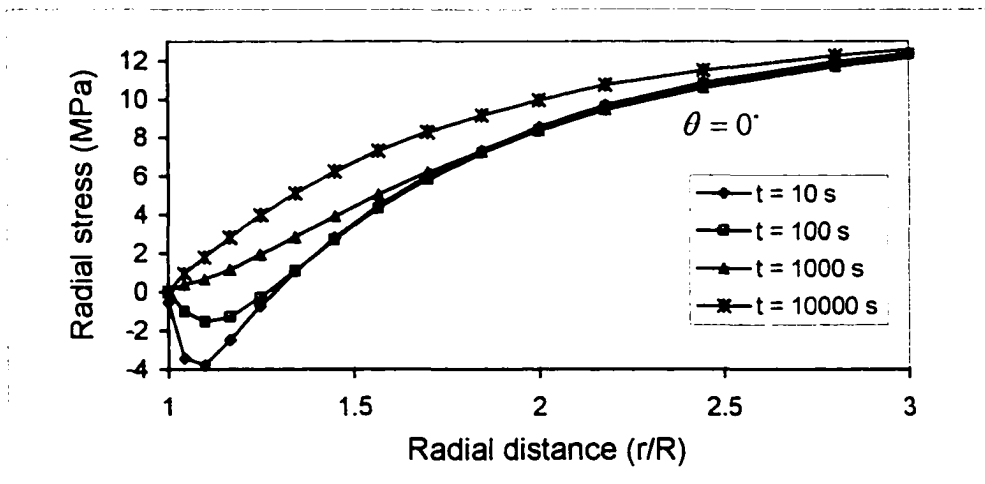


Figure 6.2.10 Effective radial stress in the maximum stress direction for different times.

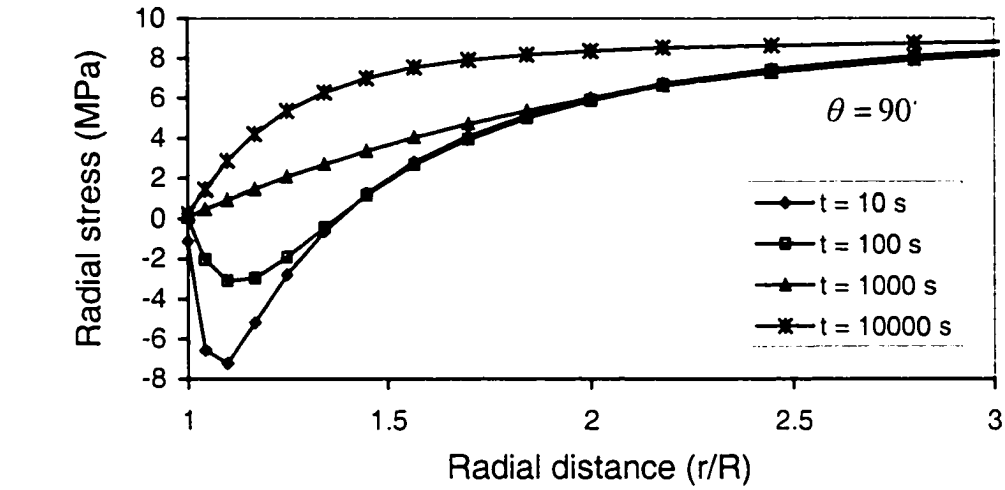


Figure 6.2.11 Effective radial stress in the minimum stress direction for different times.

Figures 6.2.12 to 6.2.14 show Terzaghi's compressive tangential stress contours around the wellbore for three different times. It is observed that a significant increase in stress concentration occurs in the minimum stress direction. In addition, as time increases, the tangential stress increases. Figure 6.2.15 plots the tangential stress as a function of the radial distance at different times for the two angles, $\theta = 0°$ and $\theta = 90°$. It is obvious that stress concentration is less pronounced in the maximum stress direction ($\theta = 0°$). Note also that the effective tangential stress does not have the non-monotonic distribution as for the effective radial stress as shown in Figures 6.2.10 and 6.2.11. This is due to the fact that the total tangential stress has a non-monotonic distribution (Figure 6.2.16) which has similar shape as the pore pressure (such as Figure 6.2.6). As a result, the effective tangential stress, which is the difference of the total tangential stress and pore pressure, has no monotonic distribution.

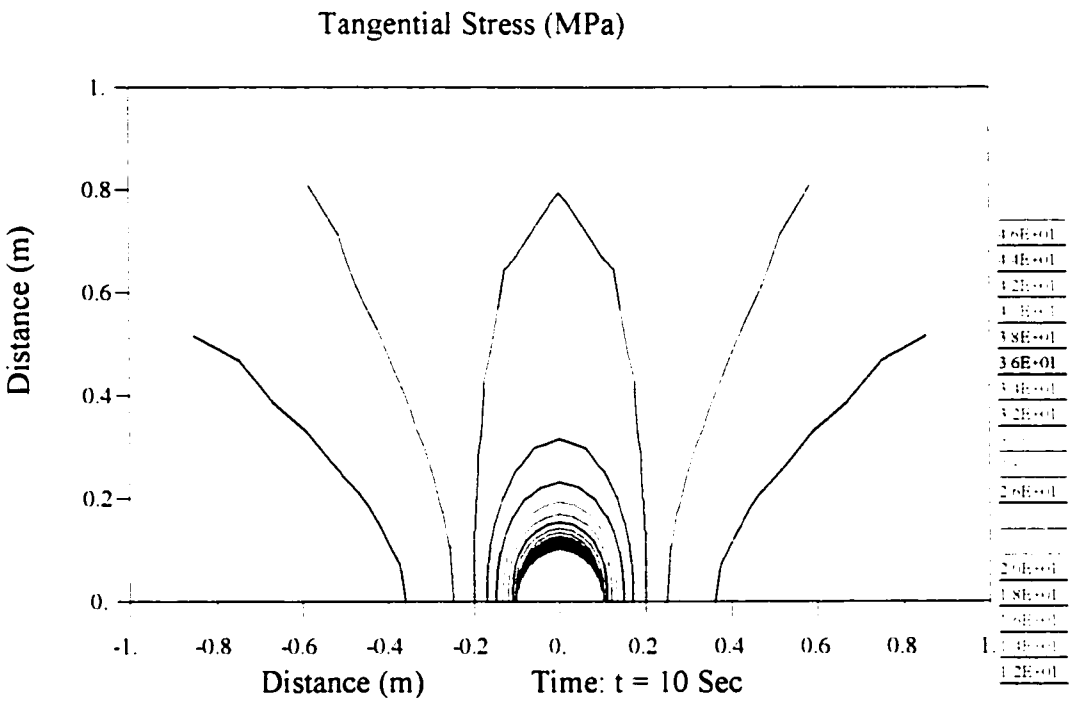


Figure 6.2.12 Tangential stress distribution around the wellbore at t = 10 s.

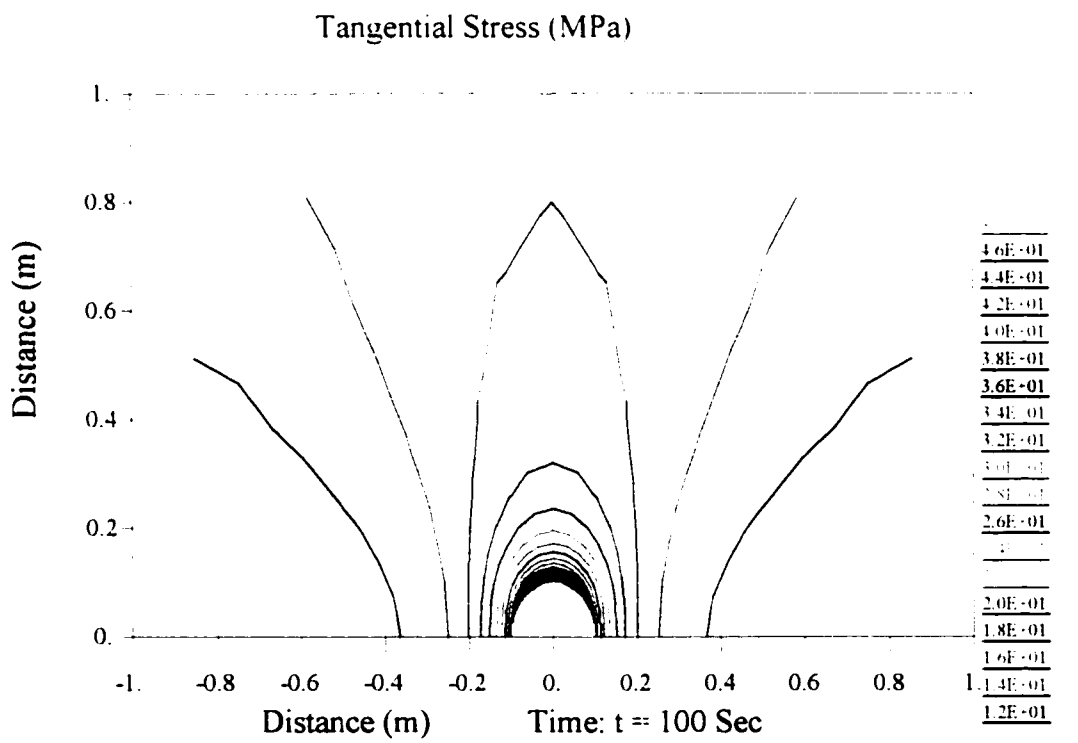


Figure 6.2.13 Tangential stress distribution around the wellbore at t = 100 s.

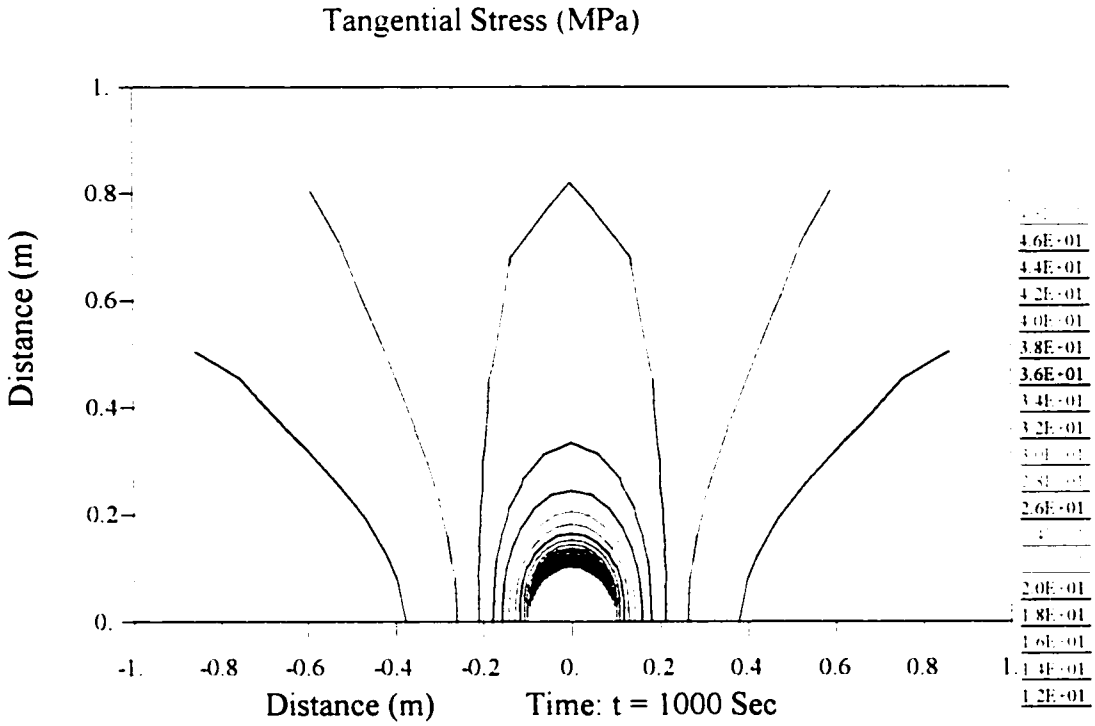


Figure 6.2.14 Tangential stress distribution around the wellbore at t = 1000 s.

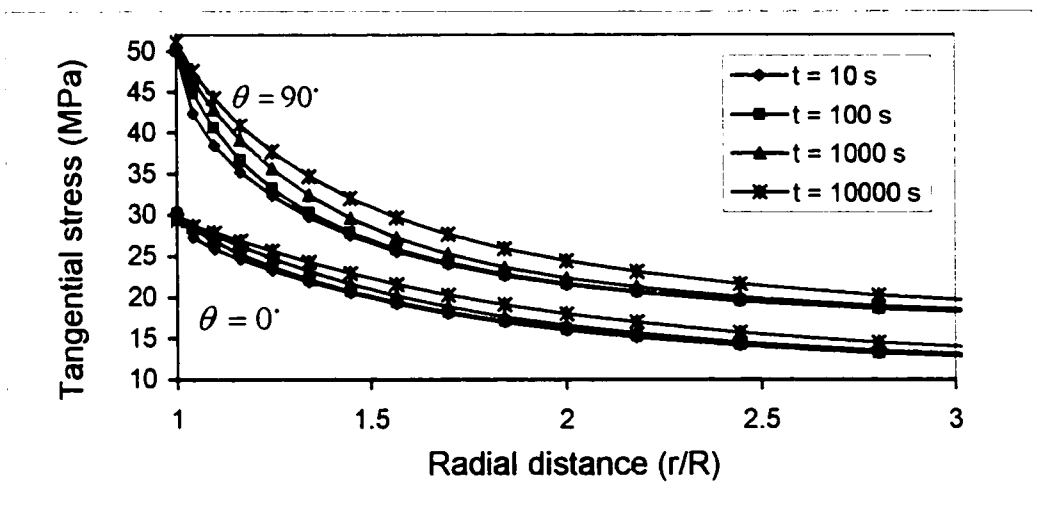


Figure 6.2.15 Effective tangential stress distribution, at $\theta = 0°$ and $\theta = 90°$, for different times.

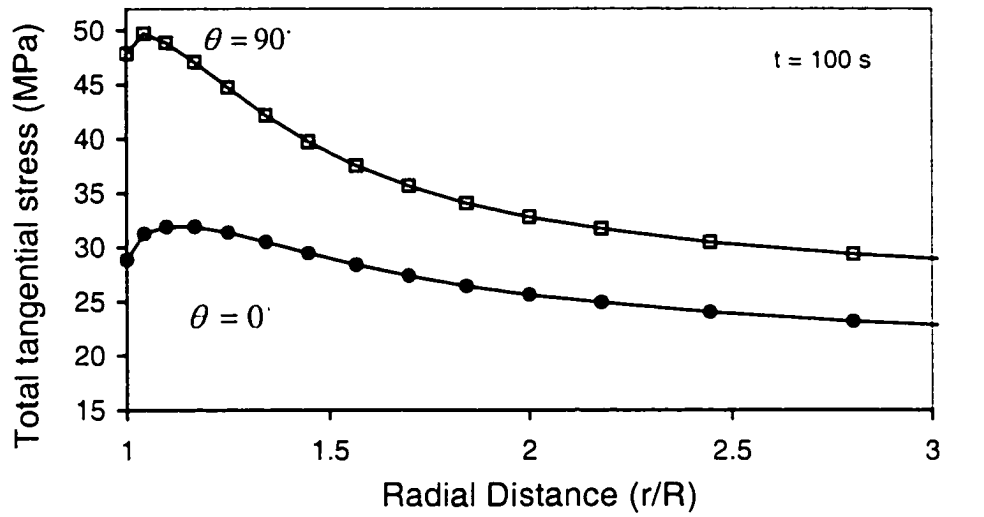


Figure 6.2.16 Total tangential stress distribution, at $\theta = 0°$ and $\theta = 90°$, for $t = 100$ s.

Figures 6.2.17 and 6.2.18 show Terzaghi's compressive axial stress as a function of the radial distance and time for $\theta = 0°$ and $\theta = 90°$. It can be seen that the axial stresses at the wellbore exhibit an increase in stress level. The stress concentration at the wellbore is less pronounced in the maximum stress direction ($\theta = 0°$) than that in the minimum stress direction ($\theta = 90°$). At small times a minimum value is found at a small distance inside the borehole wall. At large distances, the effective axial stress approaches asymptotically the local far-field value of 18.5 MPa (28.5 MPa for total stress, refer to Figure 6.1), as expected. These figures also show that the axial stresses increase and non-monotonic stress distributions disappear as time increases.

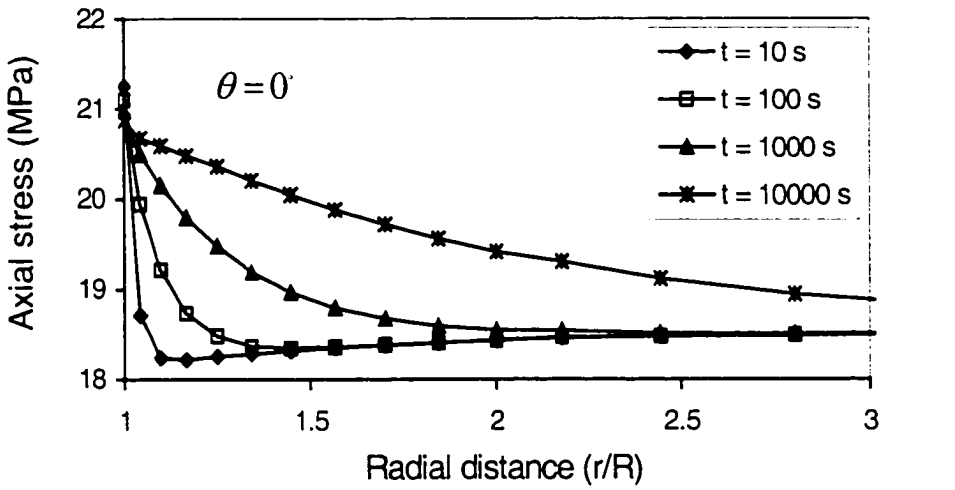


Figure 6.2.17 Effective axial stress distribution in the maximum stress direction for different times.

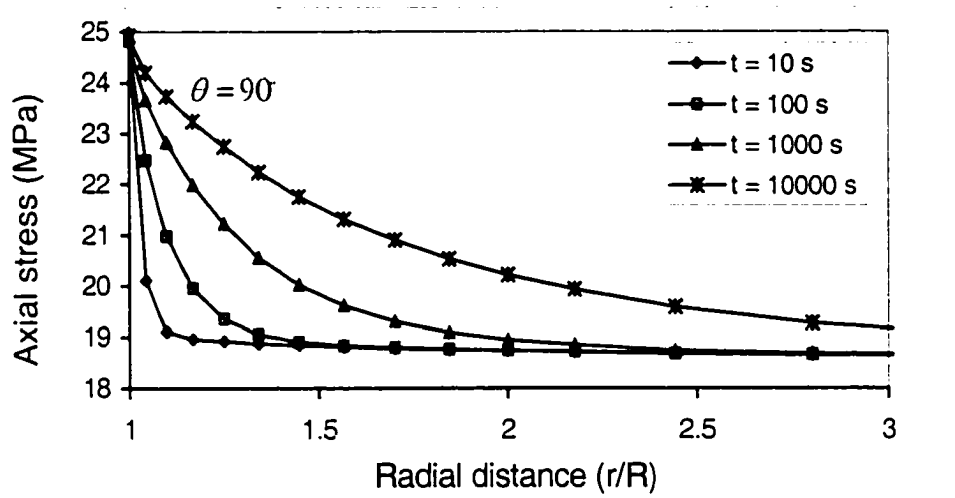


Figure 6.2.18 Effective axial stress distribution in the minimum stress direction for different times.

6.3 Fracture Spacing Effects

Figures 6.3.1 and 6.3.2 show the effect of fracture spacing on the pore pressure distributions. Fracture spacing represents fracture density: the smaller fracture spacing representing denser fractures, causes pore pressure increases and more pronounced non-monotonic pressure distributions. The reason is that smaller fracture spacing results in smaller fracture elastic modulus ($K_n s$), which causes larger fracture deformations. As fracture spacing increase gradually the pore pressure decreases, as shown in Figures 6.3.3 and 6.3.4. When the fracture spacing is sufficiently large (such as s = 100 m), the spacing variation has no further influence on the pore pressure. In this case, the formation is approaching a single-porosity medium (intact porous rock); hence, the dual-porosity solution is close to the single-porosity solution.

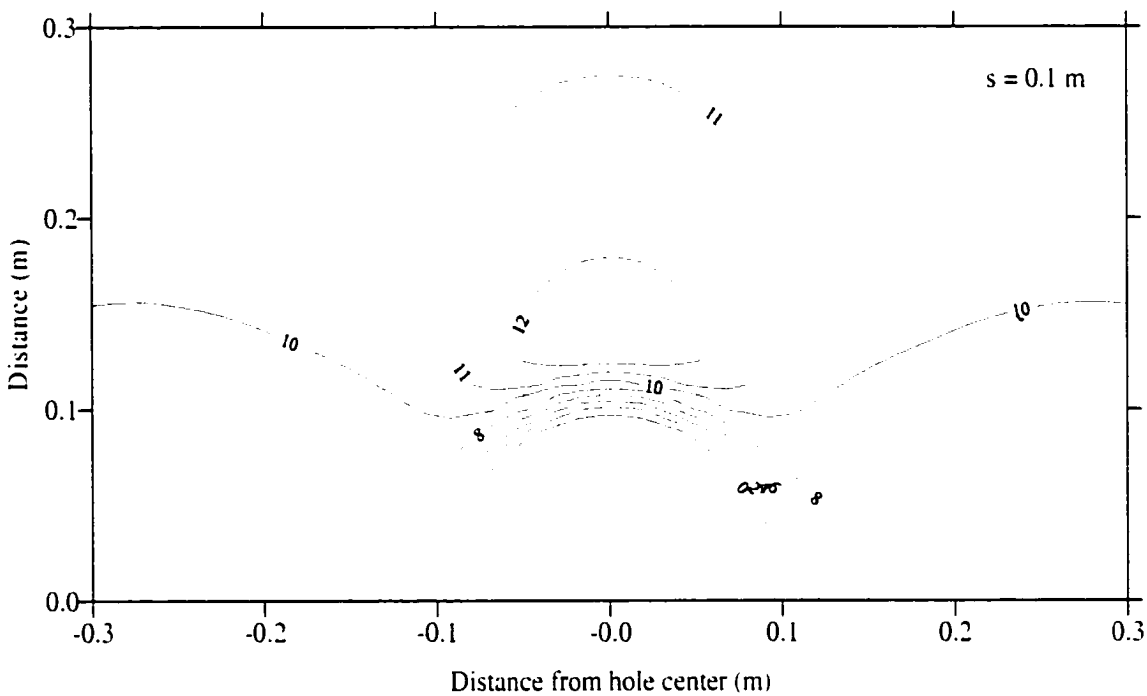


Figure 6.3.1 Pore pressure distribution around the wellbore at t = 100 s, s = 0.1 m.

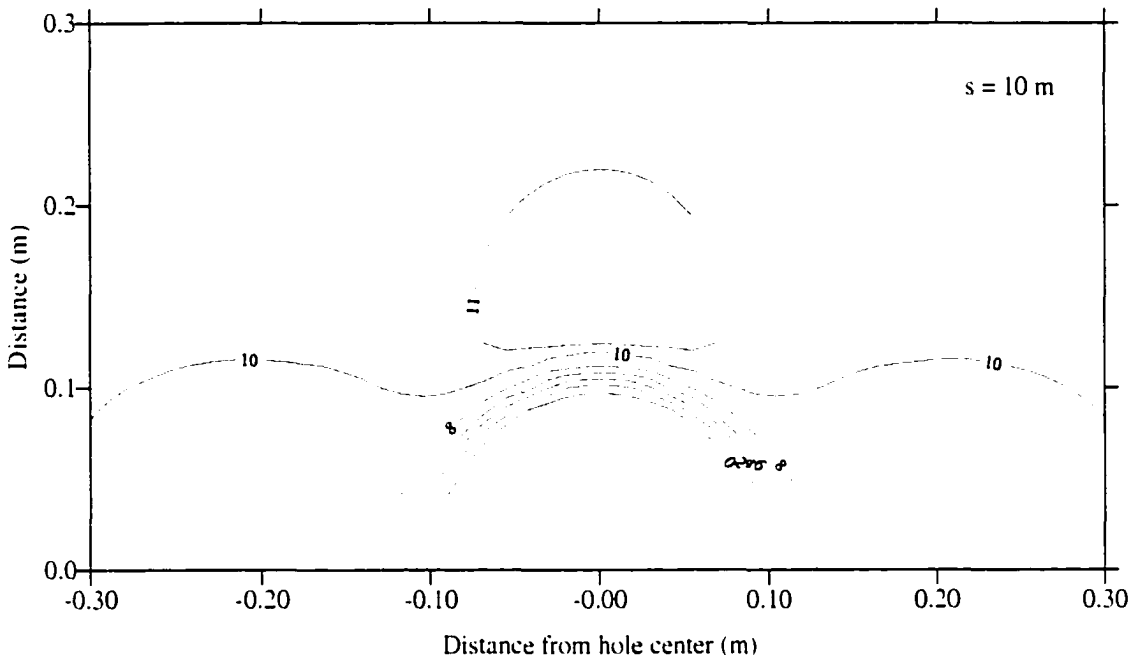


Figure 6.3.2 Pore pressure distribution around the wellbore at t = 100 s, s = 10 m.

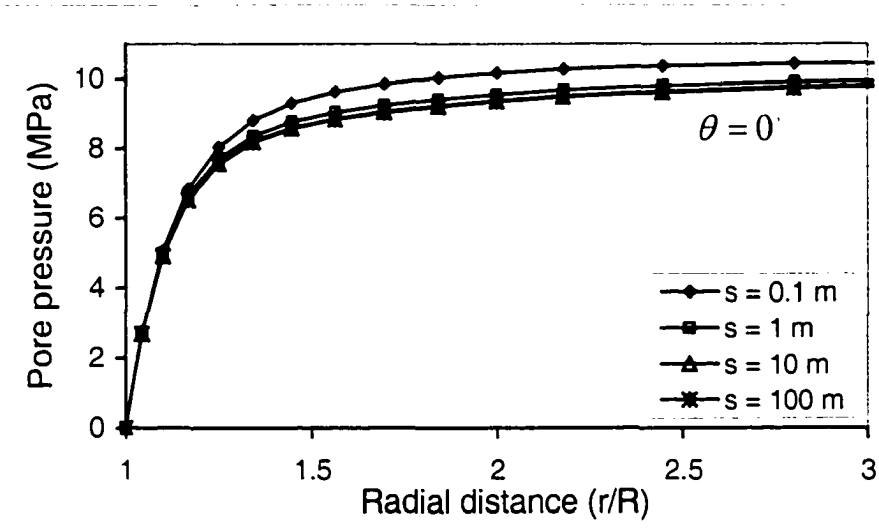


Figure 6.3.3 Pore pressure around wellbore in maximum stress direction at t = 100 s for different fracture spacings.

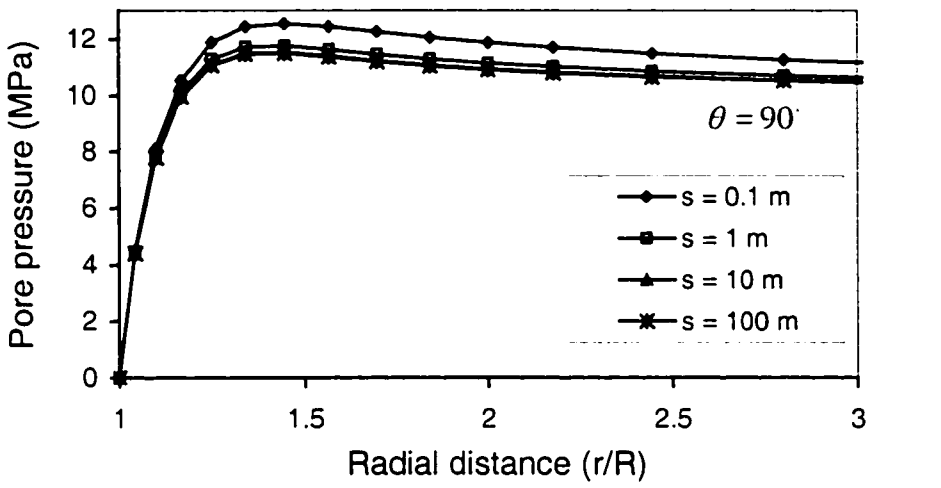


Figure 6.3.4 Pore pressure around wellbore in minimum stress direction at t = 100 s for different fracture spacings.

Figures 6.3.5 and 6.3.6 are effective radial stress contours at t = 100 s for fracture spacing of s = 0.1 m and s = 10 m. It can be observed that a larger fracture spacing causes a smaller tensile stress area. The tensile stress magnitude and area are bigger in the minimum stress direction. Figures 6.3.7 and 6.3.8 show the radial stress responses along the minimum and maximum stress directions. It is seen that the effective compressive radial stress increases and the tensile stress decreases as fracture spacing decreases. This is due to the larger fracture compliance ($1/K_n s$) inducing larger total radial stress, as discussed in section 6.1. It can be concluded that tensile failure is rather difficult to achieve for highly fractured porous media, particularly in the maximum stress direction.

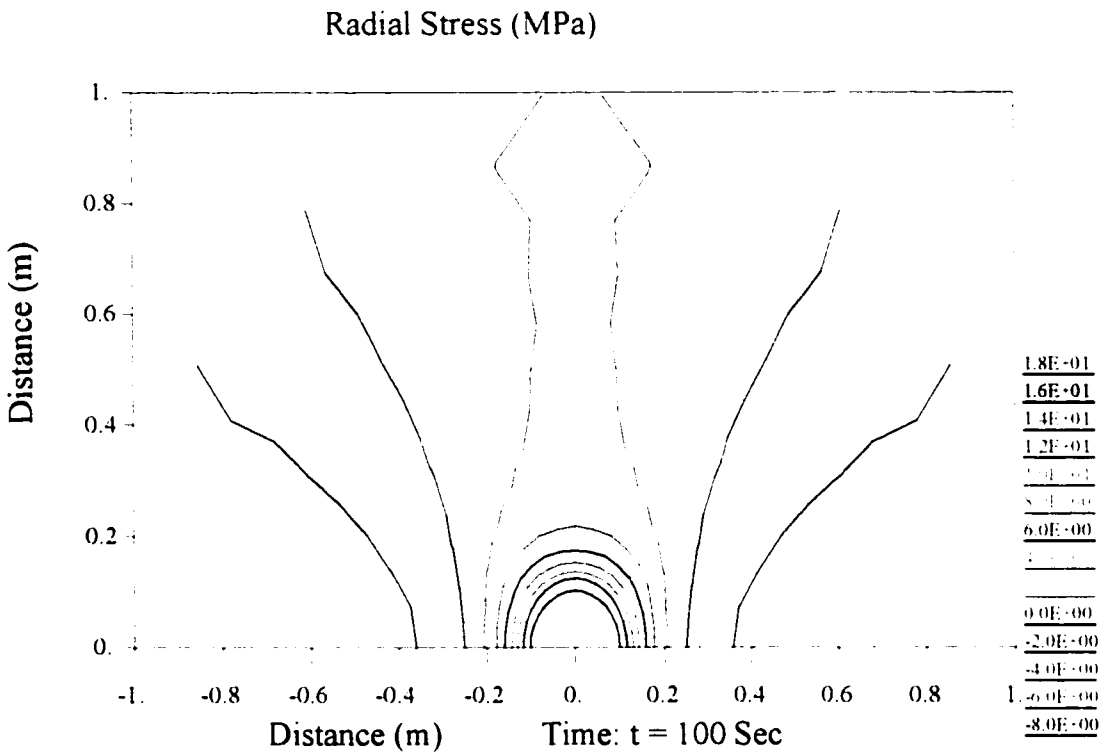


Figure 6.3.5 Radial stress distribution around the wellbore at t = 100 s, s = 0.1 m.

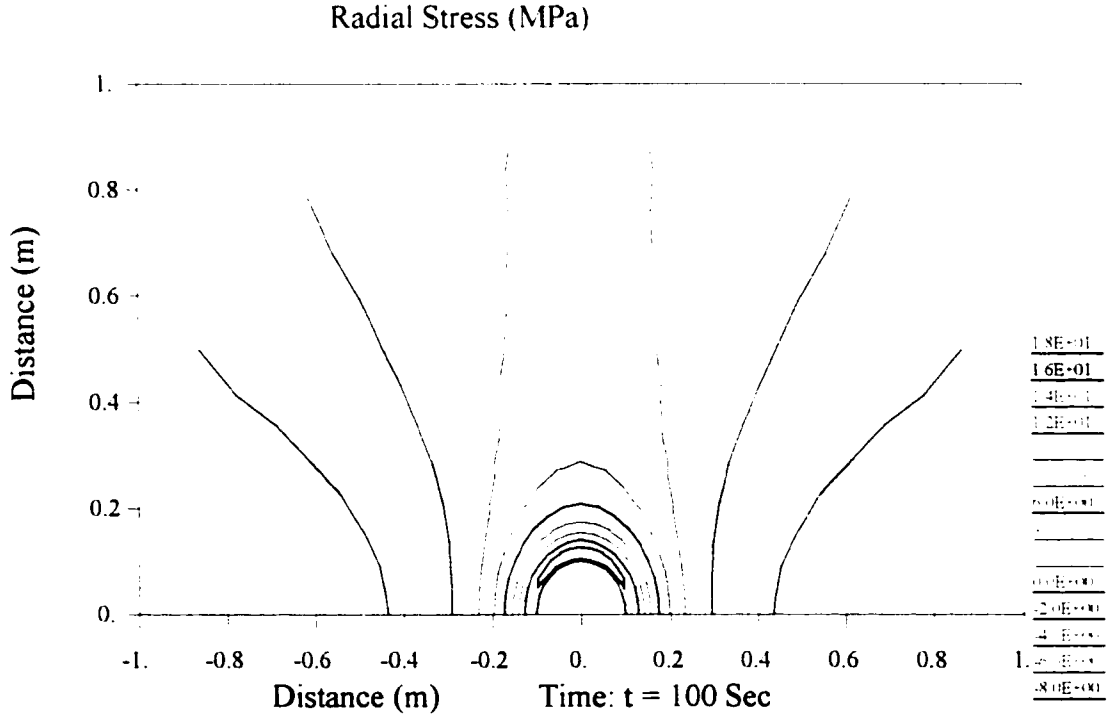


Figure 6.3.6 Radial stress distribution around the wellbore at t = 100 s, s = 10 m.

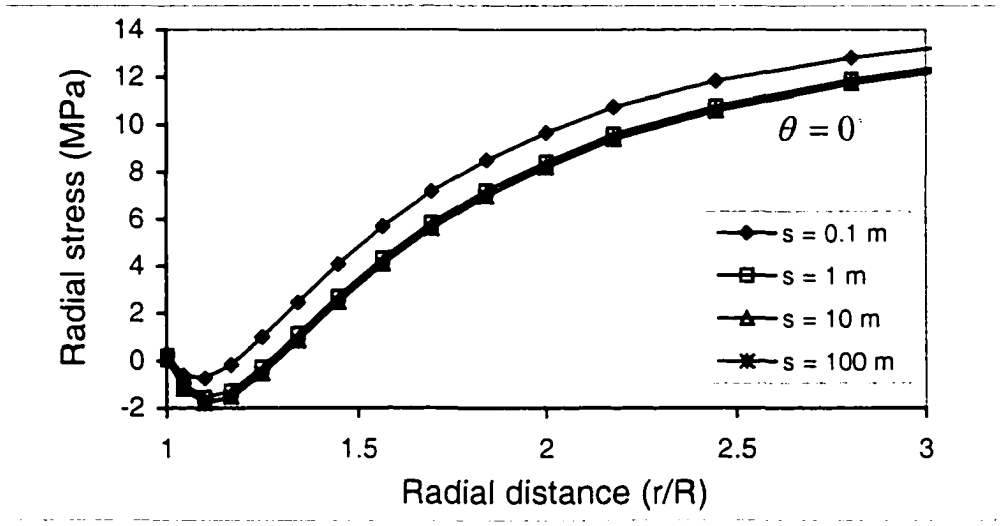


Figure 6.3.7 Radial stress around wellbore in the minimum stress direction at t = 100 s for different fracture spacings.

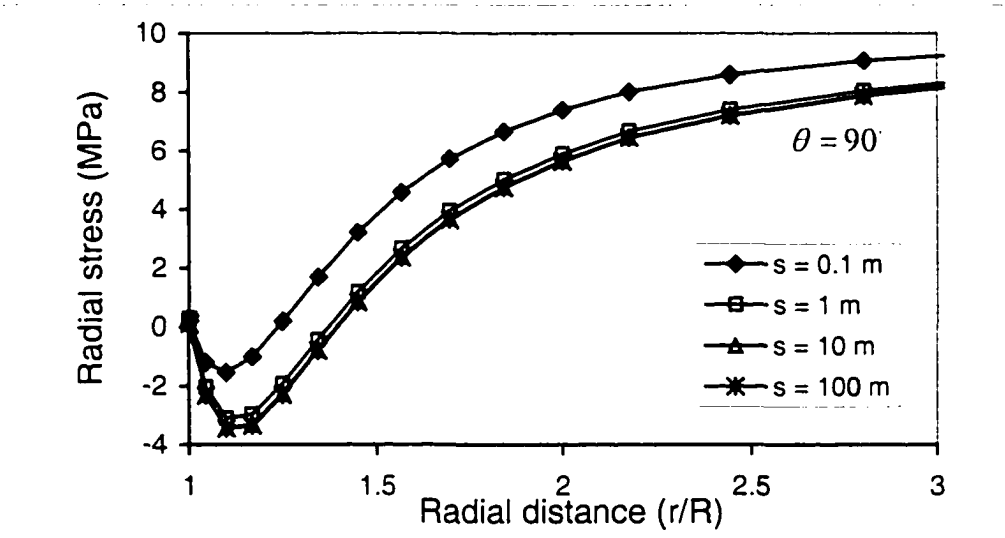


Figure 6.3.8 Radial stress around wellbore in the maximum stress direction at t = 100 s for different fracture spacings.

Figures 6.3.9 and 6.3.10 are the tangential stress contours at t = 100 s for fracture spacing of s = 0.1 m and s = 10 m. Observe that the maximum stress concentration occurs in the minimum stress direction. It can be seen from Figures 6.3.11 and 6.3.12 that the effective tangential and axial stresses increase as fracture spacing decreases. These are induced by the large fracture compliance, in which the fractures are considered as deformable.

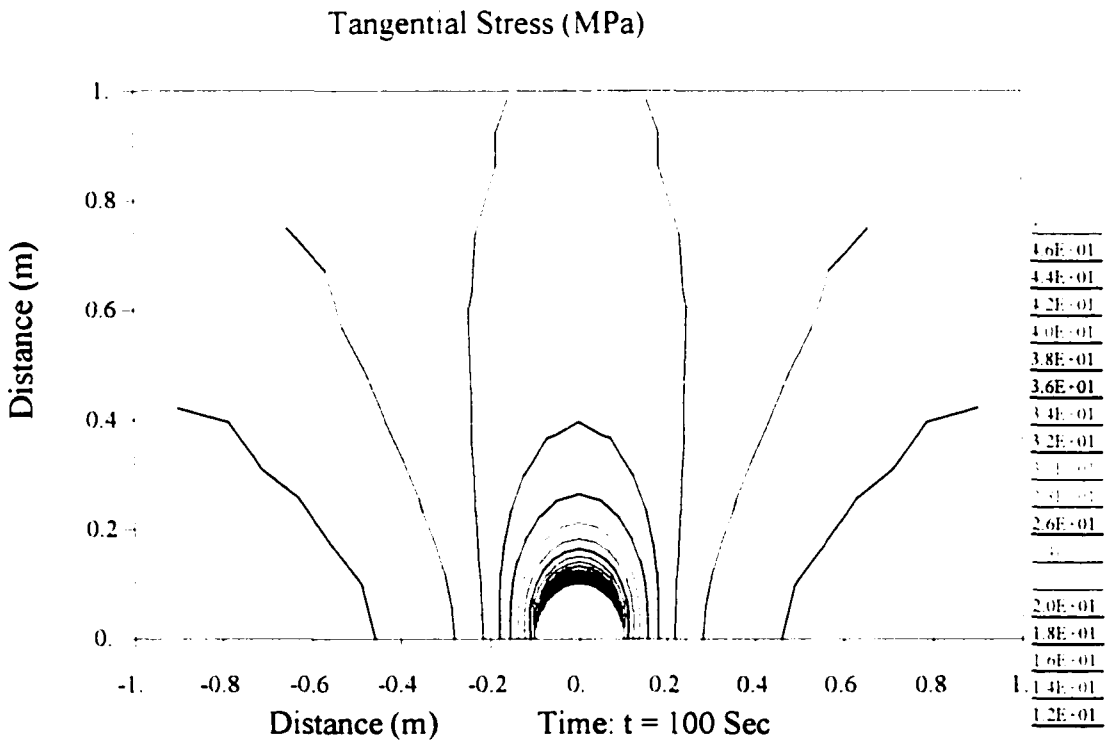


Figure 6.3.9 Tangential stress distribution around the wellbore at t = 100 s, s = 0.1 m.

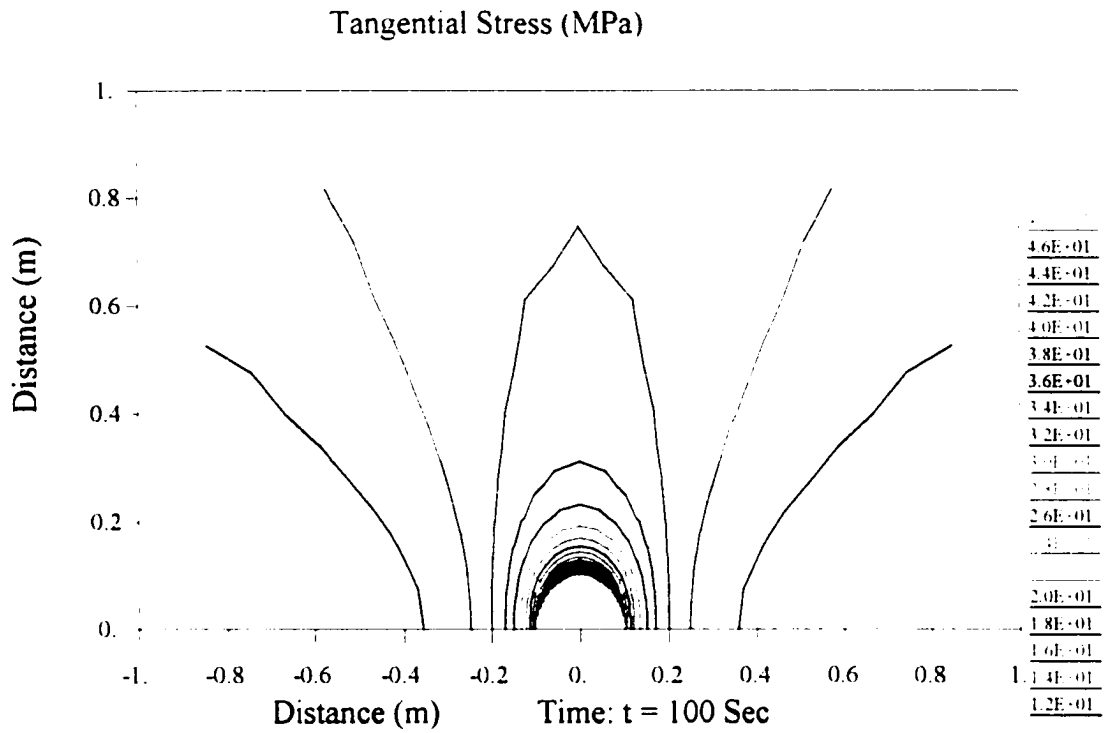


Figure 6.3.10 Tangential stress distribution around the wellbore at t = 100 s, s = 10 m.

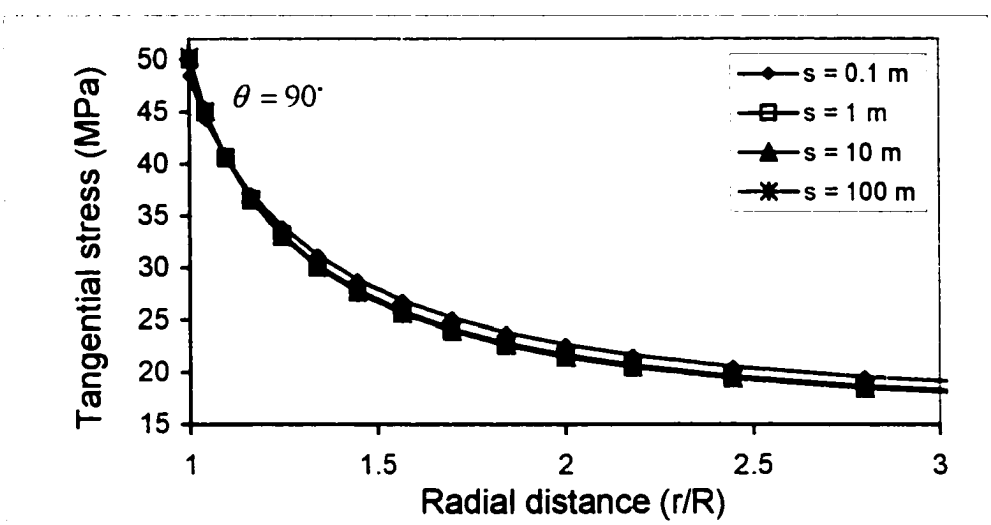


Figure 6.3.11 Effective tangential around wellbore in the minimum stress direction at t = 100 s for different fracture spacings.

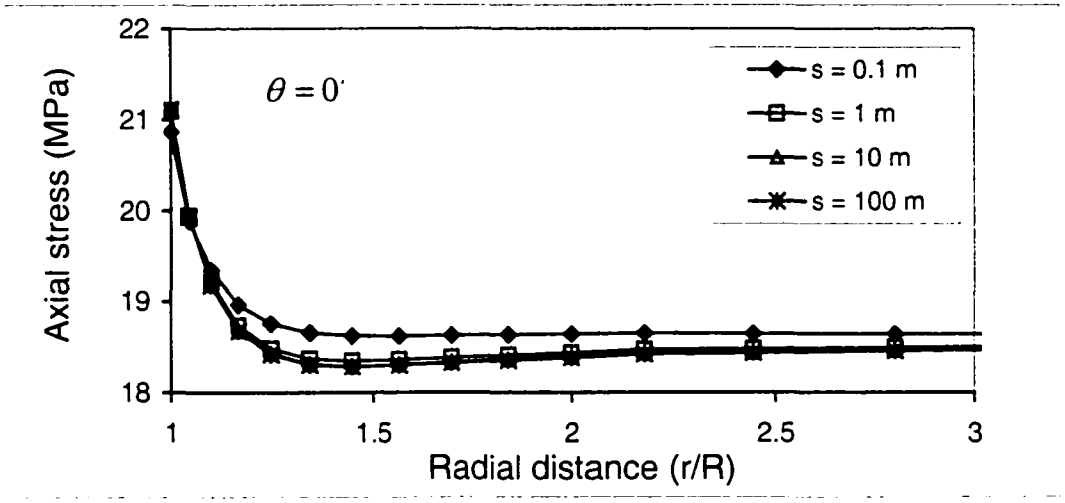


Figure 6.3.12 Effective axial stress around wellbore in the maximum stress direction at t = 100 s for different fracture spacings.

6.4 Fracture Stiffness Effects

In this section, the fracture normal stiffness effects on the dual-porosity model are examined. Figures 6.4.1 and 6.4.2 are pore pressure contours for two different fracture stiffnesses, K_n = 4.821 and 48.21 GPa, at t = 100 s. It can be seen that the pore pressure magnitude is much larger for smaller fracture stiffnesses. Figures 6.4.3 to 6.4.4 are pore pressure responses for different fracture stiffnesses along the maximum (θ = 0°) and minimum stress directions (θ = 90°). It is obvious that the pore pressure in each azimuthal direction increases as the fracture stiffness becomes increasingly smaller, which is associated larger fracture compliance ($1/K_n s$). When the stiffness is large enough, representing nearly no deformation in the fractures, the pore pressure no longer varies with fracture stiffness.

Figures 6.4.5 and 6.4.6 are the effective radial stress contours for K_n = 4.821 and 48.21 GPa, at t = 100 s. It can be observed that there is no tensile stress for smaller fracture stiffnesses. The reason is that a larger fracture compliance exists for small fracture

stiffness, which causes larger total stress, as discussed in section 6.1.1. The comparisons for effective radial stress along different radial directions indicate that the compressive stress increases while tensile stress reduces as the stiffness decreases, as shown in Figures 6.4.7 and 6.4.8. The radial tensile stress is insignificant when the fracture stiffness is very small. Figures 6.4.9 and 6.4.10 show that the tangential stress increases as fracture stiffness decreases.

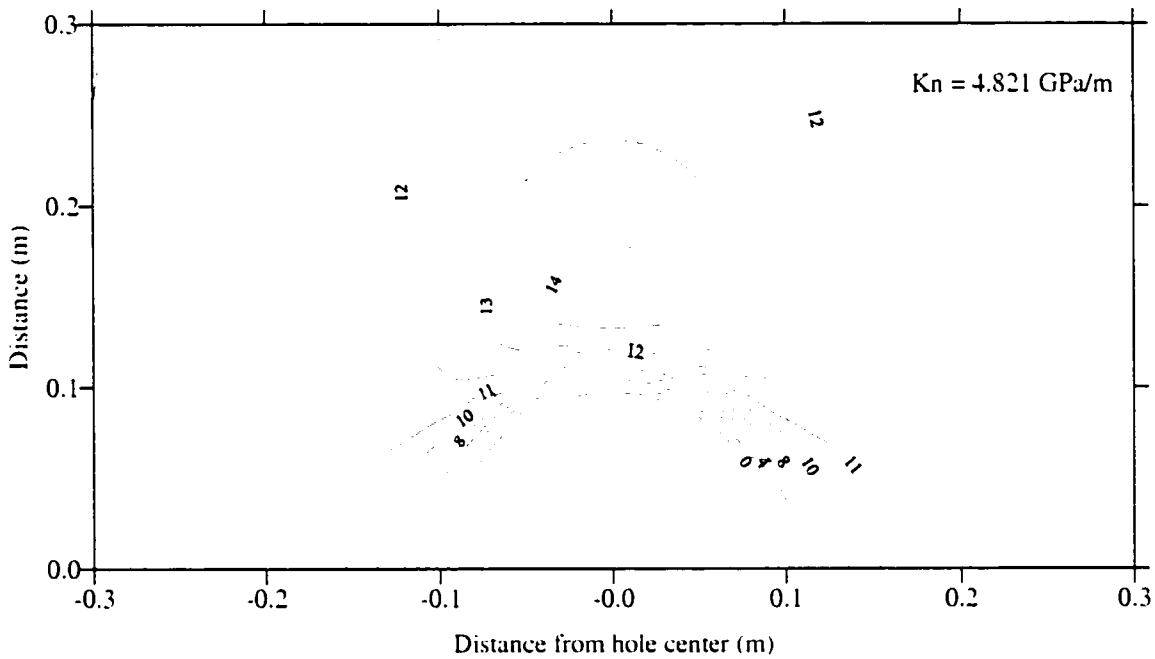


Figure 6.4.1 Radial stress distribution around the wellbore at t = 100 s and for K_n = 4.821GPa/m.

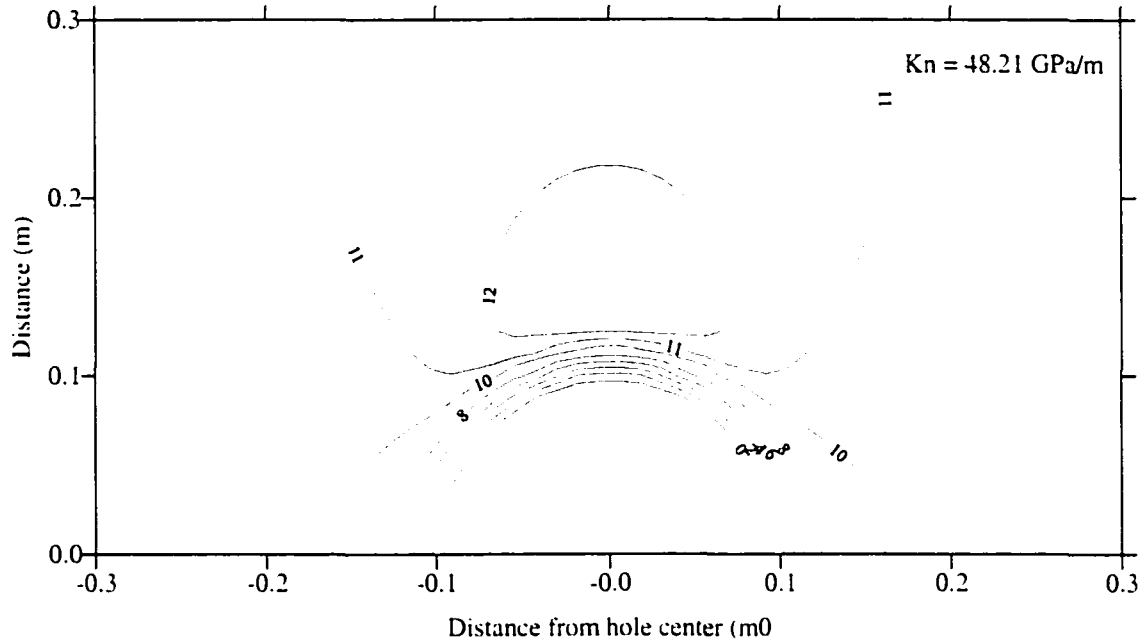


Figure 6.4.2 Radial stress distribution around the wellbore at t = 100 s and for K_n = 48.21GPa/m.

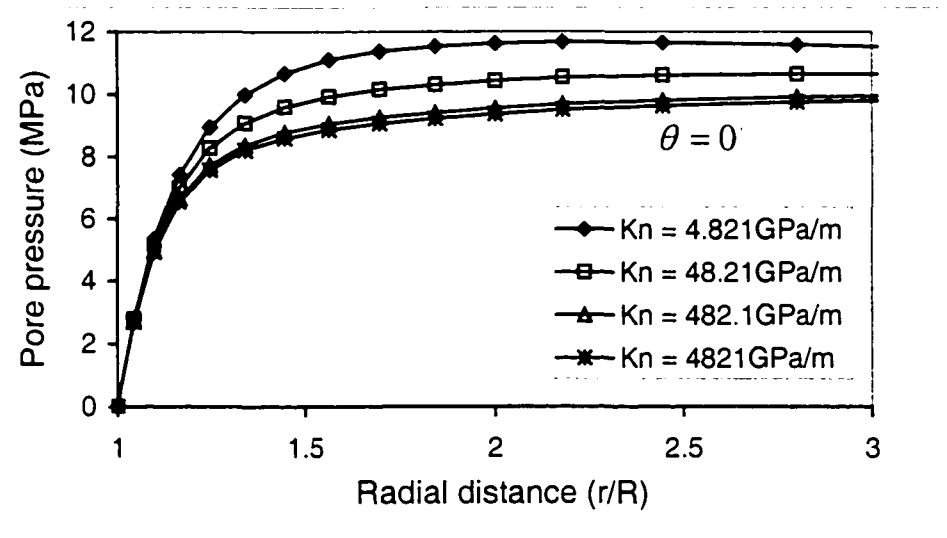


Figure 6.4.3 Pore pressure around wellbore in the maximum stress direction at t = 100 s for different fracture stiffnesses.

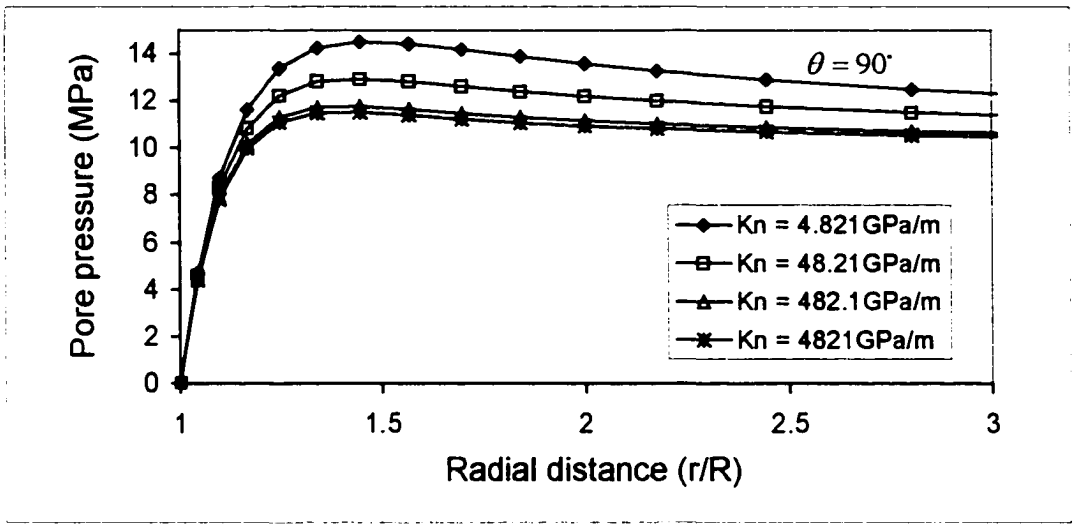


Figure 6.4.4 Pore pressure around wellbore in the minimum stress direction at t = 100 s for different fracture stiffnesses.

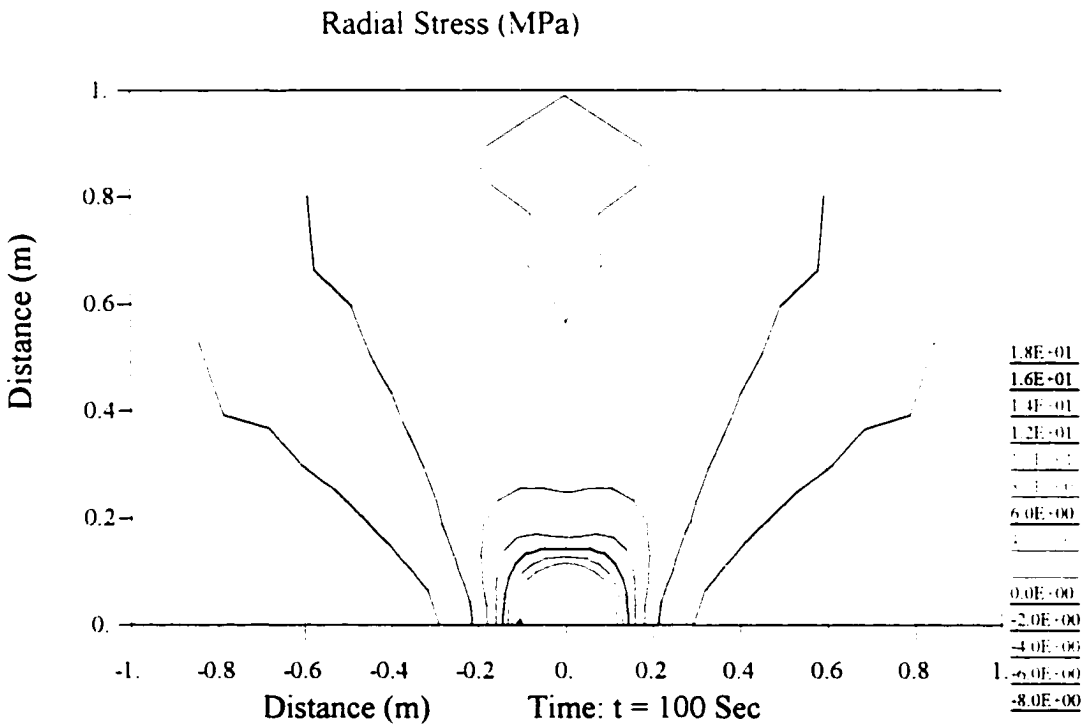


Figure 6.4.5 Radial stress distribution around the wellbore for K_n = 4.821GPa/m.

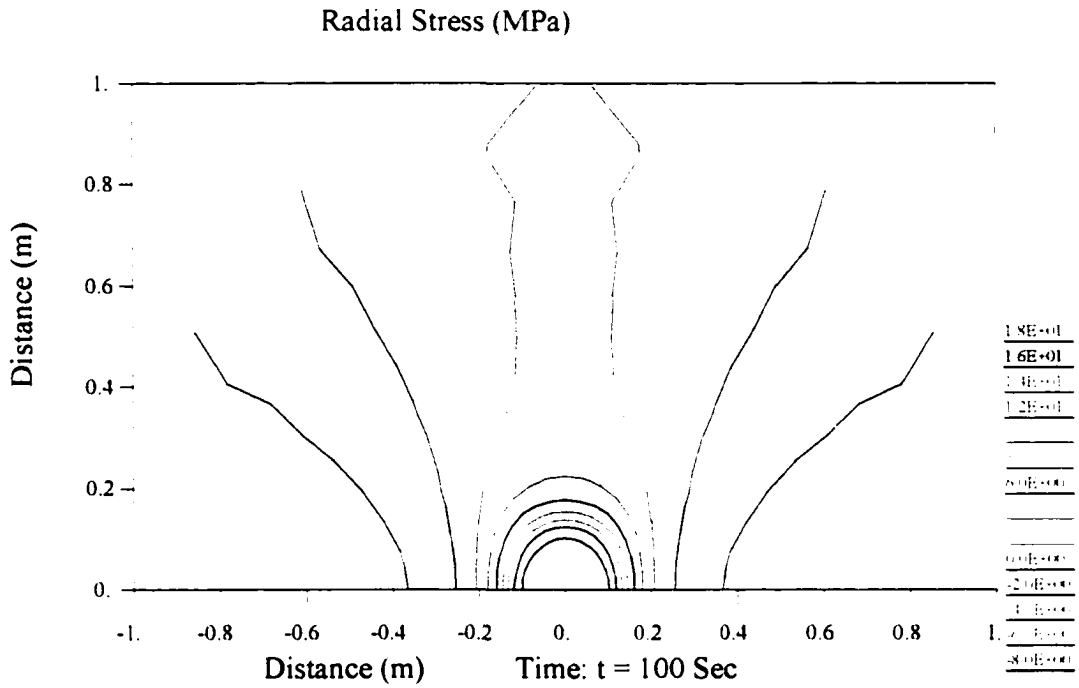


Figure 6.4.6 Radial stress distribution around the wellbore for K_n = 48.21GPa/m.

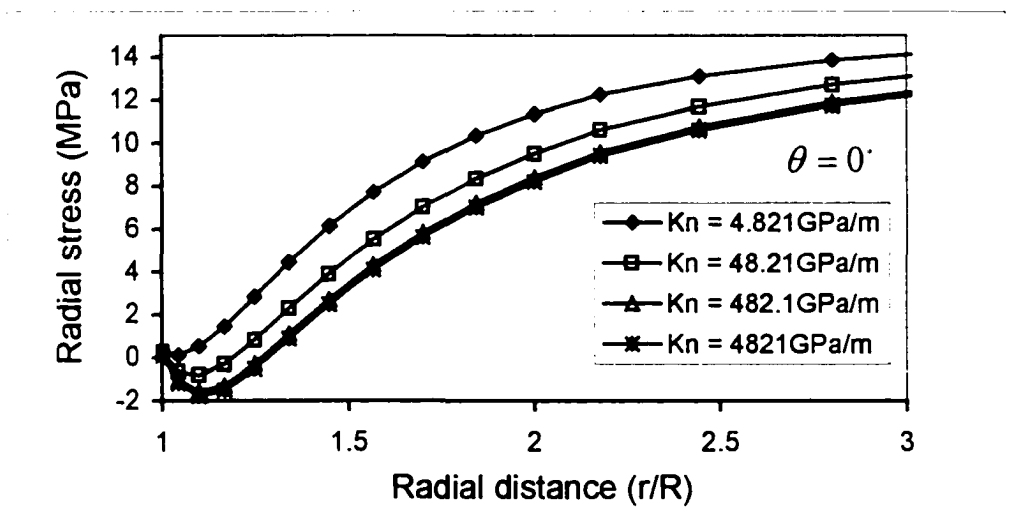


Figure 6.4.7 Radial stress around wellbore in the maximum stress direction at t = 100 s for different fracture stiffnesses.

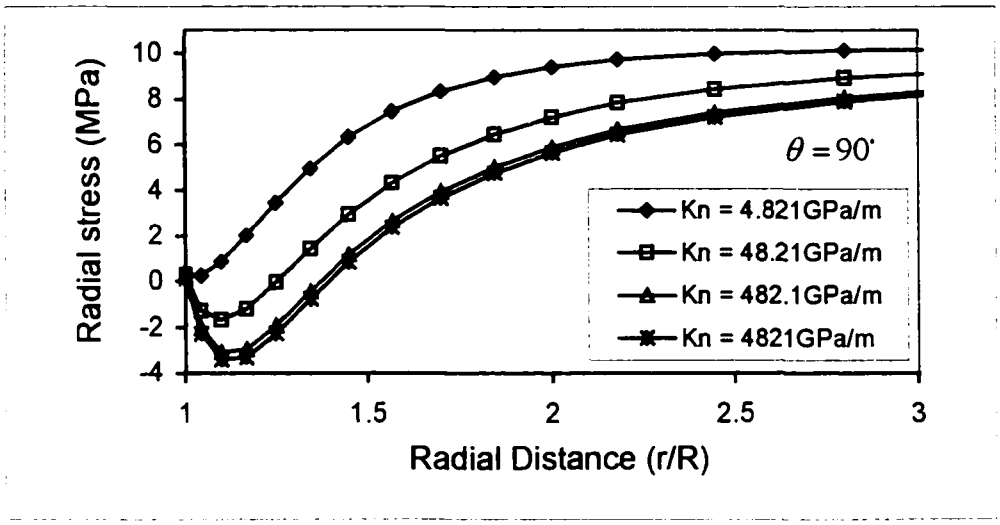


Figure 6.4.8 Radial stress around wellbore in the minimum stress direction at t = 100 s for different fracture stiffnesses.

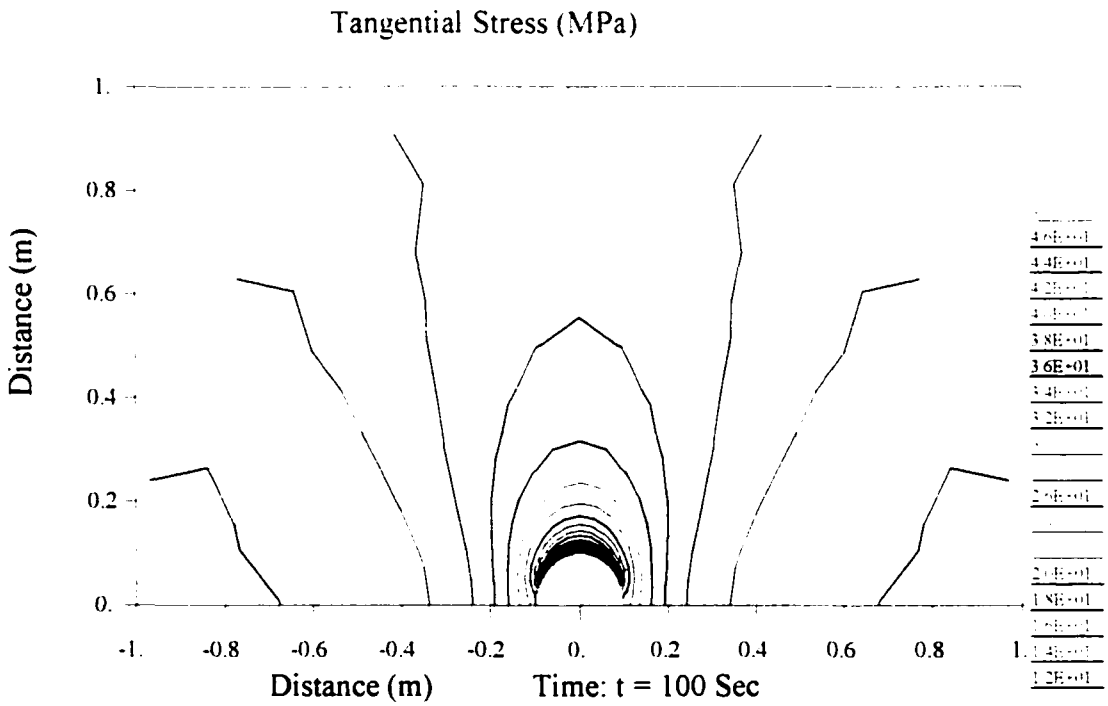


Figure 6.4.9 Tangential stress distribution around the wellbore for K_n = 4.821GPa/m.

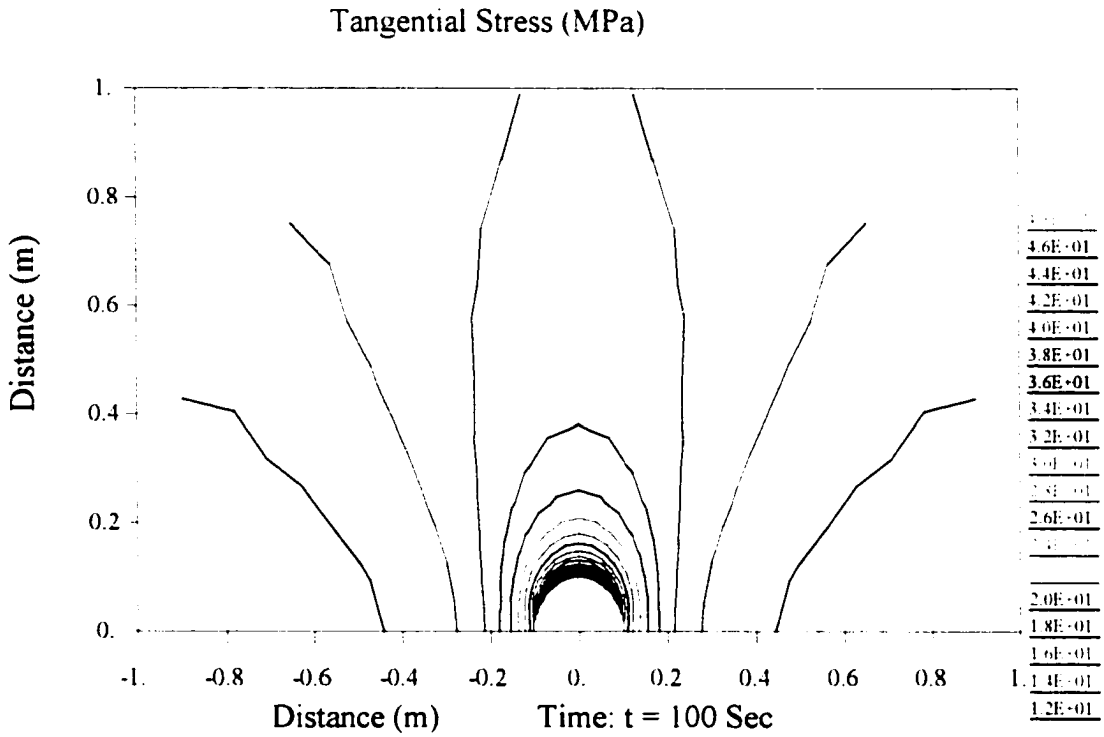


Figure 6.4.10 Tangential stress distribution around the wellbore for K_n = 4.821GPa/m.

6.5 Matrix and Fracture Permeability Effects

The influence of matrix and fracture permeability variations on the dual-porosity model are demonstrated for three cases, $k_{ma}/\ k_{fr}$ = 1, 0.1 and 0.01 in this section. Figures 6.5.1 and 6.5.2 are pore pressure responses along the maximum and minimum stress directions at t = 100 s. It can be observed that the decreasing matrix and fracture permeability ratio causes a higher pore pressure magnitude. When the permeability ratio is large enough, such as $k_{ma}/\ k_{fr}$ = 1 in Figure 6.5.1, there is no non-monotonic pore pressure distribution, or poroelastic effect. The pore pressure contours in Figures 6.5.3 and 6.5.4 show this

phenomenon clearly. A smaller matrix and fracture permeability ratio means that the matrix has a relatively smaller permeability, which induces more poroelastic effects (Cheng et al., 1993). The reason is obvious, for larger matrix permeability faster fluid flow occurs and the pore pressure concentration is less pronounced.

As a consequence, there is no tensile radial stress for the larger permeability ratios (refer to Figures 6.5.5 and 6.5.6). In addition, effective radial stress increases in the near field as the permeability ratio increases, as shown in Figures 6.5.7 and 6.5.8.

Figures 6.5.9 and 6.5.10 show the effect of the matrix and fracture permeability ratio on the effective tangential and axial stresses. The increasing permeability ratio causes increases in the tangential and axial stresses.

The reason that the stresses increase as the permeability ratio increases can easily be explained from the dual-porosity governing equations (Equations 3.3.8 to 3.3.10). It can be seen from these equations that any increase in matrix permeability (i.e., the permeability ratio increases when fracture permeability is constant) causes solid deformation to increase, which induces an increase in the total stress.

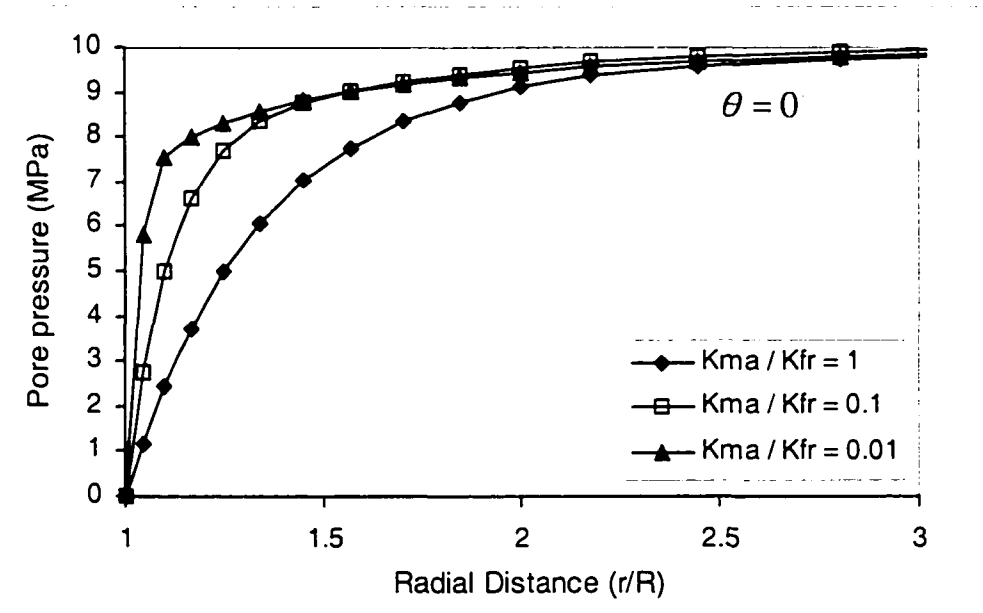


Figure 6.5.1 Pore pressure around wellbore in the maximum stress direction at t = 100 s for different permeability ratios.

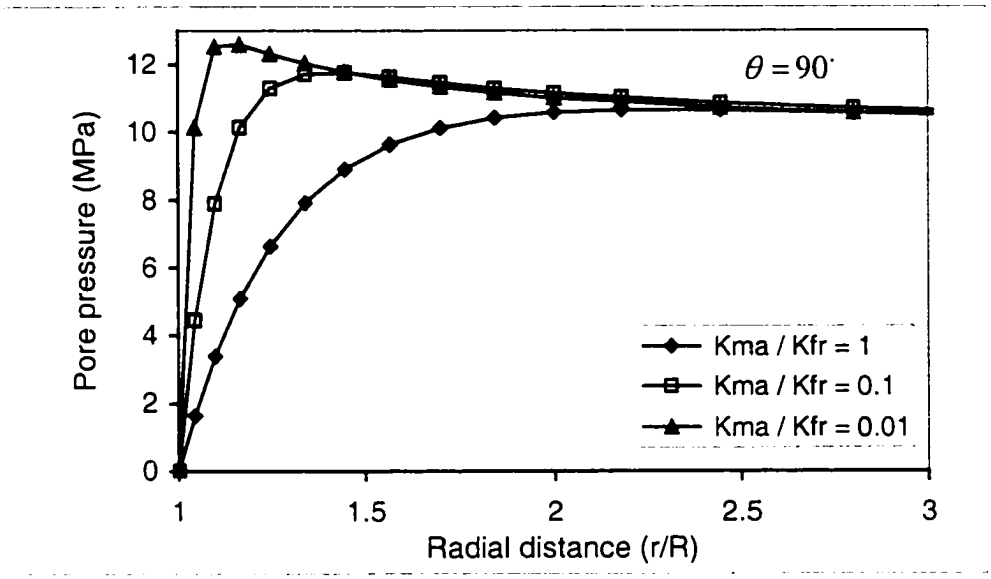


Figure 6.5.2 Pore pressure around wellbore in the minimum stress direction at t = 100 s for different permeability ratios.

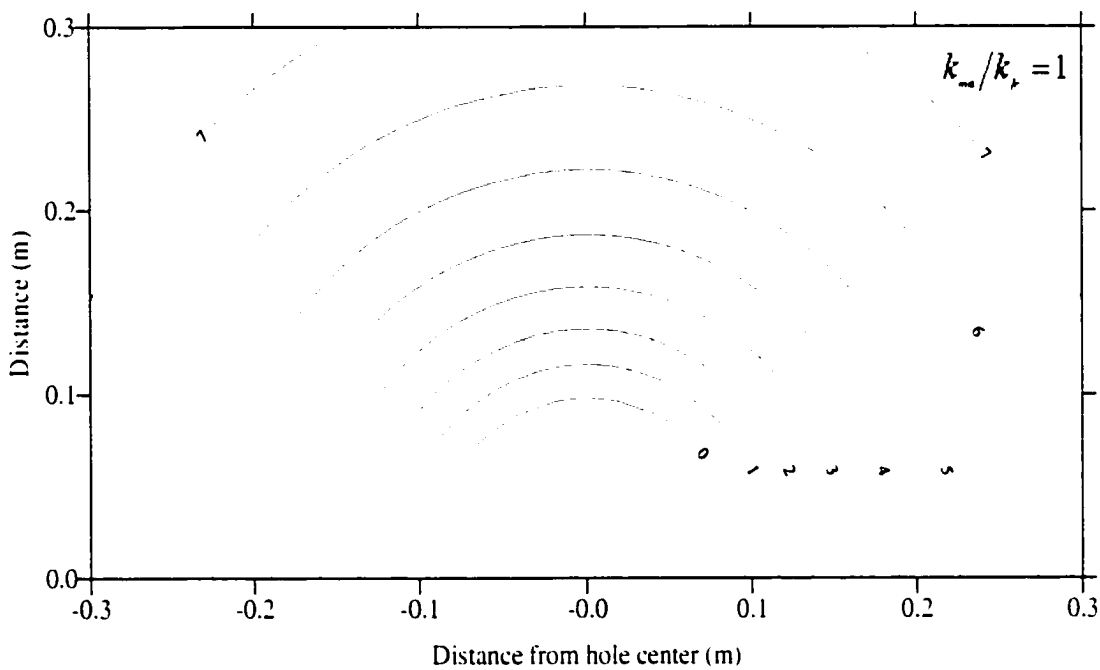


Figure 6.5.3 Pore pressure distribution at t = 100 s for a permeability ratio of k_{ma}/k_{fr} = 1.

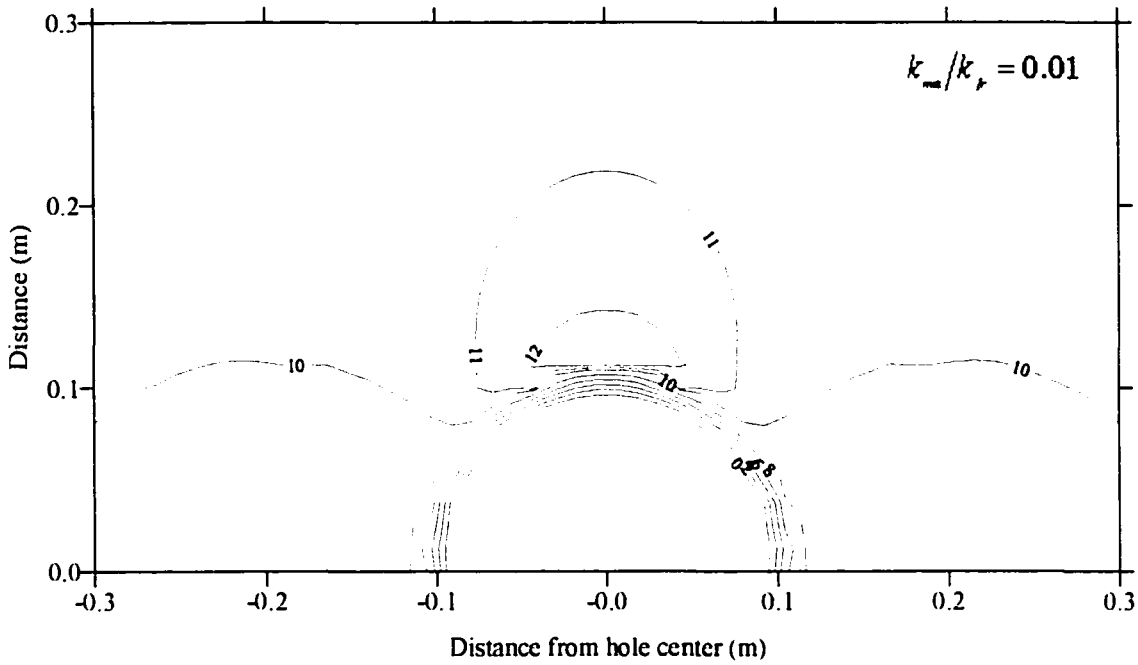


Figure 6.5.4 Pore pressure distribution at t = 100 s for a permeability ratio of k_{ma}/k_{fr} = 0.01.

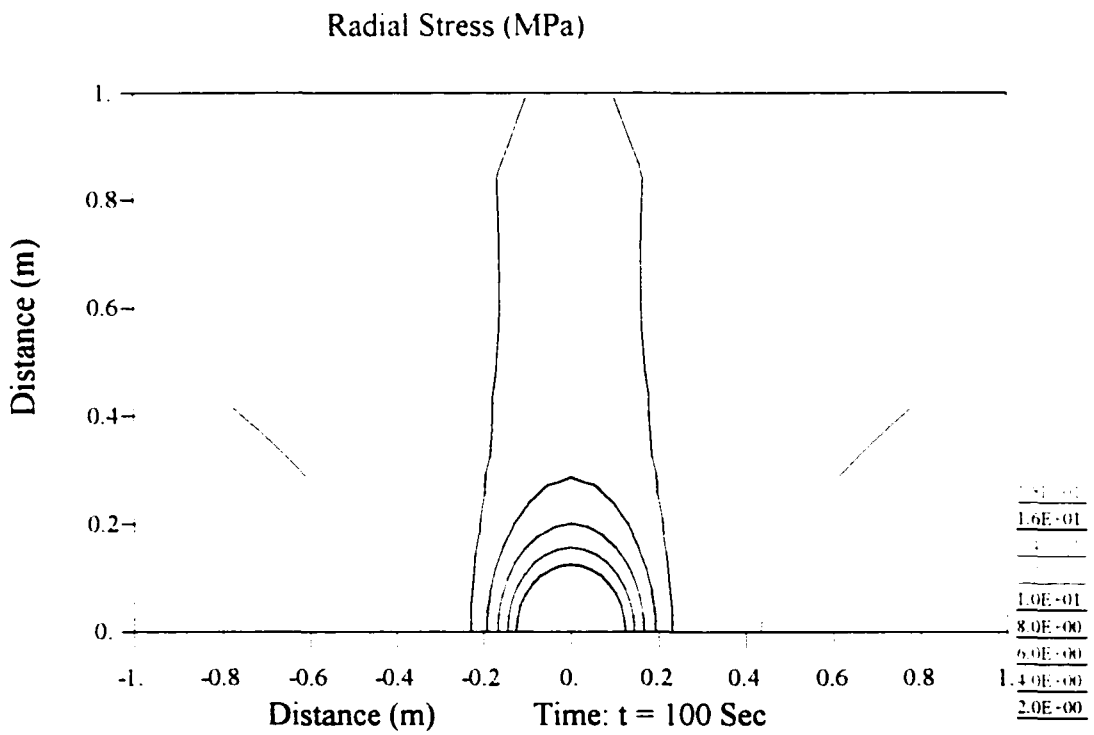


Figure 6.5.5 Radial stress distribution at t = 100 s for a permeability ratio of k_{ma}/k_{fr} = 1.

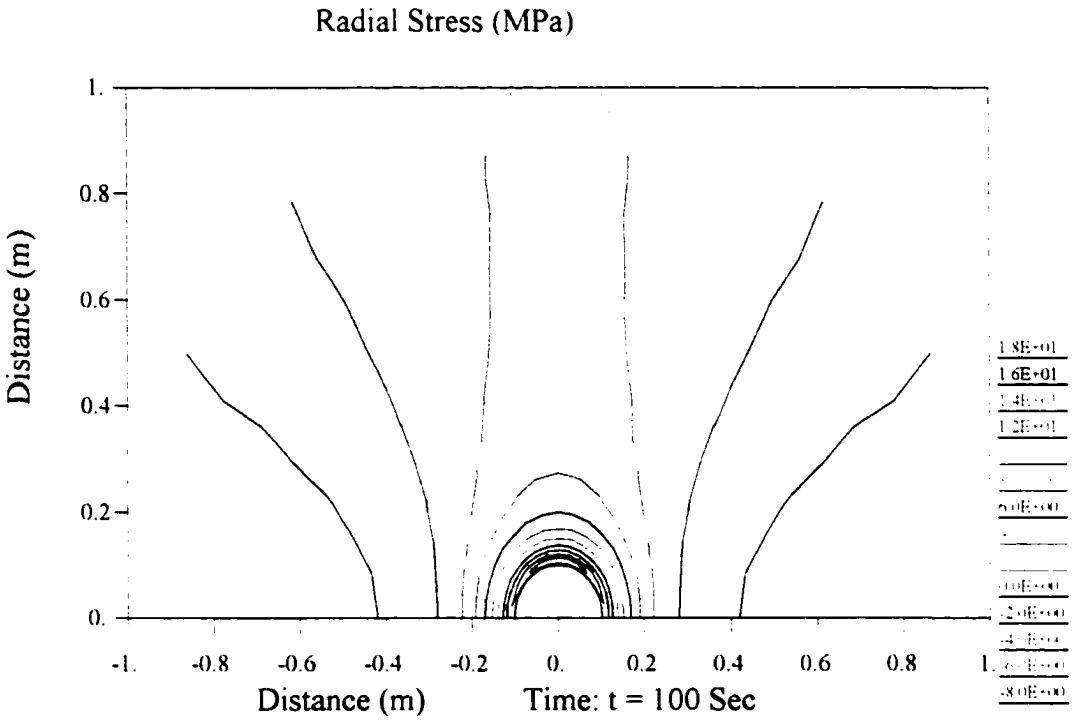


Figure 6.5.6 Radial stress distribution at t = 100 s for a permeability ratio of k_{ma}/k_{fr} = 0.01.

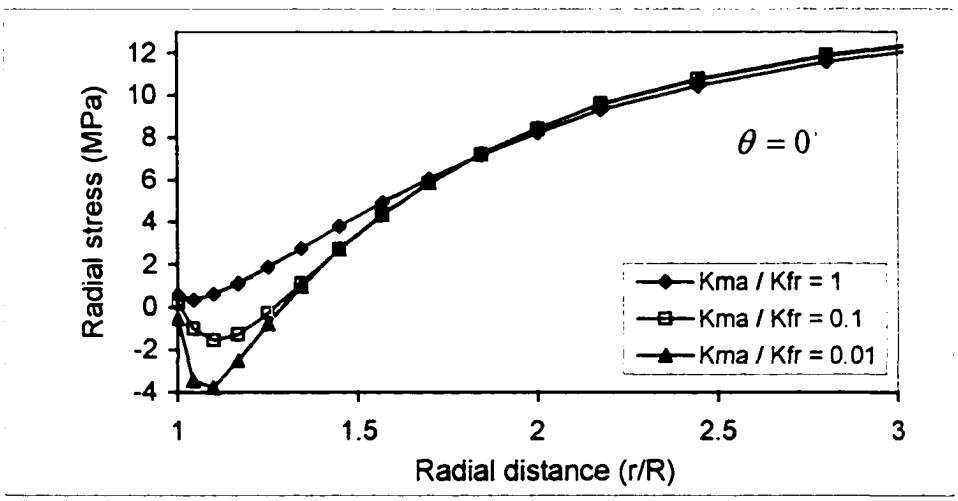


Figure 6.5.7 Radial stress around wellbore in the maximum stress direction at t = 100 s for different permeability ratios.

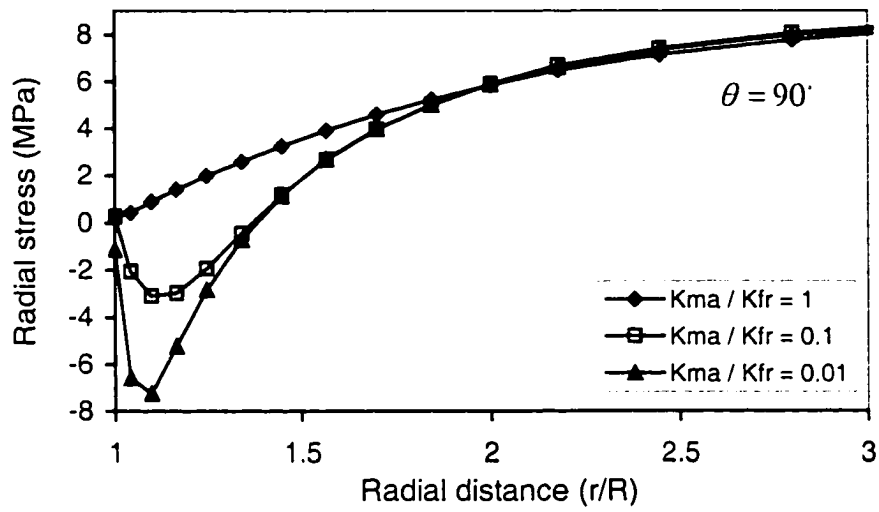


Figure 6.5.8 Radial stress around wellbore in the maximum stress direction at t = 100 s for different permeability ratios.

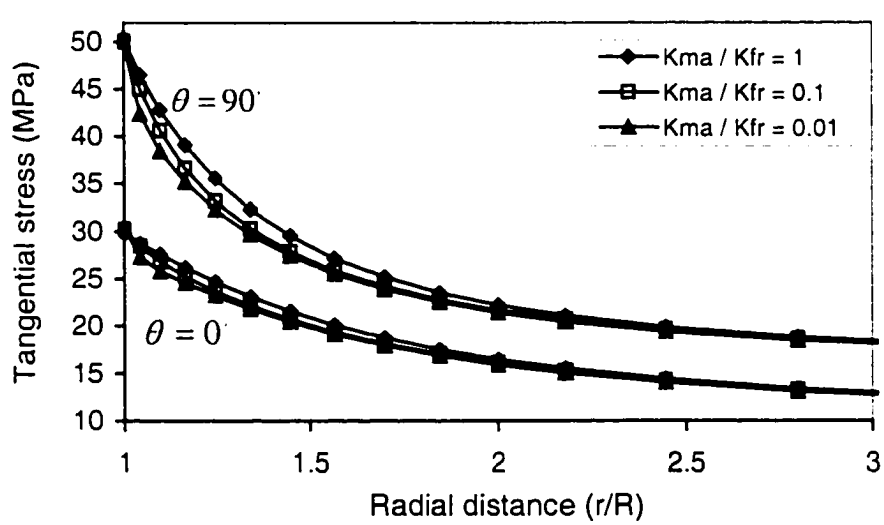


Figure 6.5.9 Effective tangential stress distribution, at t = 100 s, θ = 0° and θ = 90° for different permeability ratios.

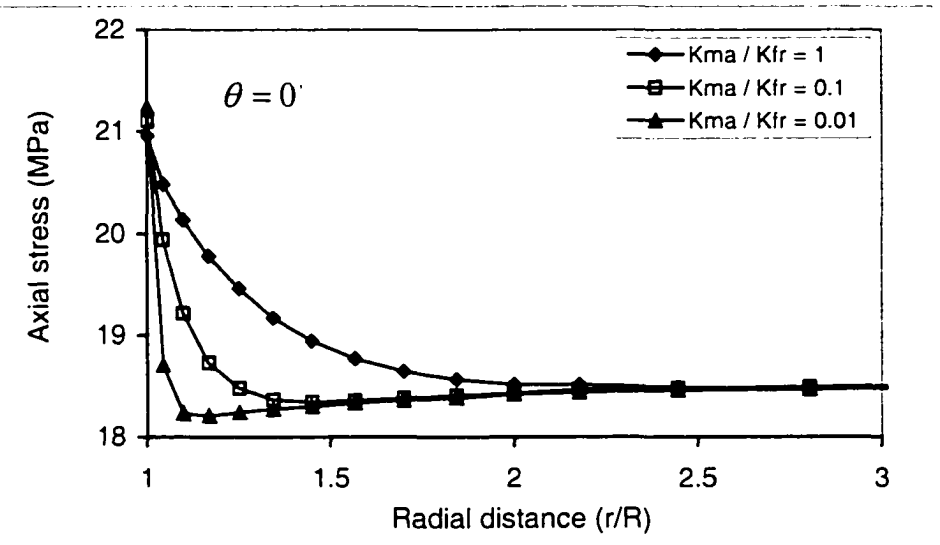


Figure 6.5.10 Effective axial stress distribution, at t = 100 s, θ = 0°, for different permeability ratios.

6.6 Borehole Inclination Effects

To assess the effect of borehole inclination, in Figure 6.6.1 the pore pressures responses at t = 100 s, θ = 0° for four different inclination angles, 0°, 40°, 70° and 90° were examined. Note that a hole inclination angle of φ_z = 0° represents a vertical hole. It is shown that the inclination increases the pore pressure magnitude in this case example, which is more obvious through comparing the pore pressure contours in Figures 6.6.2 and 6.6.3. This is the consequence of the extra pore pressure generated by Skempton's effect. At φ_z = 0° the relevant local far-field compressive stress at θ = 0° is σ_x = 29 MPa, σ_y = 20 MPa which is changed to σ_x = 25 MPa, σ_y = 20 MPa at φ_z = 90° due to the inclination (refer to Figure 6.6.4). Figure 6.6.5 shows the same pore pressure response but at the azimuthal angle θ = 90°. In this case, the trend is reversed: pore pressure decreases with increasing inclination. This is due to that the relevant far-field

compressive stress reduces from σ_x = 29 MPa with a 0° hole inclination to σ_x = 25 MPa with a 90° hole inclination.

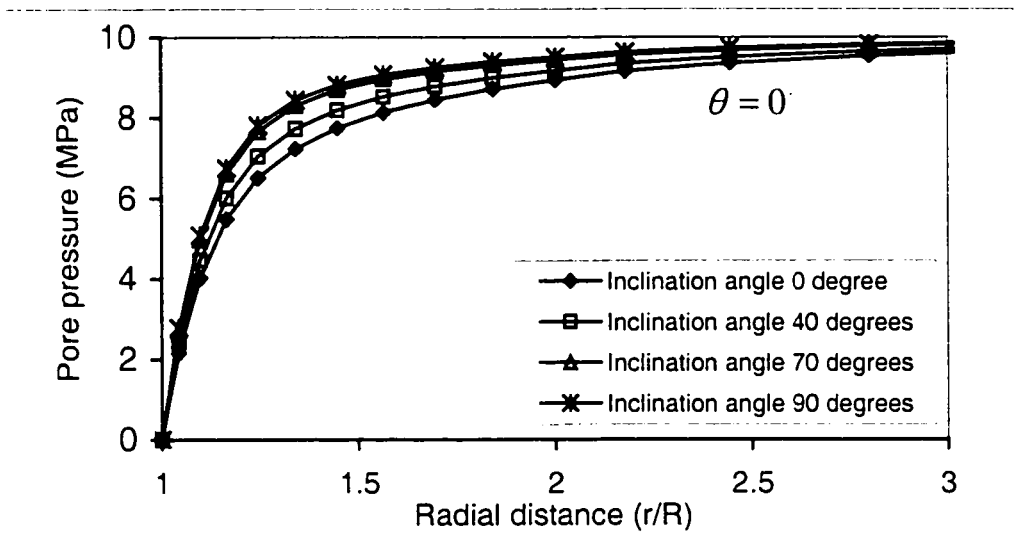


Figure 6.6.1 Pore pressure distribution at t = 100 s, θ = 0° for different borehole plunges, φ_z.

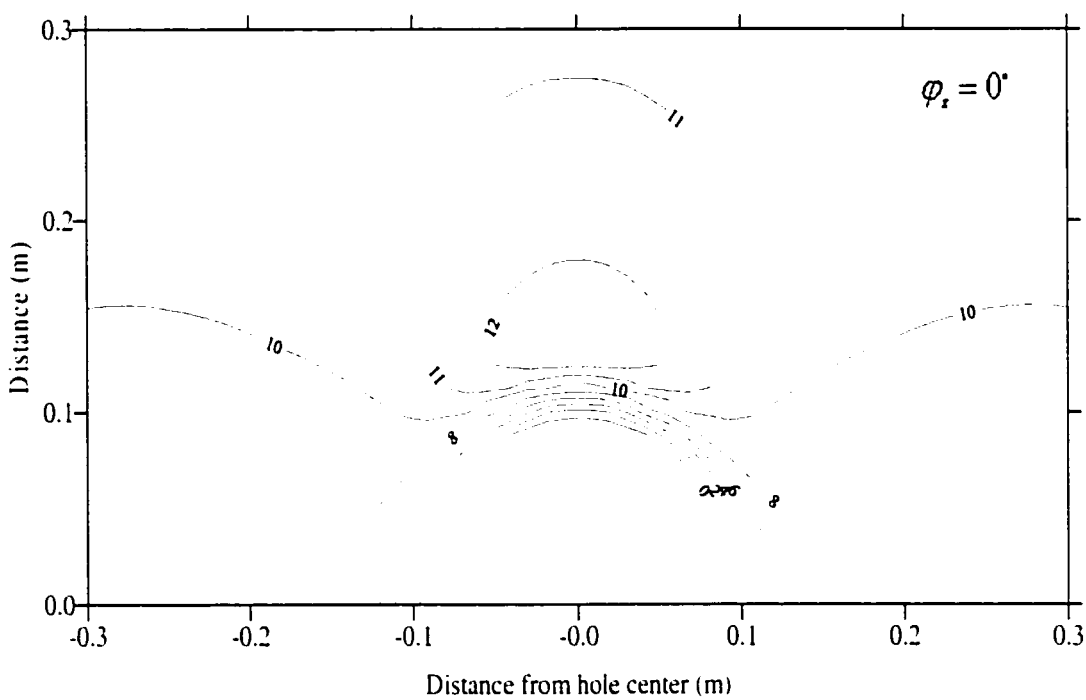


Figure 6.6.2 Pore pressure distribution at t = 100 s for a hole inclination of 0°.

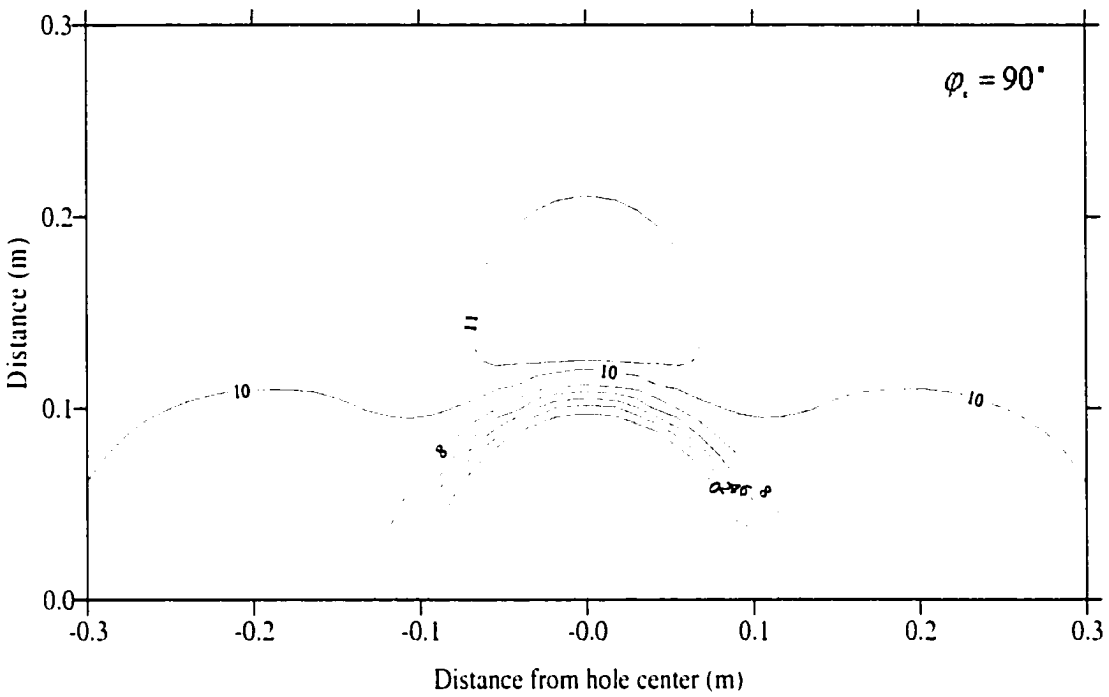
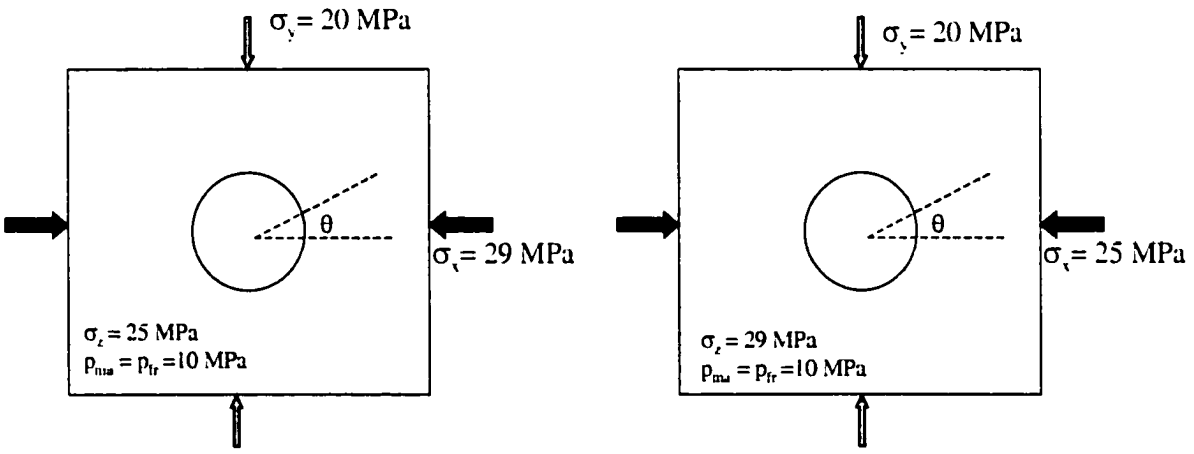


Figure 6.6.3 Pore pressure distribution at t = 100 s for a hole inclination of 90°.



(a) Hole inclination $\varphi_z = 0°$ (b) Hole inclination $\varphi_z = 90°$

Figure 6.6.4 State of stress in the local coordinate systems after 0° and 90° inclinations.

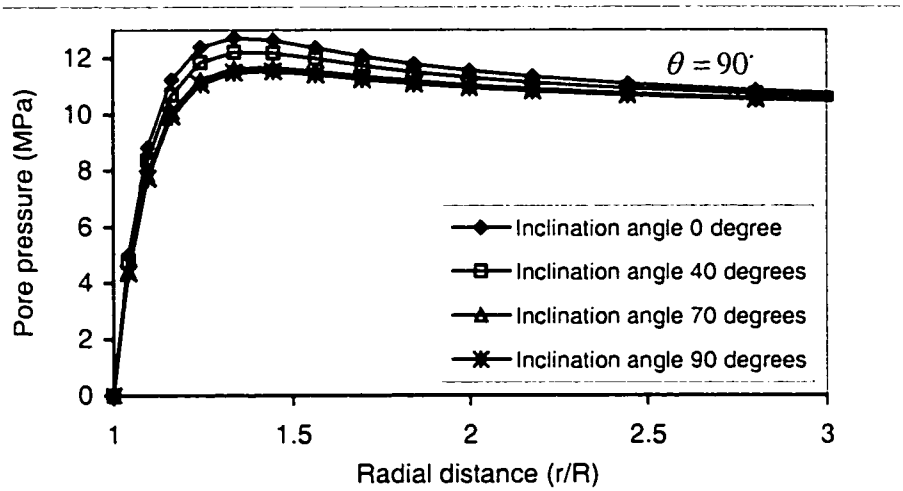


Figure 6.6.5 Pore pressure distribution at t = 100 s, θ = 90° for different borehole plunges, φ_z.

Figures 6.6.6 and 6.6.7 explore the influence of hole inclination at t = 100 s, θ = 0° and θ = 90°. The inclination causes a reduction in compressive radial stress and an increase in tensile radial stress. This trend is more pronounced at the azimuthal angle θ = 0° (See Figures 6.6.8 and 6.6.9), because the local far-field total stress varies from σ_x = 29 MPa (Effective stress 19 MPa) at a hole inclination φ_z = 0° to σ_x = 25 MPa (Effective stress 15 MPa) compared to a hole inclination φ_z = 90°; however, at an angle of θ = 90°, the local far-field total stress does not change (σ_y = 20 MPa) from a hole inclination φ_z = 0° to φ_z = 90° (Refer to Figures 6.1 and 6.6.4).

Figures 6.3.10 and 6.3.11 demonstrate the effect of borehole inclination on effective tangential and axial stresses at the azimuthal angle θ = 0°. It is clear that at larger inclination angles the tangential stress decreases and the axial stress increases because the inclination from φ_z = 0° to φ_z = 90° causes the local far-field total stress from σ_x = 29 MPa, σ_z = 25 MPa to σ_x = 25 MPa, σ_z = 29 MPa (See Figure 6.6.4).

Form the above analyses it is obvious that the effects of hole inclination on wellbore pressure and stresses depend strongly upon the far-field stress. For the given boundary

and far-field stress conditions, the borehole inclination can be optimized in order to avoid high stress concentration around the wellbore.

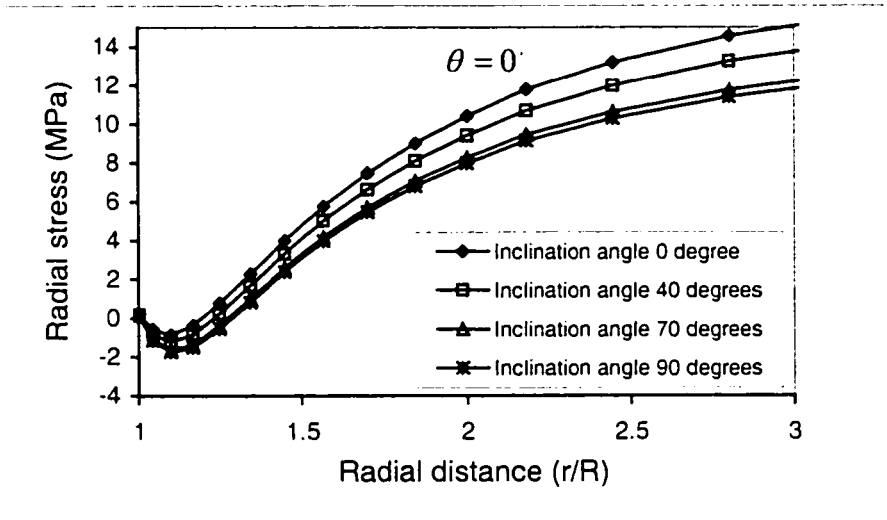


Figure 6.6.6 Effective radial stress distributions, at t = 100 s, θ = 0°, for different borehole plunges, φ_z.

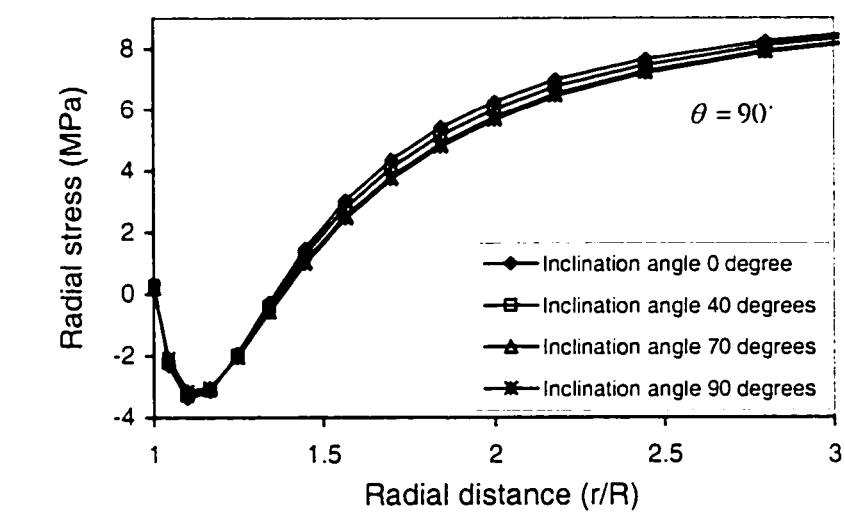


Figure 6.6.7 Effective radial stress distributions, at t = 100 s, θ = 90°, for different borehole plunges, φ_z.

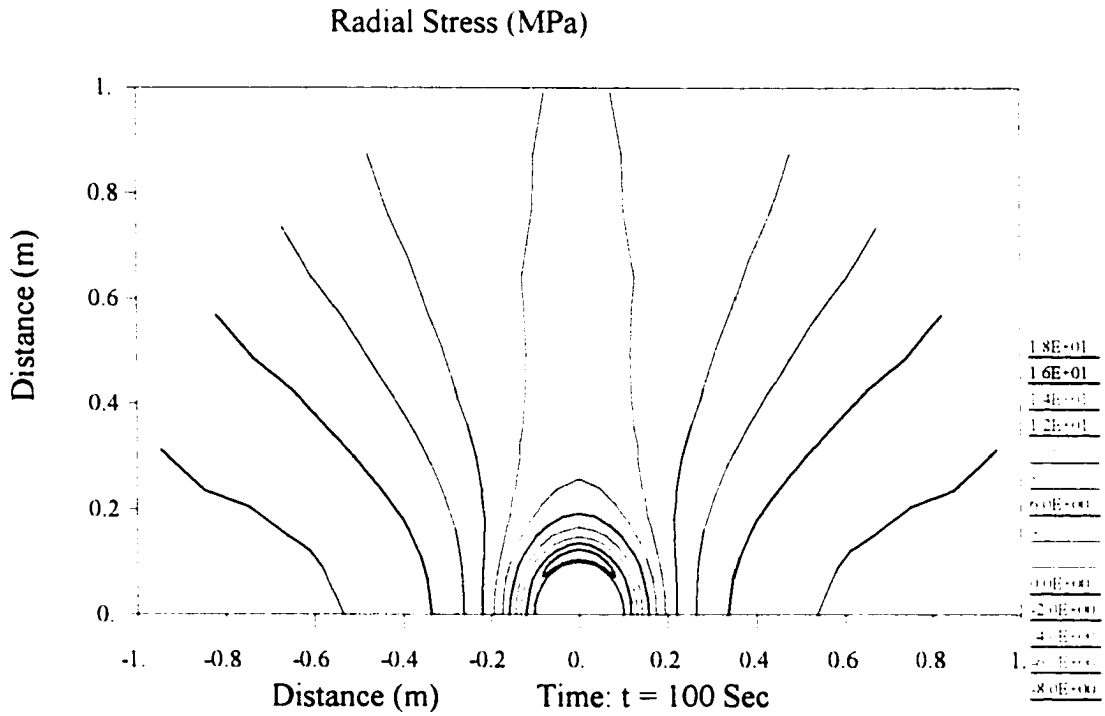


Figure 6.6.8 Radial stress distribution at t = 100 s for hole inclination of 0°.

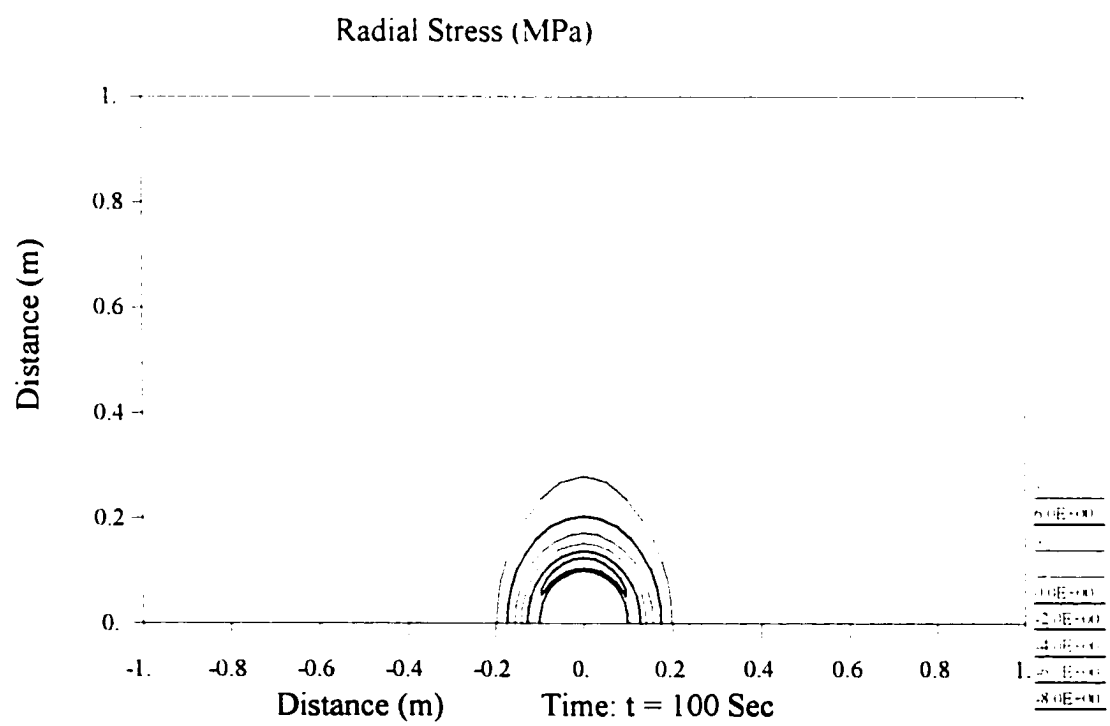


Figure 6.6.9 Radial stress distribution at t = 100 s for hole inclination of 90°.

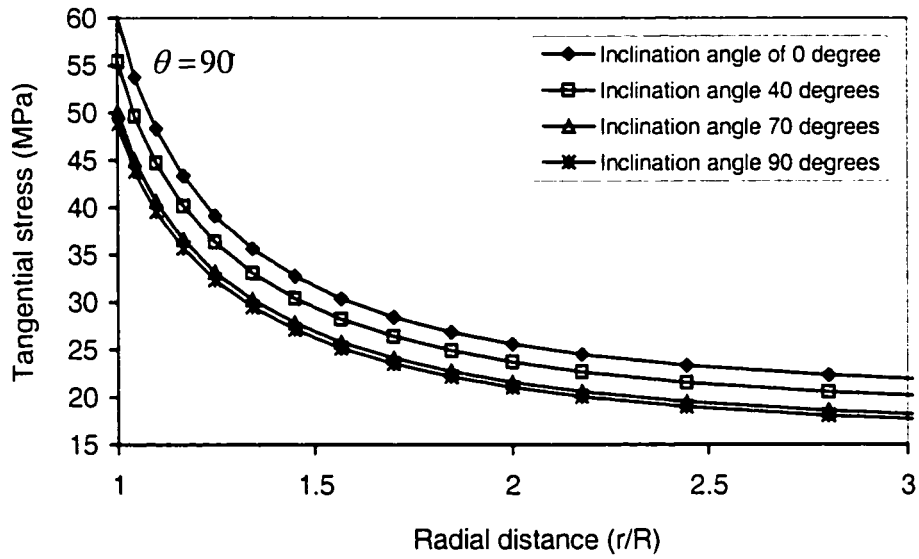


Figure 6.6.10 Effective tangential stress distributions, at t = 100 s, θ = 90°, for different plunges, φ_z.

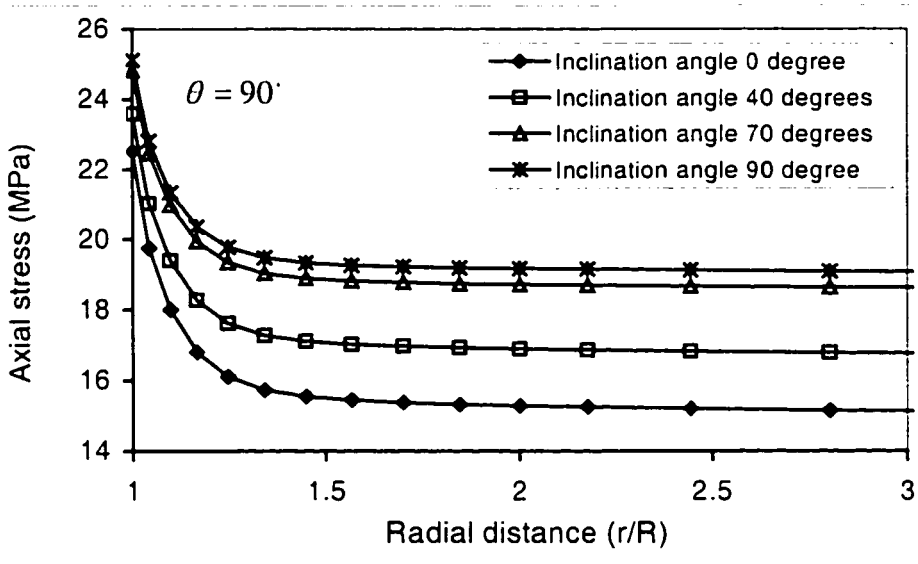


Figure 6.6.11 Effective axial stress distributions, at t = 100 s, θ = 90°, for different borehole plunges, φ_z.

6.7 Mud Weight Effects

Rock failure is likely to take place when a borehole is drilled with air or with insufficient mud pressure to support it before casing is placed. However, too large mud pressures may induce borehole instability by tensile fracturing leading to unacceptable mud losses. In the present analysis, the borehole depth was assumed to be 1000 m and four values of mud weight density were examined, i.e., $\rho_w = 0.006$, $\rho_w = 0.01$, $\rho_w = 0.02$ and $\rho_w = 0.025$ MN/m^3 corresponding to mud pressures of $p_w = 6$, $p_w = 10$, $p_w = 20$, and $p_w = 25$ MPa, other parameters remaining the same, as in previous analyses. Figures 6.7.1 and 6.7.2 are the pore pressure responses along the maximum and minimum stress directions ($\theta = 0°$ and $\theta = 90°$) at t =100 s. It is clear that the pore pressure has the same magnitude as the mud pressure at the borehole wall; and that pore pressure decreases dramatically away from the wall when the mud pressure is high. It can be observed from the pore pressure contours in Figures 6.7.3 and 6.7.4 that only for small mud pressure cases, such as $p_w = 6$ MPa, does the pore pressure have a non-monotonic distribution inside the hole along the minimum stress direction.

Due to the mud pressure, there are no tensile radial stresses inside the borehole except for the case of very small mud pressure values (e.g. $p_w = 6$ MPa), as shown in Figures 6.7.5 and 6.7.6; instead, a non-monotonic stress distribution appears for higher mud pressures, as shown in Figures 6.7.7 and 6.7.8. Furthermore, the increasing mud pressure causes increases of the compressive radial stress; this is due to that fact that the mud weight acts on the wellbore wall as an additional radial stress component.

Figures 6.7.9 and 6.7.10 show the effective compressive tangential stress response along the maximum and minimum stress directions at t = 100 s. It is obvious that the compressive tangential stress decreases as the mud pressure increases, which reduces the high stress concentration around the wellbore. From Figures 6.7.11 and 6.7.12 it is noted that the effective tangential stress becomes tensile along the local maximum stress direction ($\theta = 0°$) for high mud pressures (e.g. $p_w = 25$ MPa). This illustrates that the borehole will fail in tension or fracturing when the tensile tangential stress is larger than

the formation tensile strength. However, there is no tensile stress induced at the borehole wall along the local minimum stress direction ($\theta = 90°$, Figure 6.7.10).

Figures 6.7.13 and 6.7.14 demonstrate the effective compressive axial stress responses along the minimum and maximum stress directions, at t = 100 s. The increasing mud pressure reduces the axial stress concentration around borehole in the near field.

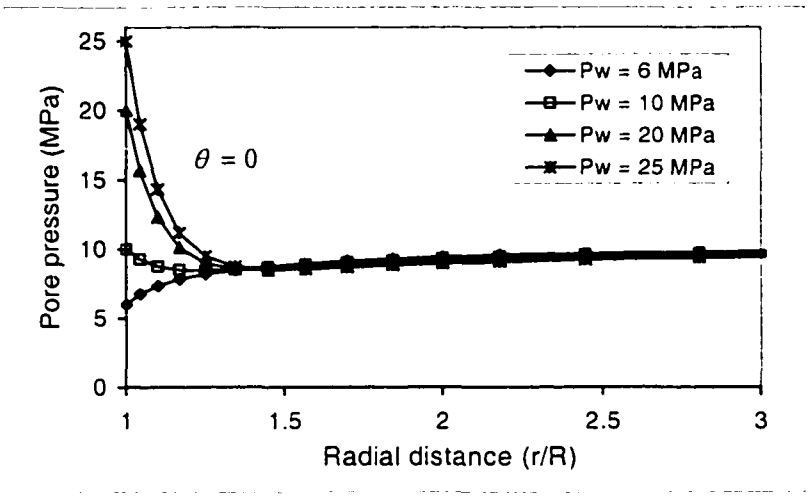


Figure 6.7.1 Pore pressure along the maximum stress direction at t = 100 s for different mud pressures.

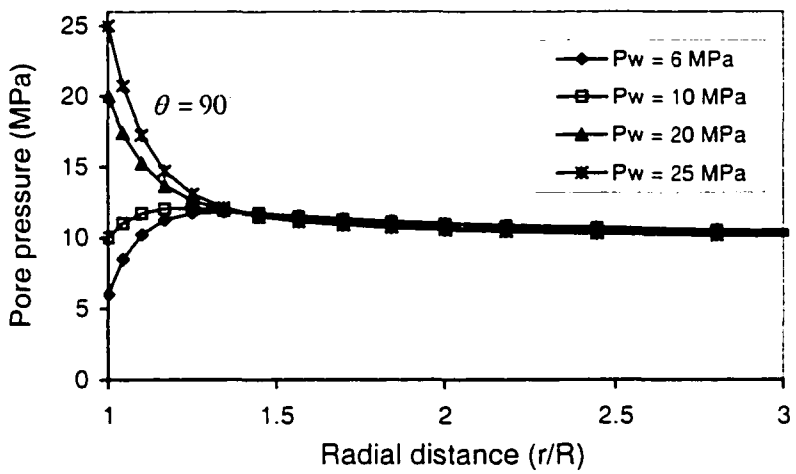


Figure 6.7.2 Pore pressure along the minimum stress direction at t = 100 s for different mud pressures.

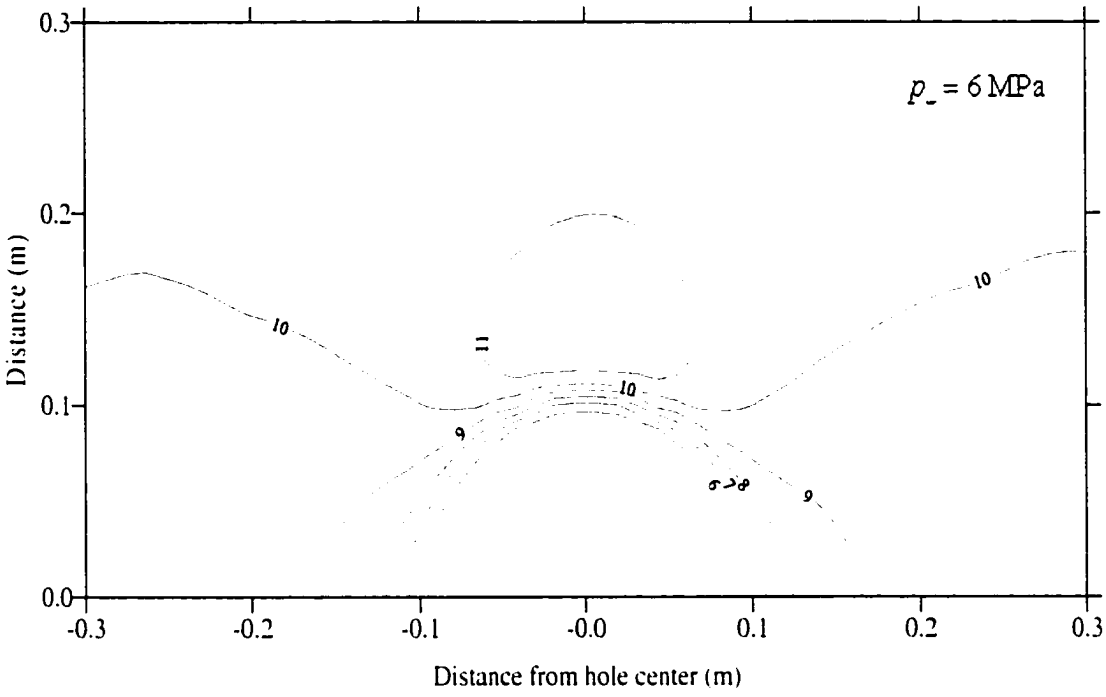


Figure 6.7.3 Pore pressure distribution at t = 100 s for a mud pressure of p_w = 6 MPa.

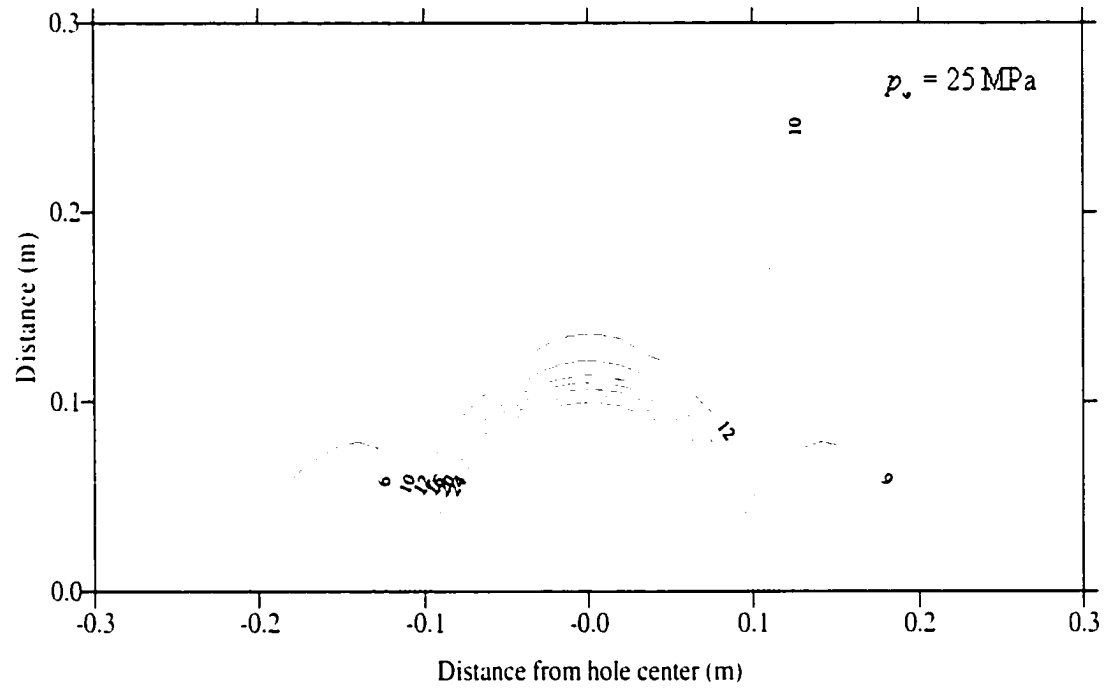


Figure 6.7.4 Pore pressure distribution at t = 100 s for a mud pressure of p_w = 25 MPa.

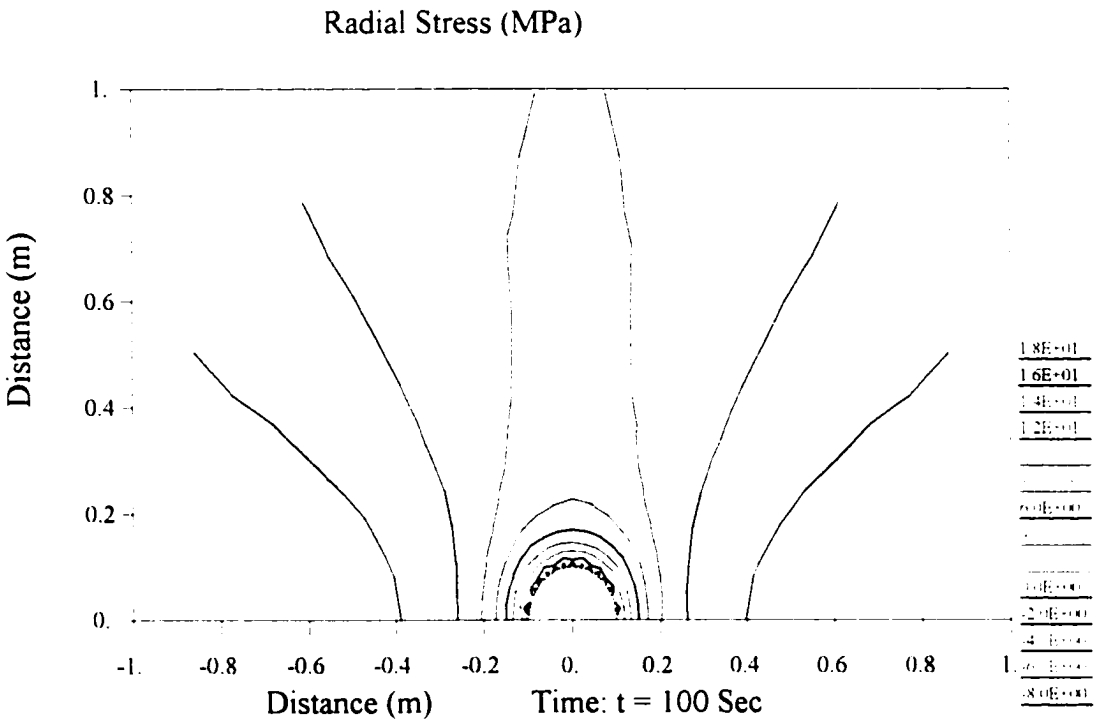


Figure 6.7.5 Radial stress distribution at t = 100 s for a mud pressure of p_w = 6 MPa.

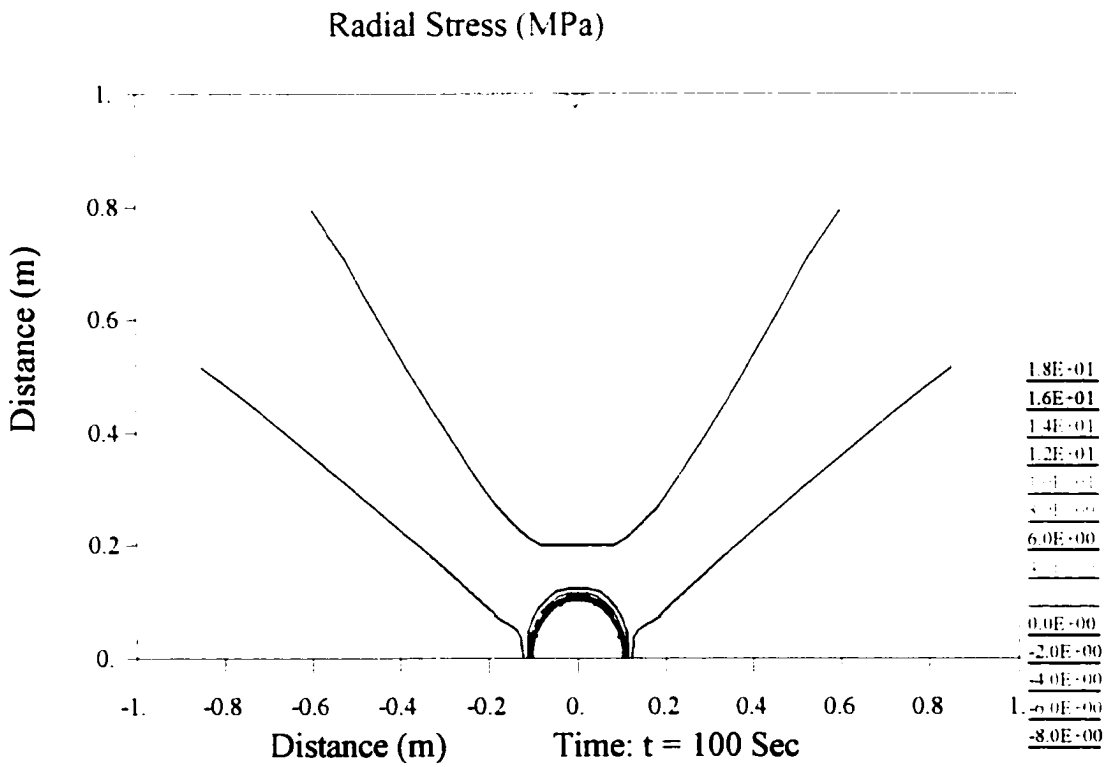


Figure 6.7.6 Radial stress distribution at t = 100 s for a mud pressure of p_w = 25 MPa.

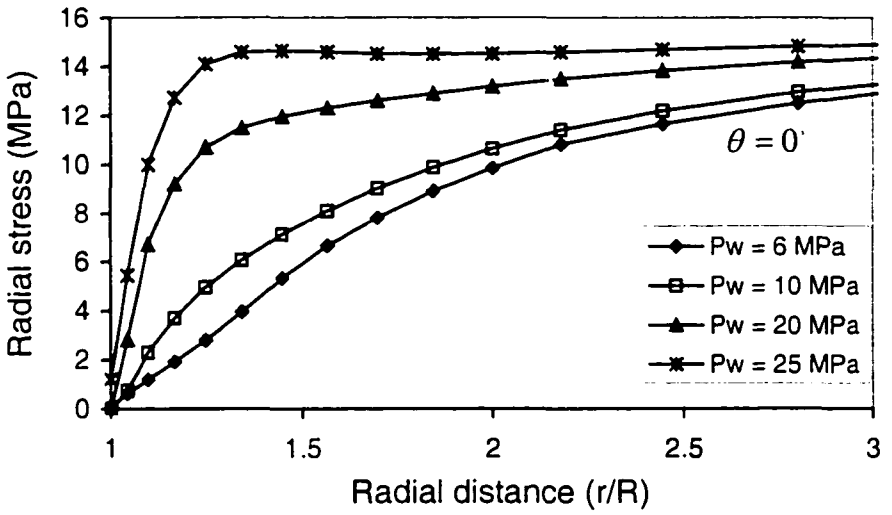


Figure 6.7.7 Effective radial stress along the maximum stress direction at t = 100 s for different mud pressures.

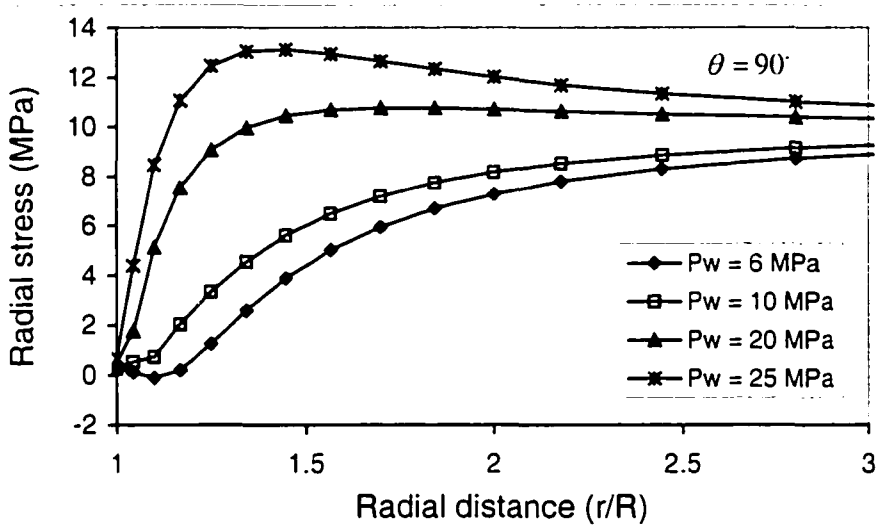


Figure 6.7.8 Effective radial stress along the minimum stress direction at t = 100 s for different mud pressures.

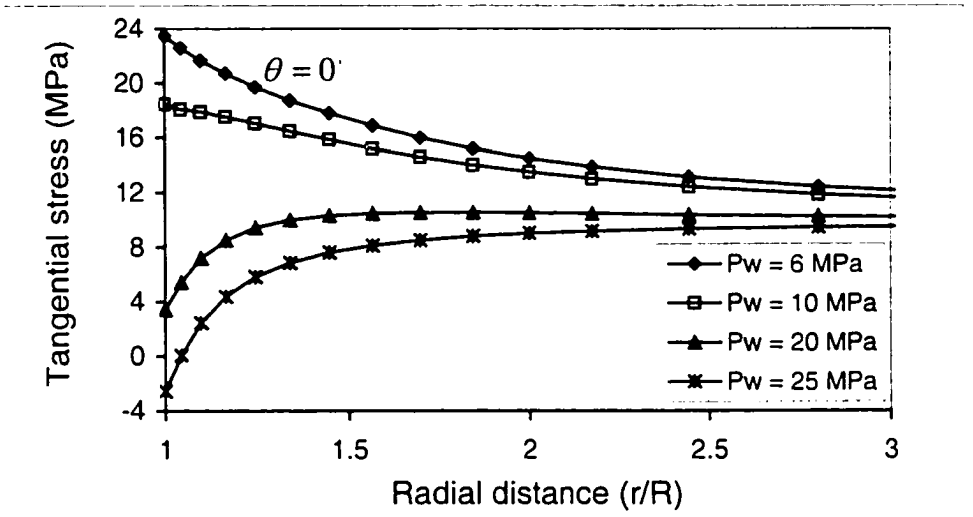


Figure 6.7.9 Effective tangential stress along the maximum stress direction at t = 100 s for different mud pressures.

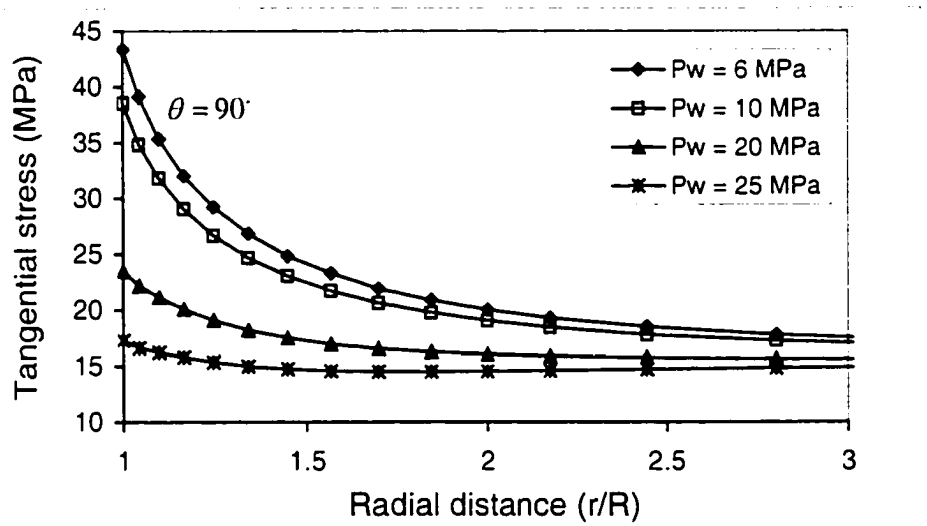


Figure 6.7.10 Effective tangential stress along the minimum stress direction at t = 100 s for different mud pressures.

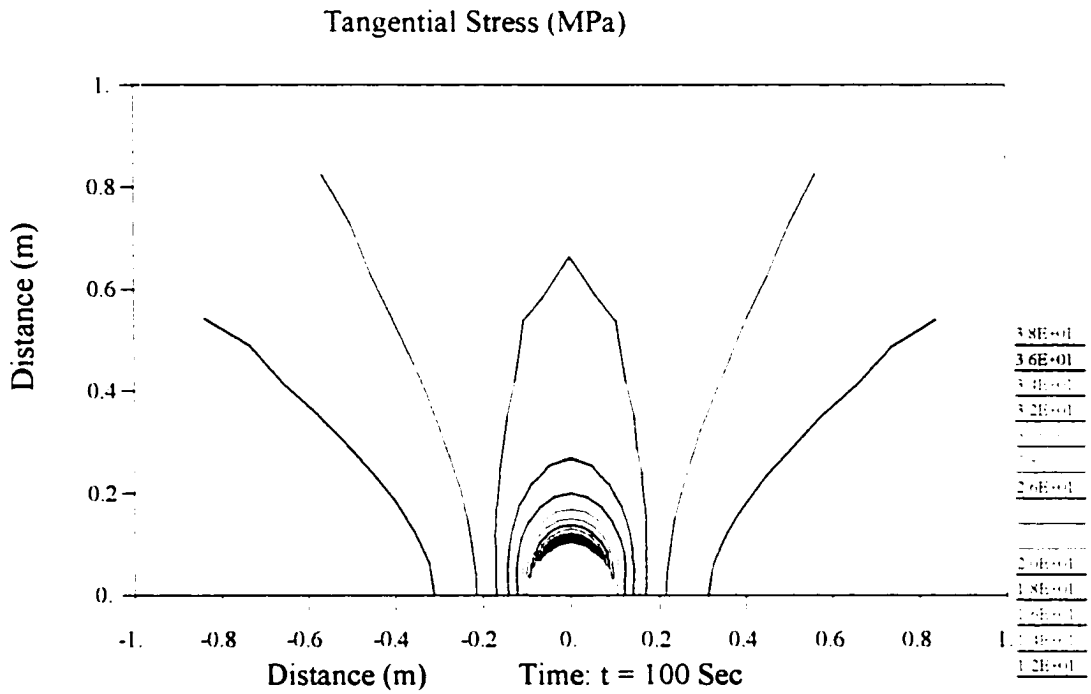


Figure 6.7.11 Tangential stress distribution at t = 100 s for a mud pressure of p_w = 6 MPa.

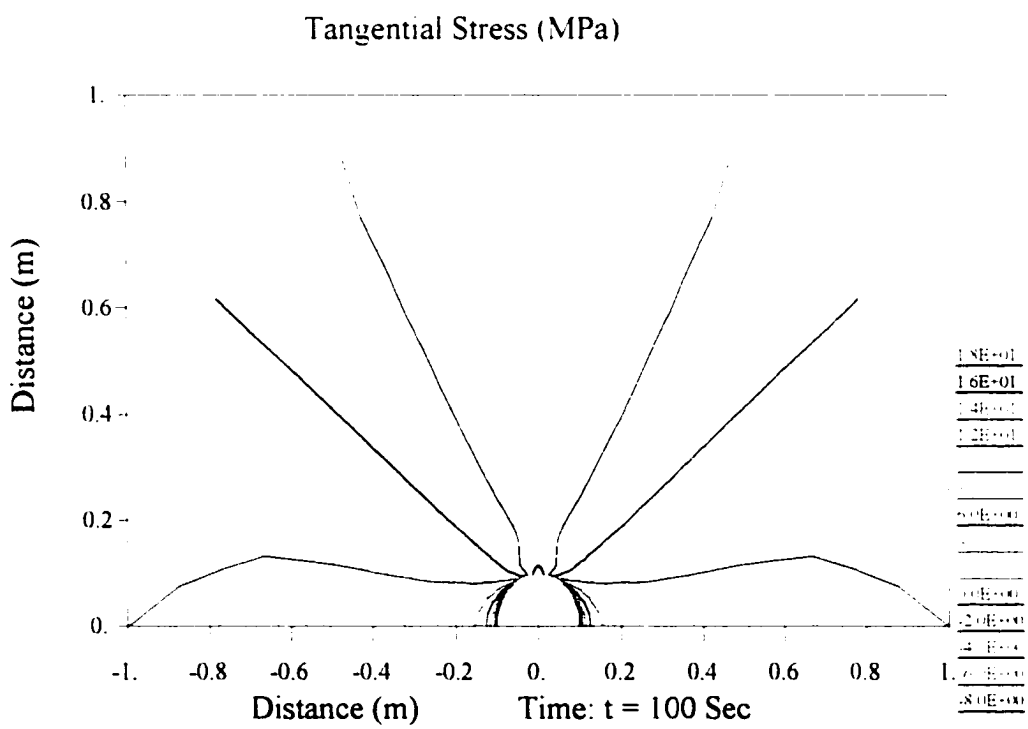


Figure 6.7.12 Tangential stress distribution at t = 100 s for a mud pressure of p_w = 25 MPa.

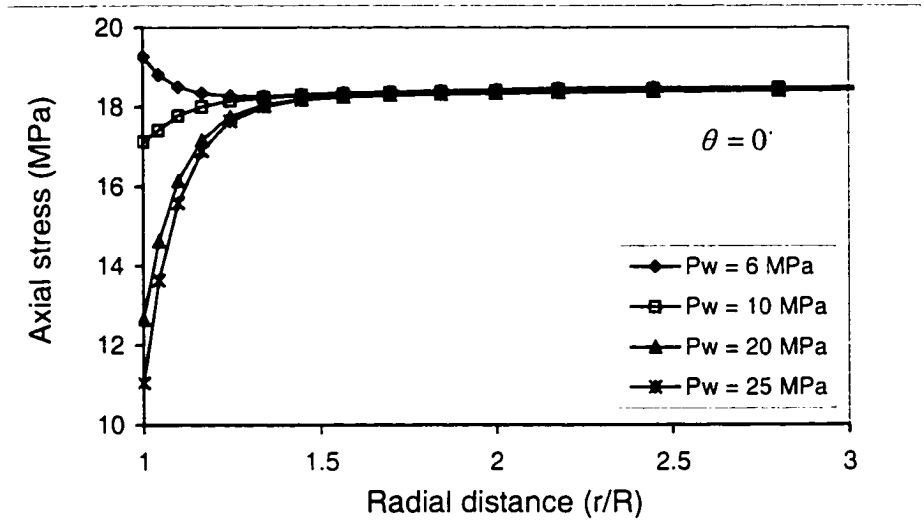


Figure 6.7.13 Effective axial stress along the maximum stress direction at t = 100 s for different mud pressures.

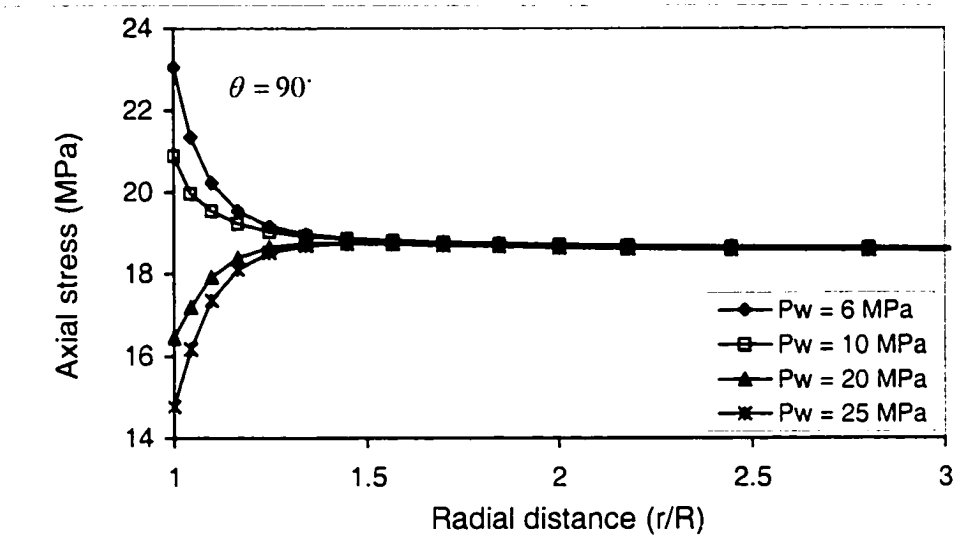


Figure 6.7.14 Effective axial stress along the minimum stress direction at t = 100 s for different mud pressures.

6.8 Mud Cake Effects

Borehole instabilities in poorly- and un-consolidated formations is mainly due to that the formation cannot be supported by hydrostatic overbalance alone. As a result, the unconsolidated sands often fall into the hole and pack off around the drill string. Problems also occur if insufficient filtercake is deposited on loose, unconsolidated sand to prevent it from flowing into the wellbore. The unconsolidated formations are highly permeable and any mud or water that invades the pore spaces also destabilizes the hole. To drill these formations, the mud should provide a good-quality filtercake to help consolidate the formation so that mud pressure can induce confining pressure and stabilize the formation. A drilling mud with a low filtrate water loss will form a thin, tough mud cake; ideally it should function as an impermeable medium. In order to demonstrate the mud cake influence, two cases was examined: a borehole with an impermeable mud cake and larger matrix permeability (k_{ma} = 10^{-10} darcy) and one without a mud cake, but a very small matrix permeability (k_{ma} = 10^{-12} darcy). The mud pressure was assumed as 10 MPa.

Figures 6.8.1 and 6.8.2 represent the pore pressure distributions along maximum and minimum stress directions at t = 100 s for the wellbore with and without mud cake. For the wellbore with mud cake, the mudweight pressure acts only as an additional radial stress component at the borehole wall; therefore, there is no effect of the mud on the pore pressure at the borehole wall. However, for the wellbore without a mud cake, although the matrix permeability is very small, it is still permeable and the pore pressure at the borehole wall is same as the mud pressure, which illustrates the interaction between the mud weight and formation pore pressure.

Figures 6.8.3 and 6.8.4 are the radial stress distributions along the maximum and minimum stress directions for the wellbore with and without mud cake. It can be observed that tensile stresses still prevail inside the wellbore in the minimum stress direction for the wellbore without mud cake (Figure 6.8.4); hence, the mud pressure is insufficient. The mud pressure for the permeable case not only provides wellbore radial support, but also provide a pore pressure that is equivalent to the mud pressure in the near field. As a consequence, the effective radial stress is reduced. However, for the

impermeable case, such as a wellbore with mud cake, the mud pressure only provides the radial support. It can be seen that effective radial stresses in both cases only have little difference near the wellbore, which is induced by pore pressure difference.

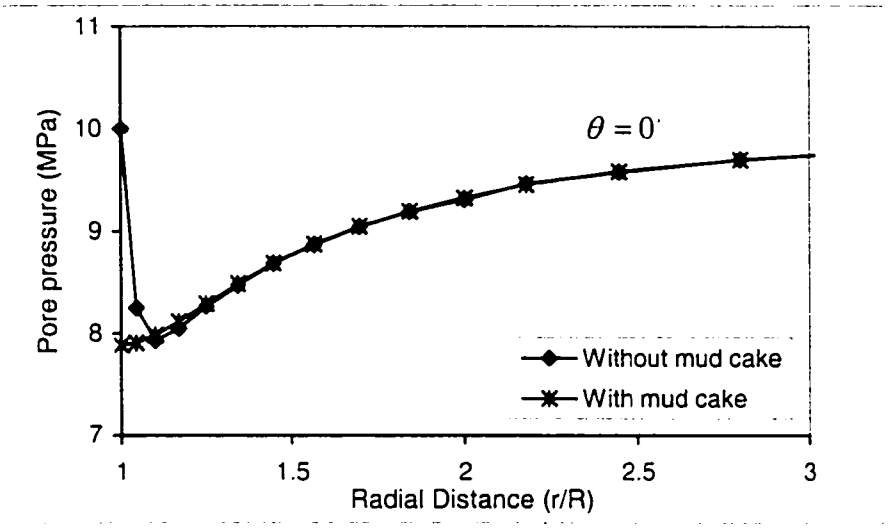


Figure 6.8.1 Pore pressure along the maximum stress direction at t = 100 s for wellbores with and without mud cake.

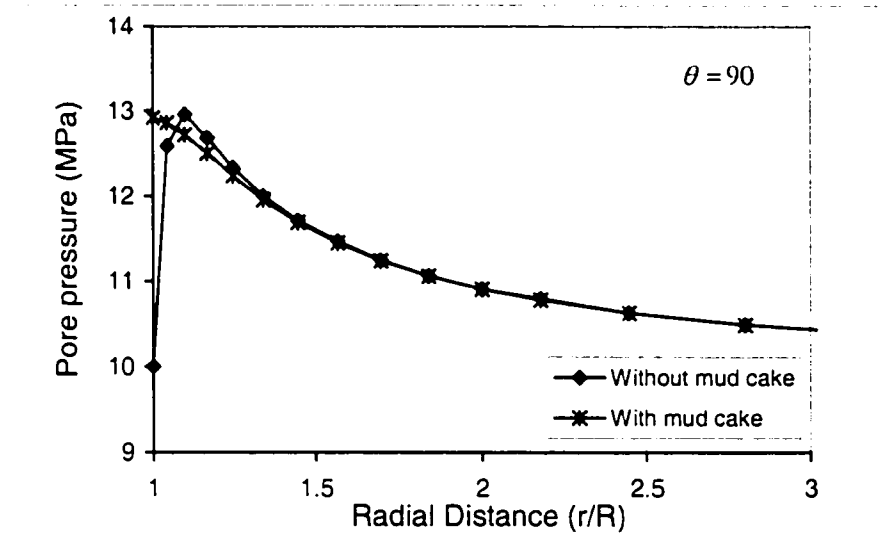


Figure 6.8.2 Pore pressure along the minimum stress direction at t = 100 s for wellbores with and without mud cake.

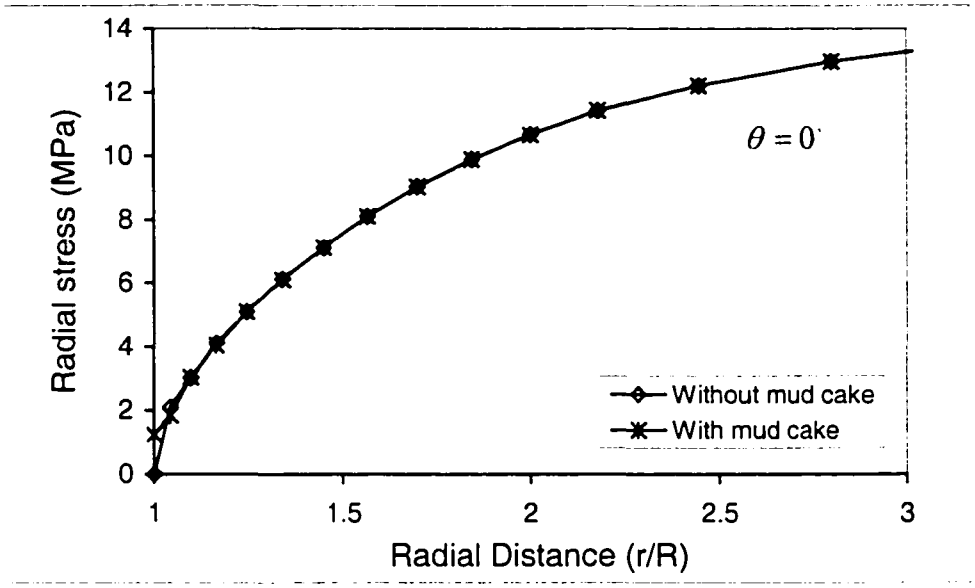


Figure 6.8.3 Radial stress along the maximum stress direction at t = 100 s for wellbores with and without mud cake.

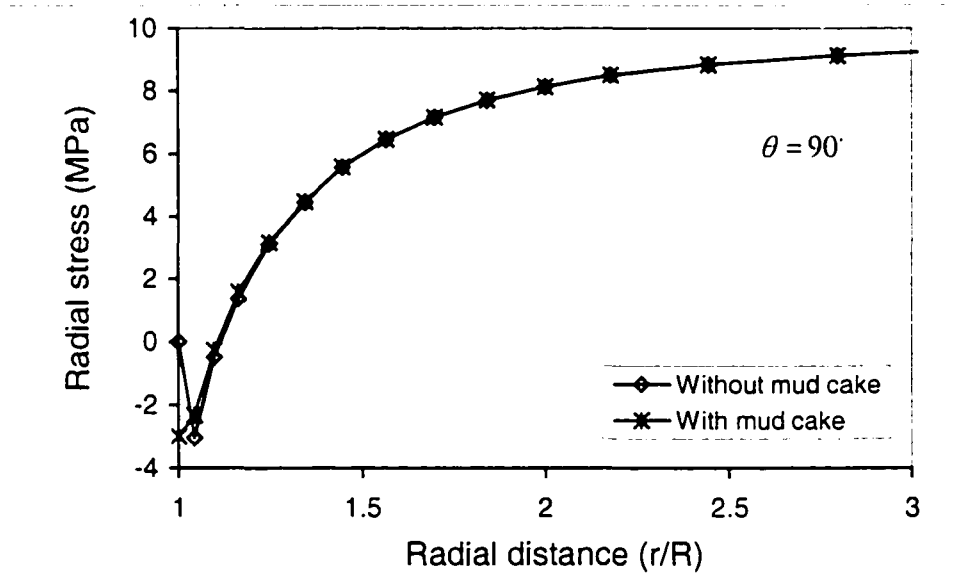


Figure 6.8.4 Radial stress along the minimum stress direction at t = 100 s for wellbores with and without mud cakes.

Figure 6.8.5 is the effective tangential stress distribution for wellbores with and without mud cakes. It is noted that the tangential stresses only have a very slightly difference.

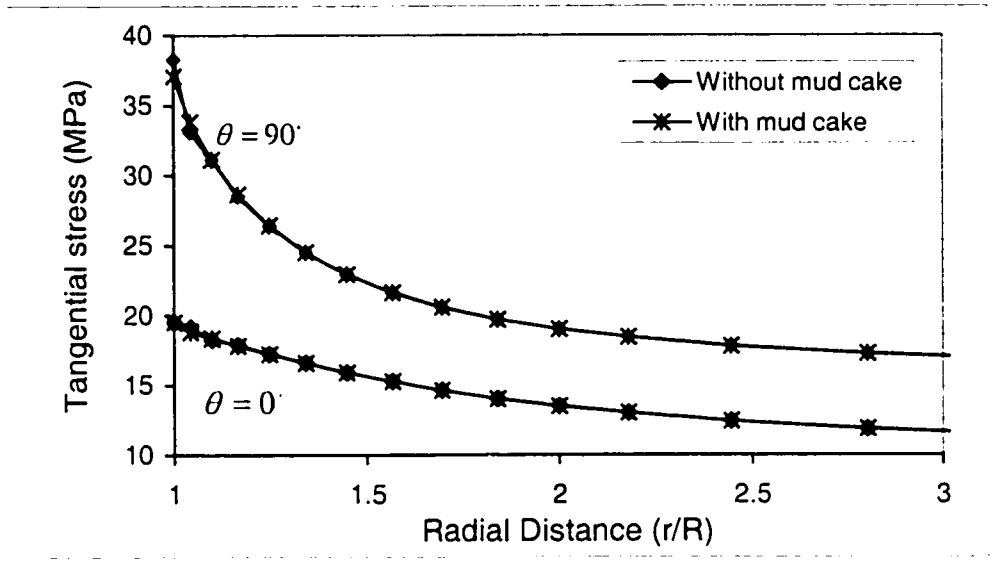


Figure 6.8.5 Tangential stress along the maximum and minimum stress directions at t = 100 s for wellbore with and without mud cakes.

The dual-porosity, time-dependent, fracture spacing, fracture stiffness, permeability, borehole inclination, mud weight and mud cake effects were analyzed in this chapter. The results demonstrated that dual-porosity media generate larger pore pressures and smaller tensile stresses than single-porosity media. Pore pressure and effective tensile radial stress decrease as time increases, and the tensile radial stress disappears when time is sufficiently large. For different fracture parameters, pore pressure increases and the tensile stress decreases as the fracture spacing and stiffness decrease. When the spacing and stiffness are large enough, the dual-porosity solution approaches the single-porosity solution. Sufficient mud weight can avoid the tensile radial stress along the borehole; however, high mud weight pressure can induce tensile tangential stress at the wellbore, which causes wellbore fracturing. Different wellbore failure criteria will be assumed to describe the wellbore breakout and tensile failures in the next chapter.

Chapter 7

Wellbore Failure Analyses

Boreholes fail either by exceeding the tensile strength, the compressive strength or by exceeding the shear strength of the rock formation; mainly caused by the effective stress concentration near the wellbore due to the far-field stress and the specific borehole orientation. It is commonly accepted that wellbore failure is controlled by Terzaghi's effective stress concept (Cui et al., 1999a):

$$\sigma'_{ij} = \sigma_{ij} - \delta_{ij} p_{ma} \tag{7.1}$$

where p_{ma} is the pore pressure.

Four kinds of failures: compressive, tensile, Mohr-Coulomb and Drüker-Prager are considered in this chapter.

7.1 Compressive Failure

The compressive failure criterion often used in borehole stability analysis is that the Terzaghi effective compressive tangential stress at the borehole wall equals the uniaxial compressive strength of the rock formation, i.e.:

$$\sigma'_{\theta} = \sigma_{\theta} - p_{ma} = \sigma_c \tag{7.1.1}$$

where σ_θ is the total tangential compressive stress, σ_c is the uniaxial compressive strength of the formation.

This failure criterion shows that the formation will fail when the effective compressive tangential stress is larger than rockmass compressive strength. The effective compressive failure stress can be defined as:

$$\sigma_{comp} = \sigma_c - \sigma'_\theta \tag{7.1.2}$$

where σ_{comp} is the effective compressive failure stress. When the compressive failure stress is below zero, the compressive failure will occur.

Applying this criterion, assuming that the compressive strength of the formation is σ_c = 41 MPa, and other parameters remain same as in the previous chapter, the compressive failure area and failure stress can be obtained. Figure 7.1.1 is the compressive failure area around the borehole for a stress-free wellbore inclined at an angle 70° and for t = 100 s. Note that the points in the figure are Gaussian points[1] in which failure occurs. The compressive failure is mainly concentrated around the borehole crown, i.e., the minimum stress direction (θ = 90°, as shown in Figure 6.1), where the borehole breakout is more likely to occur. Figure 7.1.2 shows the effective compressive stresses along the minimum stress direction at t = 100 s for three hole inclinations, i.e., φ_z = 0°, 70° and 90°. In this figure the failure, according to Equation (7.1.2), occurs when the stress is less than zero. It can be observed that for this given case the failure stress has larger negative values (meaning instability) and the unstable area increases as the hole inclination decreases.

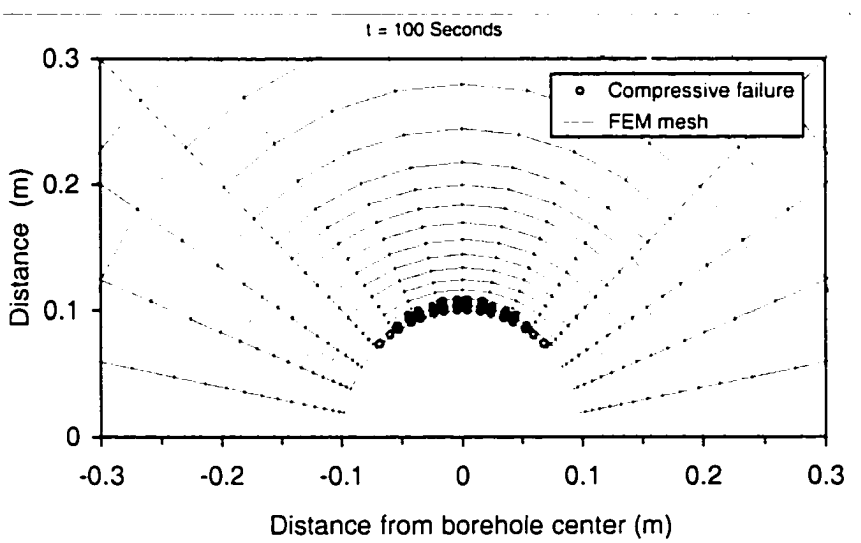


Figure 7.1.1 Compressive failure area for a stress-free borehole wall.

[1] Gaussian points are the integrated points in each element, in which the stresses are calculated.

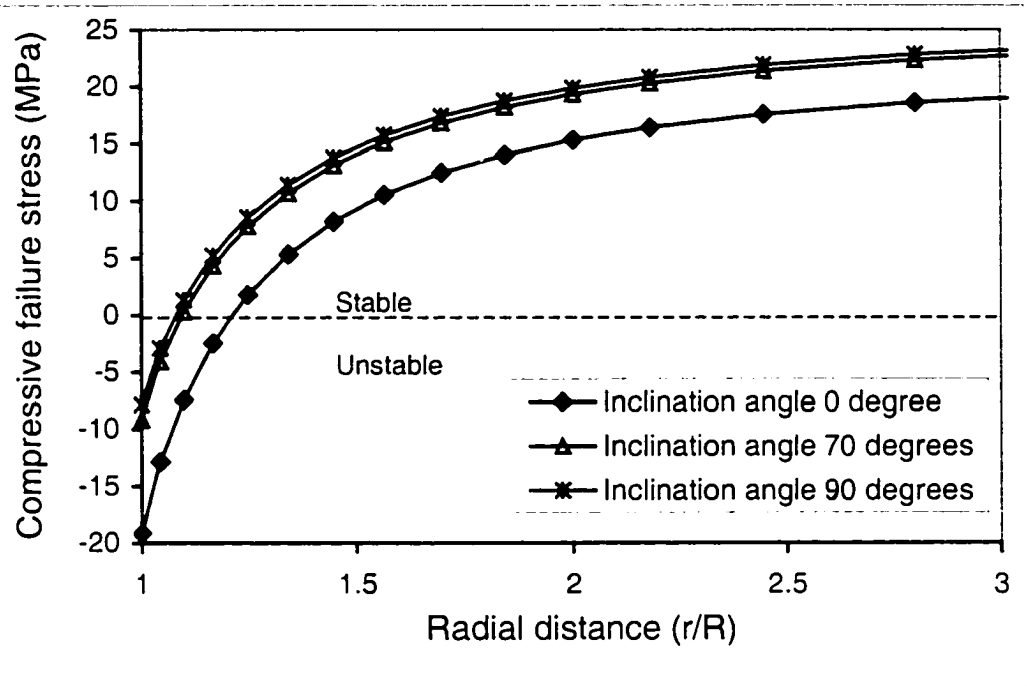


Figure 7.1.2 Effective compressive failure stresses for different hole inclinations along the minimum stress azimuth at t = 100 s.

7.2 Tensile Failure

There are two possible modes of tensile failure. One mode is due to fracturing at the borehole wall. As the mud pressure in the wellbore is increased, the stresses in the rocks become tensile, resulting in fracturing of the rock and lost circulation problems. The second mode is the outburst failure (or spalling) due to a tensile effective radial stress caused by a very rapid depressurizing borehole (Cheng et al., 1993).

7.2.1 Spalling Failure

The spalling criterion is that the effective radial tensile stress in the borehole equals the formation tensile strength, that is:

$$\sigma_r' = \sigma_r - p_{ma} = T \tag{7.2.1}$$

where σ_r is the total radial tensile stress and T is the tensile strength of the formation.

The effective spalling stress can be defined as:

$$\sigma_{spall} = T + \sigma_r' \tag{7.2.2}$$

where σ_{spall} is the effective spalling stress, note that σ_r' is negative.

This failure criterion shows that the borehole rocks will burst out when the effective tensile radial stress is larger than the rockmass tensile strength. Usually, the formation tensile strength is very small; and, especially for fractured formations, can be considered as zero. It is assumed that the tensile strength of the formation is T = 1.5 MPa in this section.

Figure 7.2.1 is the spalling area around the borehole for a stress-free wellbore for boreholes inclined at 70° and for t = 100 s. It can be observed that the spalling failure does not start at the borehole wall, but a short distance away inside the formation where the borehole is subjected to larger radial tensile stresses, and mainly occurs around the minimum stress direction. The phenomenon of rock failure inside borehole was often reported (e.g., Detournay and Roegiers, 1986; Roegiers, 1990; Cheng et al., 1993). Figures 7.2.2 and 7.2.3 show the effective spalling stresses along the minimum and maximum stress direction at t = 100 s for three hole inclinations, i.e., φ_z = 0°, 70° and 90°. Observe that along the maximum stress direction spalling occurs only for boreholes with very large inclinations; however, along minimum stress direction spalling takes place for any inclination.

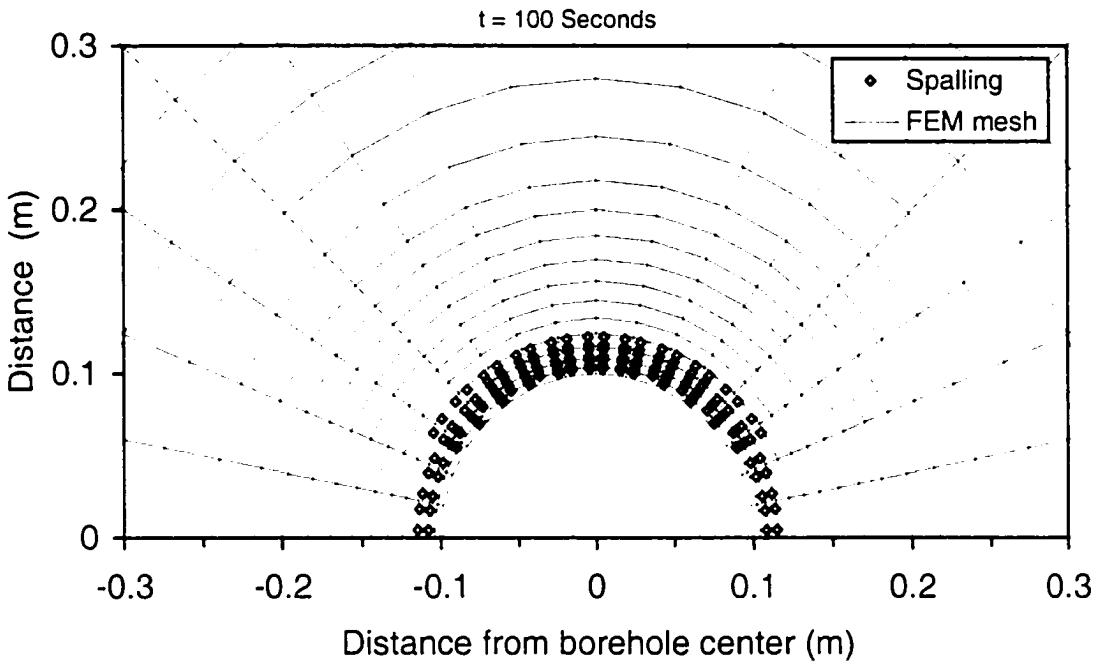


Figure 7.2.1 Spalling failure area for a stress-free borehole wall.

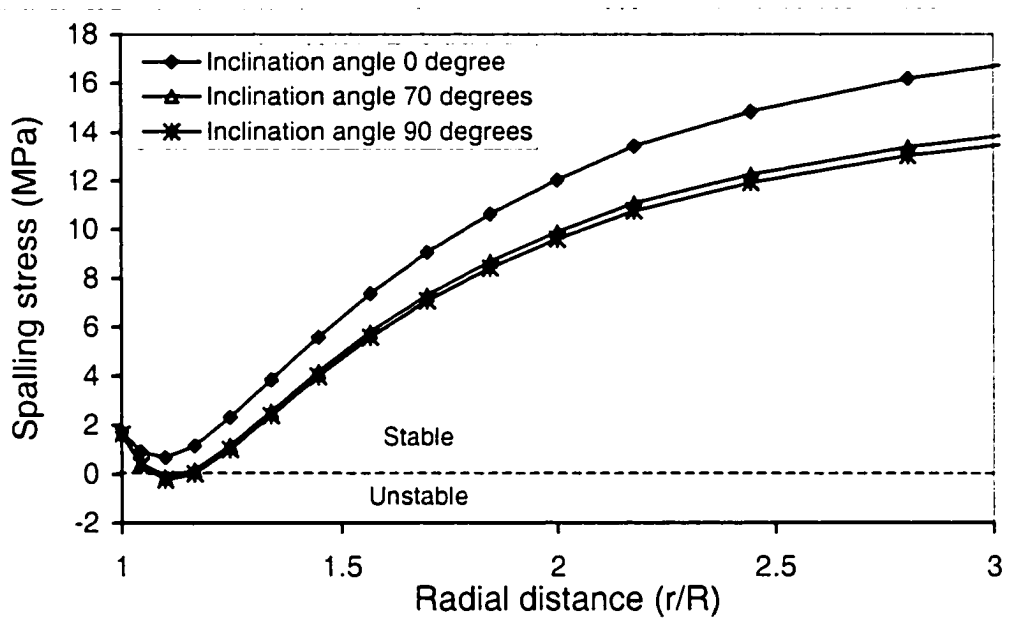


Figure 7.2.2 Effective spalling stresses for different hole inclinations along the maximum stress direction at t = 100 s.

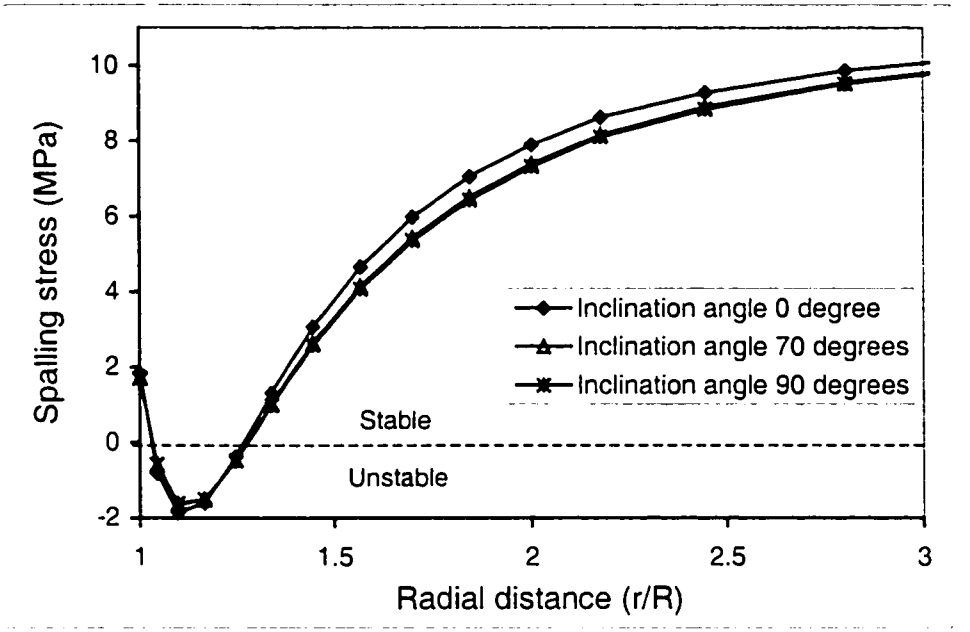


Figure 7.2.3 Effective spalling stresses for different hole inclinations along the minimum stress direction at t = 100 s.

7.2.2 Fracturing Failure

The failure criterion for fracturing is that the effective principal tensile stress (i.e., minor principal stress) at the borehole wall equals the formation tensile strength, that is:

$$\sigma'_3 = T \tag{7.2.3}$$

where, σ'_3 is the effective principal tensile stresses (note that σ'_3 is the negative value).

The effective fracturing stress can be defined as:

$$\sigma_{frac} = \sigma'_3 + T \tag{7.2.4}$$

where $\sigma_{\theta pall}$ is the effective fracturing stress. When the fracturing stress is below zero, fracturing will occur.

With sufficient mud pressure support, the wellbore spalling and compressive failure can be controlled. However, the tensile failure or fracturing may be induced in the wellbore when the mud pressure is too high. Figure 7.2.4 shows the tensile failure area for a hole inclination of 70° at t = 100 s and for a mud pressure p_w = 25 MPa. It is seen that the fracturing takes place mainly around the maximum stress direction. From Figure 7.2.5, the effective fracturing stress has larger negative values and the unstable area increases as the inclination decreases.

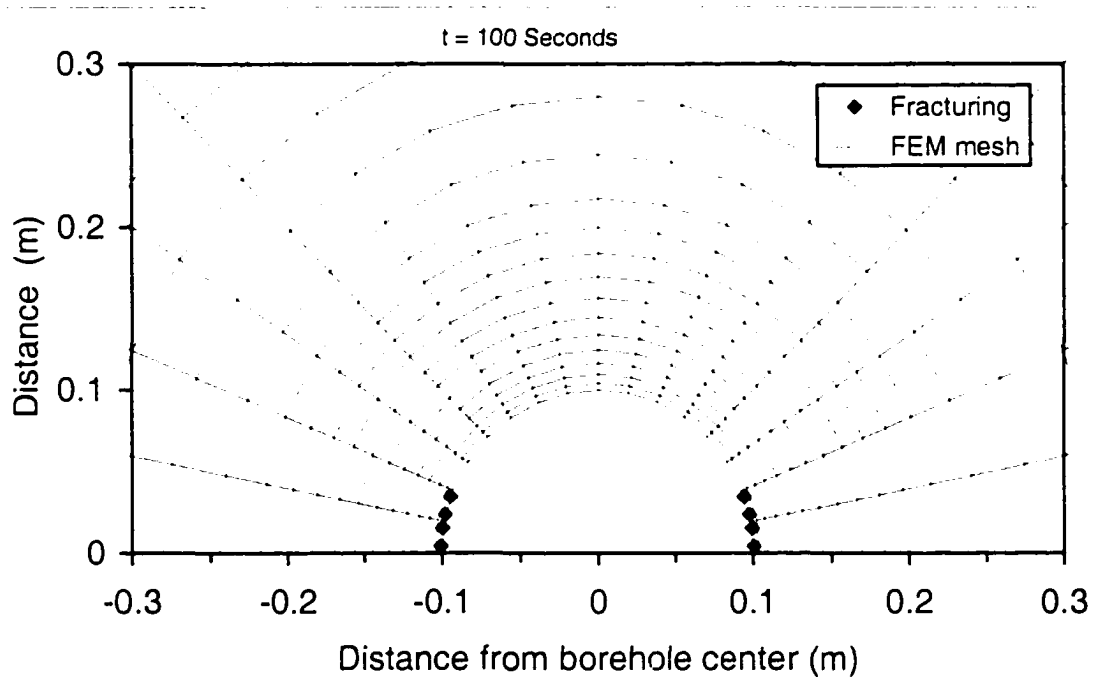


Figure 7.2.4 Fracturing area for mud pressure p_w = 25 MPa.

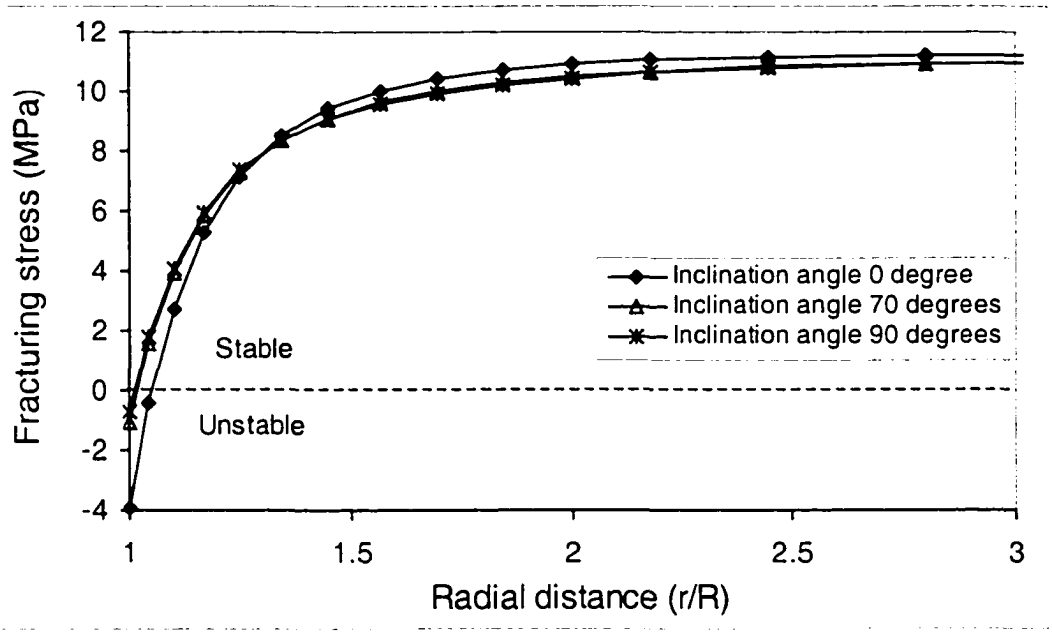


Figure 7.2.5 Effective fracturing stresses for different hole inclinations along the maximum stress direction at p_w = 25 MPa, t = 100 s.

7.3 Mohr-Coulomb Failure

Shear failure may occur around the borehole when the shear strength of formation is exceeded. Away from the wall of the borehole, where the radial stress may produce increasing confinement, shear failure is more likely to occur. The Mohr-Coulomb failure criterion can be used to determine such a failure mechanism. This criterion can be expressed as (Figure 7.3.1):

$$\tau = c + \sigma' \tan\phi \tag{7.3.1}$$

where ϕ is the angle of internal friction and c is the cohesion.

In the principal space, $(\sigma'_1, \sigma'_2, \sigma'_3)$, the Mohr-Coulomb failure criterion is represented by a right, irregular hexagonal pyramid whose axis is equally inclined with respect to the principal axis as shown in Figure 7.3.2 (Shield, 1955). In the principal form, it is:

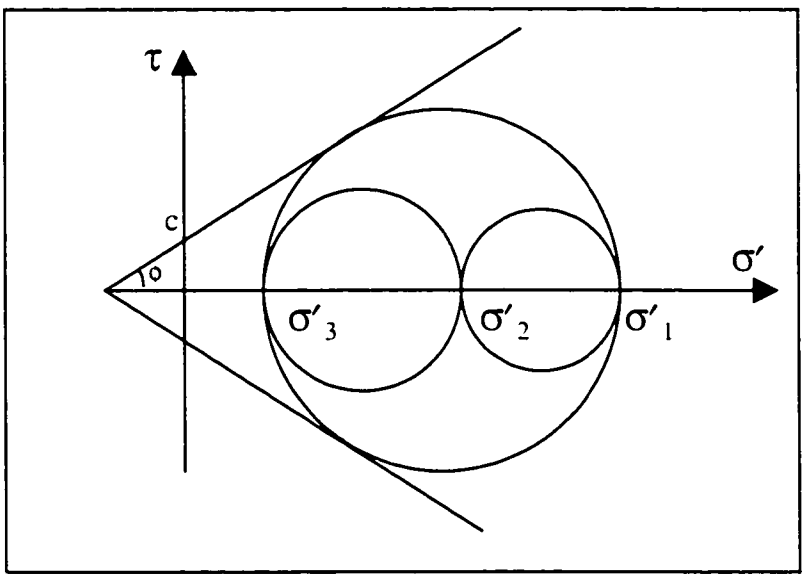


Figure 7.3.1 Mohr-Coulomb failure criterion.

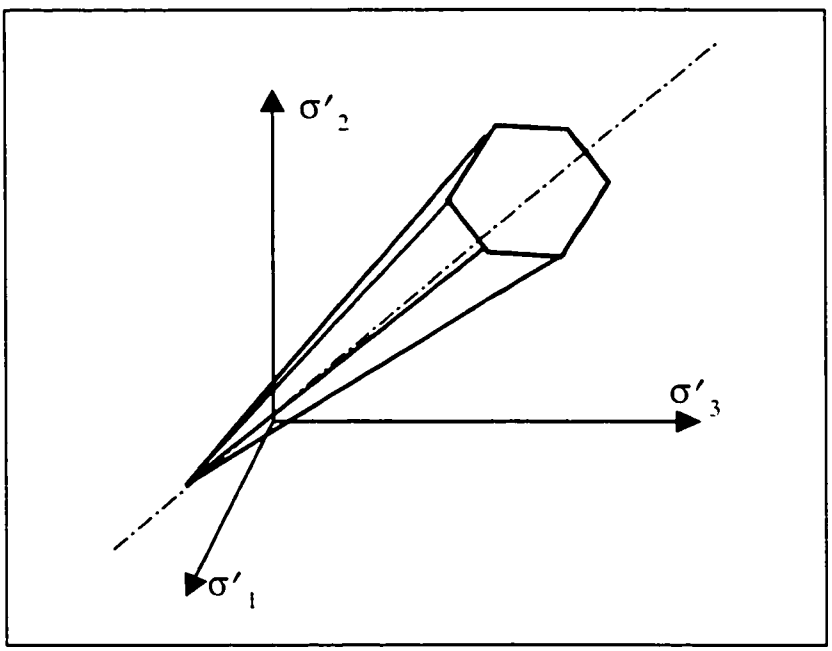


Figure 7.3.2 Mohr-Coulomb failure criterion in the principal stress space.

$$\sigma_i' = \sigma_c + q\sigma_j' \tag{7.3.2}$$

where σ_i', σ_j' are the effective principal stresses, $\sigma_i' > \sigma_j'$ and $q = (1+\sin\phi)/(1-\sin\phi)$.

The effective Mohr-Coulomb failure stress can be defined as:

$$\sigma_{mohr} = \sigma_c + q\sigma_j' - \sigma_i' \tag{7.3.3}$$

where σ_{mohr} is the effective Mohr-Coulomb failure stress. When the Mohr-Coulomb failure stress is below zero, failure will occur.

Figure 7.3.3 is the Mohr-Coulomb failure area around the borehole for a stress-free wellbore inclined at an angle of 70° and at t = 100 s, assuming that the compressive strength of the formation rock is 41 MPa and the angle of internal friction is 30°. It is obvious that the Mohr-Coulomb failure mainly concentrates around the borehole crown, i.e., in the minimum stress direction. As the hole inclination increases, the effective Mohr-Coulomb stress has a smaller negative magnitude and the unstable area decreases (Figure 7.3.4).

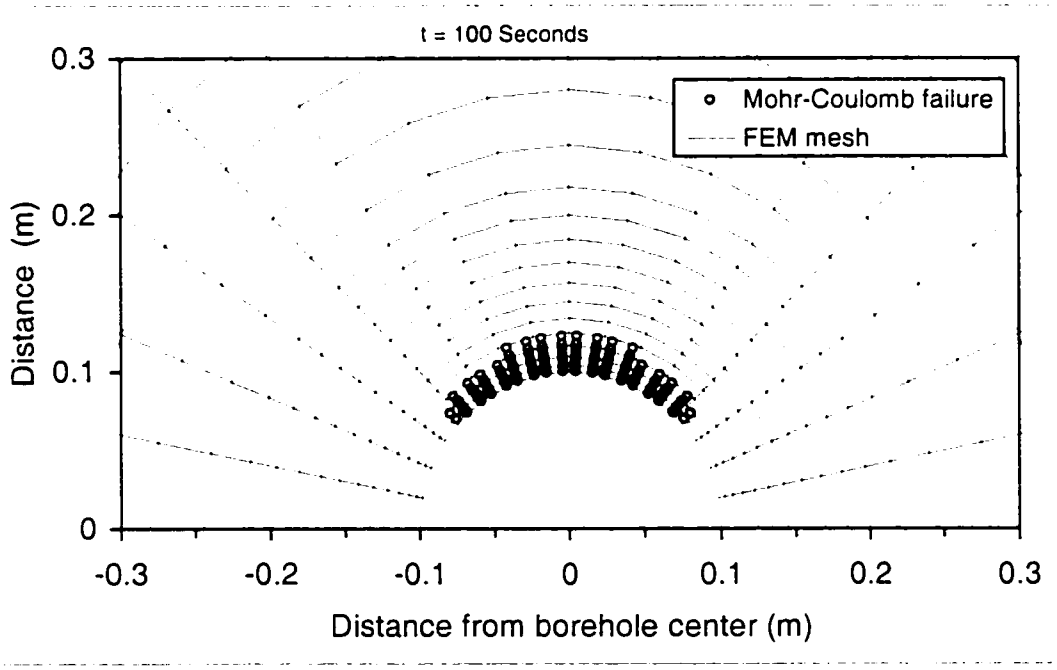


Figure 7.3.3 Mohr-Coulomb failure area for a stress-free borehole wall.

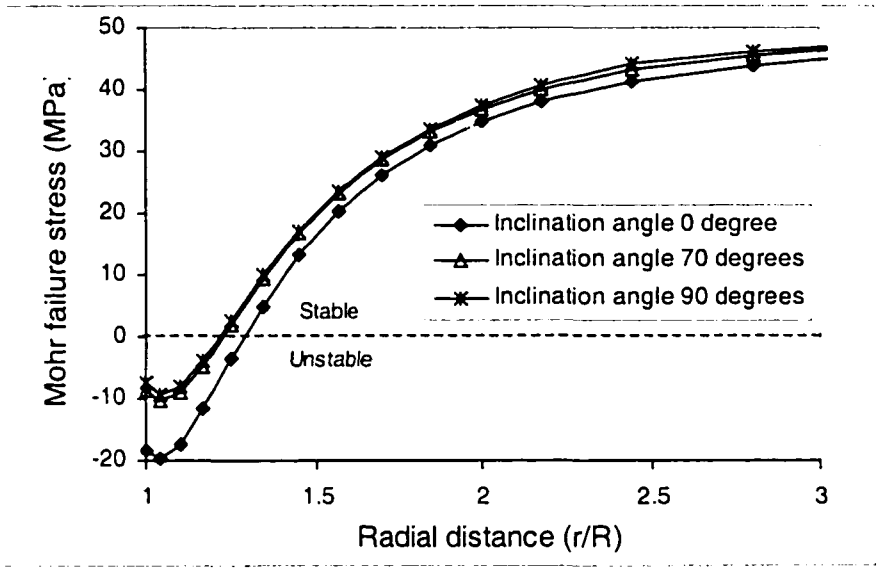


Figure 7.3.4 Effective Mohr-Coulomb failure stresses for different hole inclinations along the minimum stress direction at t = 100 s.

7.4 Drücker-Prager Failure

The effect of the intermediate principal stress is not considered in any of the failure criteria mentioned above. Research results have shown (e.g. Mogi, 1972) that the intermediate principal stress plays an important role in the failure of rocks. The effect of the intermediate principal stress on the failure of rock can be conveniently represented by the well-known Drüker-Prager yield condition:

$$\sqrt{J_2} = 3\alpha I_1' + \kappa \tag{7.4.1}$$

where α and κ are material constants and the detailed expressions of I_1' and J_2 can be found in Appendix C.

The effective collapse stress can be defined as (Bradley, 1979):

$$\sigma_{cl} = 3\alpha I_1' + \kappa - \sqrt{J_2} \tag{7.4.2}$$

where σ_{cl} is the effective collapse stress. When the collapse stress is negative, collapse will occur.

The Drüker-Prager yield condition is an extended form of the Mohr-Coulomb failure criterion. In the principal stress space, Equation (7.4.1) represents a cone with the same axis as the pyramid resulting from Shield's representation of the Coulomb criterion (Shield, 1955). The section in the deviatoric plane shows that it is possible in various ways to relate the two failure criteria (Figure 7.4.1). For plane-strain conditions it is recommended that the inside cone tangent to the pyramid is used (Kovari, 1977). In this case the conversion formulae for the material parameters from the Coulomb criterion to the Drüker-Prager criterion are (Figure 7.4.1):

$$\alpha = \frac{\tan\phi}{\sqrt{9 + 12\tan^2\phi}} \tag{7.4.3}$$

$$\kappa = \frac{3c}{\sqrt{9 + 12\tan^2\phi}} \tag{7.4.4}$$

When the external pyramid envelope is used, the conversion formulae for the material parameters from the Coulomb criterion to the Drüker-Prager criterion are:

$$\alpha = \frac{2\sin\phi}{\sqrt{3}(3 - \sin\phi)} \tag{7.4.5}$$

$$\kappa = \frac{6c\cos\phi}{\sqrt{3}(3 - \sin\phi)} \tag{7.4.6}$$

When the internal cone envelope coincident at $\theta = \pi/6$ is used, the conversion formulae for the material parameters from the Coulomb criterion to the Drüker-Prager criterion are:

$$\alpha = \frac{2\sin\phi}{\sqrt{3}(3+\sin\phi)} \tag{7.4.7}$$

$$\kappa = \frac{6c\cos\phi}{\sqrt{3}(3+\sin\phi)} \tag{7.4.8}$$

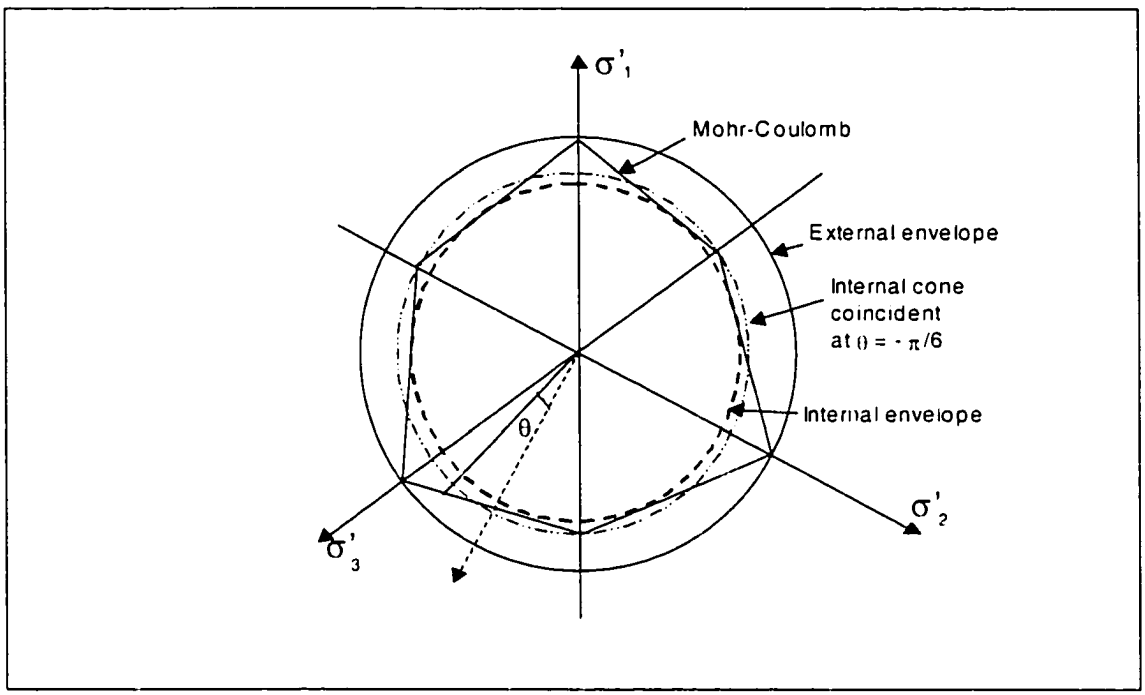


Figure 7.4.1 Coulomb yield surface and different possibilities for corresponding Drücker-Prager yield conditions.

Table 7.4.1 lists the material parameters of the Drüker-Prager criterion obtained for the above conversion formulae when the material strength parameters are $\varphi = 30°$ and c = 11.5 MPa. Obviously, the Drüker-Prager material parameters for the three envelopes are different.

Based on the failure envelope plots compiled for various rocks (Woodland, 1990), material parameters α and κ in Drücker-Prager failure criterion can range from 0.13 to 0.37, and from 5.5 MPa to 25.5 MPa, respectively. For the present analyses, it is assumed that $\alpha = 0.14$ and κ = 12 MPa.

Table 7.4.1 Material parameter conversion from the Coulomb criterion ($\varphi = 30°$ and c = 11.5 MPa) to the Drüker-Prager criterion

Envelope	α	κ (MPa)
Inside cone tangent to the pyramid	0.16	9.6
External pyramid envelope	0.23	13.8
Internal pyramid envelope	0.16	9.9

Figure 7.4.2 is the Drücker-Prager failure (collapse) around the borehole for a stress-free wellbore inclined at an angle of 70° and at t = 100 s. The collapse occurs mainly around the minimum stress direction. In the maximum stress direction (borehole sidewalls) there is no collapse. Figure 7.4.3 shows that as the hole inclination increases, the effective Mohr-Coulomb stress has a smaller negative magnitude and the unstable area decreases.

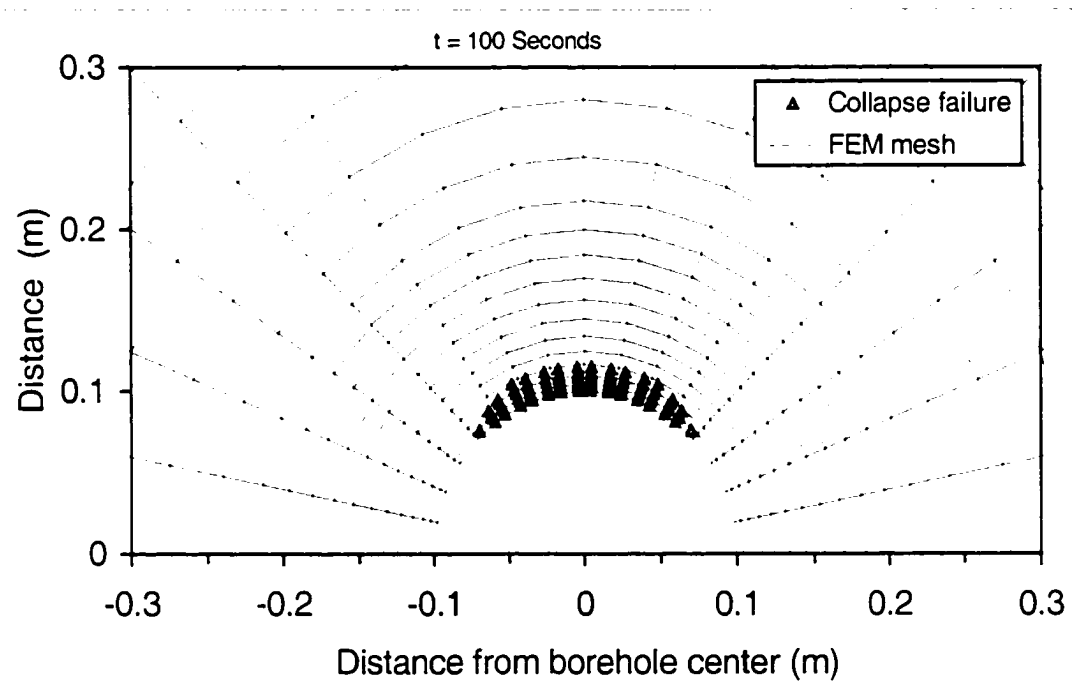


Figure 7.4.2 Collapse failure area for a stress-free borehole wall.

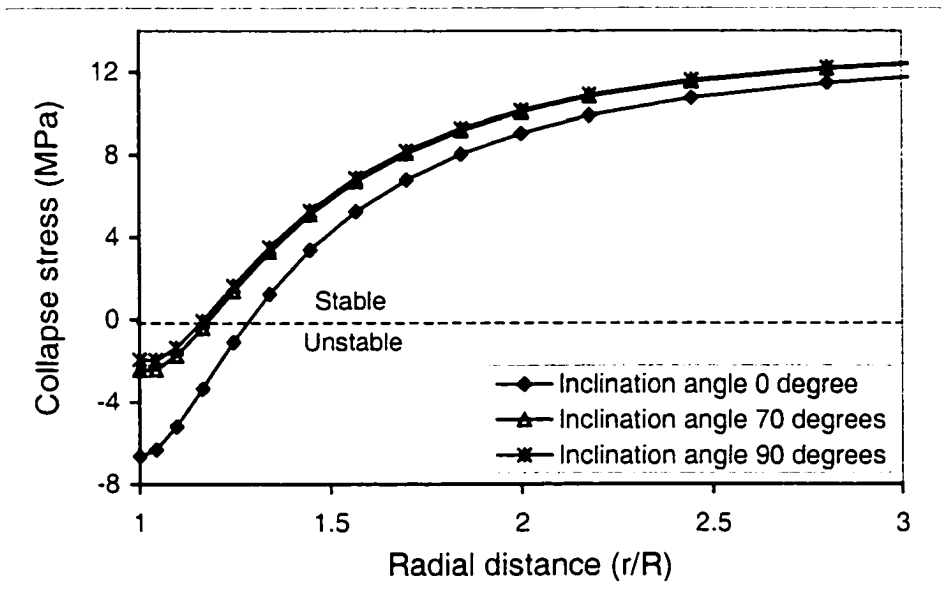


Figure 7.4.3 Effective collapse stresses for different hole inclinations along the minimum stress direction at t = 100 s.

Chapter 8

Model Application

The developed dual-porosity finite element model can not only be used to analyze wellbore problems, but can also be applied to other mechanical problems, such as tunneling, slope stability problems, surface subsidence, hydraulic fracturing simulation, fracturing pressure determination, roadways, room and pillar stability problems, and coupled hydraulic and mechanical problems. This chapter presents some applications of the finite element model to practical problems, including inclined and horizontal boreholes, stress-dependent permeability and rock cutting problems.

8.1 Inclined and Horizontal Wellbores

The capabilities of the finite element model have been demonstrated in wellbore problems presented in the previous chapters. For practical purposes, the model used here focussed on simulation of borehole stability and selection of the critical drilling mud weight. Several cases were analyzed, such as, boreholes drilled in a normal stress region (i.e., $\sigma_v > \sigma_H > \sigma_h$), in a tectonic stress region ($\sigma_H > \sigma_v > \sigma_h$) and in a faulted zone.

8.1.1 Wellbore in Normal Stress Region

The following specific geometry and material properties were used in the ongoing analysis. The radius of the borehole is R = 0.1 m. The rock is a Gulf of Mexico shale with the following properties: $G = 7.6 \times 10^2$ MPa, $\nu = 0.219$, $\nu_u = 0.461$, $B = 0.915$, n = 0.02, $k = 1\times 10^{-7}$ darcy with $\mu = 0.001$ Pa·s (Cui et al., 1999a). Table 8.1.1 lists the poromechanical parameters used in the analysis, in which some parameters were calculated from this given material properties using Equation (5.2.5).

The far-field stresses and pore pressure were: $S_{x'} = \sigma_H = 18$ KPa/m, $S_{y'} = \sigma_h = 14$ KPa/m, $S_{z'} = \sigma_v = 22.6$ KPa/m, $p_w = 10.4$ KPa/m (Bradley, 1979). All the analyses were carried out at the true vertical depth of 1000 m and concentrated on the borehole failure and mud weight selection.

Table 8.1.1 Parameters for analyses of the borehole in normal stress region

Parameter	Unit	Magnitude
Elastic modulus (E)	GN/m^2	18.53
Poisson's ratio (ν)	-	0.219
Fracture stiffness (K_n, K_{vh})	$MN/m^3/m$	4.821×10^5
Fluid bulk modulus (K_f)	MN/m^2	173.45
Grain bulk modulus (K_s)	GN/m^2	323.23
Matrix porosity (n_{ma})	-	0.02
Fracture porosity (n_{fr})	-	0.002
Matrix mobility (k_{ma}/μ)	M^4/MN s	10^{-10}
Fracture mobility (k_{fr}/μ)	M^4/MN s	10^{-9}
Fracture spacing (s)	m	1
Uniaxial compressive strength (σ_c)	MN/m^2	41
Internal friction angle (φ)	°	30
Material strength parameter (α)	-	0.14
Material strength parameter (κ)	MN/m^2	12

In order to demonstrate the characteristics of borehole failures, a stress-free wellbore (no support) was first examined. Boreholes with three different inclination angles, i.e., φ_z = 0, 50, and 90° were analyzed.

Figures 8.1.1 and 8.1.2 are Mohr-Coulomb failure areas around the borehole at t = 100 s for hole inclination 50° and 90°. It is obvious that the borehole inclination increases the failure area. Note from the calculation that no failure occurred when the hole inclination

is 0°. The reason is that inclination increases local stress as well as stress differences along the wellbore sections and therefore induces larger failure zone. Figure 8.1.3 shows that the local stress in the wellbore section are σ_x = 18 MPa, σ_y = 14 MPa for a vertical borehole (φ_z = 0°) and σ_x = 22.6 MPa, σ_y = 14 MPa for a horizontal borehole (φ_z = 90°).

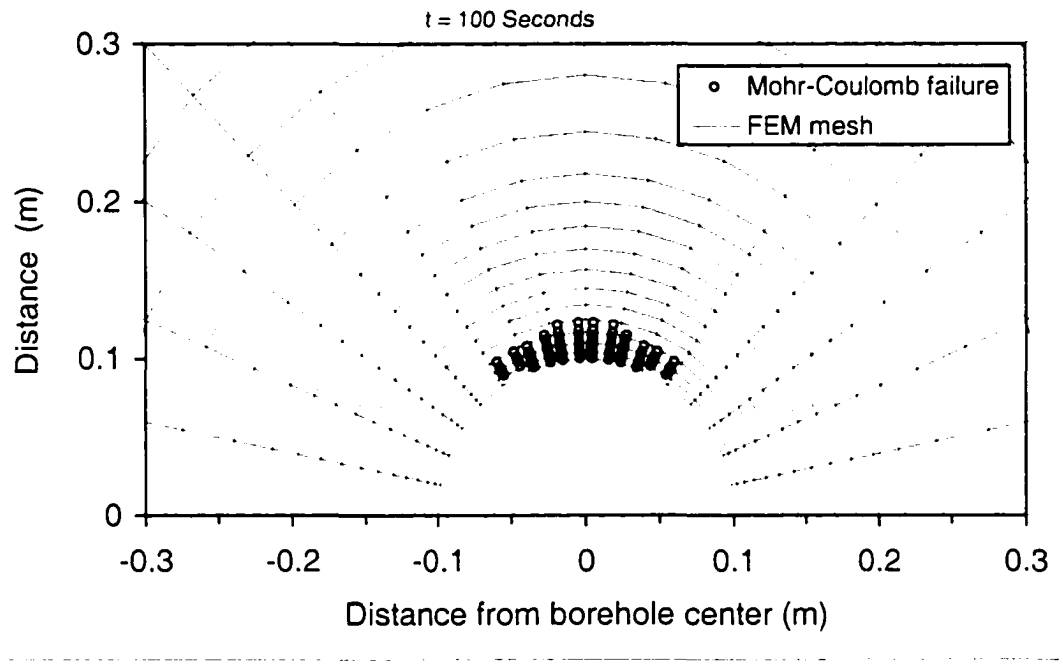


Figure 8.1.1 Mohr-Coulomb failure area in the normal stress region at t = 100 s for a borehole inclination of 50°.

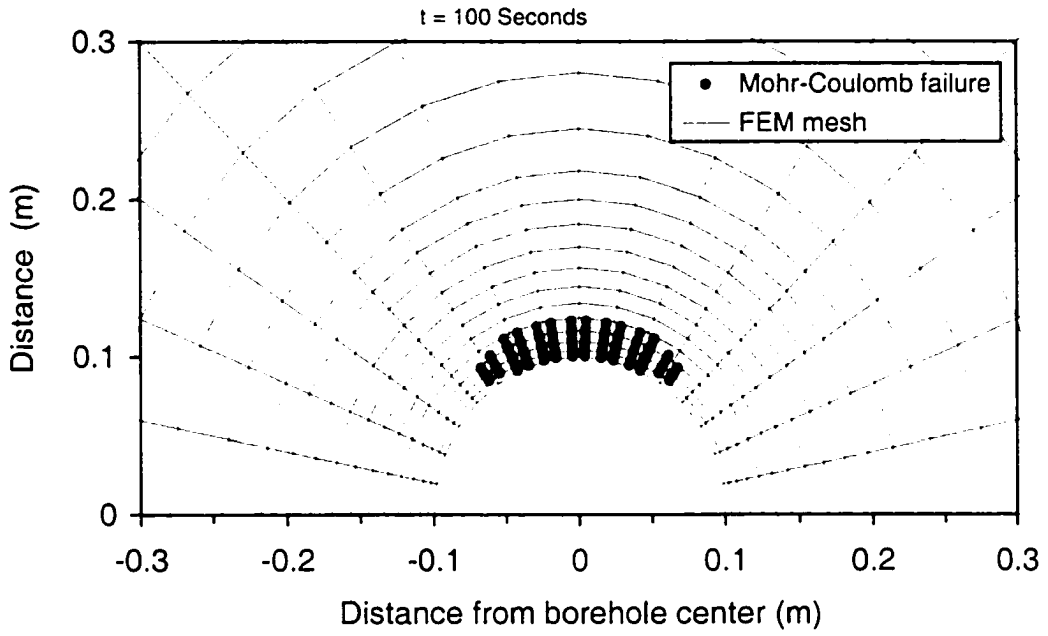
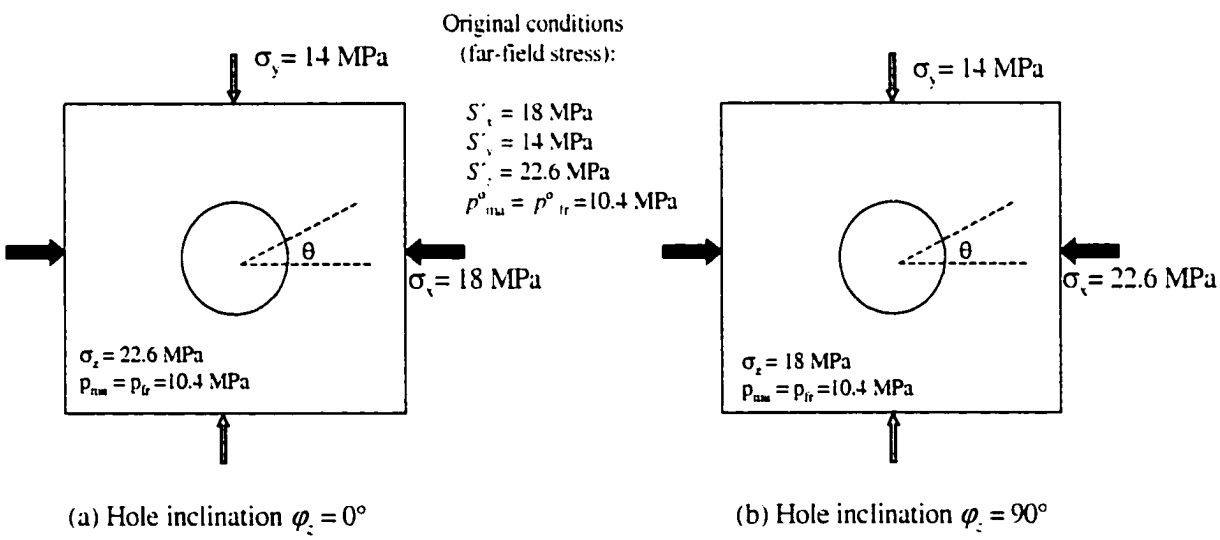


Figure 8.1.2 Mohr-Coulomb failure area in the normal stress region at t = 100 s for a borehole inclination of 90°.



(a) Hole inclination $\varphi_z = 0°$ (b) Hole inclination $\varphi_z = 90°$

Figure 8.1.3 State of stress in local system for a borehole drilled in two different orientations (φ_z = 0 and 90°).

Figures 8.1.4 and 8.1.5 show collapse areas around the borehole wall at t = 100 s for hole inclinations of 50° and 90°. The collapse area increases with the hole inclination since the stresses and stress differences increase in the case of a normal stress region.

Figures 8.1.6 and 8.1.7 are the spalling areas around the borehole section at t = 100 s for the same hole inclinations. It can be seen that spalling decreases with the hole inclination. This is due to that spalling depends directly on the tensile radial stress; in the normal stress region the inclination increases the compressive radial stress and decreases the tensile radial stress, as shown in Figure 8.1.8.

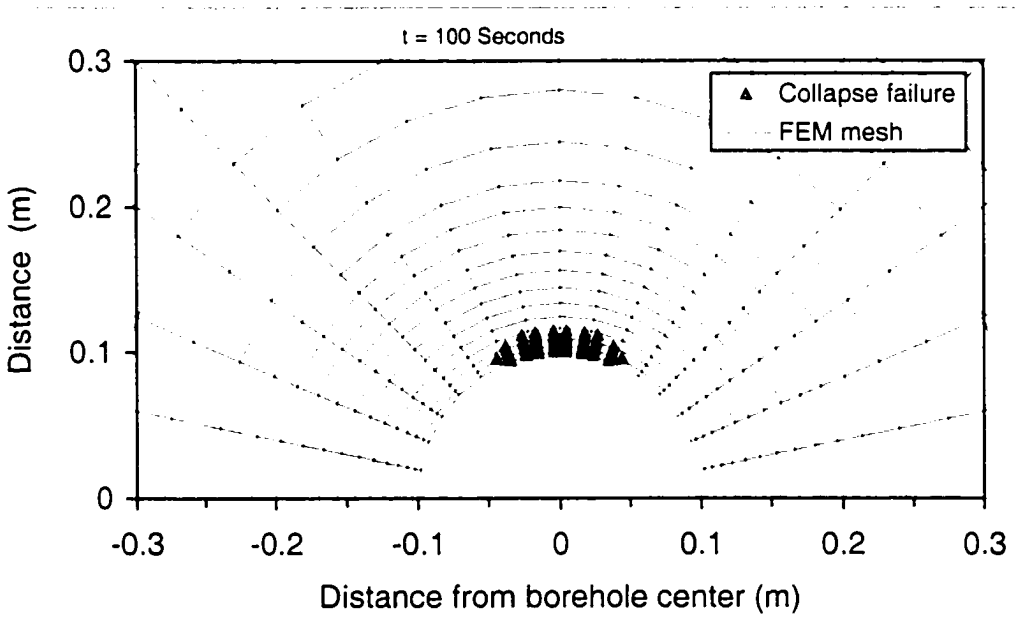


Figure 8.1.4 Collapse area in the normal stress region at t = 100 s for a hole inclination of 50°.

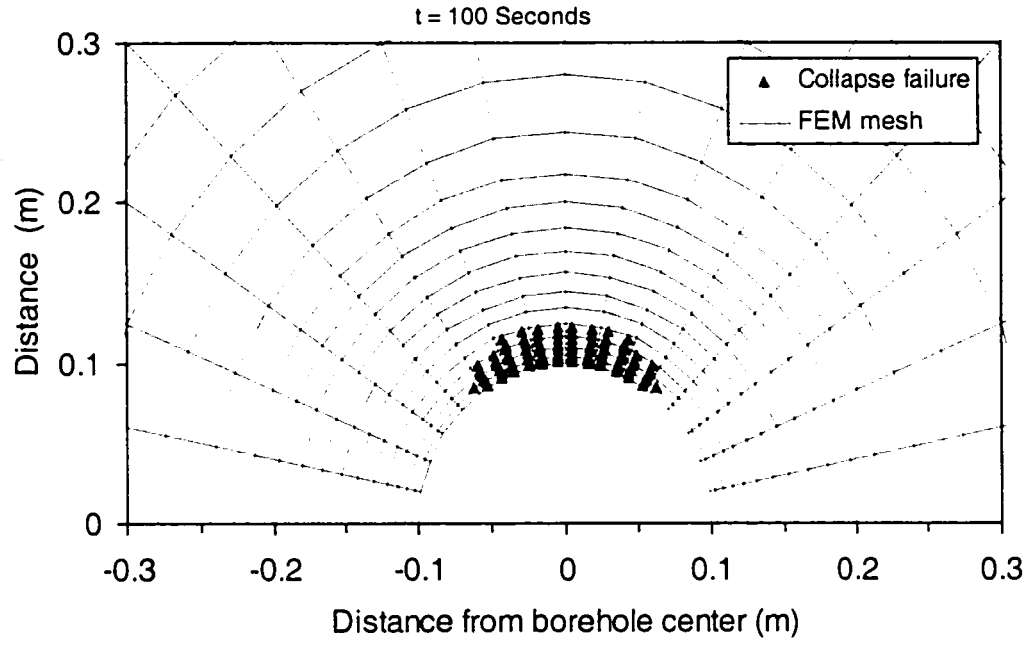


Figure 8.1.5 Collapse area in the normal stress region at t = 100 s for a hole inclination of 90°.

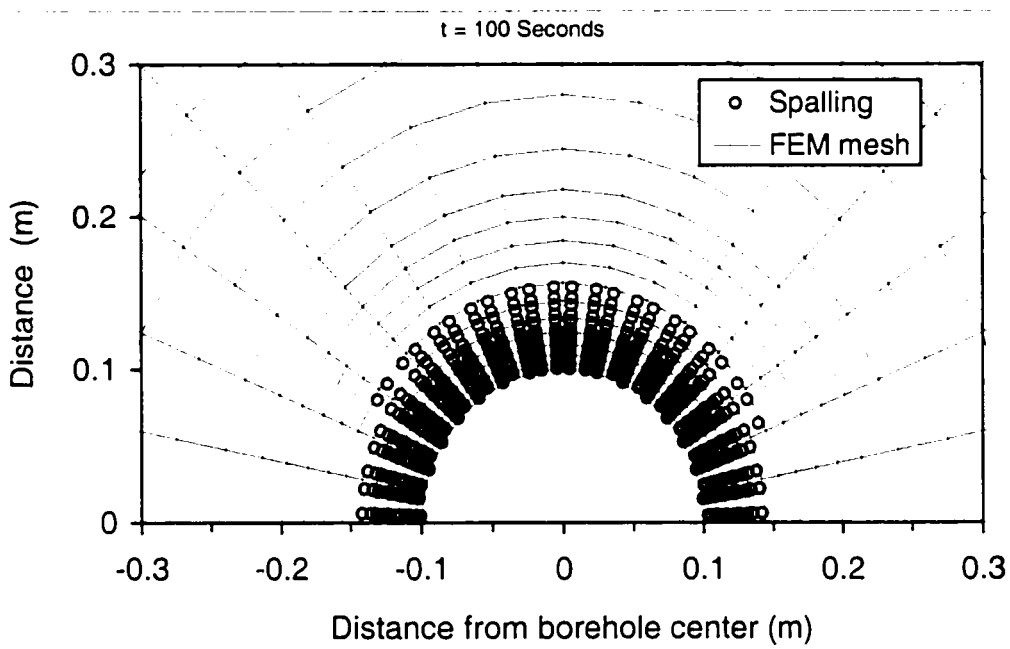


Figure 8.1.6 Spalling area in the normal stress region at t = 100 s for a hole inclination of 0°.

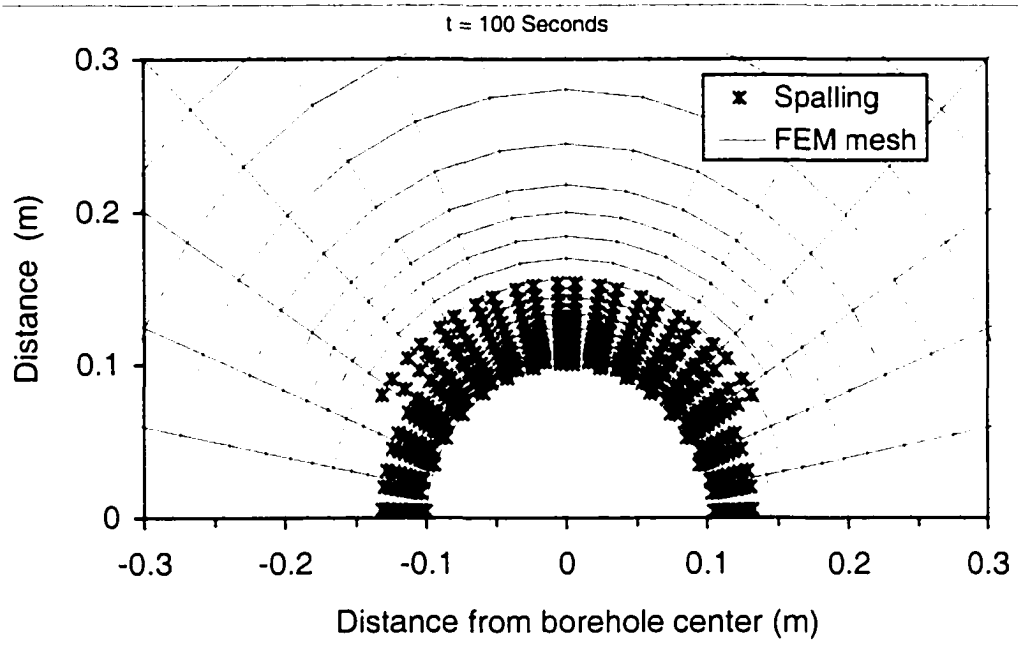


Figure 8.1.7 Spalling area in the normal stress region at t = 100 s for a hole inclination of 90°.

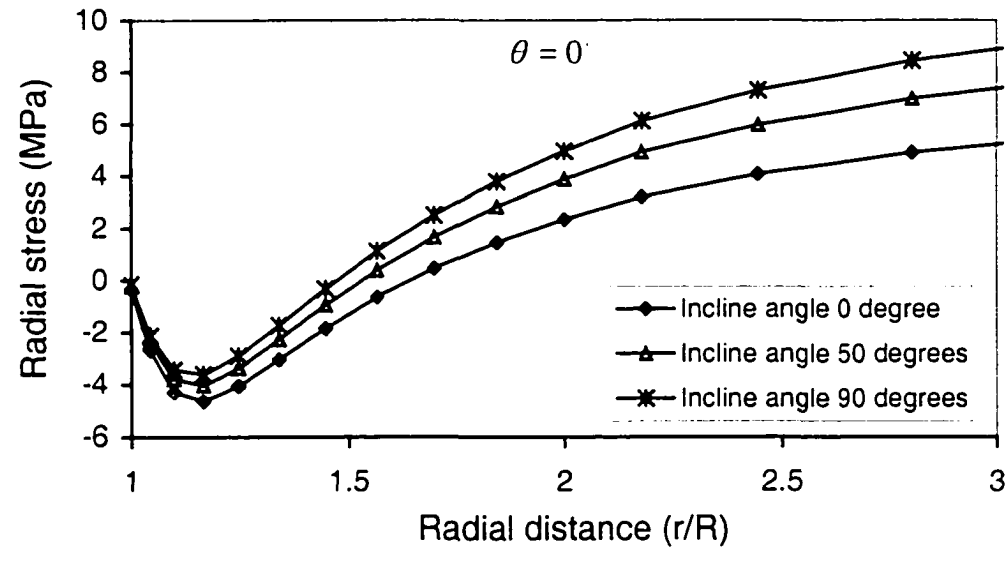


Figure 8.1.8 Effective radial stresses along borehole sidewall for a normal stress regime at t = 100 s for different hole inclinations.

With mud pressure support, borehole failure can usually be avoided; however, the borehole may be fractured and circulation loss may occur. Applying the presented finite element model, a range of mud weights for a stable hole was evaluated at each inclination angle. Figure 8.1.9 presents the envelopes that define such a safe range.

From this figure, some general observations can be made for boreholes drilled in a normal stress regime, i.e., as the inclination increase, the safe range of mud weight for collapse and fracturing decreases. At lower inclination angels, say $\varphi < 35°$, the borehole does not collapse for any mud weight. Therefore, in the normal stress region the lower deviational or vertical boreholes are more stable.

Figure 8.1.10 represents the safe range of mud weight for spalling and fracturing at t =100 s. It shows that the safe range is not much dependent on hole inclination angles.

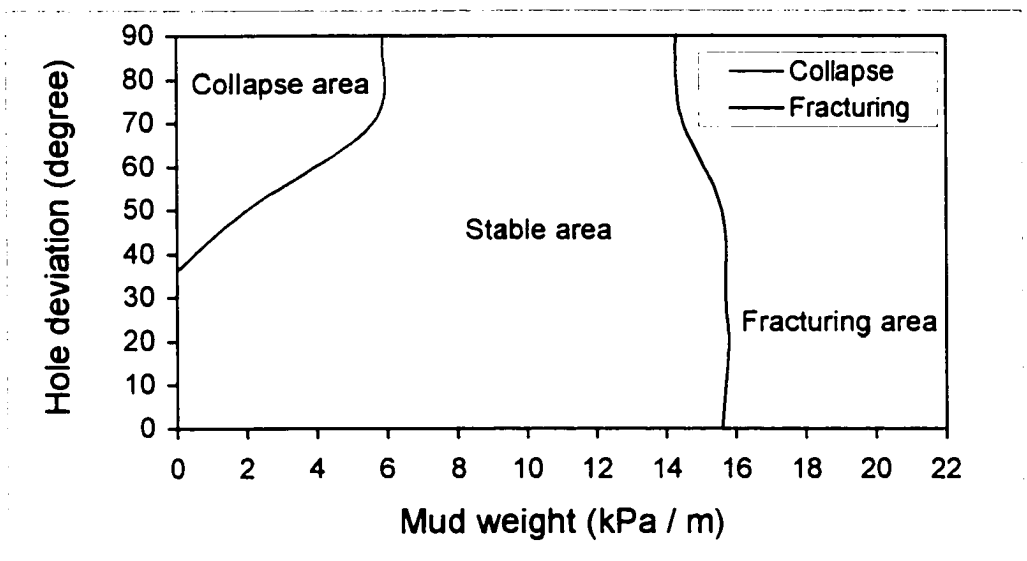


Figure 8.1.9 Mud weight range varying with the hole inclinations for collapse and fracturing at t = 100 s.

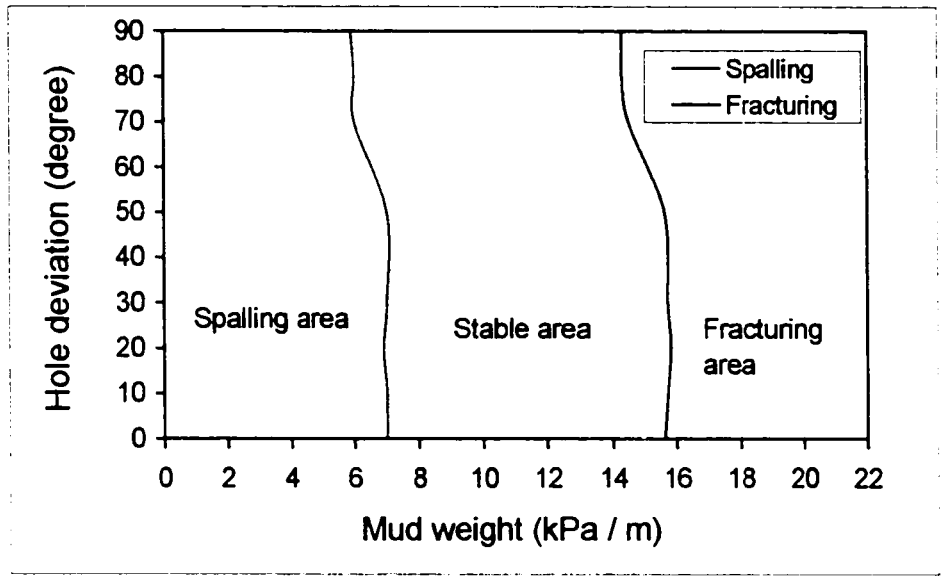


Figure 8.1.10 Mud weight range varying with the hole inclinations for spalling and fracturing at t = 100 s.

8.1.2 Wellbore in Tectonic Stress Region

In this section, the examined case is same as the example studied in the previous chapters but the maximum in-situ stress is in the horizontal plane (refer to Figure 6.1). The calculations were conducted at the true vertical depth of 1000 m.

Figures 8.1.11 and 8.1.12 are Mohr-Coulomb failure areas at t = 100 s for hole inclinations of 0° and 90°. It can be seen that the failure area decreases as the inclination angle increases. This is due to that the inclination reduces the stress and stress differences. In this case, the stresses vary from σ_x = 29 MPa, σ_y = 20 MPa at inclination φ = 0° to become σ_x = 25 MPa, σ_y = 20 MPa at inclination φ = 90°, as shown in Figure 6.6.4. Same conclusions can be drawn as for the collapse failure (Figures 8.1.13 and 8.1.14).

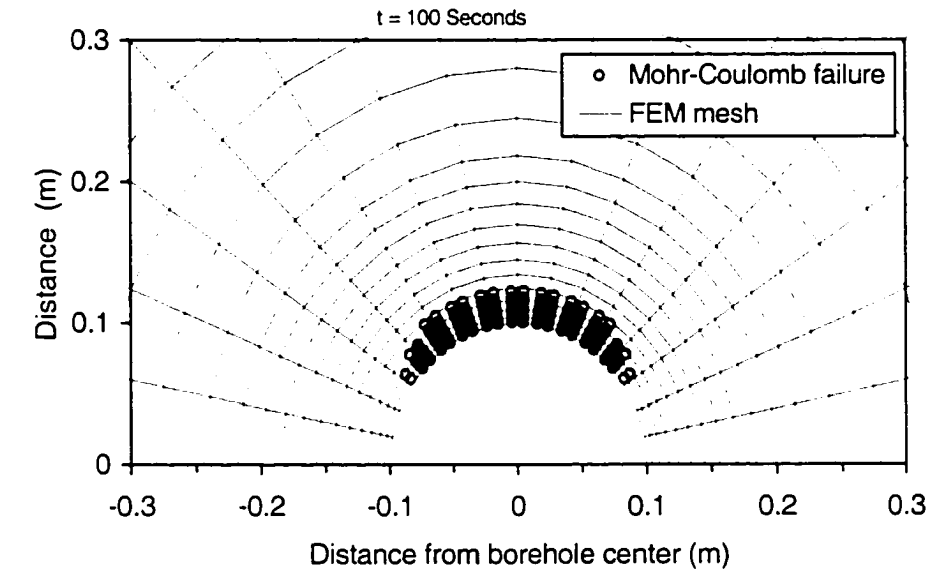


Figure 8.1.11 Mohr-Coulomb failure area in the tectonic stress region at t = 100 s for a borehole inclination of 0°.

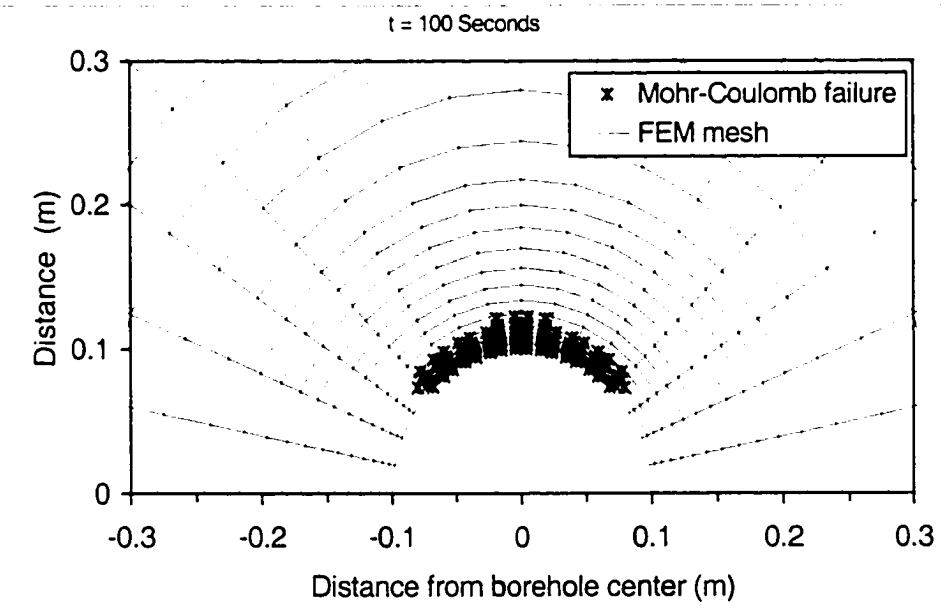


Figure 8.1.12 Mohr-Coulomb failure area in the tectonic stress region at t = 100 s for a borehole inclination of 90°.

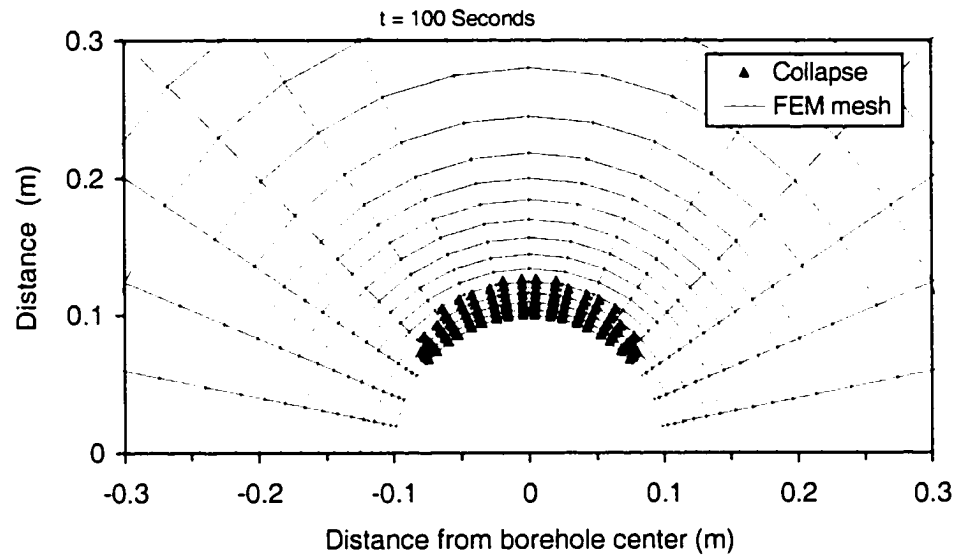


Figure 8.1.13 Collapse area in the tectonic stress region at t = 100 s for a borehole inclination of 0°.

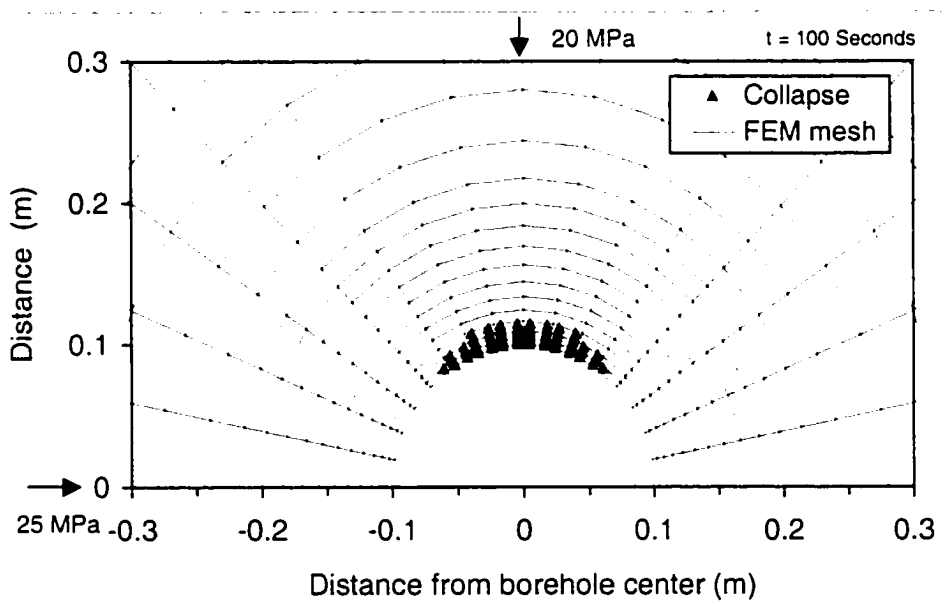


Figure 8.1.14 Collapse area in the tectonic stress region at t = 100 s for a borehole inclination of 90°.

Figure 8.1.15 is the envelopes that define the safe range of the mud weight for collapse and fracturing as a function of the inclination angles at t =100 s. It shows that the safe range of mud weight increases considerably with the hole inclination. Comparing with Figure 8.1.9, it can be concluded that the influence of the inclination on safe range of mud weight in the tectonic stress region is reversed with respect to the normal stress case.

Figure 8.1.16 represents the safe range of the mud weight for spalling and fracturing with respect to hole inclination angles. It observes that the mud weight envelope for spalling is not much dependent on borehole inclinations.

Therefore, in a tectonic stress regime, the higher the borehole deviation, the more stable the boreholes.

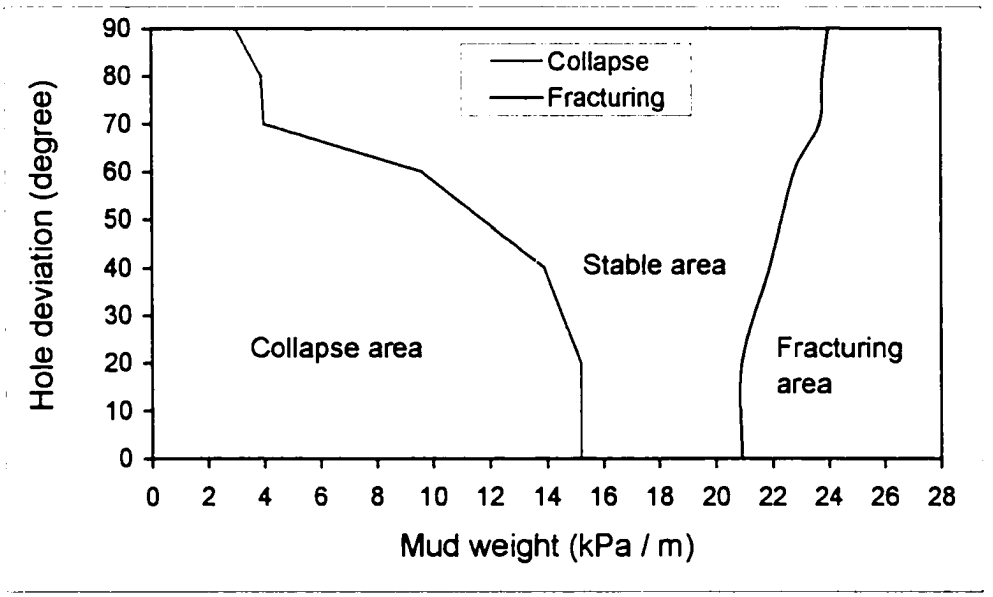


Figure 8.1.15 Mud weight range varying with the hole inclinations for collapse and fracturing at t = 100 s in a tectonic stress regime.

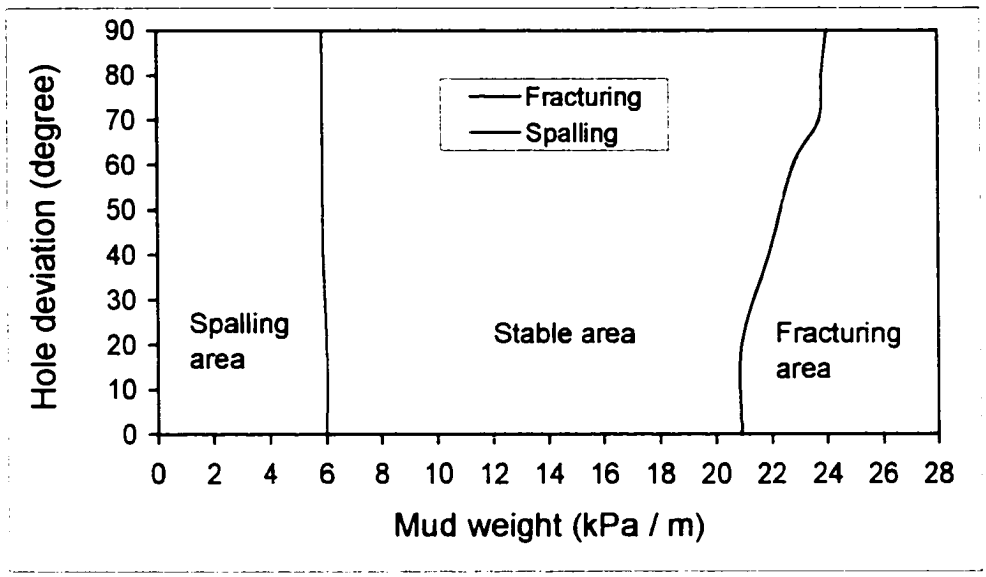


Figure 8.1.16 Mud weight range varying with the hole inclinations for spalling and fracturing at t = 100 s in a tectonic stress regime.

8.1.3 Drilling Directions for Horizontal Wellbores

Many oil companies provide horizontal drilling strategy guidelines that call for drilling in the direction of the minimum horizontal stress. Their approach for best trajectory selections and drilling guidelines is to minimize the maximum value of stress concentration on the borehole wall by controlling the drilling direction and mud weight used during drilling. However, such an approach may not always be true for all conditions. The following analyses examine wellbore failures for the following two options: parallel and perpendicular to the maximum horizontal stress directions.

8.1.3.1 Horizontal borehole in tectonic stress regime

The case example is same as that presented in Section 8.1.2. The borehole collapse failure area is given in Figure 8.1.14 for drilling parallel to the maximum horizontal stress without internal support. Figure 8.1.17 presents the collapse failure area for the borehole drilled parallel to the minimum stress without any internal support. Comparing

Figures 8.1.14 and 8.1.17, it is obvious that there is much larger failure area for the hole drilled parallel to minimum stress direction. Comparing the local stress configurations around wellbore, it is observed that the stress difference for the borehole in the maximum stress direction is $\Delta\sigma$ = 5 MPa (Figure 8.1.14), the stress difference for the borehole in the minimum stress direction is $\Delta\sigma$ = 4 MPa (Figure 8.1.17); but, the latter has much larger failure area. Therefore, the bigger stress difference does not induce larger borehole failure, which is not consistent with the conventional understanding. This is due to that the Drüker-Prager criterion is applied for the collapse failure analysis, in which the intermediate stress plays a role.

Although the selected mud pressure can keep the borehole from failure during drilling, however, during open-hole production the bottom hole pressure equals the pore pressure, assuming that no mud cake exists around the wellbore. In the present case, the bottom pressure is 10 MPa during production. Figure 8.1.18 represents the collapsed area for a at bottom hole pressure p_w = 10 MPa, t = 100 s in case of a horizontal borehole drilled parallel to the minimum stress. It is observed that collapse failure still exists. From Figure 8.1.15, there is no any collapse failure for the horizontal hole drilled parallel to the maximum stress during open-hole production (the bottom pressure is 10 MPa).

Figures 8.1.19 and 8.1.20 are the Mohr-Coulomb (shear) failure areas for a borehole without internal support drilled parallel to the maximum and minimum stresses directions. It can be seen that there is a larger shear failure area for the hole drilled parallel to the minimum stress, although the stress difference is larger in the maximum stress direction ($\Delta\sigma$ = 5 MPa) than that in the minimum stress direction ($\Delta\sigma$ = 4 MPa). The modeling results show that during the open-hole production (bottom pressure is 10 MPa) there is no shear failure for the hole parallel to maximum stress, however, it has shear failure to take place for the borehole parallel to the minimum stress (Figure 8.1.21).

Therefore, it can be concluded that in a tectonic stress regime a horizontal borehole drilled parallel to maximum stress direction is more stable during both drilling and production, which is not coincident with the traditional drilling guidelines. Drilling in this direction also allows a single fracture parallel to the borehole to be generated during

stimulation, since natural fractures are usually perpendicular to the present-day minimum horizontal stress.

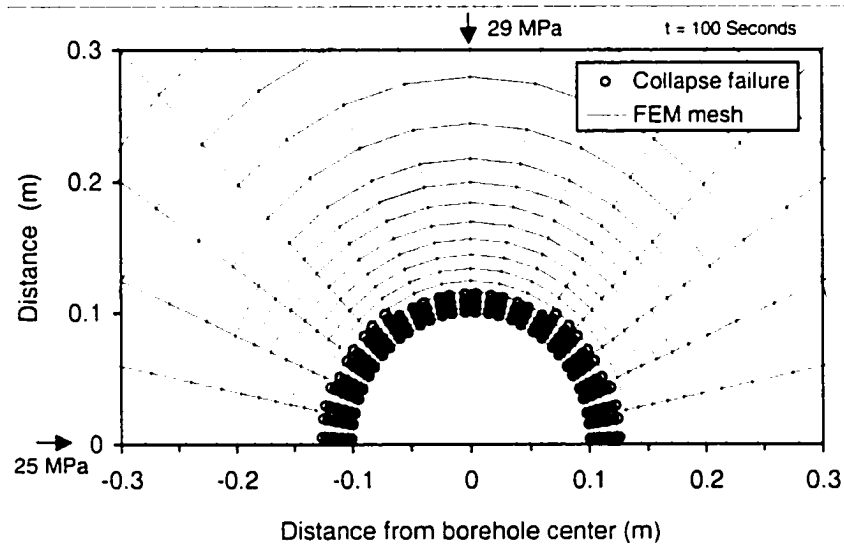


Figure 8.1.17 Collapse area in the tectonic stress region at t = 100 s for a horizontal borehole drilled parallel to the minimum stress.

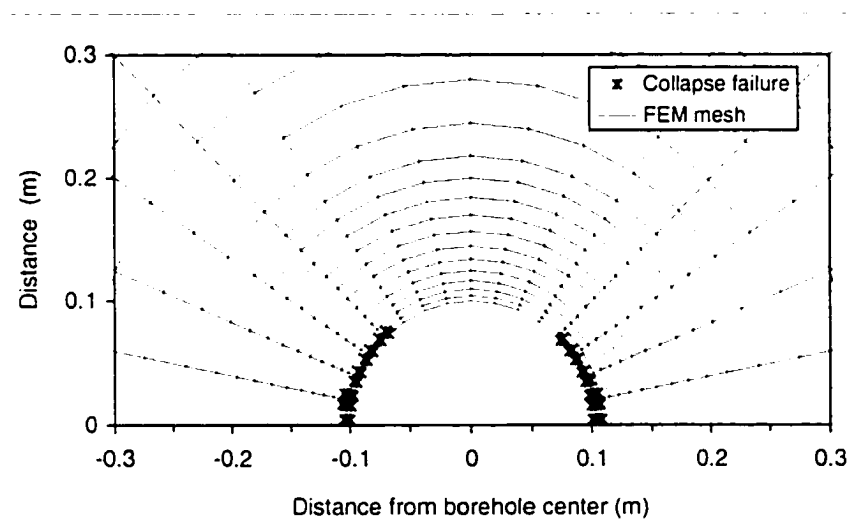


Figure 8.1.18 Collapse area in the tectonic stress region for a horizontal borehole drilled parallel to the minimum stress during production (bottom hole pressure 10 MPa).

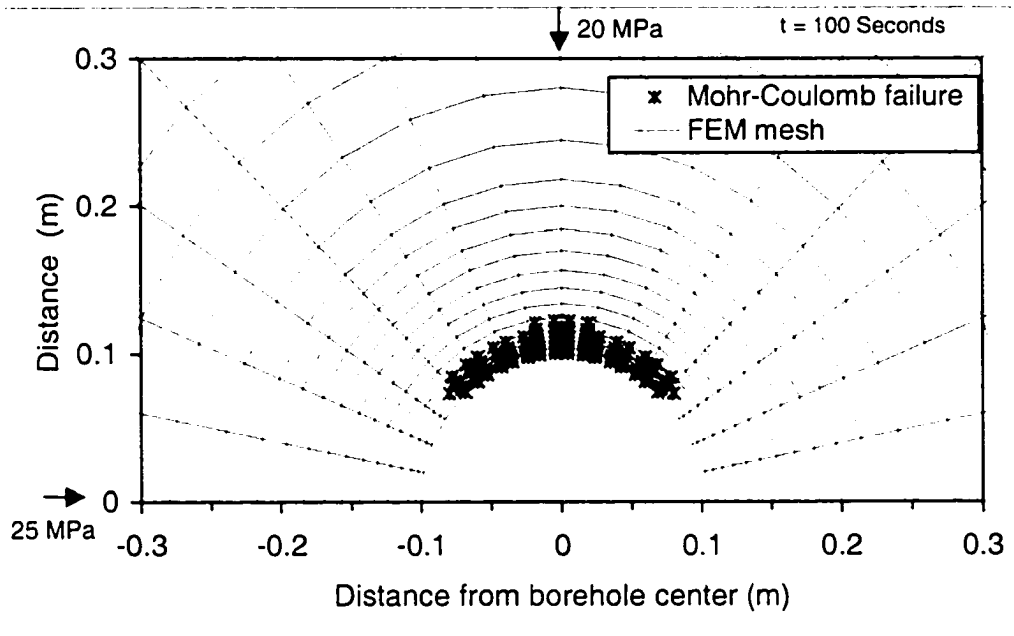


Figure 8.1.19 Shear failure area in the tectonic stress region at t = 100 s for a horizontal borehole drilled parallel to the maximum stress.

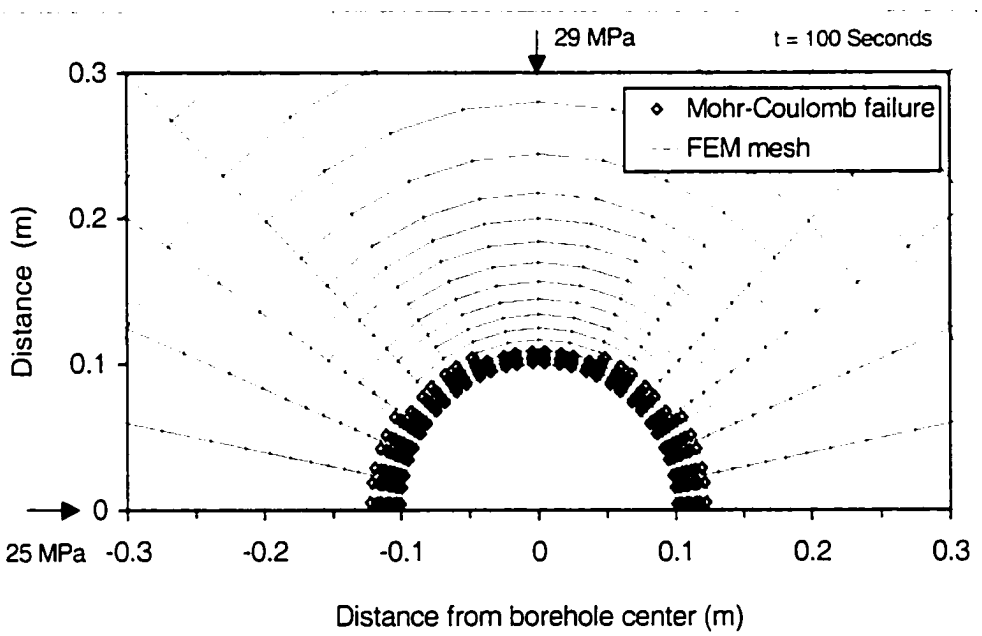


Figure 8.1.20 Shear failure area in the tectonic stress region at t = 100 s for a horizontal borehole drilled parallel to the minimum stress.

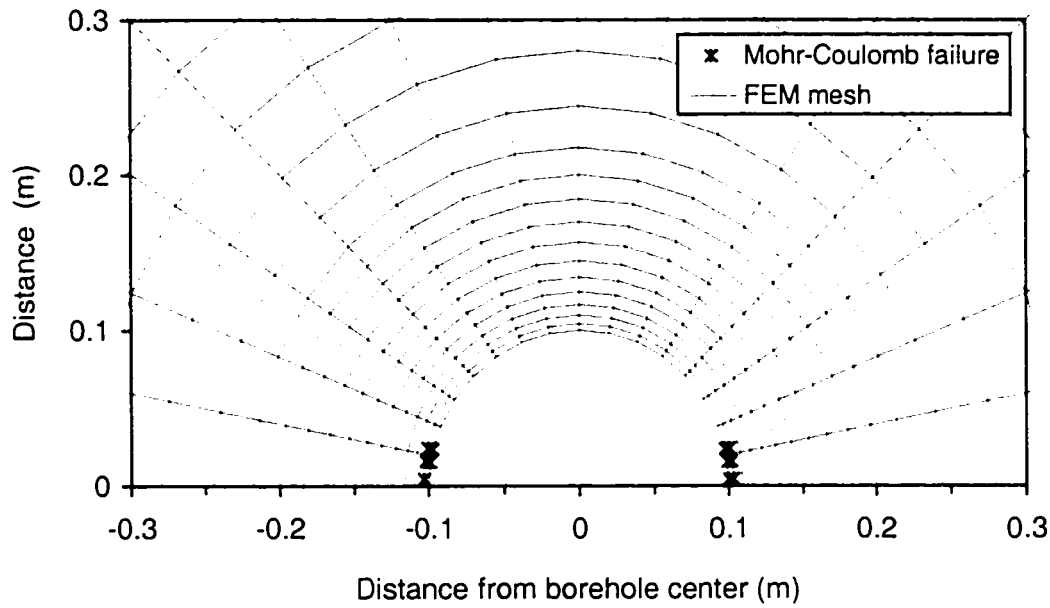


Figure 8.1.21 Shear area in the tectonic stress region for a horizontal borehole drilled parallel to the minimum stress during production (bottom hole pressure 10 MPa).

8.1.3.2 Horizontal borehole in normal stress regime

The following in-situ stress configurations are used in this analysis: the maximum vertical stress 69 MPa, the maximum and minimum horizontal stresses are 55.2 MPa and 48.3 MPa, respectively. The pore pressure is 31.7 MPa and the unconfined strength is 58.6 MPa (Zheng, 1998). The material parameter is κ = 18 MPa, other parameters are same as Table 8.1.1.

Figures 8.1.22 and 8.1.23 are the shear failure area for a borehole drilled parallel to the maximum and minimum stress directions without any internal support. It can be seen that there are larger shear failure areas for the hole drilled in the maximum direction. This is due to that in the Mohr-Coulomb failure criterion only the maximum and minimum principal stresses are considered and drilling in the minimum stress direction reduces the local far-field stress difference. In Figure 8.1.24, it is clear that the effective

Mohr-Coulomb stress has a bigger negative magnitude, meaning less stable, for the hole drilled parallel to the maximum direction. Figures 8.1.25 and 8.1.26 show the shear failure areas in the two directions during open-hole production (no mud cake effect), in which the bottom pressure is 31.7 MPa. It can be seen that there is a slightly larger shear failure for the hole drilled parallel to the minimum stress direction. Thus, it can be concluded that in a normal stress regime the hole drilled parallel to the minimum stress direction has less shear failure region during drilling, but, has a little bit larger shear failure during open-hole production.

During both drilling and open-hole production the collapse area is always larger for the hole drilled parallel to the minimum stress direction than that to maximum stress direction (See Figures 8.1.27, 8.1.28, 8.1.29 and 8.1.30), because the intermediate principal stress is considered in the Drücker-Prager failure criterion.

Therefore, in the normal stress regime the horizontal borehole drilled parallel to maximum stress direction is more stable during open-hole production.

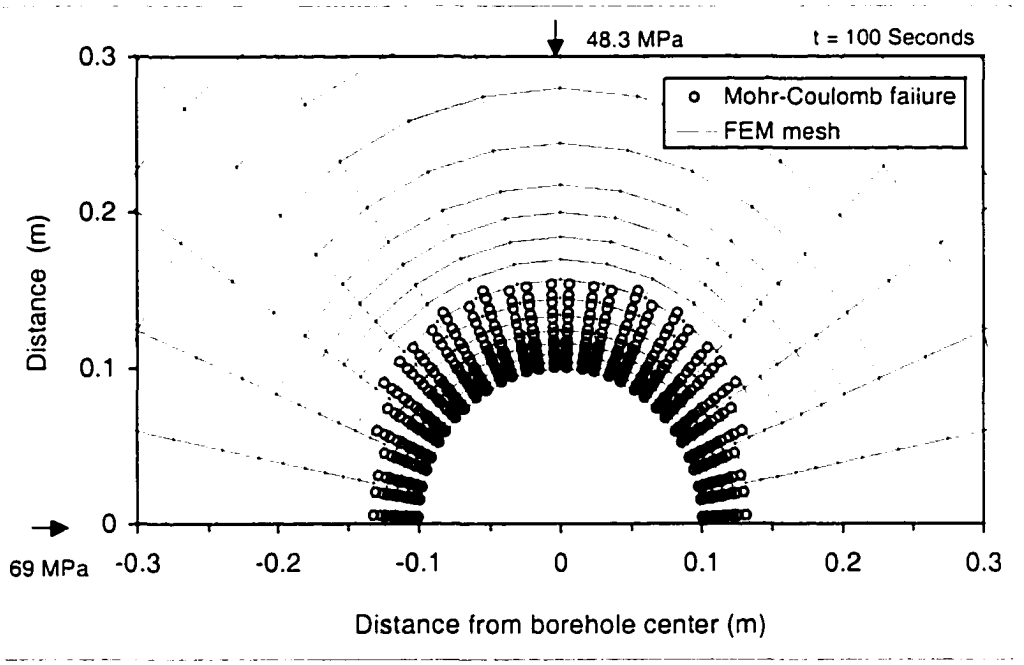


Figure 8.1.22 Shear failure area in normal stress region at t = 100 s for a horizontal borehole drilled parallel to the maximum stress.

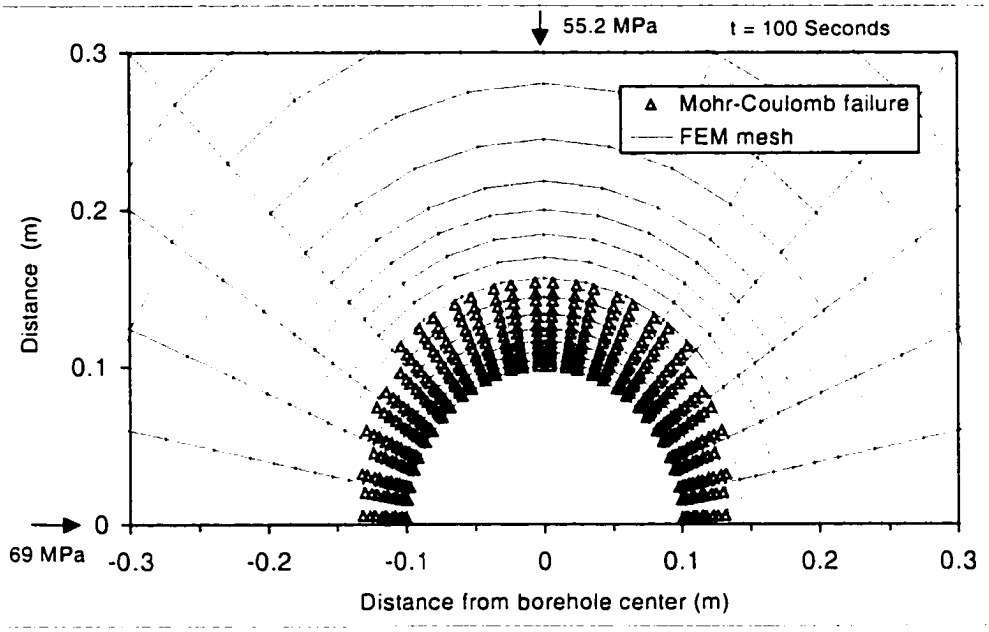


Figure 8.1.23 Shear failure area in normal stress region at t = 100 s for a horizontal borehole drilled parallel to the minimum stress.

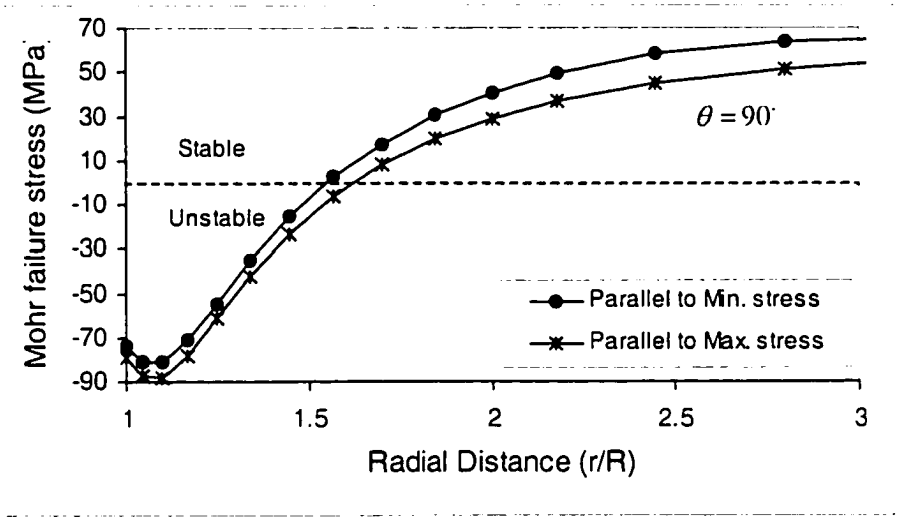


Figure 8.1.24 Mohr-Coulomb failure stresses in the hole crown at t = 100 s for a borehole without support and parallel to the minimum and maximum stress directions.

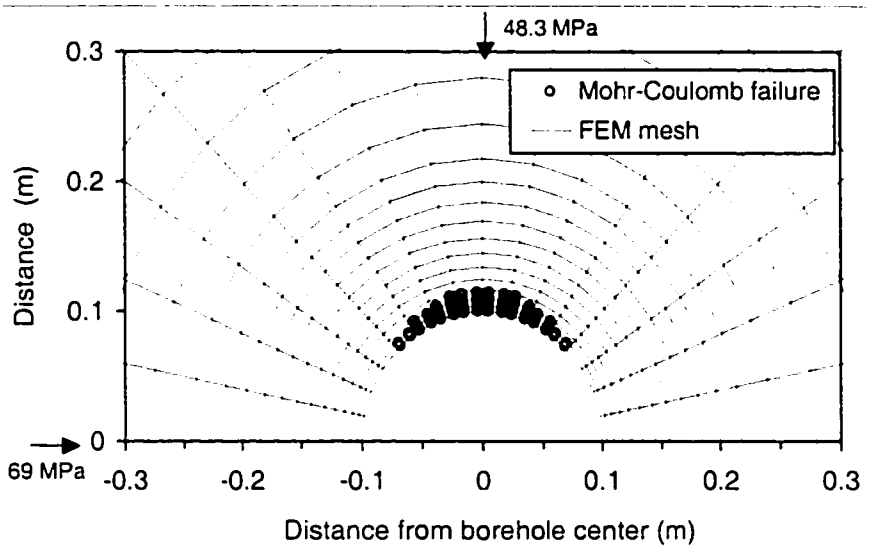


Figure 8.1.25 Shear failure area in normal stress region at t = 100 s for a horizontal borehole drilled parallel to the maximum stress during production (bottom pressure 31.7 MPa).

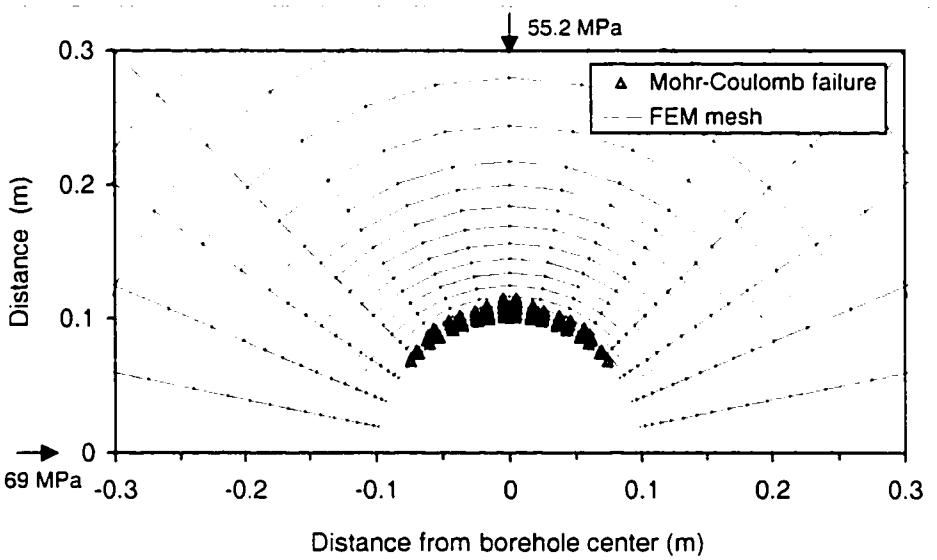


Figure 8.1.26 Shear failure area in normal stress region at t = 100 s for a horizontal borehole drilled parallel to the minimum stress during production (bottom pressure 31.7 MPa).

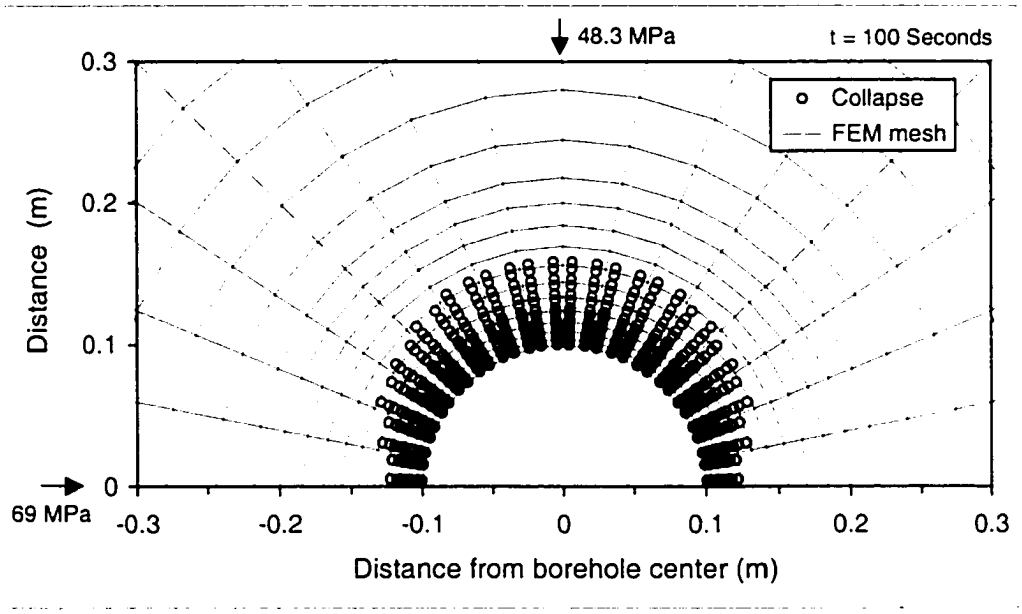


Figure 8.1.27 Collapse area in normal stress region at t = 100 s for a horizontal borehole drilled parallel to the maximum stress.

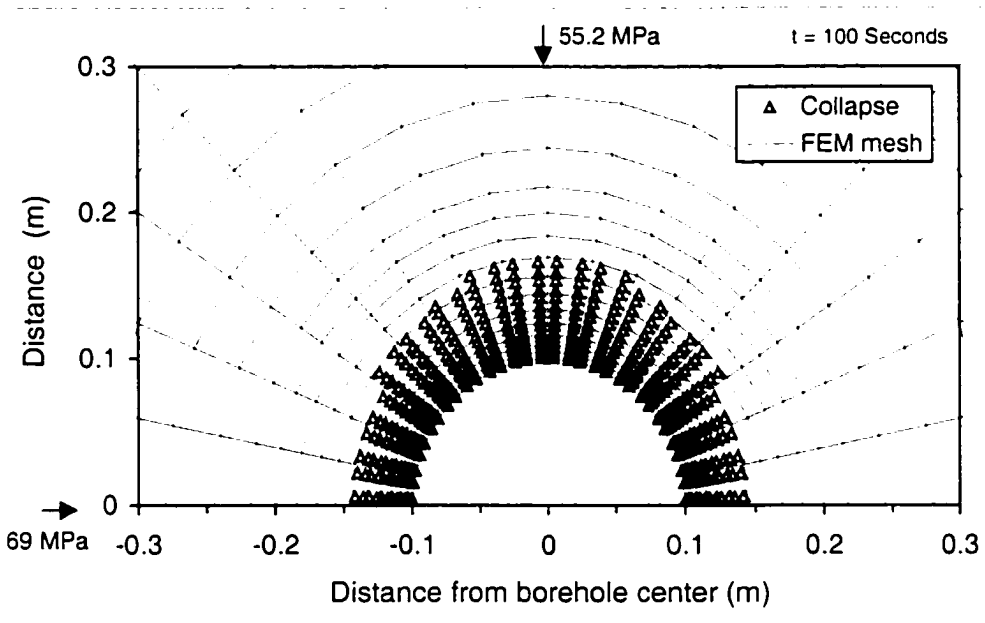


Figure 8.1.28 Collapse area in normal stress region at t = 100 s for a horizontal borehole drilled parallel to the minimum stress.

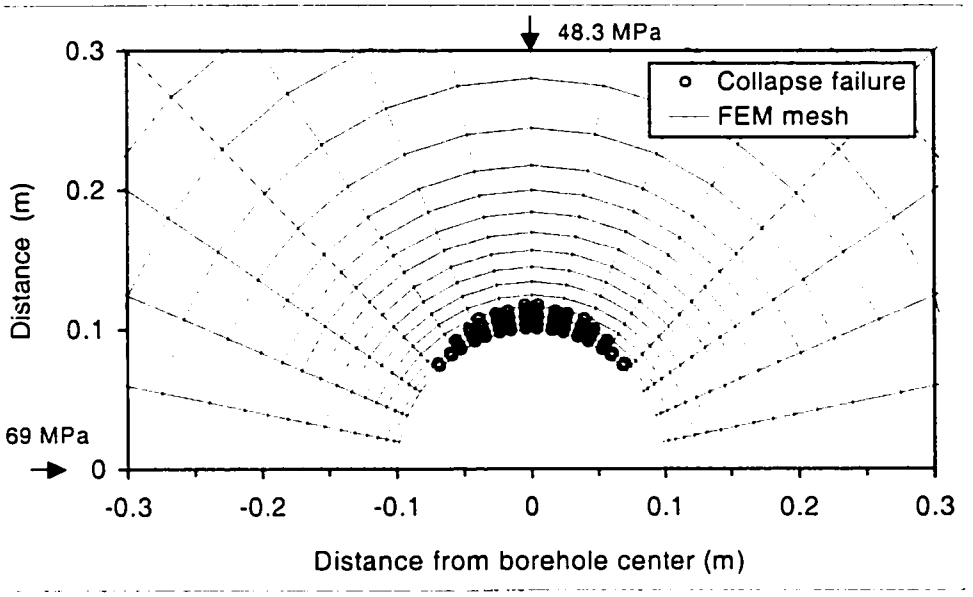


Figure 8.1.29 Collapse area in normal stress region at t = 100 s for a horizontal borehole drilled parallel to the maximum stress during production (bottom pressure 31.7 MPa).

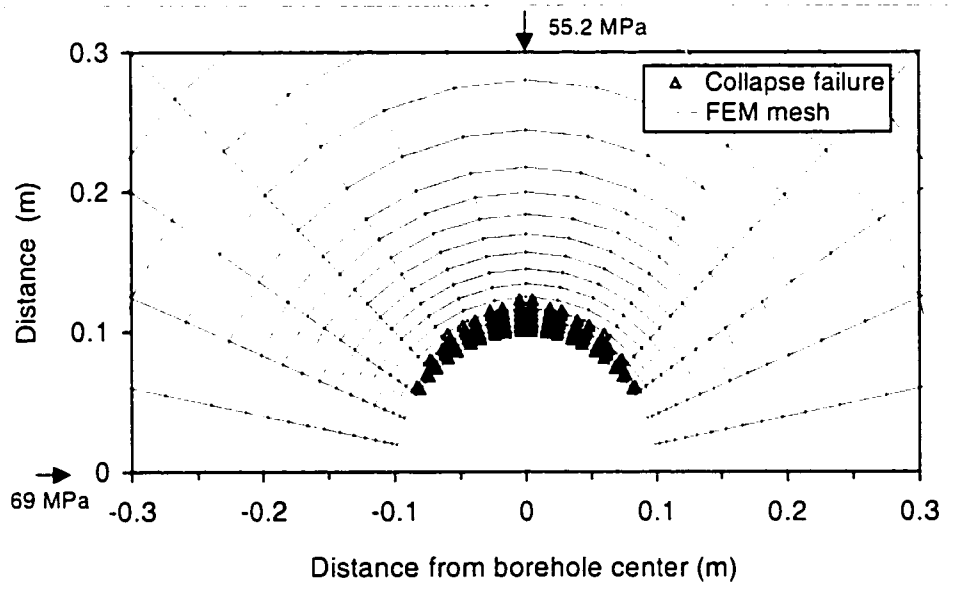


Figure 8.1.30 Collapse area in normal stress region at t = 100 s for a horizontal borehole drilled parallel to the minimum stress during production (bottom pressure 31.7 MPa).

8.1.4 Wellbore in Faulted Areas

Instability can easily occur when a borehole penetrates a pre-existing fault or planes having low or no cohesion. The finite element model can deal with this problem by using different material parameters in the finite element mesh. Figure 8.1.31 shows a half circular opening in a formation weakened by a fault zone in which the attitude of the fault is same as the borehole drilling direction. The state of stress and material parameters of the normal rock regime are same as the example given in Section 8.1.2 and previous chapters (Table 5.4.1, Chapter 5 and Chapter 7). The material parameters in the normal rock and faulted region are given in Table 8.1.2. In the faulted area, the rock has much lower strengths, Young's modulus and higher permeabilities than those in surrounding rocks. In the following analysis, the hole inclination is assumed to be 70°, and the true vertical depth of the hole is 1000 m.

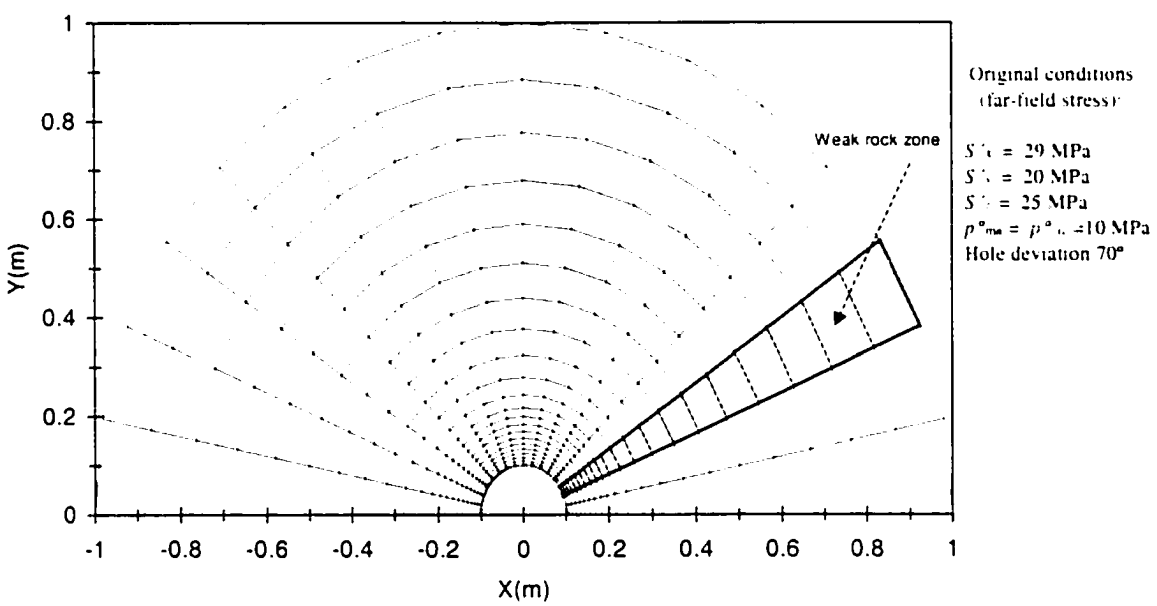


Figure 8.1.31 Finite element mesh for a half of borehole with weak rock zone.

Table 8.1.2 Material parameters in the weak and normal rock region

Parameter	Unit	Weak rock	Normal rock
Elastic modulus (E)	GN/m^2	10.6	20.6
Poisson's ratio (ν)	-	0.25	0.189
Fracture stiffness (K_n, K_{sh})	$MN/m^2/m$	4.821×10^5	4.821×10^5
Fluid bulk modulus (K_f)	MN/m^2	419.2	419.2
Grain bulk modulus (K_s)	GN/m^2	48.21	48.21
Matrix porosity (n_{ma})	-	0.02	0.02
Fracture porosity (n_{fr})	-	0.002	0.002
Matrix mobility (k_{ma}/μ)	$M^4/MN\ s$	10^{-9}	10^{-10}
Fracture mobility (k_{fr}/μ)	$M^4/MN\ s$	10^{-8}	10^{-9}
Fracture spacing (s)	m	1	1
Uniaxial compressive strength (σ_c)	MN/m^2	11	41
Internal friction angle (φ)	°	30	30
Material strength parameter (α)	-	0.1	0.14
Material strength parameter (κ)	MN/m^2	5.5	12
Tensile strength (T)	MN/m^2	0	1.5

Figures 8.1.32 and 8.1.33 are collapse and shear failure areas for the inclined borehole intersected with a weak rock zone. It can be seen that the failures occurred not only along the local minimum stress direction (borehole crown), but also near and in the weak rock region. This is due to the fact that the weak rock has a much lower strength and, furthermore, there is a much larger stress concentration at the interface between the normal and weak rocks. Figure 8.1.34 shows the fracturing areas for an inclined borehole with a mud pressure of 24 MPa. It demonstrates that fracturing induced by high mud pressure appears mainly in the weak rock zone because it has a much lower tensile strength and mud pressure can penetrate easier to this highly fractured formation. It is

also observed that the fracturing near the weak rock zone does not occur in the maximum stress direction, only far from the weak rock zone, the fracturing takes place around the maximum stress direction as the homogeneous borehole does.

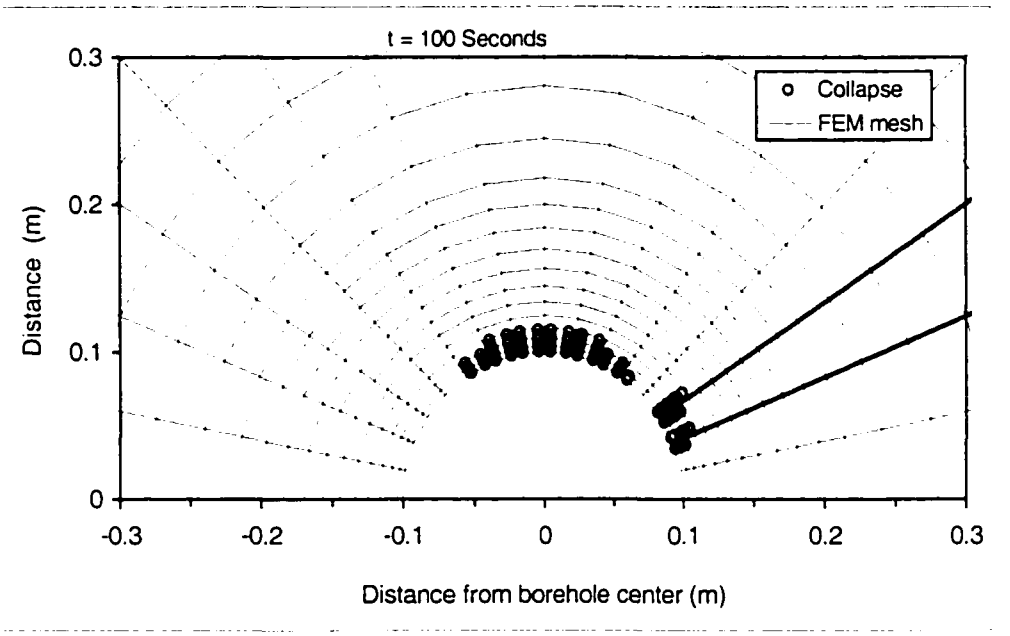


Figure 8.1.32 Collapse area in tectonic stress regime for t = 100 s in case of an inclined borehole intersected with a weak rock zone without any internal support.

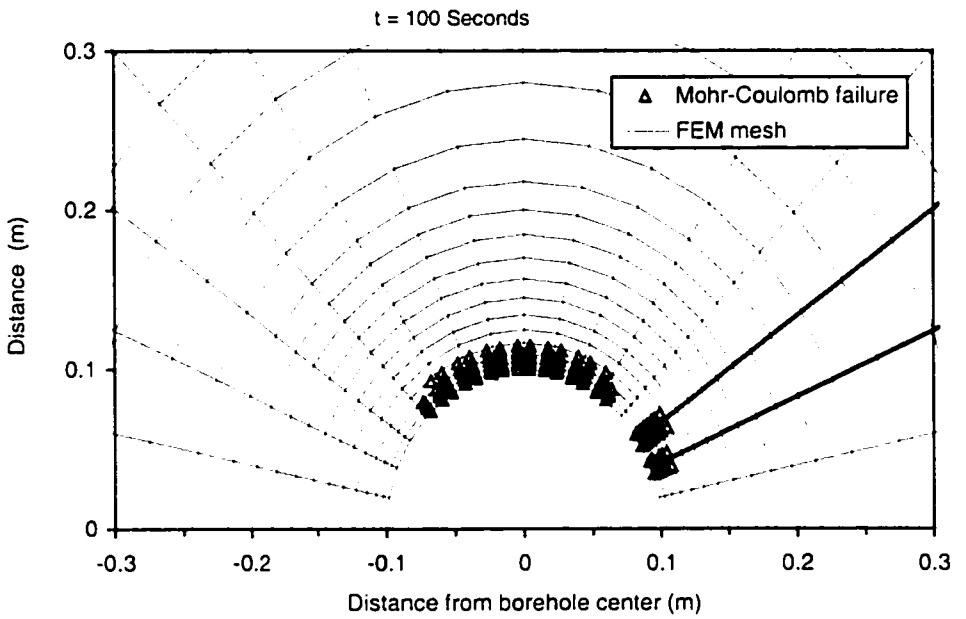


Figure 8.1.33 Shear failure area in tectonic stress regime at t = 100 s for an inclined borehole intersected by a weak rock zone without any internal support.

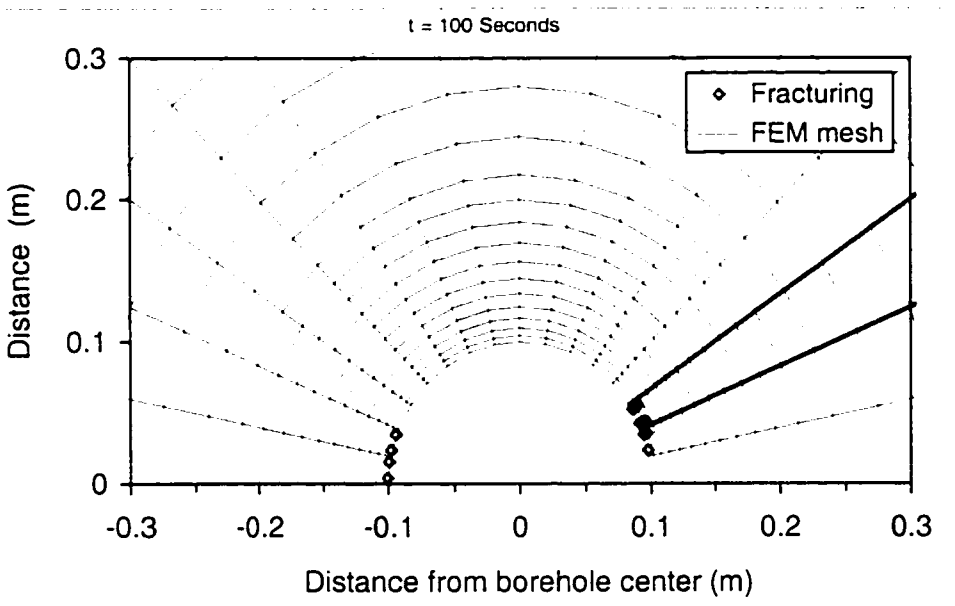


Figure 8.1.34 Fracturing area in tectonic stress regime at t = 100 s for an inclined borehole intersected by a weak rock zone with a mud pressure of 24 MPa.

8.2 Wellbore in Poorly-consolidated Formations

The dual-porosity finite element model was also applied to analyze borehole stability in poorly consolidated rocks. The case application selected was the QK17-2 oil field, located offshore in the western part of Bohai Bay, China. The geology of the QK17-2 oil field is characterized by massive sand-shale sequences from the tertiary and quaternary periods (Liu et al., 1999). Three exploration wells had already been drilled. The well records indicated that wellbore stability would be a concern for new wells. The in-situ stresses and mechanical parameters at well depth 1729.85 m are as follows:

The in-situ stresses and initial pore pressures are: σ_v = 36.32 MPa, σ_H = 38.97 MPa, σ_h = 27.16 MPa, and p^0 = 17.3 MPa (Liu et al, 1999), which wellbore inclination is φ_z = 40° (well deviation). The wellbore radius is R = 0.1 m. In the local coordinate system, these values are calculated as: S_x = 37.9 MPa, S_y = 27.2 MPa, S_z = 37.4 MPa, S_{xz} = 1.3 MPa, S_{xy} = S_{yz} = 0 MPa, and p^0 = $p_{ma}{}^0$ = $p_{fr}{}^0$ = 17.3 MPa. It can be seen that the x-direction is the maximum stress direction. The formation materials are assumed to be isotropic, characterized by the following properties: elastic modulus, E =15.6 Gpa; Poisson ratio, ν = 0.25; Biot modulus, M = 11.6 Gpa; Biot's effective stress coefficient, α = 0.8; permeability, k =1× 10^{-13} m^2; and fluid dynamic viscosity, μ = 0.001 Pa·s. The corresponding parameters for the dual-porosity poroelastic model are listed in Table 8.2.1.

In the present study, the mud weight density was taken as ρ_w = 15 KPa/m (mud pressure is 25.9 MPa). Permeable and impermeabile models were examined. The analyses were concentrated on the minimum stress direction (θ = 90°) because it was prone to have shear and collapse failures (see previous section). In Figure 8.2.1 it can be seen that for the impermeable model the pore pressure at the borehole wall is not same as the mud pressure because the wellbore is impermeable; but, there is still poroelastic effect which induces the pore pressure increase near wellbore. However, for the permeable model, the pore pressure at the borehole wall is same as the mud pressure.

Due to the mud pressure, there are no tensile radial stresses (Figure 8.2.2) and for the impermeable model one induces larger radial stresses at the wellbore. This is due to the fact that no fluid penetrates into the wellbore and the mud pressure acts only as a radial stress in the impermeable model. It will be noted that the effective tangential stress is slightly larger for the impermeable model (Figure 8.2.3); this is due to the fact that the impermeable model has smaller pore pressure values in the near field (see Figure 8.2.1).

Table 8.2.1 Parameters for inclined borehole analysis

Parameter	Unit	Magnitude
Elastic modulus (E)	GN/m^2	15.6
Poisson's ratio (ν)	-	0.25
Fracture stiffness (K_n, K_{sh})	$MN/m^2/m$	3.0×10^5
Fluid bulk modulus (K_f)	MN/m^2	326
Grain bulk modulus (K_s)	GN/m^2	38
Matrix porosity (n_{ma})	-	0.02
Fracture porosity (n_{fr})	-	0.002
Matrix mobility (k_{ma}/μ)	$M^4/MN\ s$	10^{-10}
Fracture mobility (k_{fr}/μ)	$M^4/MN\ s$	10^{-9}
Fracture spacing (s)	m	10
Uniaxial compressive strength (σ_c)	MN/m^2	10
Internal friction angle (φ)	°	30

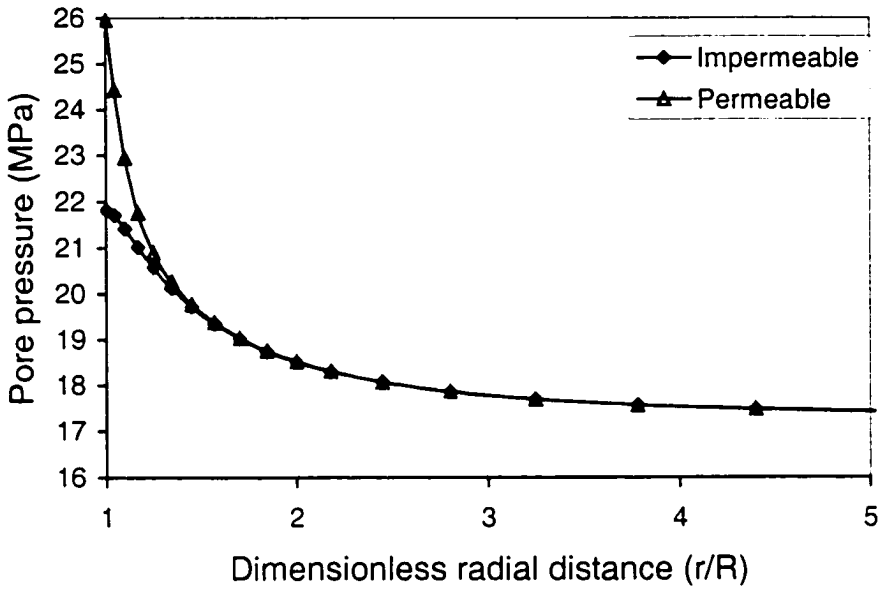


Figure 8.2.1 Pore pressure response for permeable and impermeable models in the minimum stress direction at t = 100 s.

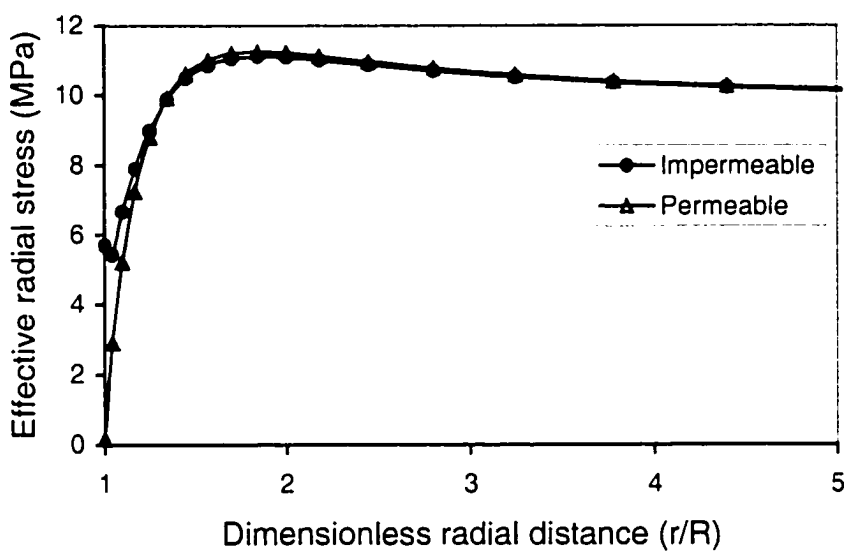


Figure 8.2.2 Radial stress response for permeable and impermeable models in the minimum stress direction at t = 100 s.

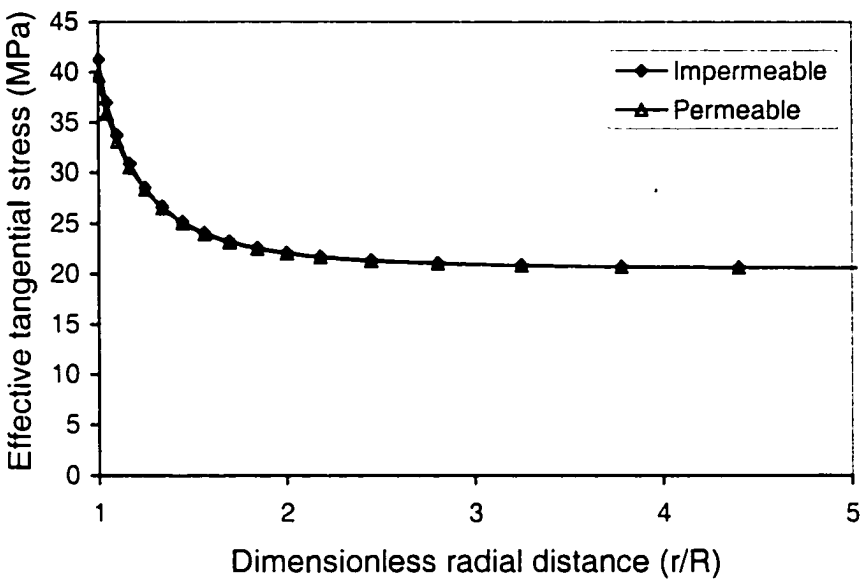


Figure 8.2.3 Tangential stress response for permeable and impermeable models in the minimum stress direction at t = 100 s.

Figure 8.2.4 is the Mohr-Coulomb failure stresses for permeable and impermeable cases for a mud weight density ρ_w = 15 KPa/m and at time t = 100 s. It can be seen that for same mud weight the borehole is stable for the impermeable model; however, it is unstable for the permeable model. In order to control failure one needs to increase the mud weight; but, if the mud pressure is too high, it will induce fracturing. Figure 8.2.5 shows that the borehole is unstable for any hole deviation for the permeable model. For the impermeable model, in which the mud fluid can not invade the pore spaces, a suitable mud weight can avoid the borehole failure and fracturing (refer to Figure 8.2.6). Thus, the impermeable mudcake provides a better support to help consolidate the formation and stabilize the borehole. In addition, the impermeable mudcake can be deposited on loose, unconsolidated sand to prevent it from flowing into the wellbore.

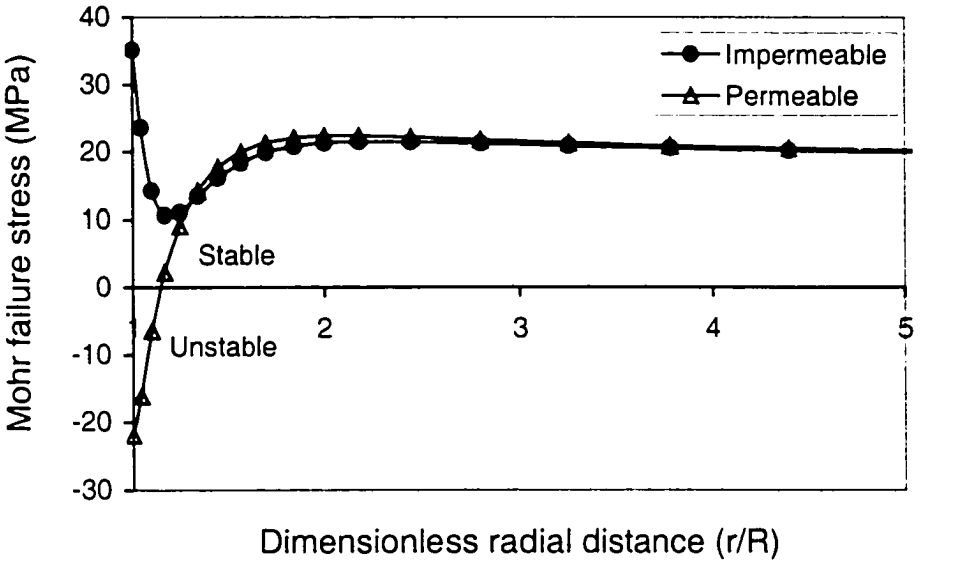


Figure 8.2.4 Effective Mohr-Coulomb failure stresses for permeable and impermeable models in the minimum stress direction at t = 100 s.

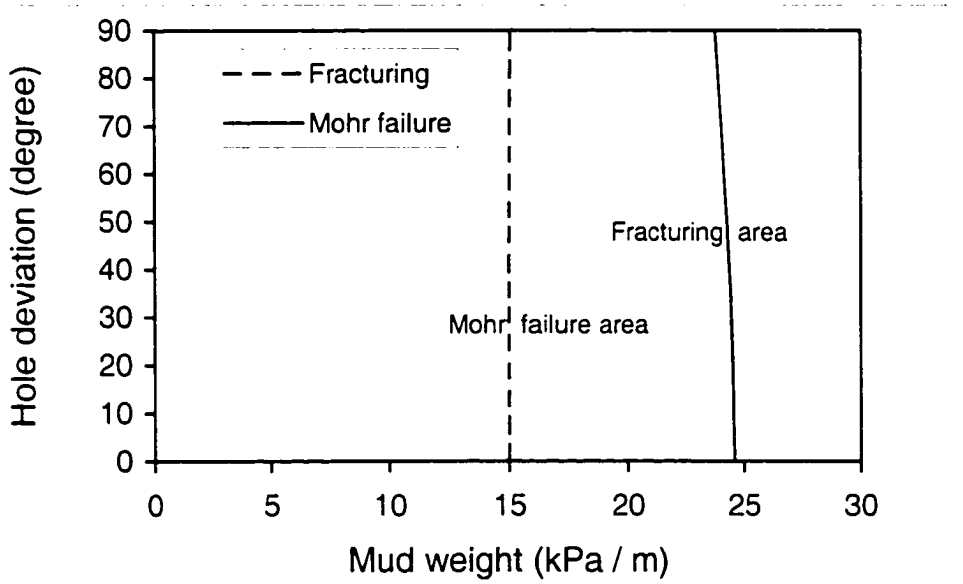


Figure 8.2.5 Mud weight range varying with the hole inclinations for permeable model at t = 100 s.

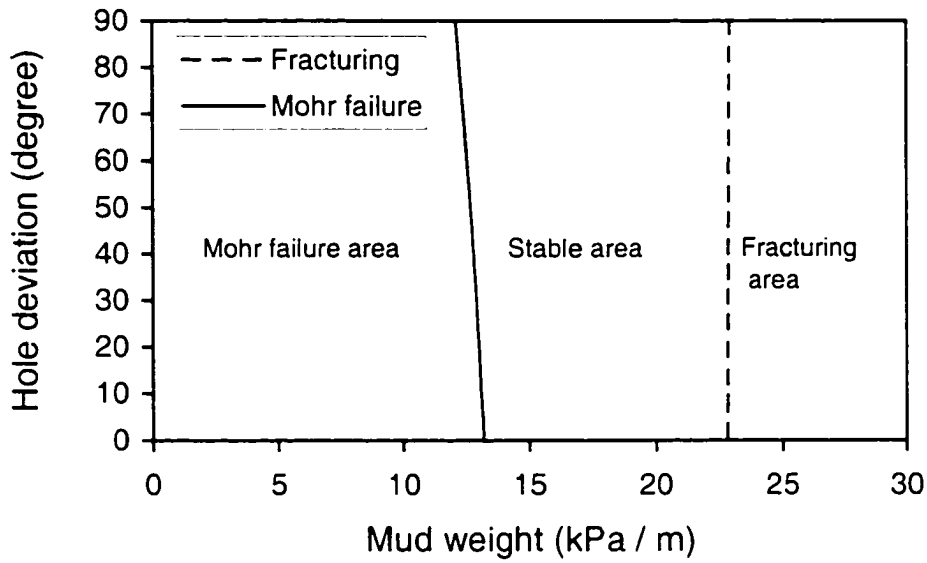


Figure 8.2.6 Mud weight range varying with the hole inclinations for impermeable model at t = 100 s.

8.3 Stress-dependent Permeability around Wellbores

The stress-dependent permeability in fractured media can be written as following (refer to Appendix D for detailed derivations):

$$k_k = k_{0k}\left\{1-\left(\frac{1}{K_m b_i}+\frac{1}{K_m s_i}-\frac{s_i}{E_r b_i}\right)\left[\Delta\sigma_i - \nu(\Delta\sigma_j+\Delta\sigma_k)\right]\right\}^3 \qquad (8.3.1)$$

where k_{0k} and k_k are the permeabilities along the k-direction before and after stress changes, $i = x, y, z$; $j = y, z, x$; $i = z, x, y$; $i \neq j \neq k$.

Introducing this equation into the finite element model, the permeability variation due to stress changes induced by borehole drilling and reservoir development can be obtained. In the case study, a borehole drilled in a normal stress regime were examined, in which the state of stress and material parameters are identical to that in Section 8.1.1 and Table 8.1.1 except for the borehole inclination which is now 70°. The horizontal and vertical permeability (permeabilities in x- and y-directions, respectively) variations in the fractured formation were analyzed. Note that the results plots in the following figures are the ratio between the changed permeability and the original permeability (k_k / k_{0k}).

Figures 8.3.1 and 8.3.2 are contours of permeability ratios in horizontal (x) and vertical (y) directions, respectively. It can be observed from Figure 8.3.1 that the horizontal permeability increases around the borehole crown area and decreases around the sidewalls. Figure 8.3.2 indicates that the vertical permeability decreases around the borehole crown and increases around the sidewalls. Figure 8.3.3 shows the horizontal permeability variations around the borehole due to stress changes induced by the hole excavation. In this figure, the permeability increase zone refers to changes exceeding 1.3 of the original permeability, and the permeability decrease zone refers to changes less than 0.7. Figure 8.3.3, the permeability increase and decrease zones are clearly determined. Figure 8.3.4 gives the vertical permeability increase and decrease zones.

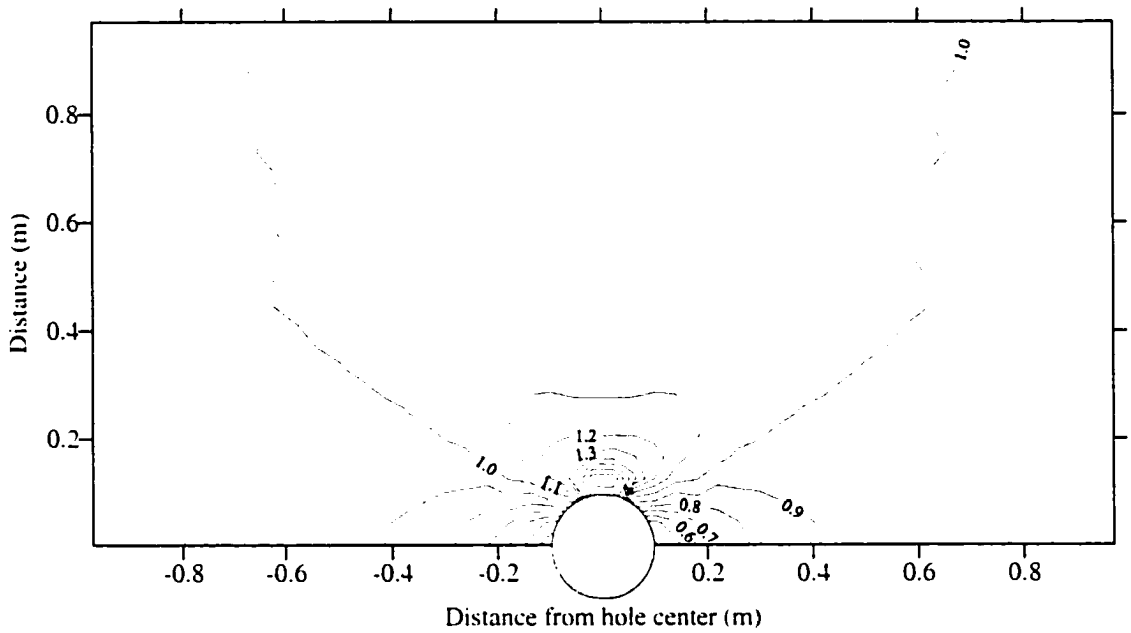


Figure 8.3.1 Contour of horizontal permeability ratio (k_r / k_0) in the fractured formation due to borehole excavation.

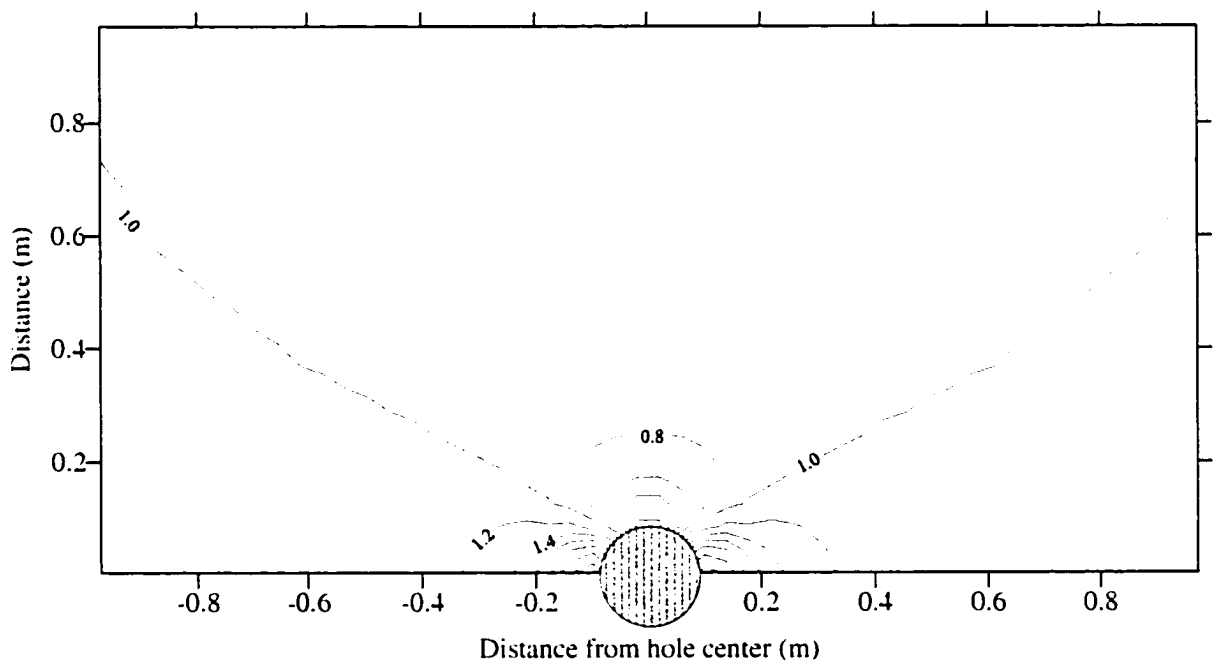


Figure 8.3.2 Contour of vertical permeability (k_v / k_0) in the fractured formation due to borehole excavation.

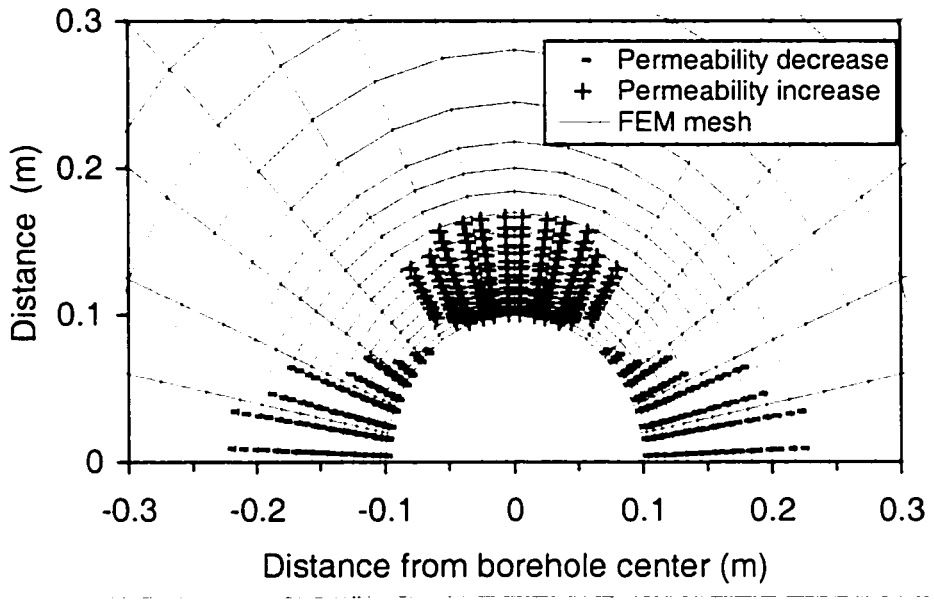


Figure 8.3.3 Permeability variations in the x-direction in the fractured formation due to borehole excavation.

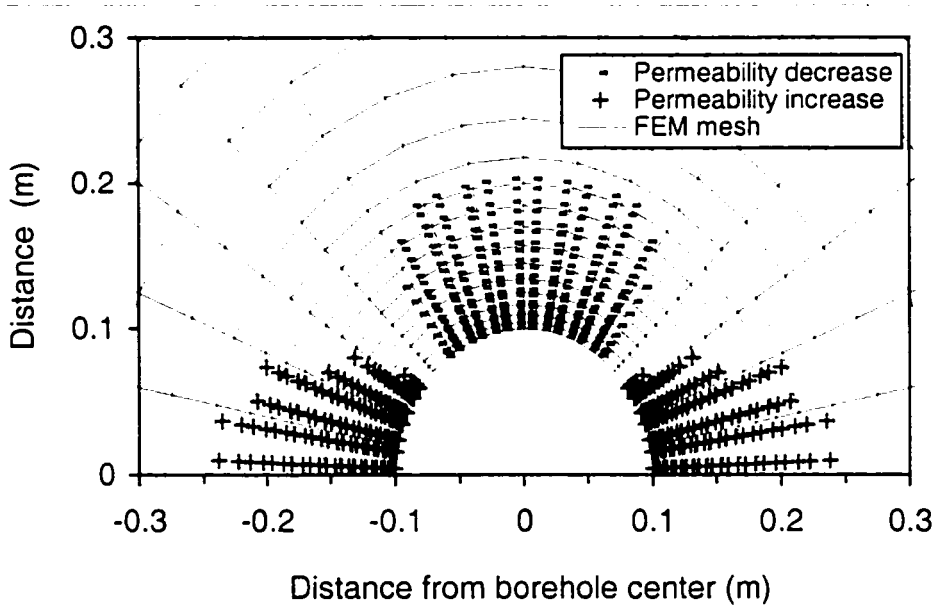


Figure 8.3.4 Permeability variations in the y-direction in the fractured formation due to borehole excavation.

8.4 Rock Comminution

There are two types of rock failures, one induced by bit indentation; the other caused by the bit dragging or shearing. The present study concentrates on the rock indentation by the drilling bit. Figure 8.4.1 is the finite element mesh used to analyze the interaction between the bit and the formation. Plane stress conditions are assumed to be valid. Two cases were examined, one is the normal stress regime; the other is the tectonic stress regime. Applying Mohr-Coulomb and tensile failure criteria, assuming that the compressive strength of the formation is σ_c = 20 MPa, tensile strength is T = 0 MPa. All other parameters are similar to those given in Table 8.2.1, the shear and tensile failure areas due to the cutter loading in different stress regions can be obtained from the finite element model.

Figure 8.4.3 presents the formation shear failure in the case when the cutter loading is 40 MPa. It is obvious that the shear failure mainly concentrates on the downward of the cutter. Figure 8.4.4 is the formation tensile failure in normal stress region for the cutter loading 50 MPa. The tensile failure also occurs in downwards of the cutter.

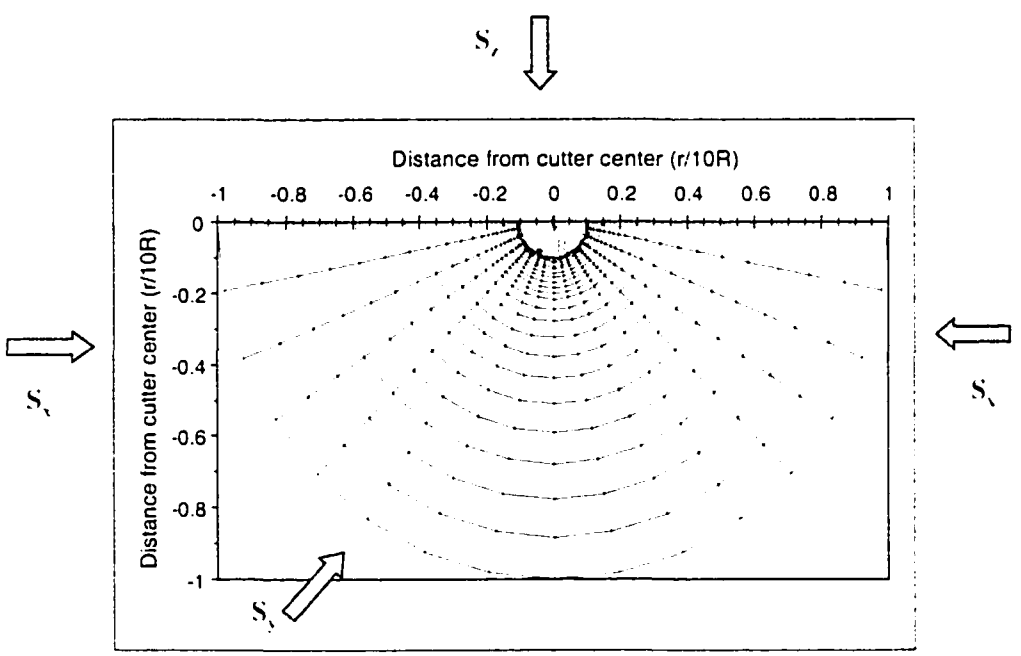


Figure 8.4.1 Finite element mesh for drilling bit cutting problem.

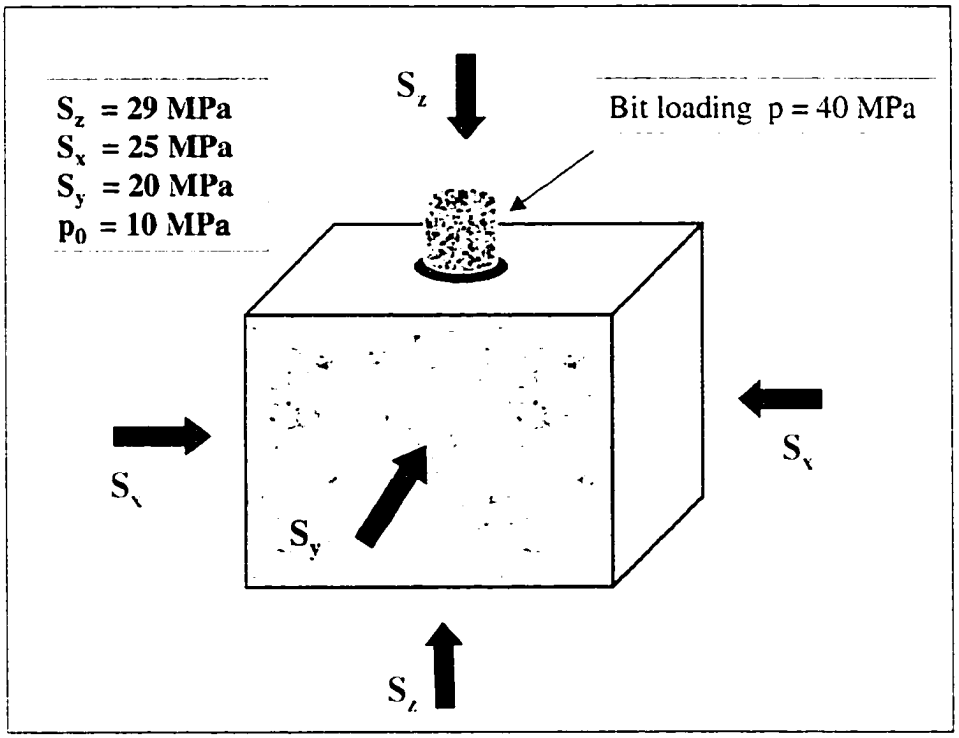


Figure 8.4.2 Stress configration for the bit and rock interaction in normal stress regime.

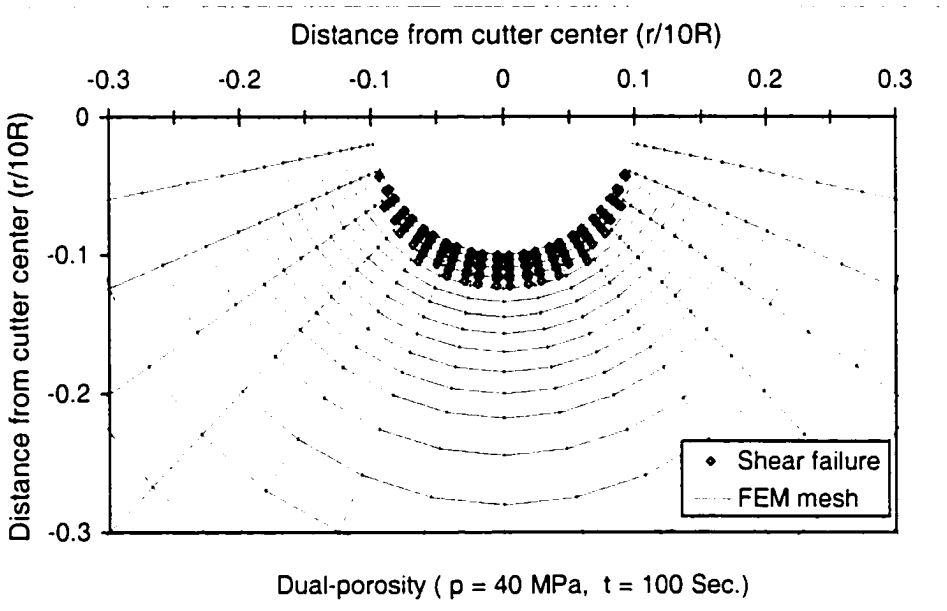


Figure 8.4.3 Formation shear failure area around the cutter in normal stress regime for cutter loading 40 MPa at t = 100 s.

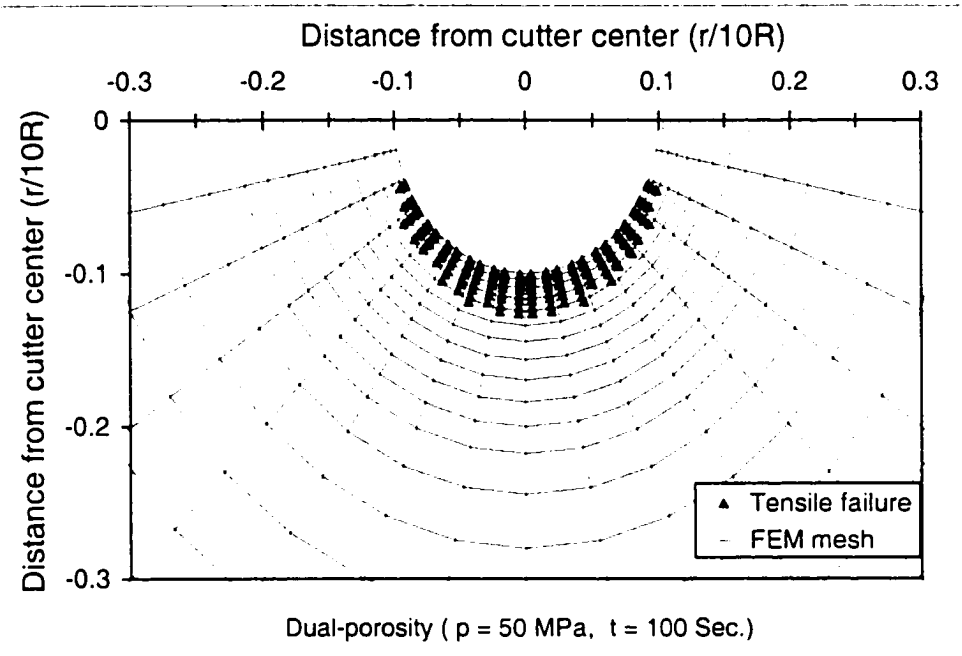


Figure 8.4.4 Formation tensile failure area around the cutter in normal stress regime for cutter loading 50 MPa at t = 100 s.

The other case is the rock cutting in a tectonic stress regime, as shown in Figure 8.4.5. Figures 8.4.6 and 8.4.7 show the formation shear and tensile failure due to the cutter loadings (p = 40 MPa) at t = 100 s. It is obvious that the maximum shear and tensile failures concentrate two wings of the cutter and there is basically no failure to occur in the cutter downward direction.

It can be concluded that the state of stress has a significant impact on the rock comminution. When rock cutting is performed in a normal stress regime, the rock shear and tensile failures concentrate downwards; however, in a tectonic stress regime, the rock shear and tensile failures are located on two sides of the cutter (Figure 8.4.9).

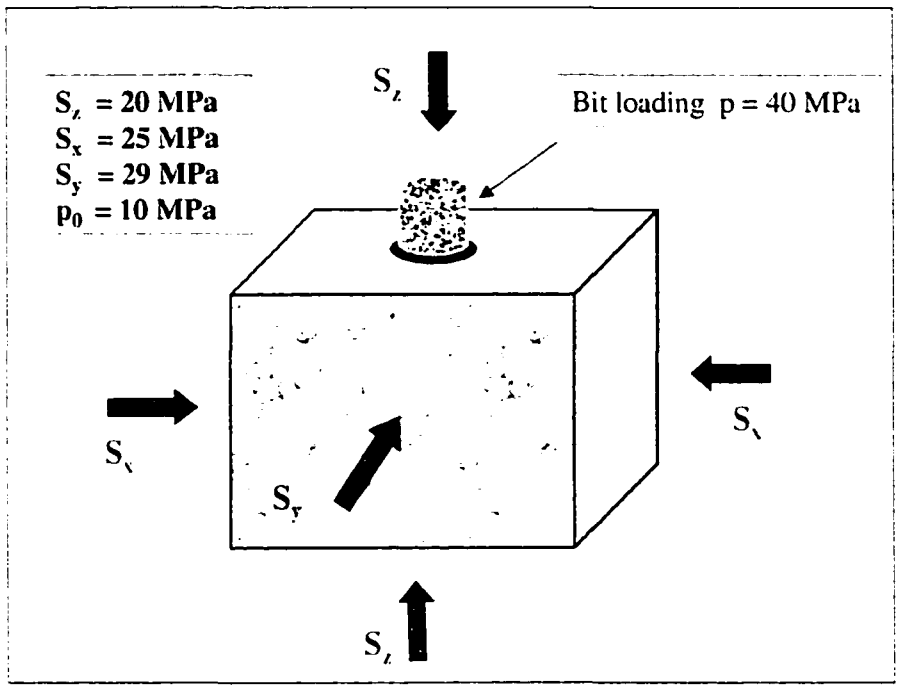


Figure 8.4.5 Stress configration for the bit and rock interaction in tectonic stress regime.

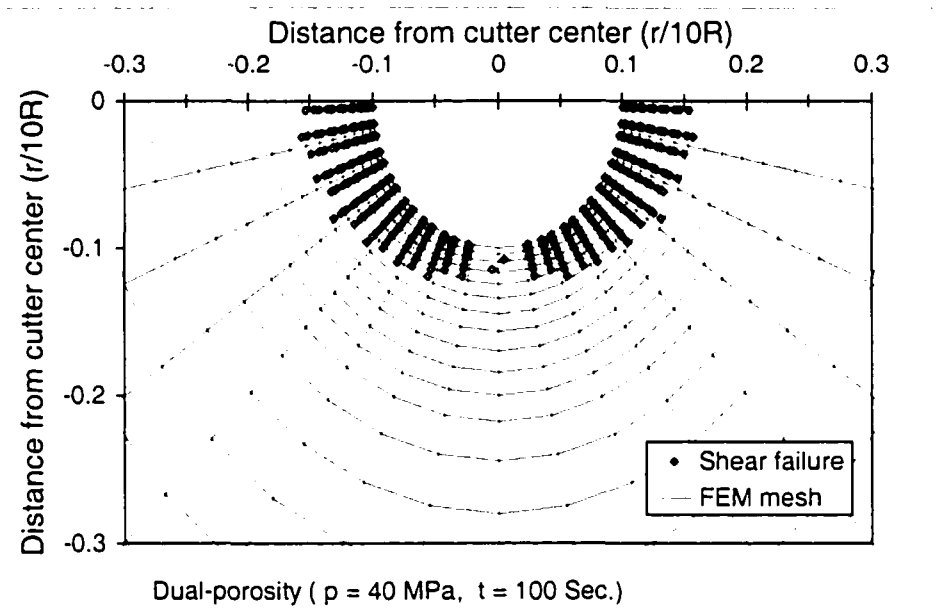


Figure 8.4.6 Formation shear failure area around the cutter in normal stress regime for cutter loading 40 MPa at t = 100 s.

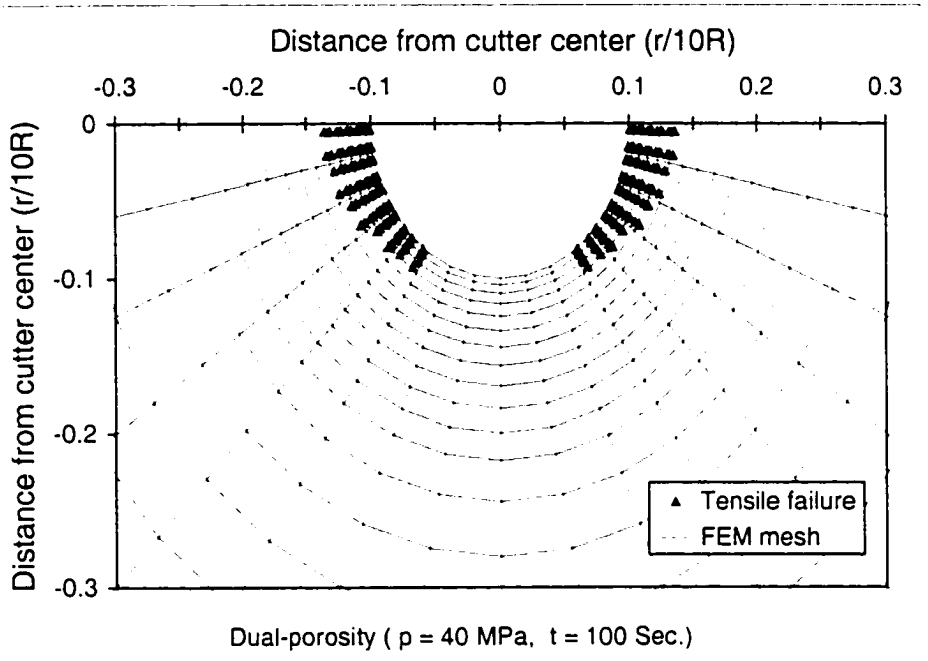


Figure 8.4.7 Formation tensile failure area around the cutter in normal stress regime for cutter loading 40 MPa at t = 100 s.

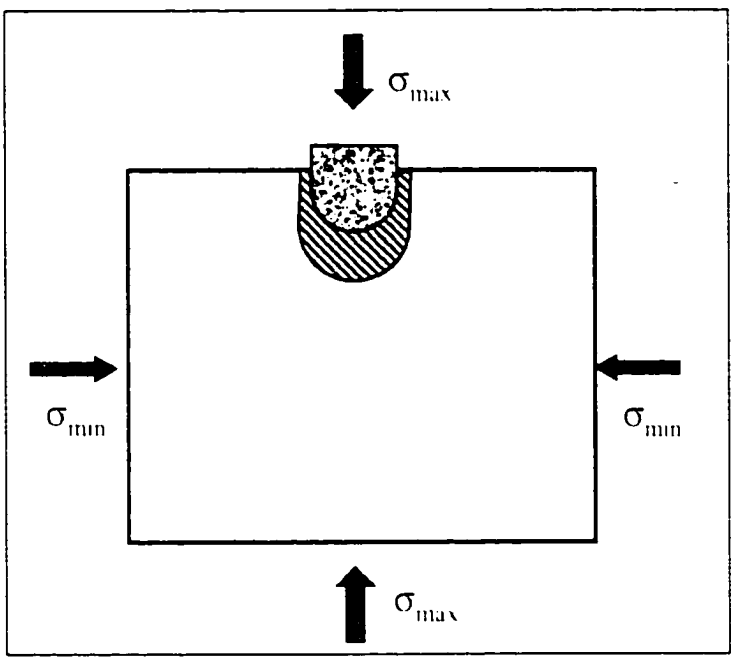


Figure 8.4.8 Schematic diagram of formation failure around the cutter in normal stress regime.

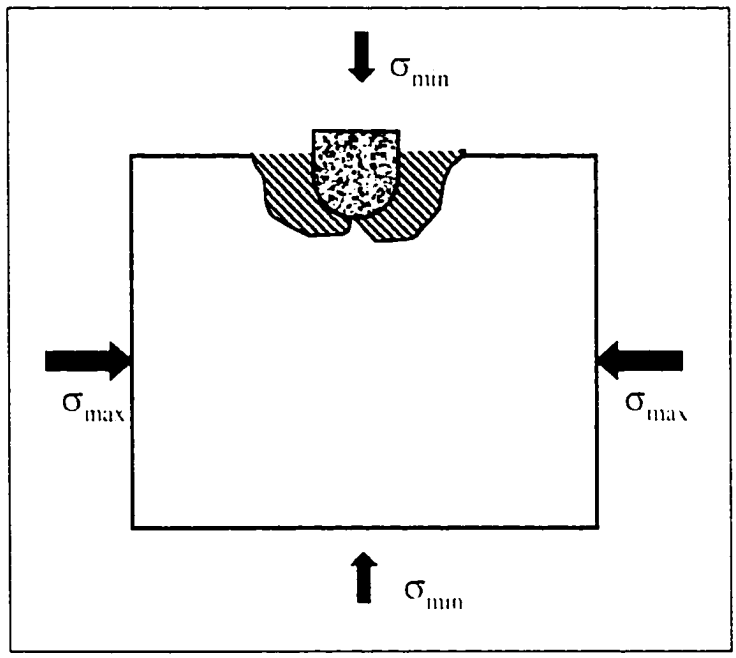


Figure 8.4.9 Schematic diagram of formation failure around the cutter in tectonic stress regime.

Chapter 9

Conclusions and Recommendations

9.1 Conclusions

The naturally fractured reservoir was modeled by using a dual-porosity poromechanics approach, in which rock matrix and fractures have different mechanical and hydraulic parameters. Using separate and overlapping rock matrix and fractures models subjected to double effective laws, in which deformations and fluid flow in the matrix and fractures are fully coupled, the dual-porosity formulation was presented. The finite element numerical method was applied to solve the coupled equations. The solution was validated by comparing with a consolidation problem and by validating elastic and single-porosity analytical solutions. Wellbore problems were examined and dual-porosity borehole solutions were given for different boundary conditions in naturally fractured reservoirs. Through case studies and example applications, it was found that the developed numerical model was a powerful means to solve different and difficult problems in petroleum engineering as well as in other engineering areas. The major conclusions drawn in this dissertation can be summarized as follows:

1. Using the separate and overlapping model, the governing equations for solid deformations and fluid flow in dual-porosity media were presented as a model for naturally fractured porous media. The solid deformation, fluid flow and transfer between rock matrix and fractures were fully coupled.
2. Applying dual-porosity poro-mechanics and generalized plain strain theory, a windows-based pseudo-three-dimensional finite element software, which can generate automatically the finite element mesh and give graphical outputs, has been developed for simulating inclined borehole stability and fluid flow in naturally fractured reservoirs. In addition, a finite difference software was

developed to model non-isothermal consolidation problems in elastoplastic dual-porosity media.

3. As one of the important application areas, wellbore problems were investigated. Through stress conversion and transformation as well as fluid mudweight considerations, the finite element solution was shown to be suitable to model any directional borehole with different boundary conditions.
4. The developed numerical code has been extensively verified by considering the known solution of the one-dimensional consolidation problem and by validating wellbore problems with known elastic and poroelastic analytical solutions.
5. The developed code can be used for simulating different mechanical problems including elastic, steady flow, single-porosity and dual-porosity problems.
6. Parametric analyses showed that neglecting any one of fracture deformation, poroelastic and dual-porosity effects, the pore pressure near wellbore will be underestimated. And, the non-monotonic pressure distribution and tensile radial stress occur at a small distance inside the borehole wall at small times, which are attributed to the poroelastic effect. The tensile stress induced by the poroelastic effect is an incentive factor of borehole outburst failure, or spalling.
7. Several failure criteria were incorporated to the finite element model in order to simulate different wellbore failure types. They included the compressive, spalling, fracturing, shear and collapse failure criteria.
8. The case studies showed that the lower deviational or vertical boreholes are more stable in the normal stress regime. However, in a tectonic stress regime the higher the borehole deviation, the more stable the boreholes.
9. The horizontal borehole drilled parallel to the maximum stress direction is more stable during both drilling and production in a tectonic stress regime, which is not coincident with traditional drilling guidelines. Drilling in this direction also allows a single fracture parallel to the borehole to be generated during stimulation, since natural fractures are usually perpendicular to the present-day minimum horizontal stress. In a normal stress regime the horizontal borehole drilled parallel to maximum stress direction is more stable during open-hole production.

10. When a borehole penetrates a pre-existing fault, failures occurred not only along the local minimum stress direction, but also near and in the weak rock region. And, fracturing induced by high mud pressure appears mainly in the weak rock zone because it has a much lower tensile strength and mud pressure can penetrate easily into this highly fractured formation.
11. The impermeable mudcake provides a better support to help consolidate the formation and stabilize the borehole, this is critically important for a borehole drilled in an unconsolidated formation.
12. Stress-dependent permeability was studied and permeability variations induced by stress changes due to the borehole perturbation was examined. The results indicated that the skin factor is not a constant around the wellbore.

9.2 Recommendations for Future Research

New simulation and computational methods appear, which challenge current technology in petroleum engineering and push continuously progress. Also, new problems and challenges are met in the field. Under those circumstances, research methods and simulating tools on wellbore stability as well as reservoir simulation need to satisfy new requirements. The future research in wellbore stability should include the following aspects:

1. Incorporate temperature effects in the coupled dual-porosity equations for deep formations where such effects cannot be neglected.
2. Incorporate chemical effects in the dual-porosity equations for chemically sensitive formations.
3. Extend the current model to multi-phase fluid flow problems.
4. Extend the present model to elasto-visco-plastic and other mechanical models to make it solve more complex formations.
5. Incorporate the effect of non-Darcy flow, particularly for fluid flow in fractures.

6. Improve the code interface to make the software more user-friendly, and extend the software to real three-dimensional solutions.

References

1. Aadnøy, B.S., 1987. Modeling of the stability of highly inclined boreholes in anisotropic rock formations, paper SPE 16526 presented at 1987 SPE Offshore European Conf., Aberdeen.
2. Aadnøy, B.S. and Chenevert, M.E., 1987. Stability of highly inclined boreholes, *SPE Drilling Engineering*, 12 p.264-374.
3. Abousleiman, Y., Cui, L., Cheng, A.H.-D. and Roegiers, J.-C., 1995. Poroelastic solution of an inclined borehole in a transversely isotropic medium, *Proc. 35th US Sypm. on Rock Mech.*, p.313-318.
4. Abousleiman, Y., Cheng, A.H.-D., Jiang, C. and Roegiers, J.-C., 1996. Poroviscoelastic analysis of borehole and cylinder problems, *Acta Mechanica*, Vol.119, p.119-219.
5. Addis, T., Boulter, Roca-Ramisa, L. and Plumb, D., 1993. The question for borehole stability in the Cusiana field, Colombia, *Schlumbeger Oilfield Review*, April/July, p.33-43.
6. Aifantis, E.C., 1977. Introducing a Multi-Porous Medium, *Developments in Mechanics*, Vol.8, p.209-211.
7. Aifantis, E.C., 1980. On the Problem of Diffusion in Solids, *Acta Mechanica*, Vol.37, p.265-296.
8. Amadei, B., 1983. *Rock Anisotropy and the Theory of Stress Measurements*, Springer.
9. Aoki, T., Tan, C.P. and Bamford, W.E., 1993. Effects of deformation and strength anisotropy on borehole failures in saturated shales, *Int. J. Rock Mech. Min. Sci. & Geomech. Abstr.*, Vol.30, 7, p.1031-1034.
10. Aoki, T., Tan, C.P. and Bamford, W.E., 1994. Stability analysis of inclined wellbores in saturated anisotropic shale, *in Proc. 8th Int. Con. On Computer Methods and Advances in Geomech.*, Siriwardane H.J. and Zaman, M.M. (eds.), Vol.3, Balkema, Rotterdam, p.2025-2030.

11. Bai, M., Elsworth, D. and Roegiers, J.-C., 1993. Multi-Porosity/Multi-Permeability Approach to the Simulation of Naturally Fractured Reservoirs, *Water Resour. Res.*, Vol.29, No.6, p.1621-1633.

12. Bai, M., Ma, Q. and Roegiers, J.-C., 1994. A Nonlinear Dual-Porosity Model, *Appl. Math. Modeling*, Vol. 18, p.602-610.

13. Bai, M. and Meng, F.H., 1994. Study of Naturally-Fractured Reservoirs Using Three-Dimensional Finite Elements, *Report for the Rock Mechanics Research Institute*, The University of Oklahoma.

14. Bai, M. and Roegiers, J.-C., 1994. On the Correlation of Nonlinear Flow and Linear Transport with Application to Dual-Porosity Modeling, *Journal of Petroleum Science and Engineering*, Vol.11, p.63-72.

15. Bai, M., Elsworth, D., Roegiers, J.-C. and Meng F.H., 1995. A Three-Dimensional Dual-Porosity Poroelastic Model, in Int. Symp. on mining Technology, Rock Mechanics and Strata Control in Mining and Geological Engineering, Beijing, China.

16. Bai, M., Roegiers, J.-C. and Elsworth D., 1995. Poromechanical Response of Fractured-Porous Rock Masses, *J. Petroleum Science and Engineering*, Vol.13, p.155-168.

17. Bai, M. and Roegiers, J.-C., 1995. Modeling of Heat Flow and Solute Transport in Fractured Rock Masses, in *Proc. 8th Int. Congress Rock Mechanics*, Japan.

18. Bai, M. and Roegiers, J.-C., 1997. Triple-porosity analysis of solute transport, *J. Contaminant hydrology*. 28, p.247-266.

19. Bai, M., Abousleiman, Y., Cui, L., and Zhang J., 1999. Dual-porosity Porous Elastic Modeling of Generalized Plane Strain, *Int. J. Rock Mech. Min. Sci.*, 36, 1087-1094.

20. Barenblatt, G.I., Zheltov, I.P. and Kochina, I.N., 1960. Basic Concepts in the Theory of Seepage of Homogeneous Liquids in Fissured Rocks, *Prikl. Mat. Mekh.*, Vol.24, No.5, p.852-864.

21. Barenblatt, G.I., Entov, V.M. and Ryzhik, V.M., 1990. *Theroy of Fluid Flow Through Natural Rocks*, Kluwer Acedimic Publisher, Dordrecht, pp395.

22. Bashin, R. and Hoeg, K., 1998. Parametic study for a large cavern in joined rock usinga distinct element model (UDEC-BB), *Int. J. Rock Mech. Min. Sci. Geomech. Abstr.*, 35 (1), p.17-29.

23. Biot M.A., 1941. General Theory of Three-Dimensional Consolidation, *J. Appl. Phys.*, Vol.12, p.155-164.

24. Biot M.A., 1955. Theory of Elasticity and Consolidation for a Porous Anisotropic Media, *J. Appl. Phys.*, Vol.26, p.182-185.

25. Bol, G.M.Wong, S.-W., Davidson, C.J. and Woodland, D.C., 1992, Borehole stability in shales, paper SPE 24975 presented at the 1992 SPE European Petroleum Conference, Cannes.

26. Boresi, A.P. and Chong, K.P. 1974. *Elasticity in engineering mechanics*, Elsevier.

27. Bradford, I.D.R. and Cook, J.M., 1994. A semi-analytic elastoplastic model for wellbore stability with applications to sanding, *Proc. SPE/ISRM Eurock'94*, Rotterdam, Balkema, p.347-354.

28. Bradley, W.B., 1979. Failure of inclined boreholes, *Trans. of ASME*, Vol. 101, p.232-239.

29. Brady, B.G.H. and Bray, J.W., 1978. The Boundary Element Method for Determining Stress and Displacements around Long Opening in a Triaxial Stress Field, *Int. J. Rock Mech. Min. Sci. & Geomech. Abstr.*, 15, p.21-28.

30. Bratli, R.K., Horsrud, P. and Risnes, R., 1983. Rock mechanics applied to the region near a wellbore, *Proc. 5th Int. Congress on Rock Mechanics*, p.F1-F17.

31. Brown S.R. and Scholz, C.H., 1986. Closure of rock joints, *J. of Geophysical Res.*, Vol.91, No. B5, p. 4939-4948.

32. Charlez P.A., 1991. *Rock Mechanics, Volume 1, Theoretical Fundamentals*, Editions Technip, Paris.

33. Charlez P.A., 1999. *Rock Mechanics, Volume 2, Petroleum Application*, Editions Technip, Paris.

34. Charlez P.A., 1994. The impact of constitutive laws on wellbore stability: A general review, *Proc. EUROCK*, Delft, Rotterdam, Balkema.

35. Chen, W.F. and Han, D.J., 1995. *Plasticity for Structural Engineers*, Gau Lih Book Co., Ltd.

36. Cheng, H. and Dusseault, M.B., 1993. Deformation and diffusion behavior in a solid experencing damage: a continuous damage model and its numerical implementation. *Int. J. Rock Mech. Min. Sci. & Geomech. Abstr.*, Vol.30, p.1323-1331.

37. Cheng, A.H.-D., Abousleiman, Y. and Roegiers, J.-C., 1993. Review of some poroelastic effects in rock mechanics, *Int. J. Rock Mech. Min. Sci. & Geomech. Abstr.*, Vol.30, p.1119-1126.

38. Cheng, A.H.-D., 1998. On generalized plain strain poroelasticity, *Int. J. Rock Mech. Min. Sci. & Geomech. Abstr.*, Vol.35, p.183-193.

39. Christian, J.T. and Boehmer, J.W., 1970. Plane strain consolidation by finite elements, J. Soil Mech. Foundations Div., ASCE, Vol.96 SM4, p.1435-1457.

40. Cui, L., Cheng. A.H.-D. and Abousleiman, Y., 1997a. Poroelastic solution of an inclined borehole, *ASME J. Applied Mechanics*, Vol.64, p.32-38.

41. Cui, L., Kaliakin, V.N., Abousleiman, Y. and Cheng, A.H.-D., 1997b. Finite element formulation and application of poroelastic generalized plane strain problems, *Int. J. Rock Mech. Min. Sci.*, 34(6), 953-962.

42. Cui, L., Abousleiman, Y., Cheng. A.H.-D. and Roegiers, J.-C., 1999a. Time-dependent failure analysis of inclined boreholes in fluid-saturated formations, *ASME J. Energy resources Technology*, Vol.121, p.31-39.

43. Cui, L., Abousleiman, Y., Ekbote, S. Roegiers, J.-C. and Zaman, M., 1999b. A software for poroelastic analyses of borehole stability. Paper SPE 54013 presented at Latin American and Caribbean Petroleum Engineering Conference held in Caracas, Venezula.

44. Desai and Johnson, 1972. Evaluation of two finite element formulations for one-dimensional consolidation, *Comput. Struct.*, 2, p.469-486.

45. Detournay E. 1986. An approximate statical solution of the elastoplastic interfact problem of Galin with a cohesive-fractional material, *Int. J. Solid Structures*, Vol.22, p.1435-1454.

46. Detournay E. and Cheng A.H-D., 1988. Poroelastic Response of a Borehole in a Non-Hydrostatic Stress Field, *Int. J. Rock Mech. Min. Sci. Geomech. Abstr.*, Vol.25, No.3, p.171-182.

47. Detournay, E. and Cheng, A.H-D., 1993. Fundamental of Poroelasticity, Ch.5 in *Comprehensive Rock Engineering*, Vol.2, Editor, Fairhurst C., Pergamon Press.

48. Detournay E. and Fairhurst, C., 1987. Two-dimensional elastoplastic analysis of a long cylindrical cavity under non-hydrostatic loading, *Int. J. Rock Mech. Min. Sci.*

Geomech. Abstr., Vol.24, No.4, p.197-211.

49. Detournay, E. and Roegiers, J.-C., 1986. Comment on "Well Bore Breakouts and In Situ Stress", *J. Geoghys. Res.*, 91, p.14161-14162.
50. Detournay, E., Roegiers, J.-C. and Cheng, A.D., 1987. Some new examples of poroelastic effects in rock mechanics, in *Proc. 28th U.S. Rock Mech. Symp.*, Rotterdam, Balkema.
51. Dusseault, M.B., 1994. Analysis of borehole stability, in Siriwardane, H.J. and Zaman,M.M. (eds), in *Proc. 8th Int. Conf. On Computer Methods and Advances in Geomechanics*, Vol.3, Balkema, Rotterdam, P.125-137.
52. Ekbote, S., Abousleiman, Y. and Zaman, M.M., 2000. Porothermoelastic solution for an inclined borehole in transversely isotropic porous media, *Rock Around the Rim*, Balkema, Rotterdam, p.253-259.
53. Ekbote, S., 2001. Personal communication.
54. Elsworth D. and Bai M., 1992. Flow-Deformation Response of Dual-Porosity Media, *Journal of Geotechnical Engineering*, Vol.118, No.1, Jan. 1992.
55. Evans R.D., 1981. A Proposed Model for Multiphase Flow Through Naturally Fractured Reservoirs, paper SPE 9940 presented at SPE-AIME, Dallas, TX.
56. Fairhurst, C., 1968. *Methods of Determining In Situ Rock Stress at Great Depth*, TRI-68 Missouri River Div. Corps of Engineering.
57. Ghaboussi, J. and Wilson, E.L, 1973. Flow of compressible fluid in porous elastic media, *Int. J. Num. Methods Eng.*, Vol.5, p.419-442.
58. Ghafouri H.R. and Lewis R.W., 1996. A Finite Element Double Porosity Model for Heterogeneous Deformable Porous Media, *Int. J. Analytic. Numer. Meth. Geomech.*, Vol.20, p.831-844.
59. Gnirk, P.F., 1972. The mechanical behavior of the uncased wellbores situated in elastic/plastic media under hydrostatic stress, *SPEJ*, Feb., p.45-59.
60. Goodman, R.E., 1966. On the distribution of stresses around circular tunnels in nonhomogeneous rocks, in: *Proc. 1st Int. Congr. ISRM*, Lisbon, 1966. P.249-255.
61. Gupta, D. and Zaman, M.M., 1994. Wellbore stability in a transversely isotropic medium, in Siriwardane, H.J. and Zaman, M.M. (eds), in *Proc. 8th Int. Conf. On Computer Methods and Advances in Geomechanics*, Vol.3, Balkema, Rotterdam,

p.125-137.

62. Gupta S.K. and Tanki K.K., 1976. A Three-Dimensional Galerkin Finite Element Solution of Flow Through Multiaquifers in Sutter Basin, California, *Water Resour. Res.*, Vol.12, No.2, p.155-162.
63. Hawkes, C.D. and McLellan, P.J., 1996. Modelling of yielded zone enlargement around a wellbore, *Rock Mechanics*, Aubertin, Hassani & Mitri (eds), Balkema, Rotterdam, p.1051-1058.
64. Hoek, E., Kaiser, P.K., Bawden, W.F., 1995. *Support of underground excavation in hard rock.* Balkema, Rotterdam, 215 pp.
65. Hubbert, M.K. and Willis, D.G. 1957. Mechanics of hydraulic fracturing, *JPT*, Trans. AIME 210, p.153-166.
66. Huyakorn, P.S. and Pinder, G.F., 1983. *Computational Methods in Subsurface Flow*, Academic Press, New York.
67. Hoffers, B., Engeser, B., and Rischmuller, H., 1994. Wellbore stability of a superdeep borehole in crystalline rock, The KTB-Hauptbohrung, Germany, Eyrock'94, Balkema, Rotterdom, p.371-378.
68. Istok J., 1989. *Groundwater Modeling by the Finite Element Method*, Water Resources Monograph 13, American Geophysical Union.
69. Jaeger J.C. and Cook N.G.W., 1979. *Fundamentals of Rock Mechanics*, 3rd edition, Chapman and Hall.
70. Javandel I. and Witherspoon P.A., 1968. Application of the Finite Element Method to Transient Flow in Porous Media, Society of Petroleum Engineers Journal, Vol.8, No.3, p.241-252.
71. Kazemi H., Seth M.S. and Thomas G.W., 1969. The Interpretation of Interference Tests in Naturally Fractured Reservoirs with Uniform Fracture Distribution, *Soc. Pet. Eng. J.*, 9, p.463-472.
72. Kazemi H., 1969. Pressure Transient Analysis of Naturally Fractured Reservoirs with Uniform Fracture Distribution, *Soc. Pet. Eng. J.*, 9, p.451-462.
73. Kazemi H. and Gilman J.R., 1993. Multiphase Flow in Fractured Petroleum Reservoirs. *Flow and Contaminant Transport in Fractured Rock*, p.267-270, Academic Press, Inc.

74. Khaled M.Y., Beskos D.E. and Aifantis E.C., 1984. On the Theory of Consolidation with Double Porosity - III A Finite Element Formulation, *Int. J. Analytic. Numer. Meth. Geomech.*, Vol.8, p.101-123.

75. Kennedy, T.C. and Lindberg, H.E., 1978. Model tests for plastic response of lined tunnels, *ASCE J. Eng. Mech, Div.* Vol.104, p.399-420.

76. Kovari, K., 1977. The Elasto-plastic Analysis in the Design Practice of Underground Openings, *Finite Elements in Geomechanics*, ed. G. Gudehus, John Wiley & Sons, 377-412.

77. Kwong, A. and Kaiser, P.K., 1991. Failure mechanisms of boreholes in rock with anisotropic strength and local weaknesses, *Proc. 44th Canadian Geotechnical Conf.*, Calgary, Canada, Vol.1, 35, p.1-10.

78. Ladanyi, B., 1974. Use of the long-term strength concept in the determination of ground pressure on tunnel linings. *Proc. 3rd Int. Congress on Rock Mech.*, p.1150-1156.

79. Last, N.C. and McLean, M.R., 1995. Assessing the impact of trajectory on wells drilled in an overthrust region, paper SPE 30465 presented at Annual Technical Conference, Dallas, p.161-171.

80. Lekhnitskii, S.G., 1981. *Theory of Elasticity of an Anisotropic Body*, Mir Publ., Moscow.

81. Lewis R.W. and Ghafouri H.R., 1997. A Novel Finite Element Double Porosity Model for Multiphase Flow Through Deformable Fractured Porous Media, *Int. J. Analytic. Numer. Meth. Geomech.*, Vol.21, p.789-816, 1997.

82. Lewis R.W. and Schrefler B.A., 1987. *The Finite Element Method in the Deformation and Consolidation of Porous Media*, Wiley, Chichester, 1987.

83. Lewis R.W. and Sukirman Y., 1993a, Finite Element Modeling of Three-Phase Flow in Deforming Saturated Oil Reservoirs, *Int. J. Analytic. Numer. Meth. Geomech.*, Vol.17, p.577-598.

84. Lewis R.W. and Sukirman Y., 1993b. Finite Element Modeling for Simulating the Surface Subsidence above a Compacting Hydrocarbon Reservoir, *Int. J. Analytic. Numer. Meth. Geomech.*, Vol.18, p.619-639.

85. Li, X., 1998. *Thermoporomechanical Modeling of Inclined Boreholes*, Ph.D.

dissertation, The University of Oklahoma.

86. Li, X., Cui, L. and Roegiers, J.-C., 1998. Thermoporoelastic analyses of inclined boreholes, SPE/ISRM presented at Eurock'98 held in Trondheim, Norway.
87. Li, X., Tan, C.P. and Roegiers, J.-C., 1997. Collaborative development of a wellbore stability analysis software with dertermation of horizontal stress bounds from wellbore data, *in Prediction and Performance in Rock Mechanics and Rock Engineering*, Barla, G. ed., Torino, Italy.
88. Liu, C., Heliot, D., Cao, S. and Wang, A., 1999. Integrated Geomechanics Evalution of Wellbore Stability in Bohai Bay China, *Int. Symp. on Coupled Phenomena in Civil, Min. & Petro. Eng.*, Hainan, China.
89. Mattax C.C. and Dalton R.L., 1990. *Reservoir Simulation*, SPE Monograph, Vol.13.
90. Mandel, J., 1953. Consolidation des sols, *Geotechnique*, 3, p.287-299.
91. Maury, V. and Sauzay, J.M., 1987. Borehole instabilities: case histories, rock mechanics approach, and results, paper SPE 16051 presented at the 1987 SPE/IADC Drilling Conference held in New Orleans, LA.
92. Maury, V. and Zurdo, C., 1996. Drilling-induced lateral shifts along pre-existing fractures: a common cause of drilling problems, *SPE Drilling & Completion*, March.
93. Mclean, M.R. and Addis, M.A., 1990. Wellbore stability analysis: A review of current methods analysis and their field application, Pro SPE/IADC 19941, Drilling Conf., Houston, p.261-274.
94. Meng, F., 1998. *Three-dimensional Finite Element Modeling of Two-phase Fluid Flow in Deformable Naturally Fractured Reservoirs*, The University of Oklahoma.
95. Mody, F.K. and Hale, A.H., 1993. A borehole stability model to coupled the mechanics and chemistry of drilling fluid shale interaction, paper SPE 25728 presented at 10th SPE/IADC Drilling Conference, Amsterdam.
96. Mogi, K., 1972. Fracture and flow of rocks into the upper mantle, *Tectonal Physics*, Vol. 13(1-4), p.541-568.
97. Monus, F. L., Broussard, F. W., Ayoub, J. A. and Norman, W. D., 1992. Fracturing unconsolidated sand formations offshore Gulf of Mexico, paper SPE 24844 presented at the 67th Annual Technical Conference and Exhibition held in Washington DC, October 4-7, p. 817-831.

98. Nair, R., Bai, M., Abousleiman, Y. and Zaman, M.M., 2000. Finite element modeling of an inclined wellbore in a fractured porous medium saturated with oil and gas, *Rock Around the Rim*, Balkema, Rotterdam, p.189-196.

99. Nair, R., 2001. Personal communication.

100. Odeh A.S., 1965. Unsteady-state Behavior of Naturally Fractured Reservoirs, *Soc. Pet. Eng. J.*, 5, p.60-66.

101. Ong, S.H., 1994. *Borehole stability*, Ph.D. dissertation, The University of Oklahoma.

102. Ong, S.H. and Roegiers, J.-C., 1993a. Horizontal wellbore collapse in an anisotropic formation, paper SPE 225504.

103. Ong, S.H. and Roegiers, J.-C., 1993b. Influence of anisotropies in borehole stability, *Int. J. Rock Mech. Min. Sci. & Geomech. Abstr.*, Vol.30, 7, p.1069-1075.

104. Papamichos, E., Vardoulakis, I. and Sulem, J., 1994. Generalized continuum models for borehole stability analysis. Proc. SPE/ISRM Eurock'94, Rotterdam, Balkema, p.37-44.

105. Pande, G.N., Beer, G. and Williams, J.R. 1990, *Numerical Methods in Rock Mechanics*, Wiley.

106. Pinder G.F. and Frind E.O., 1972. Application of Galerkin's Procedure to Aquifer Analysis, *Water Resour. Res.*, Vol.8, No.1, p.108-120.

107. Plumb, R., Papanastasiou, P. and Last, N.C., 1998. Constraining the state of stress in tectonically active settings, paper SPE/ISRM 47240 presented at the SPE/ISRM Eurock'98 Conference, Trondheim, Norway.

108. Pruess K. and Tsang Y.W., 1990. On Two-Phase Relative Permeability and Capillary Pressure of Rough-Walled Rock Fractures, *Water Resources Research*, Vol.26, No.9, p.1915-1926.

109. Payne, M.L., Wilton, B. and Ramos, G., 1995. Recent advances and emerging technologies for extended reach drilling , paper SPE 29920 presented at Int. Mtg. Petr. Eng., Beijing, p.291-308.

110. Ramos, G.G., Mouton, D.E., Wilton, B.S. and Leksmono, 1998. Integrating rock mehanics with drilling strategies in a Tectonic belt, offshore Bali, Indonesia, paper SPE/ISRM 47286 presented at the SPE/ISRM Eurock'98 Conference, Trondheim,

Norway.

111. Ramos, G.G., Wilton, B.S. and Polillo, A.F., 1996. Usage and applicability of pseudo-3D stress analysis in borehole stability problems in petroleum drilling and production operations, in *Rock Mechanics*, Aubertin, Hassani & Mitri (eds), Balkema, Rotterdam, p.1067-1073.

112. Risnes, R., Bratli, R.K. and Horsrud, P., 1982. Sand stresses around a wellbore, *SPEJ*, Dec., p.883-894.

113. Roegiers, J.-C., 1990. Stability and Failure of Circular Openings, *Rock at Great Depth*, Maury & Fourmaintraux (eds), Balkema, Rotterdam, p.1115-1121.

114. Roegiers, J.-C., 1999. *Advanced Rock Mechanics* (*Class Notes*), The University of Oklahoma.

115. Roegiers, J.-C., 2001. Importance of rock mechanics to the petroleum industry, SPE Distinguished Lecture presented in Oklahoma City.

116. Roegiers, J.-C. and Detournay, E., 1988. Considerations on failures initiation in inclined boreholes, Key Questions in Rock mechanics, Cundal, P. et al., eds., *Proc. 29th U.S. Rock Mech. Symp.*, Rotterdam, Balkema.

117. Saada, A.S., 1974. *Elasticity: Theory and Application*, Pergamon Press, New York.

118. Santareli, F.J., 1987. *Theoretical and Experimental Investigation of the Stability of the Axisymmetric Wellbore*, Ph.D. thesis, Imperial College of Science and Technology, The University of London.

119. Santareli, F.J. and Brown, E.T., 1987. Performance of deep boreholes in rock with a confining pressure dependent elastic modulus, in *Proc. 6th Int. Society of Rock Mech.*, Herger, G. and Vongpaisal, S. (eds.), Vol.2, Balkema, Rotterdam, p.1217-1222.

120. Shao, J.F. and Khazraei, R., 1994. Wellbore stability analysis in brittle rocks with continuos damage model, *Proc. SPE/ISRM Eurock'94*, Rotterdam, Balkema, p. 215-222.

121. Sherwood, J.D. and Bailey, L., 1994. Swelling of shale around a cylindrical wellbore. *Proc. R. Soc. Lond.* A 444, p.161-184.

122. Shen B. and Barton, N., 1997. The distributed zone around tunnels in jointed

rock masses. *Int. J. Rock Mech. Min. Sci. Geomech. Abstr.*, 34 (1), p.117-125.

123. Shield, R.T., 1955. On Coulomb's law of failure in soils, *J. Mech. and Phys. Solids*, 4.

124. Smith, I.M. and Griffiths, D.V., 1988. *Programming the Finite Element Method*, 2nd edition, John Wiley & Sons, New York.

125. Terzaghi K., 1943. *Theory Soil Mechanics*, John Wiley & Sons, New York.

126. Wang, Y. and Dusseault, M.B., 1991. Borehole yield and hydraulic fracture initiation in poorly consolidated rock media. *Int. J. Rock Mech. Min. Sci. & Geomech. Abst.*, Vol.28, No.4, 247-260

127. Warren J.E. and Root P.J., 1963. The Behavior of Naturally Fractured Reservoirs, *Soc. Pet. Eng. J., Trans., AIME*, Vol.228, p.245-255.

128. Wilson, R.C. and Willis, D.N., 1986. Successful high angle drilling in the Stratfjord Field, paper SPE 15465 presented at the 61st Annual Technical Conference & Exhibition, New Orleans, LA.

129. Wilson R.K. and Aifantis E.C., 1982. On the Theory of Consolidation with Double Porosity, *Int. J. Eng. Sci.*, Vol.20, No.9, p.1009-1035.

130. Willson, S.M., Last, N.C., Zoback M.D. and Moos, D., 1999. Drilling in South America: a wellbore stability approach for complex geologic conditions, paper SPE 53940 presented at Litin America and Caribbean Petroleum Engineering Conference held in Caracas, Venezuela.

131. Wiprut, D.J. and Zoback, M.D., 1998. High horizontal stress in the Visund field, Norwegian North Sea: Consequences for borehole stability and sand production, paper SPE/ISRM 47244 presented at the SPE/ISRM Eurock'98 Conference, Trondheim, Norway.

132. Woodland, D.C., 1990. Borehole instability in the western Canadian overthrust belt, *SPS Drilling Engineers*, Vol.5, p.23-33.

133. Zaman, M.M., Cao, J., Bai, M. and Roegiers, J.-C., 1998, Modeling flow in heterogeneous dual-porosity media, *Int. J. Rock Mech. Min. Sci.*, 35, 4/5, 473.

134. Zhang, J., Roegiers, J.-C. and Bai, M., 2000. Horizontal borehole stability for naturally fractured reservoir, *paper SPE 65513 presented at International Conference on Horizontal Well Technology*, Calgary, Canada, 6-8 November.

135. Zhang, H., Bai, M., Abousleiman, Y. and Roegiers, J.-C., 1999. An elastoplastic analysis of non-isothermal consolidation, *Int. J. Num. Anal. Meth. Geomech.*, 23, p.1535-1557.

136. Zheng, Z., Kemeny, J. and Cook, N.G.W., 1989. Analysis of borehole breakouts, *JGR*, 94, B6, p.7171-7182.

137. Zheng, Z., 1998. Integrated borehole stability analysis – against tradition, paper SPE 47282 presented at SPE/ISRM Eurock '98, Trondheim, Norway.

138. Zienkiewicz O.C., 1977. The Finite Element Method, McGraw-Hill, 3rd edition, New York.

139. Zienkiewicz O.C. and Shiomi, T., 1984. Dynamic behavior of saturated porous media: the generalized Biot formulation and its numerical solution, *Int. J. Numer. Anal. Methods Geomech.*, Vol.8, p.71-96.

Appendix A

Terms in Finite Element Matrices

The following equations are the terms of the finite element formulations given in Chapter 4:

$$\mathbf{K} = \int_{\Omega} \mathbf{B}^{\mathrm{T}} \mathbf{D}_{\mathrm{mf}} \mathbf{B} d\Omega \tag{A.1}$$

$$\mathbf{R}_1 = \alpha_{ma} \int_{\Omega} \mathbf{B}^{\mathrm{T}} \mathbf{D}_{\mathrm{mf}} \mathbf{C}_{\mathrm{ma}} \mathbf{m} \mathbf{M} d\Omega \tag{A.2}$$

$$\mathbf{R}_2 = \alpha_{fr} \int_{\Omega} \mathbf{B}^{\mathrm{T}} \mathbf{D}_{\mathrm{mf}} \mathbf{C}_{\mathrm{fr}} \mathbf{m} \mathbf{M} d\Omega \tag{A.3}$$

$$\mathbf{L}_1 = \frac{1}{\mu} \int_{\Omega} \nabla \mathbf{M}^{\mathrm{T}} \mathbf{k}_{\mathrm{ma}} \nabla \mathbf{M} \mathrm{d}\Omega \tag{A.4}$$

$$\mathbf{L}_2 = \frac{1}{\mu} \int_{\Omega} \nabla \mathbf{M}^{\mathrm{T}} \mathbf{k}_{\mathrm{fr}} \nabla \mathbf{M} \mathrm{d}\Omega \tag{A.5}$$

$$\mathbf{N}_1 = \beta_{ma} \int_{\Omega} \mathbf{M}^{\mathrm{T}} \mathbf{M} d\Omega \tag{A.6}$$

$$\mathbf{N}_2 = \beta_{fr} \int_{\Omega} \mathbf{M}^{\mathrm{T}} \mathbf{M} d\Omega \tag{A.7}$$

$$\mathbf{Q} = -\omega \int_{\Omega} \mathbf{M}^{\mathrm{T}} \mathbf{M} d\Omega \tag{A.8}$$

$$\mathbf{M}_1 = \alpha_{ma} \int_{\Omega} \mathbf{N}^{\mathrm{T}} \mathbf{D}_{\mathrm{mf}} \mathbf{C}_{\mathrm{ma}} \mathbf{m} \mathbf{B} d\Omega \tag{A.9}$$

$$\mathbf{M}_2 = \alpha_{fr} \int_{\Omega} \mathbf{N}^{\mathrm{T}} \mathbf{D}_{\mathrm{mf}} \mathbf{C}_{\mathrm{fr}} \mathbf{m} \mathbf{B} d\Omega \tag{A.10}$$

$$\mathbf{f} = \int_{\Gamma} \mathbf{N} \mathbf{f}^{*} d\Gamma \tag{A.11}$$

$$\mathbf{q}_{\mathrm{ma}} = \int_{\Gamma} \mathbf{M} \dot{\mathbf{q}}^{*}_{\mathrm{ma}} d\Gamma \tag{A.12}$$

$$\mathbf{q}_{\mathrm{fr}} = \int_{\Gamma} \mathbf{M} \dot{\mathbf{q}}^{*}_{\mathrm{fr}} d\Gamma \tag{A.13}$$

Appendix B

Invariants of the Stress and Stress Deviator Tensors

There are three invariants of the stress, three invariants of the effective stress, three invariants of the stress deviator, and three invariants of the effective stress deviator in poro-mechanics. These invariants used in Chapter 4 and Chapter 7 are listed as follows:

- Invariants of the stress

$$I_1 = \sigma_{ii} = \sigma_x + \sigma_y + \sigma_z \tag{B.1}$$

$$I_2 = \frac{1}{2}\sigma_{ij}\sigma_{ji} = \sigma_x\sigma_y + \sigma_y\sigma_z + \sigma_z\sigma_x - \tau_{xy}^2 - \tau_{yz}^2 - \tau_{zx}^2 \tag{B.2}$$

$$I_3 = \frac{1}{3}\sigma_{ij}\sigma_{jk}\sigma_{ki} = \sigma_x\sigma_y\sigma_z + 2\tau_{xy}\tau_{yz}\tau_{zx} - \sigma_x\tau_{yz}^2 - \sigma_y\tau_{zx}^2 - \sigma_z\tau_{xy}^2 \tag{B.3}$$

- Invariants of the effective stress:

$$I_1' = \sigma_{ii}' = \sigma_x' + \sigma_y' + \sigma_z' \tag{B.2}$$

$$I_2' = \frac{1}{2}\sigma_{ij}'\sigma_{ji}' = \sigma_x'\sigma_y' + \sigma_y'\sigma_z' + \sigma_z'\sigma_x' - \tau_{xy}^2 - \tau_{yz}^2 - \tau_{zx}^2 \tag{B.3}$$

$$I_3' = \frac{1}{3}\sigma_{ij}'\sigma_{jk}'\sigma_{ki}' = \sigma_x'\sigma_y'\sigma_z' + 2\tau_{xy}\tau_{yz}\tau_{zx} - \sigma_x'\tau_{yz}^2 - \sigma_y'\tau_{zx}^2 - \sigma_z'\tau_{xy}^2 \tag{B.4}$$

- Invariants of the stress deviator:

$$J_1 = s_{ii} = 0 \tag{B.5}$$

$$J_2 = \frac{1}{2} s_{ij} s_{ji} = \frac{1}{6}[(\sigma_x - \sigma_y)^2 + (\sigma_y - \sigma_z)^2 + (\sigma_z - \sigma_x)^2] + \tau_{xy}^2 + \tau_{yz}^2 + \tau_{zx}^2 \tag{B.6}$$

$$J_3 = \frac{1}{3} s_{ij} s_{jk} s_{ki} = s_x s_y s_z + 2\tau_{xy}\tau_{yz}\tau_{zx} - s_x \tau_{yz}^2 - s_y \tau_{zx}^2 - s_z \tau_{xy}^2 \tag{B.7}$$

where s_{ij} is the deviatoric stress, $s_{xy} = \tau_{xy}$, $s_x = (2\sigma_x - \sigma_y - \sigma_z)/3$, etc.

Invariants of the effective stress deviator are same as the invariants of the stress deviator.

Appendix C

Terms in Elastoplastic One-dimensional Consolidation

The following equations are coefficients of the one-dimensional elastoplastic consolidation formulations in Chapter 5:

$$g_{11} = \frac{\mu}{k_1}\left(\frac{D_{12}^2 C_1^2 \alpha_1^2}{\eta_{12}} + \varphi_1^{\cdot} \right) \tag{C.1}$$

$$g_{12} = \frac{\mu D_{12}^2 C_1 C_2 \alpha_1 \alpha_2}{k_1 \eta_{12}} \tag{C.2}$$

$$g_{13} = \frac{\mu \omega}{k_1} \tag{C.3}$$

$$g_{14} = \frac{\mu}{k_1}\left(\frac{D_{12}^2 C_1^2 \alpha_1 \beta_1}{\eta_{12}} + \alpha_{h1} \right) \tag{C.4}$$

$$g_{15} = \frac{\mu D_{12}^2 C_1 C_2 \alpha_1 \beta_2}{k_1 \eta_{12}} \tag{C.5}$$

$$g_{21} = \frac{\mu D_{12}^2 C_1 C_2 \alpha_1 \alpha_2}{k_2 \eta_{12}} \tag{C.6}$$

$$g_{22} = \frac{\mu}{k_2}\left(\frac{D_{12}^2 C_1^2 \alpha_{21}^2}{\eta_{12}} + \varphi_2^{\cdot} \right) \tag{C.7}$$

$$g_{23} = \frac{\mu \omega}{k_2} \tag{C.8}$$

$$g_{24} = \frac{\mu D_{12}^2 C_1 C_2 \alpha_2 \beta_1}{k_2 \eta_{12}} \tag{C.9}$$

$$g_{25} = \frac{\mu}{k_2}\left(\frac{D_{12}^2 C_2^2 \alpha_2 \beta_2}{\eta_{12}} + \alpha_{h2} \right) \tag{C.10}$$

$$g_{31} = \frac{\beta_1 T_{10} D_{12} C_1 \alpha_1}{k_1^{\bullet} \eta_{12}} \tag{C.11}$$

$$g_{32} = \frac{\beta_1 T_{10} D_{12} C_2 \alpha_2}{k_1^{\bullet} \eta_{12}} \tag{C.12}$$

$$g_{34} = \frac{1}{k_1^{\bullet}}\left(\frac{D_{12} C_1 \beta_1^2 T_{10}}{\eta_{12}} + S_1^{\bullet} \right) \tag{C.13}$$

$$g_{35} = \frac{\beta_1 \beta_2 T_{10} D_{12} C_2}{k_1^{\bullet} \eta_{12}} \tag{C.14}$$

$$g_{36} = \frac{\Gamma^{\bullet}}{k_1^{\bullet}} \tag{C.15}$$

$$g_{41} = \frac{\beta_1 T_{20} D_{12} C_1 \alpha_1}{k_2^{\bullet} \eta_{12}} \tag{C.16}$$

$$g_{42} = \frac{\beta_2 T_{20} D_{12} C_2 \alpha_2}{k_2^{\bullet} \eta_{12}} \tag{C.17}$$

$$g_{44} = \frac{\beta_1 \beta_2 T_{10} D_{12} C_1}{k_2^{\bullet} \eta_{12}} \tag{C.18}$$

$$g_{46} = \frac{\Gamma^{\bullet}}{k_2^{\bullet}} \tag{C.19}$$

$$g_{11}^{p} = \frac{\mu}{k_1}\left(\frac{(D_{12}^{p} C_1^{p} \alpha_1)^2}{\eta_{12}^{p}} + \varphi_1^{\bullet} \right) \tag{C.21}$$

$$g_{12}^{p} = \frac{\mu (D_{12}^{p})^2 C_1^{p} C_2 \alpha_1 \alpha_2}{k_1 \eta_{12}^{p}} \tag{C.22}$$

$$g_{13}^{p} = \frac{\mu \omega}{k_1} \tag{C.23}$$

$$g_{14}^{p} = \frac{\mu}{k_1}\left(\frac{(D_{12}^{p} C_1^{p})^2 \alpha_1 \beta_1^{p}}{\eta_{12}^{p}} + \alpha_{h1} \right) \tag{C.24}$$

$$g_{15}^{p} = \frac{\mu (D_{12}^{p})^2 C_1^{p} C_2 \alpha_1 \beta_2^{p}}{k_1 \eta_{12}^{p}} \tag{C.25}$$

$$g_{21}^{p} = \frac{\mu (D_{12}^{p})^{2} C_{1}^{p} C_{2} \alpha_{1} \alpha_{2}^{p}}{k_{2} \eta_{12}^{p}} \tag{C.26}$$

$$g_{22}^{p} = \frac{\mu}{k_{2}} \left(\frac{(D_{12}^{p} C_{1}^{p} \alpha_{1})^{2}}{\eta_{12}^{p}} + \varphi_{2}^{\bullet} \right) \tag{C.27}$$

$$g_{23}^{p} = \frac{\mu \omega}{k_{2}} \tag{C.28}$$

$$g_{24}^{p} = \frac{\mu (D_{12}^{p})^{2} C_{1}^{p} C_{2} \alpha_{2} \beta_{1}^{p}}{k_{2} \eta_{12}^{p}} \tag{C.29}$$

$$g_{25}^{p} = \frac{\mu}{k_{2}} \left(\frac{(D_{12}^{p} C_{2})^{2} \alpha_{2} \beta_{2}^{p}}{\eta_{12}^{p}} + \alpha_{h2} \right) \tag{C.30}$$

$$g_{31}^{p} = \frac{\beta_{1}^{p} T_{10} D_{12}^{p} C_{1}^{p} \alpha_{1}}{k_{1}^{\bullet} \eta_{12}^{p}} \tag{C.31}$$

$$g_{32}^{p} = \frac{\beta_{1}^{p} T_{10} D_{12}^{p} C_{2} \alpha_{2}}{k_{1}^{\bullet} \eta_{12}^{p}} \tag{C.32}$$

$$g_{34}^{p} = \frac{1}{k_{1}^{\bullet}} \left(\frac{D_{12}^{p} C_{1}^{p} (\beta_{1}^{p})^{2} T_{10}}{\eta_{12}^{p}} + S_{1}^{\bullet} \right) \tag{C.33}$$

$$g_{35}^{p} = \frac{\beta_{1}^{p} \beta_{12}^{p} T_{10} D_{12}^{p} C_{2}}{k_{1}^{\bullet} \eta_{12}^{p}} \tag{C.34}$$

$$g_{36}^{p} = \frac{\Gamma^{\bullet}}{k_{1}^{\bullet}} \tag{C.35}$$

$$g_{41}^{p} = \frac{\beta_{1}^{p} T_{20} D_{12}^{p} C_{1}^{p} \alpha_{1}}{k_{2}^{\bullet} \eta_{12}^{p}} \tag{C.36}$$

$$g_{42}^{p} = \frac{\beta_{42}^{p} T_{20} D_{12}^{p} C_{2} \alpha_{2}}{k_{2}^{\bullet} \eta_{12}^{p}} \tag{C.37}$$

$$g_{44}^{p} = \frac{\beta_{1}^{p} \beta_{12}^{p} T_{10} D_{12}^{p} C_{1}^{p}}{k_{2}^{\bullet} \eta_{12}^{p}} \tag{C.38}$$

$$g_{45}^{p} = \frac{1}{k_{2}^{\bullet}} \left(\frac{D_{12}^{p} C_{2} (\beta_{12}^{p})^{2} T_{20}}{\eta_{12}^{p}} + S_{2}^{\bullet} \right) \tag{C.39}$$

$$g_{46}^{p} = \frac{\Gamma^{\bullet}}{k_{2}^{\bullet}} \tag{C.40}$$

Appendix D

Stress-dependent Permeability in Fractured Media

D.1 Introduction

The fractured rock mass can be described as a composition of series of blocks of intact rock separated by natural fractures. Fluid flow through the rock mass is determined both by the properties of the rock matrix and the fractures. The rock matrix usually has such low permeability that the fractures are dominant and fluid flow occurs mainly through fractures. Conceptualization of flow in a single fracture can be given through the parallel plate analogy where a fracture is idealized as a planar opening having a constant aperture. The magnitude of permeability of a single fracture, parallel to its plane, is the given by:

$$k_f = \frac{b^2}{12} \tag{D.1.1}$$

where b is the effective fracture aperture, and k_f is the fracture permeability.

The permeability of a set of parallel fractures is constant in every direction parallel to the set and its magnitude is given by:

$$k_{fr} = \frac{b^3}{12s} \tag{D.1.2}$$

where k_{fr} is the set permeability, and s is the mean fracture spacing.

The permeability change in the fracture set due to the aperture change can be expressed as follows:

$$k = \frac{(b+\Delta b)^3}{12s} = k_0(1+\frac{\Delta b}{b})^3 \qquad \text{(D.1.3)}$$

where k is the permeability change due to the aperture increment Δb, and $k_0 = b^3/12s$.

With changing stresses, the aperture, the relative contact surface area and the degree of asperity contact of a fracture change. Thus, fluid flow through fractures and the subsequent permeabilities of the rock mass are directly related to stress and resultant deformations. A lot of in-situ and laboratory experiment results have shown the flow through fractured rock to be highly sensitive to changes in effective stresses. Various authors have proposed many models to describe the variation of fracture permeability with stress. In the present study, fracture aperture and permeability changes due to three-dimensional stress variations in the fractured media are studied.

D.2 Permeability-stress Relation in Fractured Media

In order to determine stress-dependent permeability in fractured media, both the fracture aperture variation and the rock matrix deformation need to be considered. To derive the permeability and stress relation, an idealized three-dimensional regularly spaced fracture-matrix system is assumed, as illustrated in Figure D.2.1.

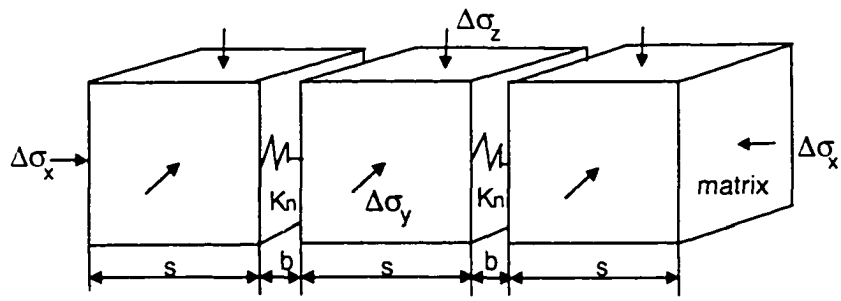


Figure D.2.1 Coupled fracture-matrix system with stresses.

The change of total displacement along x-direction is the sum of the fracture displacement change and the matrix displacement change; i.e.

$$\Delta u_{tx} = \Delta u_{fx} + \Delta u_{rx} \tag{D.2.1}$$

where Δu_{tx}, Δu_{fx}, and Δu_{rx} are the displacements of total fracture-matrix system, fracture and rock matrix, respectively.

Therefore, the displacement across the fracture can be obtained by:

$$\Delta u_{fx} = \Delta u_{tx} - \Delta u_{rx} \tag{D.2.2}$$

The above equation can be expressed as the strain form:

$$\Delta u_{fx} = (s_x + b_x)\Delta \varepsilon_{tx} - s_x \Delta \varepsilon_{rx} \tag{D.2.3}$$

where s_x and b_x are the fracture spacing and aperture along x-direction, respectively; $\Delta \varepsilon_{tx}$ and $\Delta \varepsilon_{rx}$ are the total and matrix strains, respectively.

The total strain along x-direction can be obtained according to Hooke's law:

$$\Delta \varepsilon_{tx} = \frac{1}{E_{mx}} \left[\Delta \sigma_x - \nu (\Delta \sigma_y + \Delta \sigma_z) \right] \tag{D.2.4}$$

where E_{mx} is the Young's modulus of the rockmass in x-direction.

According to Hooke's law, the matrix strain along the x-direction may be discribed by:

$$\Delta\varepsilon_{rx} = \frac{1}{E_r}\left[\Delta\sigma_x - \nu(\Delta\sigma_y + \Delta\sigma_z)\right] \tag{D.2.5}$$

where, E_r is the Young's modulus of the rock matrix.

Substituting Equations (D.2.4) and (D.2.5) into Equation (D.2.3), one can obtain the change of the fracture aperture due to the stress variation; i.e.

$$\Delta u_{fx} = \left(\frac{(s_x + b_x)}{E_{mx}} - \frac{s_x}{E_r}\right)\left[\Delta\sigma_x - \nu(\Delta\sigma_y + \Delta\sigma_z)\right] \tag{D.2.6}$$

The Young's modulus of the rockmass (E_{mx}) related to the properties of the intact rock matrix and the fractures can be expressed as follows:

$$\frac{1}{E_{mx}} = \frac{1}{E_r} + \frac{1}{K_{nx}s_x} \tag{D.2.7}$$

where K_{nx} is the fracture normal stiffness in x-direction.

Substituting Equation (D.2.7) into Equation (D.2.6), the fracture displacement in x-direction can be obtained:

$$\Delta u_{fx} = \left(\frac{1}{K_{nx}} + \frac{b_x}{K_{nx}s_x} - \frac{s_x}{E_r}\right)\left[\Delta\sigma_x - \nu(\Delta\sigma_y + \Delta\sigma_z)\right] \tag{D.2.8}$$

The fracture permeability in the direction perpendicular to x-direction can be calculated directly from the parallel plate analog defined in Equation (D.1.3). With reference to Equations (D.2.8) and (D.1.3), the change of fracture permeability may be evaluated as:

$$k_z = k_{0z}\left\{1-\left(\frac{1}{K_{nx}b_x}+\frac{1}{K_{nx}s_x}-\frac{s_x}{E_r b_x}\right)\left[\Delta\sigma_x-\nu(\Delta\sigma_y+\Delta\sigma_z)\right]\right\}^3 \qquad \text{(D.2.9)}$$

where k_{0z} and k_z are the permeabilities along z-direction before and after stress change, respectively.

The generalized permeability-stress relation may be written according to the above equation:

$$k_k = k_{0k}\left\{1-\left(\frac{1}{K_{ni}b_i}+\frac{1}{K_{ni}s_i}-\frac{s_i}{E_r b_i}\right)\left[\Delta\sigma_i-\nu(\Delta\sigma_j+\Delta\sigma_k)\right]\right\}^3 \qquad \text{(D.2.10)}$$

where k_{0k} and k_k are the permeabilities along k-direction before and after stress changes, $i = x, y, z; j = y, z, x; i = z, x, y; i \neq j \neq k$.

Only one set of fractures is examined in the above analysis. When three parallel fracture sets exist in the x-, y- and z-directions, respectively, permeability changes along k-direction may be written as:

$$\begin{aligned} k_k = k_{0k}\Bigg\{1&-\left(\frac{1}{K_{ni}b_i}+\frac{1}{K_{ni}s_i}-\frac{s_i}{E_r b_i}\right)\left[\Delta\sigma_i-\nu(\Delta\sigma_j+\Delta\sigma_k)\right] \\ &-\left(\frac{1}{K_{nj}b_j}+\frac{1}{K_{nj}s_j}-\frac{s_j}{E_r b_j}\right)\left[\Delta\sigma_j-\nu(\Delta\sigma_i+\Delta\sigma_k)\right]\Bigg\}^3 \end{aligned} \qquad \text{(D.2.11)}$$